

# Kinetic and fluid modeling of ion thruster plumes

INAUGURALDISSERTATION

zur

Erlangung des akademischen Grades eines

Doktors der Naturwissenschaften

(Dr. rer. nat.)

der

Mathematisch-Naturwissenschaftlichen Fakultät

der

Universität Greifswald

vorgelegt von

Daniel Lars Kahnfeld

geboren am 24. Dezember 1990

in Stralsund, Deutschland

Greifswald, den 26. September 2019

Dekan: Prof. Dr. Werner Weitschies  
1. Gutachter: Prof. Dr. Ralf Schneider  
2. Gutachter: Dr. Francesco Taccogna  
Tag der Disputation: 03. Februar 2020





## Abstract

The importance of ion propulsion devices as an option for in-space propulsion of space crafts and satellites continues to grow. They are more efficient than conventional chemical thrusters, which rely on burning their propellant, by ionizing the propellant gas in a discharge channel and emitting the heavy ions at very high velocities. The ion emission region of a thruster is called the plume and extends several meters axially and radially downstream from the exit of a thruster. This region is particularly important for the efficiency of a thruster, because it determines energy and angular distribution of the emitted ions. It also determines the interaction with the carrier space craft by defining the electric potential shape and the fluxes and energies of the emitted high energy ions, which are the key parameters for sputter erosion of satellite components such as solar panels. Developing new ion thrusters is expensive because of the high number of prototypes and testing cycles required. Numerical modeling can help to reduce the costs in thruster development, but the vastly differing length and time scales of the system, particularly the large differences of scales between the discharge chamber and the plume, make a simulation challenging. Often both regions are considered to be decoupled and are treated with different models to make their simulation technically feasible. The coupling between channel and plume plasmas and its influence on each other is disregarded, because there is no interaction between the two regions. Therefore, this thesis investigates the physical effects which arise from this coupling as well as models suitable for an integrated simulation of the whole coupled problem of channel and plume plasmas. For this purpose the High Efficiency Multistage Plasma Thruster (HEMP-T) ion thruster is considered.

For the discharge channel plasma, a fully kinetic model is required and the Particle-in-Cell (PIC) method is applied. The PIC method requires very high spatial and temporal resolutions which makes it computationally costly. As a result, only the discharge channel and the near-field plume close to the channel exit can be simulated. In the channel, the results show that electrons are magnetized and follow the magnetic field lines. The orientation of the magnetic field there is mostly parallel to the symmetry axis and the channel walls which results in a high parallel electron transport and leads to a flat electric potential and a reduced plasma-wall sheath. Only at the magnetic cusps, which are characteristic of HEMP-Ts the electrons are guided towards the wall, with ions following due to quasineutrality, where a classical plasma-wall sheath develops. The ion-wall contact is thus limited to the cusp region. The small radial drop of the potential towards the wall gives rather low energies of ions impinging at the wall and minimizes erosion in the HEMP-T.

In the near-field plume, which extends from the thruster exit plane to some centimeters downstream, the ion emission characteristics is defined. The ratio of radial and axial electric field components in this region determines the ion emission angle which should be minimized for maximum thruster efficiency. The plasma discharge in the channel produces high plasma densities and the subsequent drop from plasma to vacuum potential occurs further downstream for higher densities. This increases the ratio of radial and axial electric field components because the plasma expands radially outside of the confinement from the dielectric discharge channel walls. The potential structure in the near-field plume impacts also the supply of electrons for the channel discharge because the electrons enter the channel from the plume. An effect which arises from this coupling is the breathing mode oscillation. It is an oscillation which is observed in all plasma quantities and is located near the thruster exit. The oscillation frequency measured in the simulation is in good agreement with a predator-prey estimate which validates this ansatz. However, the electron temperature, assumed constant in the predator-prey model, correlates inversely with the oscillation, i.e. it is minimal at the current maximum and vice versa, which contributes to the observed oscillations. Because of the oscillation of the plasma number density, the potential drop also oscillates in the exit region and thus the ratio of radial to axial electric field components, which results in the oscillation of the mean ion emission angle.

Regarding suitable models for a combined simulation of channel and plume plasmas, the PIC model for channel and near-field plume is explicitly coupled to a hybrid fluid-PIC model for the plume. The latter treats the electrons as a fluid, hence increasing the effective spatial and temporal resolutions which can be applied in the plume simulations at the cost of reduced accuracy of the electron model. Plasma densities decrease by two orders of magnitude two meters downstream from the channel exit. The explicitly coupled kinetic and hybrid PIC models are well suited for the computation of a HEMP-T and its plume expansion, but they disregard the coupling of channel and plume plasmas for which other methods are necessary. For this purpose a new approach is presented with a proof-of-principle validation. The limited spatial resolution in the plume can be overcome with the mesh-coarsening method, which increases the resolution in regions of low plasma density without numerical artifacts. Sub-cycling for the electrons in the plume can then be used to increase the temporal resolution in the plume. The combination of both methods, called the sub-cycling mesh-coarsening (SMC) algorithm in the scope of this work, promises high savings in computational cost which can make a combined simulation of plume and channel plasmas feasible.

# Contents

<b>1</b>	<b>Motivation</b>	<b>1</b>
<b>2</b>	<b>Basics</b>	<b>7</b>
2.1	Basic ion thruster physics . . . . .	7
2.2	Plasma modeling . . . . .	11
2.2.1	The Particle-In-Cell method . . . . .	12
2.2.2	Fluid modeling of plasmas . . . . .	19
<b>3</b>	<b>Simulation results</b>	<b>25</b>
3.1	Discharge channel . . . . .	26
3.1.1	Electrons . . . . .	26
3.1.2	Ions . . . . .	29
3.1.3	Neutrals . . . . .	30
3.1.4	Comparison to experiments and limits of the simulation . . . . .	31
3.2	Near-field plume . . . . .	33
3.3	Breathing mode oscillations . . . . .	36
3.4	Plume expansion . . . . .	40
3.5	Kinetic plume simulation . . . . .	44
<b>4</b>	<b>Conclusions</b>	<b>49</b>
<b>5</b>	<b>Bibliography</b>	<b>53</b>
<b>6</b>	<b>Cumulative thesis articles</b>	<b>63</b>
6.1	[P1] D. Kahnfeld et al. (2019), <i>Reviews of Modern Plasma Physics</i> <b>3</b> (1): 11 .	67
6.2	[P2] D. Kahnfeld et al. (2018), <i>Plasma Sources Science and Technology</i> <b>27</b> (12): 124002 . . . . .	110
6.3	[P3] J. Duras et al. (2017), <i>Journal of Plasma Physics</i> <b>83</b> (1): 595830107, Reprinted with permission . . . . .	120

6.4	[P4] J. Duras et al. (2016), <i>Plasma Physics and Technology</i> <b>3</b> (3): 126–130 .	132
6.5	[P5] T. Brandt et al. (2016), <i>Trans. JSASS Aerospace Tech. Japan</i> <b>14</b> (ists30): Pb_235–Pb_242 . . . . .	137
6.6	[P6] K. Lüskow et al. (2018), <i>Physics of Plasmas</i> <b>25</b> (1): 013508 Reproduced with the permission of AIP Publishing . . . . .	145
6.7	[P7] P. Matthias et al. (2019), <i>Contributions to Plasma Physics</i> : e201900028	152

**7 Declaration** **165**

**8 Acknowledgements** **167**

# 1 Motivation

Satellites play an important role in science and technology. They are used in technological applications impacting everyday life, such as communication [1, 2], geo positioning [3] and earth imaging services [4, 5]. In science, their use ranges from earth orbiting experimental facilities [6, 7] to deep space [8–11] and interplanetary missions [12, 13]. With smaller satellite systems becoming available [14] and with an increased number of players in the space sector, private [15] or national, launch costs reduce continually, all leading to an expected growth of the satellite market in coming years [16]. To further reduce launch costs of spacecrafts, the payload ratio, the fraction of the payload mass over the total mass of the spacecraft, must be increased. A high fraction of a satellites' non-payload mass is occupied by a thruster and its propellant which are required for propulsion, orbit stationing and orbit corrections [17]. The payload ratio can be increased by improving the efficiency of the thruster, which would reduce the amount of propellant required on a satellite.

A thruster generates a force to accelerate the space craft it is mounted on by ejecting a propellant with mass  $m_p$  from its exhaust. This force is called thrust,

$$T = -v_{ex} \frac{dm_p}{dt} = -v_{ex} \Gamma_p, \quad (1.1)$$

which depends on the exhaust velocity  $v_{ex}$  and the mass flow rate  $\Gamma_p$  of the propellant. To characterize the propellant efficiency of a thruster, the rocket equation,

$$\Delta v = v_{ex} \ln \left( \frac{m_S}{m_S + m_p} \right), \quad (1.2)$$

can be used. It quantifies the total change in velocity  $\Delta v$  a thruster can achieve for a space craft with an empty mass  $m_S$ . Note that  $\Delta v$  depends only on the exhaust velocity of the propellant for a constant propellant mass. As an efficiency measure which is independent

of space craft or propellant mass the so called specific impulse,

$$I_{sp} = \frac{v_{ex}}{g_0}, \quad (1.3)$$

is used, with the standard earth surface gravity  $g_0 = 9.8067 \text{ ms}^{-2}$ . This quantity is a measure of how effectively a thruster utilizes its propellant. For high efficiency, the  $I_{sp}$  of an ion thruster must be maximized. Thrusters for space propulsion can be distinguished based on their operational characteristics.

Chemical thrusters are used to launch rockets into space because they achieve very high thrusts. They rely on burning the propellant, which limits the maximum exhaust velocity and hence their  $I_{sp}$  to around 400 s [18]. Here, ion thrusters offer great benefits over chemical thrusters, because their  $I_{sp}$  is typically up to ten times higher at 3000 – 4000 s and can even reach 10000 s [18]. Their operational principle is based on the ionization of a propellant gas and the consequent extraction of the heavy ions at very high velocities at the thruster exit. The generated thrusts vary in a wide range from some  $\mu N$  to some  $N$ , but is in general much lower compared to chemical devices. This limits their use to in-space propulsion. Due to their high  $I_{sp}$ , ion thrusters are attractive for long term space missions which require a high  $\Delta v$  at small thrusts, such as scientific deep space exploration and orbit stationing of satellites. Ion thrusters are commonly used on satellites today, with the two most popular thruster types, Hall-effect thrusters (HETs) and gridded ion thrusters (GITs) mounted on over 70% of all GEO satellites in 2017 [19].

The common operational principle of ion thrusters is the ionization of a propellant gas and the extraction and acceleration of the heavy ions to generate a thrust. The plasma generation occurs in a chamber which is called the discharge channel. Most commonly, xenon is used as an ion thruster propellant because of its high molecular mass, low reactivity and non-hazardousness. It will be exclusively considered as a propellant in this work. The gas is injected from a nozzle often placed at the channel bottom. It is ionized by electrons and forms an ion-electron plasma. At the channel exit the ions are extracted by an electric field which accelerates them downstream into the plume at very high velocities. To achieve linear acceleration along the symmetry axis, most ion thrusters have a cylindrical symmetry. The ratio of radial and axial electric field components plays an important role for shaping the ion emission characteristics. Lower ion emission angles result in higher thrust contributions for a constant exit velocity.

In the plume, the plasma expands into space. This leads to a decrease in plasma densities

---

for all species and results in a drop from plasma to vacuum potential. Downstream from the thruster exit, residual magnetic and ambipolar electric fields lead to a diverging plume which can have a conical or pronounced annular beam shape. Despite the plasma expansion, channel and plume plasmas are still coupled. The channel physics influence the plume, because the discharge characteristics determine, among others, the ion beam current and the number density of residual neutrals. The latter interact with the emitted ion beam via momentum transfer and charge exchange collisions which changes the ion distribution and influences the plume physics. In thrusters without an acceleration grid, the channel plasma influences the electric field structure at the thruster exit which shapes the emitted ion beam. On the other hand, the plume plasma influences the distribution of hot electrons which enter the discharge channel and therefore influences the overall discharge characteristics. An overview of different ion thrusters types and their operational principles can be found in Ref. [18]. In the scope of this work, the High Efficiency Multistage Plasma Thruster (HEMP-T) is considered. It utilizes a characteristic magnetic field structure to ensure good electron confinement for efficient thruster operation without an acceleration grid for the ion extraction. The basic concept of the HEMP-T and other thruster types are discussed in section 2.1.

Because of their low thrusts, ion thrusters must be capable of operating for thousands of hours to reach their potential  $\Delta v$  for high efficiency. The thruster potentially undergoes a high number of plasma ignitions with ideally little performance degradation during its lifetime. Therefore, extensive long-term qualification testing in large vacuum vessels is necessary before a thruster model can be mounted on a commercial satellite [20–22]. To maximize the life time of a thruster the erosion of important components due to impinging high energy ions must be minimized. For a high thruster life time a good plasma confinement is beneficial, because it reduces the plasma-wall contact. This can be achieved by thruster geometry, magnetic field topology and the choice of plasma discharge conditions. This requires a high number of prototypes that has to be tested for long-term operation characteristics. Furthermore, while the global performance characteristics of the thrusters can be monitored accurately for these tests, the ion beam expansion in the plume can typically not be completely evaluated in test chambers due to the large length scales of the plume expansion in the range of several meters radially and axially from the thruster exit. Knowledge of the plume expansion is important for spacecraft manufacturers because impinging ions can inflict sputtering damage to other parts of the satellite. In summary, the long testing cycles and the length-scales introduced by the coupled channel-plume dynamics make thruster development and optimization challenging, expensive and time consuming.

Numerical modeling can help to reduce the development time and costs of new ion thruster models. Spatially resolved experimental measurements of the plasma parameters are difficult to obtain because of the plasma discharge conditions in the channel. A numerical thruster model is not limited by experimental constraints and can therefore help to gain knowledge of the thruster physics. If the physical principles are reproduced qualitatively, trends in thruster operation can be recognized and applied for the optimization of real-life models. Quantitative agreement between model and experiment would lead to an even better quality of predictions which could significantly reduce the number of prototypes required for the thruster optimization. Moreover, if the ion energy and velocity distribution functions are known, sputter analysis can contribute to realistic life time estimates of thruster models [23]. This would reduce the number of very long validation and qualification tests required. Numerical models can also help to investigate the expansion of the plume beyond the limits presented by experimental measurements. To find a suitable simulation method for HEMP-Ts, some knowledge of the plasma discharge conditions in the channel is required.

In the low temperature plasmas in the discharge channel of HEMP-Ts, typical number densities of charged particles reach  $10^{13} - 10^{14} \text{ cm}^{-3}$  with electron Debye lengths between  $10^{-3} - 10^{-4} \text{ cm}$ . The electrons are trapped and magnetized by the magnetic field structure of the HEMP-T with mean temperatures below 10 eV. The mean-free path of electron collisions is higher than the characteristic system length  $L$ , which in this case is the length of the discharge channel on a scale of about 1 – 10 cm. As will be shown later, the electron distribution is not thermalized, which makes a kinetic model necessary for the simulation of a HEMP-T. The Particle-In-Cell (PIC) method is a direct solution of the Vlasov equation and is therefore well-suited for modeling such a plasma [24, 25]. Together with a Monte-Carlo collision (MCC) model for the short-range particle collisions a realistic plasma description can be achieved [26, 27]. However, the PIC method is computationally costly because of the spatial and temporal resolutions required. For the discharge channel, several centimeters must be covered in each spatial dimension with a resolution on the scale of the electron Debye length. The discrete time step  $\Delta t$  by which the system is incrementally advanced must be small enough to resolve the inverse of the electron plasma frequency. This results in time steps of  $10^{-12} - 10^{-13} \text{ s}$  for a total simulation time of up to one second. Therefore, even for a PIC model of the discharge channel with a length of up to 10 cm, a reduction in spatial dimensions along with advanced numerical models is necessary. First axisymmetric 2D simulations of the HEMP-T were carried out in Ref. [23, 28, 29] starting in 2009. The basic principles of ion acceleration were identified and the low wall erosion in the channel of the HEMP-T compared to a HET was shown. In Ref. [30] it was found that the electrons

---

in the HEMP-T discharge channel have a non-Maxwellian energy distribution. Moreover, in first proof-of-principle 3D simulations the importance of anomalous electron diffusion caused by azimuthal instabilities in the magnetic cusp region during thruster operation was shown and an estimate of the transport coefficient was given.

Because the full PIC model for the discharge channel is already computationally expensive, it is not feasible to cover a full plume expansion on the scale of several meters with a fully kinetic PIC simulation which solves the coupled problem of channel and plume plasmas. As a result most plume simulations treat the plume expansion separately from the discharge channel and disregard the coupling between them. Because the particle number densities decrease in the plume the required spatial and temporal resolutions of a PIC model decrease as well. With this advantage, the simulation of a plume expansion becomes feasible. Both, fully kinetic models as well as fluid models which treat all plasma species as a fluid, have been applied for this purpose [31, 32]. Popular is the combination of fluid and kinetic models, where the electrons are treated as a fluid with fully kinetic ions in so called hybrid PIC codes. In fluid models, assumptions about the distribution function of each fluid species are required to enable the solution of the fluid equations. Moreover, plume models which disregard the thruster channel require input data for e.g. the ion fluxes from other kinetic simulations or experiments.

The coupling between channel and plume plasmas is an important aspect which is often neglected, and their influence on the plume expansion is not fully understood. For a realistic thruster model the full coupled system of channel and plume plasmas must be solved. Therefore, the main research questions of this thesis are:

**Which physical effects arise from the coupling between channel and plume plasma, and which models can be applied for the simulation of the full coupled system of channel and plume plasma in a HEMP-T ion thruster?**

The structure of the thesis to investigate these question is as follows. In chapter 2 the basics for the investigation of these aspects is outlined. An overview of different ion thrusters with an emphasis on different HEMP-T thruster models is given before the fully kinetic and hybrid PIC models used in this thesis are outlined. Chapter 3 offers an overview of the simulation results. To understand the coupling between channel and plume plasmas, the results of a fully kinetic simulation of a HEMP-T discharge channel and near-field plume as well as their influence on the thruster performance are discussed. The so-called breathing mode oscillation, which is an effect arising from the coupling of both plasmas, is investigated

in HEMP-Ts. After this discussion, a coupling of fully kinetic and hybrid PIC methods is used to compute a HEMP-T plume expansion. In the end a fully kinetic simulation method capable of solving the combined channel-plume systems is proposed, and first proof-of-principle simulation results are presented. Finally, chapter 4 summarizes the results and gives an outlook on pressing problems and future points of research for simulations of the HEMP-T.

## 2 Basics

In this chapter the basic principles required for the investigation of the research questions outlined in chapter 1 are summarized. First, an overview of different ion thrusters with an emphasis on the HEMP-T and its different models is given in section 2.1. Section 2.2 discusses the numerical models used for the simulations of HEMP-Ts and their plume. For this purpose the Particle-in-Cell (PIC) and fluid plasma models are discussed in section 2.2.1 and section 2.2.2, respectively.

### 2.1 Basic ion thruster physics

Ion thrusters rely on the acceleration of a heavy ion species from a plasma that is generated in a discharge channel. The first commercially used models are gridded ion thrusters (GITs), also simply referred to as ion thrusters. They are distinguished by the type of plasma discharge in the channel, such as DC, RF or microwave discharges. With ISPs in the range of 3000 s – 4000 s and reaching up to 10000 s, GITs achieve the highest ISPs among ion thrusters [18]. GITs utilize two or more acceleration grids for the extraction of the heavy ions from the plasma to generate the thrust. Between the grids, a voltage is applied which accelerates the ions downstream into the plume. The accelerator grid is subject to ion sputtering which can constrain the thruster lifetime. However, the heating mechanism in GITs increases system cost, complexity and weight and can make the system less robust. Depending on the mission requirements, other ion propulsion devices might be attractive.

A common alternative are Hall-effect thrusters (HETs including the stationary plasma thruster SPT), which are used commercially since the 1970s [33]. Its discharge channel has an annular shape and is coated with a dielectric material such as boron nitride. At the channel bottom a voltage is applied to the metal anode. The propellant gas nozzle is also placed at the channel bottom with the same cylindrical symmetry as the discharge channel. A radially oriented magnetic field is applied by magnets. In the channel, the electrons are

confined by a Hall current resulting from the perpendicular structure of electric and magnetic fields while ionizing the propellant gas. Because the magnetic field geometry guides the electrons towards the channel walls, wall effects such as secondary electron emission strongly impact the discharge conditions. As a result, the wall erosion caused by impinging high energy ions is relatively high [34] but can be reduced with so-called magnetic shielding which guides the magnetic field lines away from the channel walls [35–37]. Outside of the channel, an electron cathode neutralizes the emitted ions and provides electrons for the discharge. Compared to GITs the thruster geometry is rather simple and no additional electron heating mechanism is required. HETs have ISPs typically in the range of 1500 – 2500 s [18]. Because of the high plasma-wall contact, lower erosion alternatives with potentially higher thruster lifetime can be more attractive for some space missions.

Such a promising alternative to HETs is the High Efficiency Multistage Plasma Thruster (HEMP-T). First patents were registered in 1998 [38] by Thales Deutschland GmbH and actual thruster development started in the early 2000s. In 2003 the first experimental results were published [39]. The discharge channel of the HEMP-T thruster has a hollow cylinder shape with a channel length that is three to six times higher than its radius. The radial channel walls are coated with a dielectric with a high sputtering threshold for impinging ions. As is the case in HETs, boron nitride is a common choice and is used in all thrusters considered here. At the channel bottom is a metal anode with an applied voltage in the range of 300 – 2000 V. The propellant gas nozzle is also placed at the channel bottom. Outside the channel, electrons are injected by a neutralizer, which neutralizes the emitted ion beam and provides electrons for the plasma discharge.

In the channel a unique magnetic field configuration is generated by circular periodic permanent magnets (PPMs) with pairwise opposite magnetization direction, which determine the discharge channel physics. The magnetic field structure is axially flat in most channel regions, but is interrupted by radially oriented cusps at the interfaces of the permanent magnets. At the cusps, the magnetic field strength is close to zero near the symmetry axis but increases towards the channel walls. In radial direction towards the channel wall this creates a magnetic field structure which resembles a magnetic mirror capable of reflecting charged plasma particles directed at the channel wall. The magnetic field strength in the axially flat regions must be high enough to magnetize the electrons while leaving the ions mostly unaffected. As a result, the electrons follow the magnetic field lines and are guided towards the wall only at the cusps. There a classic plasma-wall sheath develops. A high number of electrons is reflected by the combination of plasma-wall sheath and magnetic mir-

ror which leads to an oscillating motion of the electrons between the cusps. This leads to a non-Maxwellian electron energy distribution function (EEDF) in the whole channel which will be shown in section 3.1. In between the cusps, the size of the sheath is reduced to the scale of the electron Larmor radius because the parallel structure of dielectric wall and magnetic field guides the magnetized electrons away from the wall [40]. Hence, significant plasma-wall contact only occurs at the cusps, but the energies of impinging ions are too low to cause sputtering erosion. Overall the wall erosion is reduced which increases the thruster lifetime.

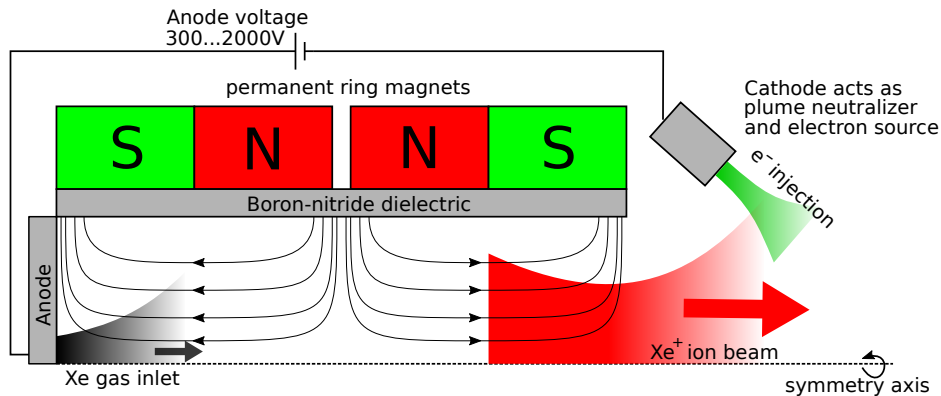


Figure 2.1: Sketch of the HEMP-T DM3a ([P1]).

The HEMP-T concept is attractive for a wide variety of applications, with thrust levels ranging from some  $\mu\text{N}$  [41–43] up to 250 mN [39, 44, 45]. Long term endurance tests in vacuum chambers are necessary, e.g. in the qualification for the SmallGEO project, where the HEMP-T has undergone a 4000 h operation test [21]. The total lifetime is expected to reach at least 18000 h, based on a 250 h test run at a thrust level of 57 mN of the HEMP-T 3050 model [45]. Yet, interaction with the vacuum vessel by sputtered and redeposited wall material can completely alter thruster operation and must be accounted for accordingly [20, 30, 46].

The HEMP-T model considered in sections section 3.1 and section 3.2 is the HEMP-T DM3a. Its discharge channel has a radius of 9.2 mm and channel length of 51.14 mm with one central magnetic cusp. At the channel exit the dielectric is covered by a metal pole piece which is at ground potential in the simulations carried out here. First measurements of the HEMP-T DM3a model were published in Ref. [39]. A sketch of the system is shown in figure 2.1.

Another type of ion thruster is the  $\mu\text{HEMP-T}$  with two central magnetic cusps. It is designed for thrusts in the  $\mu\text{N}$  range [41–43]. With a small and lightweight system design, this is

attractive for small satellites such as cubesats [14]. In publication [P5] in the appendix, a kinetic PIC model was used for the simulation of the device. Those simulations showed that the plasma in the discharge channel is strongly affected by plasma-wall effects due to the small system size, which results in a deteriorated thruster performance.

Recently, new HEMP-T designs were developed using only numerical modeling without experimentally tested prototypes. The first such example is the HEMP-T DP1 model. It was first published in Ref [47], where the principles on which the thruster was designed are outlined. The discharge channel is 64 mm long with a radius of 15.1 mm. Discharge currents between 0.5 – 1.5 A with anode voltages of 200 – 800 V are targeted to provide a thrust of up to 25 mN with an  $I_{sp} \approx 1200$  s. The magnetic field data was generated with a finite element magnetics code [48] and was also published. It features two central magnetic cusps and magnetic field strengths between 0.1 – 0.5 T in most discharge channel regions. First numerical studies of the DP1 were carried out with the axisymmetric 2D3v PIC-MCC model described in section 2.2.1 [47].

Another numerically designed HEMP-T is the S1 thruster [49, 50]. It was created with a multi-objective design optimization (MDO) of the semi-empirical zero-dimensional power balance model of the HEMP-T from Ref. [51]. The discharge channel is 21 mm long with a radius of 9.91 mm and two central magnetic cusps. A first PIC simulation of the S1 thruster was carried out in the publication [P7] in the appendix. It showed that the thrusters operational parameters obtained with the MDO deviated from the ones obtained with the fully kinetic PIC model. Some estimated parameters used in the power balance model were retrieved from the PIC simulation and can be used for an improved MDO approach. In the future, the combination of the MDO method for the generation of new thruster geometries together with a refinement of the underlying power balance model with a fully kinetic PIC simulations can greatly improve the development of new HEMP-Ts.

Besides the ion thrusters described above, other electric propulsion devices exist. Among those are the arcjet and resistojet thrusters, which heat the propellant neutral gas before it is emitted without ionization [18]. However, their  $I_{sp}$  is limited to below 700 s because of the heating mechanism, resistive heating in resistojets and heating with a plasma arc discharge in an arcjet, respectively [18]. Another type of ion thruster is the pulsed plasma thruster. There, the propellant is supplied as a solid which is sputtered by pulsed plasma arcs and then ionized. The electric and magnetic field then accelerate the heavy ions outward and generate thrust. An example of this type of thruster is the cathodic arc thruster [52, 53].

A first kinetic simulation of this thruster type was carried out in publication [P6] in the appendix.

## 2.2 Plasma modeling

The plasmas in the HEMP-T discharge channel are generally weakly ionized with electron densities between  $10^{13} - 10^{14} \text{ cm}^{-3}$ . They are also weakly collisional, but collisions still have to be reproduced accurately because the distribution of plasma sources is an important aspect for the overall thruster performance which will be discussed in section 3.2. Because of the low collisionality, the EEDF is not thermalized and can not be assumed to be Maxwellian. Moreover, the plasma-wall interaction and the (in some channel regions) strongly varying magnetic field structure have to be resolved. Therefore a fully kinetic model is required for the simulation of the HEMP-T discharge channel. A suitable method, the Particle-in-Cell (PIC) method is described in section 2.2.1.

In the plume the charged particle densities gradually decrease downstream from the thruster exit. Collisionality is weaker than in the channel and no significant ionization occurs. Plasma-wall contact and magnetic field effects can be neglected as well. However, the time and length scales encountered in the plume are much higher, which makes a combined simulation of the coupled channel and plume plasmas challenging. As a result, fluid models or hybrid fluid-PIC models, which either treat all charged species or only the electrons as a fluid, are popular choices for plume simulation models. The fluid method is discussed in section 2.2.2.

Both kinetic PIC and fluid models solve the Boltzmann equation

$$\left. \frac{\partial f}{\partial t} \right|_{coll} = \frac{\partial f}{\partial t} + \mathbf{v}_s \frac{\partial f}{\partial \mathbf{x}_s} + \frac{\mathbf{F}_s}{m_s} \frac{\partial f}{\partial \mathbf{v}_s}, \quad (2.1)$$

for the distribution function  $f_s$  of each plasma species  $s$ . In three dimensional space, it is a 7D function of the time  $t$  and the spatial  $\mathbf{x}_s$  and temporal  $\mathbf{v}_s$  phase space coordinates. It is a measure of the number of particles at the location  $\mathbf{x}_s$  with velocity  $\mathbf{v}_s$  at time  $t$ . In low temperature plasmas, the Lorentz force,

$$\mathbf{F}_{L,s} = q_s (\mathbf{v}_s \times \mathbf{B}(\mathbf{x}_s, t) + \mathbf{E}(\mathbf{x}_s, t)), \quad (2.2)$$

acts on the particles with charge  $q_s$  and velocity  $\mathbf{v}_s$  in the electromagnetic field consisting of the magnetic  $\mathbf{B}(\mathbf{x}_s, t)$  and electric  $\mathbf{E}(\mathbf{x}_s, t)$  fields, respectively. The term  $\left. \frac{\partial f}{\partial t} \right|_{coll}$  denotes the change of  $f_s$  because of particle collisions.

In the HEMP-T, the magnetic field applied by the PPMs is much larger than the one induced by the plasma currents. Thus the electrostatic approximation is used in all simulation models considered here. The magnetic field is approximately constant, and the electric field is computed as the gradient of the electric potential  $\Phi$ , i.e.  $\mathbf{E} = -\nabla\Phi$ . To obtain the potential, Poisson's equation,

$$\Delta\Phi(\mathbf{x}, t) = -\frac{1}{\varepsilon(\mathbf{x})\varepsilon_0} \sum_s q_s n_s(\mathbf{x}, t), \quad (2.3)$$

has to be solved. There,  $n_s$  is the number density of species  $s$  with charge  $q_s$  and  $\varepsilon$  and  $\varepsilon_0$  are the relative and vacuum electric permittivity, respectively.

For a numeric plasma model of the HEMP-T, the set of equations consisting of eq. 2.1, eq. 2.2 and eq. 2.3 has to be solved. The PIC method, which will be discussed in section 2.2.1, is a direct solution of this system while the fluid model discussed in section 2.2.2 solves it approximately.

## 2.2.1 The Particle-In-Cell method

The PIC method can be derived directly from eq. 2.1 through a linearization ansatz for a small advance in time  $t \rightarrow t + \Delta t$ . The distribution at time  $t + \Delta t$  can be written as

$$f(t + \Delta t) = f(t) + \frac{\partial f}{\partial t} \Delta t + \mathcal{O}(\Delta t^2). \quad (2.4)$$

For brevity, the species index  $s$  was dropped. The operator form of eq. 2.1 is

$$\hat{J}f = \frac{\partial f}{\partial t} - \hat{D}f, \quad (2.5)$$

with the collision operator  $\hat{J}$  and the operator of collisionless plasma motion  $\hat{D}$ . Solving it for  $\frac{\partial f}{\partial t}$  and substituting it into eq. 2.4 results in the expression

$$f(t + \Delta t) = (1 + \Delta t \hat{J})(1 + \Delta t \hat{D})f(t) + \mathcal{O}(\Delta t^2), \quad (2.6)$$

after a rearrangement of the coefficients. Eq. 2.6 shows that the distribution function at the time  $t + \Delta t$  can be calculated by application of the operators  $\hat{J}$  and  $\hat{D}$  to the distribution function at time  $t$ . The nonlinear term  $\sim \Delta t^2 \hat{J} \hat{D} f(t)$  vanishes if only terms linear in  $\Delta t$  are considered. This results in the calculation scheme

$$f(t + \Delta t) = f(t) + \Delta t \hat{J} f(t) + \Delta t \hat{D} f(t) + \mathcal{O}(\Delta t^2), \quad (2.7)$$

which is linear in the operators  $\hat{J}$  and  $\hat{D}$ . This scheme solves eq. 2.1 directly when  $\Delta t$  is sufficiently small [24].

In PIC models, the simulation domain which contains the particles is divided into cells. The charge density of each particle is then interpolated onto the cell corners which create a mesh. Because the electrostatic approximation is used, Poisson's equation for the electric potential  $\Phi$  has to be solved on the mesh from which the electric field is calculated. The Lorentz force in eq. 2.2 which acts on each particle is then interpolated back from the mesh onto each particle. It is necessary to use the same interpolation function for the interpolation of charge densities and forces, respectively, to avoid the introduction of artificial self-forces [24]. After the force interpolation all particles are moved by integrating each particle's equation of motion. The simulation time is advanced by the discrete time step  $\Delta t$  and the cycle starts over. A sketch of the PIC scheme can be found in figure 2.2.

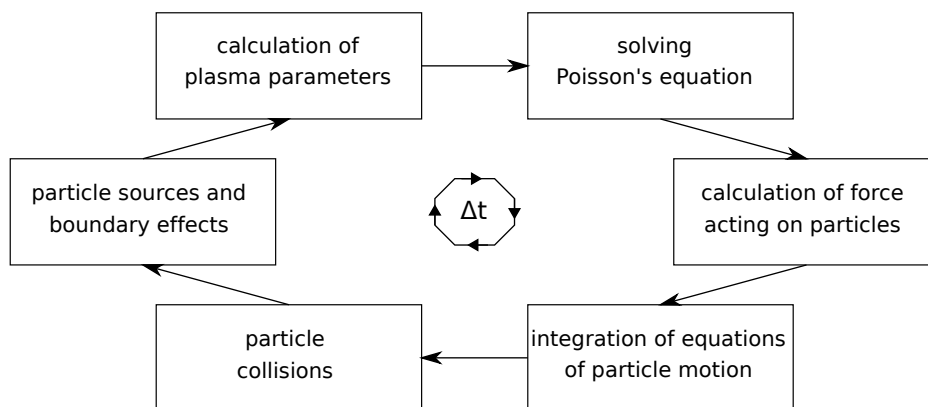


Figure 2.2: Basic scheme of the PIC method ([P1]).

The computational effort is reduced by tracking so called super-particles, each consisting of a large number of real particles. They follow the same trajectories as real particles, because they have the same charge to mass ratio and therefore undergo the same acceleration  $\mathbf{F}_L/m$  from the Lorentz force. With the PIC method, the computation of the long-range Coulomb interaction between particles, which scales with the square of the total number of particles, is reduced to a linear scaling. This approach represents the application of the collisionless plasma motion operator  $\hat{D}$  from eq. 2.5 to the distribution function  $f(t)$ . It

accurately models the collective (long range) plasma dynamics, but short range forces are underestimated and collisional effects are neglected [54]. The collision operator  $\hat{J}$  from the same equation can be included with an independent model performing collisions within each cell.

The advantage of the PIC method, besides the exact solution of the Boltzmann eq. 2.1, is that the full particle distribution function for all species is known at all times. This enables the diagnostic of all plasma properties at all times if statistical effects are neglected. Furthermore, particle based effects, such as wall processes which include ion recombination, neutral reflection and secondary electron emission (SEE), can be implemented in a straightforward particle based manner. The same is true for particle injections, i.e. for correctly modeling the distribution of neutrals injected from the nozzle in the discharge chamber.

However, the drawback of the PIC method is the high computational cost. This is the result of the required grid spacing and time step. Firstly, the mesh spacing  $\Delta r$  must be of the order of the electron Debye scale  $\lambda_{D,e}$  of the plasma to avoid artificial heating through the finite-grid-instability [55–57]. As a result, the number of required cells in a PIC simulation of a HEMP-T is very high. This increases the computation time for the solution of Poisson’s equation (which scales with the number of mesh points) and the total number of super-particles in the simulation because good particle statistics have to be ensured within each cell. Secondly, the time step  $\Delta t$  must resolve the electron plasma frequency  $\omega_{p,e}$  with the requirement  $\Delta t \omega_{p,e}^{-1} \lesssim 2$  to avoid instabilities [24]. Therefore, the time step is often many orders of magnitude smaller than a second and a high number of time steps is required for the simulation of an ion thruster plasma. In the following, each sub-module of the PIC model used for the simulation of HEMP-Ts is discussed in more detail. A thorough discussion can be found in publication [P1] in the appendix.

**General considerations** The HEMP-T is axisymmetric and a 2D axisymmetric model with a simulation domain in the  $(r, z)$ –plane is used to reduce computation time. The symmetry axis of the simulation domain coincides with the symmetry axis of the simulated thruster. Still, all three velocity components of the particles are traced to ensure energy and momentum conservation in the Monte-Carlo-Collision (MCC) algorithms used here to represent the collision operator  $\hat{J}$  from eq. 2.7. Therefore the model is referred to as an electrostatic axisymmetric 2D3v PIC-MCC model. The propellant gas is xenon and the species covered in the simulation model are xenon neutrals Xe, electrons e and singly and doubly charged xenon ions,  $\text{Xe}^+$  and  $\text{Xe}^{2+}$ , respectively. Because mass spectroscopy

measurements have shown that higher charge states contribute less than 1% combined to the ion current [39], they are neglected in the simulation. The simulation code is written in C++.

**Mesh interpolation** To obtain the particles' charge densities on the mesh, an interpolation function is necessary. Here, the cloud-in-cell (CIC) method is used [54]. Each particle is represented by a charge cloud and each of the four closest mesh points is assigned a fraction of the total particle charge, depending on proximity. Although this approach is computationally more costly, it introduces less numerical noise than the nearest-grid-point (NGP) method, where the total particle charge is assigned to the closest mesh point. Every time a particle leaves or enters a cell noise is introduced in the NGP approach, whereas in CIC this is a smooth process. The same interpolation function is used for the calculation of the electric and magnetic fields at the particle positions, which guarantees energy and momentum conservation.

**Field solve** Because an electrostatic model is used, the field calculation is reduced to the solution of Poisson's equation instead of the full set of Maxwell's equations. The equation is discretized on the mesh using a five-point finite difference scheme on the mesh [58]. Because of the radial symmetry of the simulation domain, the resulting matrix coefficients differ from the Cartesian case and a special treatment is required at the symmetry axis for  $r = 0$ . There L'Hôpital's rule is used to derive a scheme which guarantees the automatic fulfillment of the von-Neumann boundary condition [28]. Material interfaces are also handled in the discretization, and include dielectric and conducting materials (notably grounded metal parts). The solution of the linear system of equations is obtained with an enhanced version of the LU decomposition from the SuperLU 4.3 package [59–61]. After  $\Phi$  was calculated, the electric field is obtained on the mesh with a symmetric difference scheme for the gradient calculation.

**Particle mover** The particles are moved according to the Lorentz force in eq. 2.2. Their equations of motion are integrated with the Boris integrator [62]. It is stable when the condition  $\Delta t \omega_{p,e}^{-1} \lesssim 2$  is fulfilled but typically a stricter timestep of  $\Delta t \omega_{p,e}^{-1} \sim 0.2$  is chosen to ensure stability. The Boris algorithm is symplectic in the case of a zero electric field. This is rarely the case in plasmas but a global upper error bound exists even in the presence of an electric field [63]. Because particle positions and velocities are defined a half time-step apart

due to the integration scheme, momentum conservation can not be ensured exactly. For the heavy species which are slow compared to the electrons, sub-cycling is used to reduce their computational effort [64]. Those species are moved only after a number of electron push steps, while they undergo the acceleration of the averaged electric field during those electron push steps. As a result, the computational cost for the heavy species is much reduced.

**Particle boundary conditions** Particle boundary conditions are treated as a sub-module of the particle mover in the simulation. The top and right domain boundaries in the two dimensional  $(r, z)$  –plane represent vacuum boundary conditions and all particles leaving the domain there are removed from the simulation. Particles leaving the domain at the symmetry axis are reflected. The left domain boundary presents the metal anode in the discharge channel. Electrons are removed there, while neutrals are reflected thermally and all ion species recycle as thermal neutrals. All ions and neutrals are treated equally at the dielectric and grounded metal parts of the discharge channel, and only at the dielectrics the space charge is increased according to the charge of the impinging ion. Electrons are removed at grounded metal parts, while at the dielectric they can cause secondary electron emission (SEE) with a coefficient of 0.5. This value presents a lower bound for the secondary electron emission because in the high and low energy limits, the real emission coefficients are expected to be much higher [65, 66].

**Particle injection** Particle injection is introduced in a straightforward manner by adding the desired number of particles in a certain region of the simulation domain. In the HEMPT simulations considered in this work, neutral injection occurs upstream at the metal anode and centered around the symmetry axis for a fraction of the total channel radius. Unless stated otherwise, neutrals are injected with a drift Maxwellian distribution, with an axial drift energy of 0.03 eV and a thermal component of 0.017 eV. The electron injection provides electrons for the plasma in the channel and is located outside the channel exit in most cases. Variation of the injection current has proven to be a suitable method for controlling the plasma discharge parameters, with higher injection current generally resulting in higher plasma densities and discharge currents. The injection current can be chosen to be constant or variable, with the latter varying the injection current to keep the electron density in a desired range. This variable injection scheme is called a feedback injection. It is similar to the experimental control of the discharge current, where the neutral flux is varied. However, this approach is not suitable for PIC simulations due to the long neutral relaxation times in

the system, which present the longest time scale that must be covered. Therefore, a control of the electron injection current is more practical.

**Monte-Carlo collisions** Although the mean free paths of most collisions are larger than the characteristic system size, the channel length  $L$ , the physical properties of the HEMP-T lead to long travel lengths and lifetimes of electrons in the discharge channel. Therefore, the particle collisions, represented by the operator  $\hat{J}$  in eq. 2.5, have to be modeled correctly for the simulation of an ion thruster. This is achieved with a Monte-Carlo collision (MCC) model. The collisions included in this model are direct single and double  $e^-$ -Xe impact ionization, single  $e^-$ -Xe<sup>+</sup> impact ionization, integral elastic Xe<sup>+</sup>-Xe collisions (including charge exchange and momentum transfer), as well as integral elastic and inelastic  $e^-$ -Xe collisions. Electron-electron Coulomb collisions are also included. For the latter the binary collision model first proposed by Takizuka and Abe is used [67] where two randomly selected particles within a cell are collided. All other collisions are modeled using an approach similar to the one proposed in [68]. Particles from both collision species are randomly divided into pairs, and a collision probability  $0 \leq P_{coll} < 1$  is calculated based on the particle energies and the cross sections from Ref. [69]. If a uniform random number is smaller than  $P_{coll}$ , a collision occurs. For non-ionization collisions, the particles are scattered and energy is dissipated for non-elastic collisions. If an ionization collision occurs, a new electron is created at the position of the particle that was ionized, and the ionization energy is removed. Then, the incident and newly created particles perform a Coulomb collision. All collision algorithms strictly conserve energy and momentum and have been tested thoroughly [26]. A more detailed description of the collision algorithms can be found in [26, 27, 64].

**Similarity scaling** To make the simulation of the HEMP-T feasible, a similarity scaling scheme is used. It aims to reduce the physical size of the modeled system, which decreases the amount of cells required to cover the simulation domain with the required resolution. The scheme is based on dimensionless invariants of the Boltzmann eq. 2.1, which are derived in Ref. [70]. In this context, two systems are called similar if those invariants are preserved. For low temperature plasmas four invariants have to be considered:

- (i) The particle trajectory relative to the system size  $L$ ,  $C_1 = \frac{L}{vt}$
- (ii) The kinetic energy a particle obtains in an electric field,  $C_2 = \frac{q_s EL}{m_s v^2}$

(iii) The influence of the magnetic field on the particle trajectory, i.e. the Hall parameter,

$$C_3 = \frac{q_s B L}{m_s v}$$

(iv) The influence of collisions, represented by the Knudsen number as the ratio of mean-free-path  $\lambda_{\text{mfp}}$  and system size,  $C_4 = \frac{\lambda_{\text{mfp}}}{L}$

In the following, the quantities in the down-scaled system are denoted by a prime. Because the scaling shall reduce the system size by the factor  $\xi$ , the size in the small system is  $L^* = L/\xi$ . Then, it follows from (i) that the time is scaled equally,  $t^* = t/\xi$  while the particle velocities remain constant,  $v^* = v$ . The electric field is scaled  $\mathbf{E}^* = \mathbf{E}\xi$ , which is automatically fulfilled if both the solution of Poisson's equation and the calculation of the electric field are performed in the down-scaled system. The magnetic field increases linearly as well,  $B^* = B\xi$  as obtained from (iii). Finally, (iv) requires a reduced mean-free-path,  $\lambda_{\text{mfp}}^* = \lambda_{\text{mfp}}/\xi$ , which is achieved with linearly increased collision cross sections  $\sigma^* = \sigma\xi$ . From those considerations scaling laws for all physical quantities can be derived. Notably, the number density of particles  $n_s$  is not scaled. Because each dimension is scaled down linearly by  $\xi$ , the total number of cells to cover the simulation domain is reduced by the factor  $\xi^2$ . However, the ratio of electron Debye length and system length is not preserved because the former remains unscaled while the system length is reduced. Therefore, the Debye scale is artificially increased when the results are extrapolated from the down-scaled to the physical system. This can lead to seemingly violated quasineutrality in regions where the Debye scale increases such as the plume of ion thrusters.

**Parallelization** To further speed up computations, the simulation code is parallelized using the MPI protocol [71]. It aims to reduce the computing effort for the particle mover by dividing the simulation domain into smaller sub-domains in a so called domain decomposition approach. A weight of one is assigned to each computational electron and one divided by the sub-cycling factor to each heavy species particle. The 2D simulation domain is cut in half horizontally into two sub-domains with almost equal weights (single cells can not be cut). Each sub-domain is again cut in half vertically into two new sub-domains of equal weight. This algorithm is continued with alternating horizontal and vertical cuts of each sub-domain until the desired number of sub-domains is reached. To ensure load balancing the total number of sub-domains has to be a power of two. Although domain sizes can vary drastically, the scaling for the particle mover and the charge density weighting is excellent. Figure 2.3 shows the domain decomposition of a typical HEMP-T simulation.

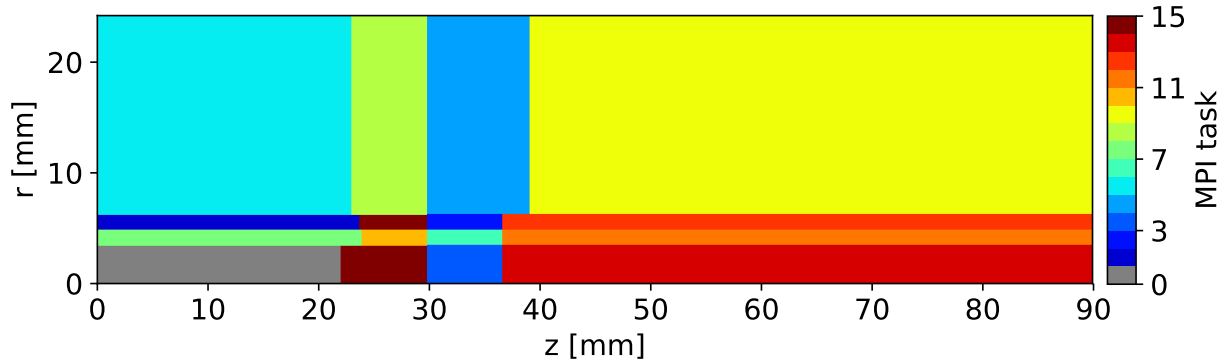


Figure 2.3: Map of the domain decomposition parallelization in a typical simulation of the HEMP-T DM3a [39] with 16 MPI tasks. Although the size of the sub-domains is very uneven, the computational effort for the particle push is balanced ([P1]).

### 2.2.2 Fluid modeling of plasmas

Compared to the fully kinetic PIC model, a numerical plasma fluid model computes the macroscopic plasma quantities on a mesh instead of tracking individual particles. It can be derived from the moments of eq. 2.1 where the  $n$ -th moment is obtained by multiplication of the equation with  $\mathbf{v}^n$  and integration over velocity space. This results in a hierarchy of fluid equations, because the  $n$ -th moment depends on the  $(n-1)$ -th and  $(n+1)$ -th moments, respectively. In this hierarchy, the continuity equation,

$$\frac{\partial n_s}{\partial t} + \nabla \cdot (n_s \mathbf{v}_s) = 0, \quad (2.8)$$

and the momentum conservation equation,

$$\frac{\partial (m_s n_s \mathbf{v}_s)}{\partial t} + \nabla \cdot \mathbf{P}_s - q_s n_s (\mathbf{E} + \mathbf{v}_s \times \mathbf{B}) = \mathbf{F}_s, \quad (2.9)$$

are obtained from the zeroth and first moments, respectively. Eq. 2.8 describes the change of the number density  $n_s$  due to sources of the particle flux  $n_s \mathbf{v}_s$ . The second, eq. 2.9, describes the change of momentum as a result of the electromagnetic force in the form of the Lorentz force in eq. 2.2, collisional friction  $\mathbf{F}_s$  and the momentum transfer expressed by the stress tensor  $\mathbf{P}_s$ . Both equations are coupled directly through  $n_s$  and  $v_s$ , and indirectly through Poisson's equation, which must be solved to obtain  $\mathbf{E}$  from the particle number densities  $n_s$  in the electrostatic case. The second moment is equivalent to the equation of energy conservation, but is not considered here.

In a hybrid PIC model for ion thruster plumes, only the electrons are treated as a fluid

while the ions are treated fully kinetic using the PIC algorithm. The macroscopic electron quantities are only calculated on a mesh. As a result, the PIC grid only has to resolve the much larger ion Debye length instead of the electron Debye length. Moreover, the time step of the simulation increases because individual electron motion is not resolved anymore because only their macroscopic quantities are considered. This increases both grid spacing and time step in the simulation. It is therefore possible to cover larger length and time scales in hybrid PIC simulations which is necessary for the simulation of ion thruster plumes.

However, the hierarchy of the electron fluid equations must be closed. A rigorous approach requires an asymptotic closure scheme, where the limit of a small parameter expansion is derived from eq. 2.1. An example for this is the derivation of the Braginskii equations for a fluid description of a magnetized plasma [72]. Due to the plasma discharge conditions it is not always possible to derive or apply such a parameter limit approximation and other methods are necessary. The easiest approach is a truncation of the fluid hierarchy by assuming all higher moments as zero, resulting in only a gross approximation of the real system. If available, additional information such as experimentally measured plasma quantities can be used. However, the most common approach is the closure of the hierarchy on the  $n$ -th level by making assumptions about plasma quantities to satisfy the  $(n + 1)$ -th equation.

A simple approach for the closure on the momentum balance level is the assumption of a Maxwellian EEDF with a neglected magnetic field. The Maxwellian distribution represents the equilibrium state in a collisional plasma, which results in a zero collision term in eq. 2.9. The pressure tensor  $\mathbf{P}_e$  can then be assumed to be isotropic and can be replaced with the scalar pressure  $p_e = n_e k_B T_e$  using the Boltzmann constant  $k_B$  and the electron temperature  $T_e$ . On the time scale of the ion movement, the electrons react almost instantly to fluctuations of the electric field because their mass is much lower than the ion mass. Hence the electron inertia can be neglected in eq. 2.9. If the electrons are now also considered to be isothermal, the pressure force term reduces to  $\nabla p_e = k_B T_e \nabla n_e$  in eq. 2.9 which leads to the Boltzmann relation for the calculation of the electron density,

$$n_e(\mathbf{r}) = n_{e0} \exp \left[ \frac{e(\Phi(\mathbf{r}) - \Phi_0)}{k_B T_e} \right], \quad (2.10)$$

with the reference values  $n_{e,0}$  and  $\Phi_0$ . This equation leads to a non-linear coupling with Poisson's equation for the calculation of the electric potential which can be easily decoupled using a quasineutral approach where the net charge density becomes zero. If a non-quasineutral

approach is used, Poisson's eq. 2.3 becomes non-linear and a suitable solver is required.

The non-linear system can be solved elegantly with an iterative scheme. The successive over-relaxation (SOR) algorithm can be applied for this purpose [58]. In Ref. [73], this algorithm was investigated in a fully kinetic PIC simulation of the HEMP-T DM3a model and compared to the current solver implementation from the SuperLU package. The SOR algorithm is based on a modified version of the also iterative Jacobi algorithm, the Gauss-Seidel algorithm [58], where each value on the grid is updated in-place during each iteration. Its iteration matrix is  $B(\omega) = \omega^{-1}(D + \omega L)$ , where the matrices  $D$  and  $L$  are the diagonal and lower triangular matrices arising from the finite-difference discretization of eq. 2.3, respectively. The parameter  $\omega$  is called the relaxation parameter and an ideal value exists in the interval  $\omega \in (1, 2)$  which increases the speed of convergence [58]. However, the ideal  $\omega$  depends on the system's discretization matrix and must be found empirically for each geometry, e.g. with a hill climb algorithm. The empirically determined ideal relaxation parameter was  $\omega_{opt} = 1.981$ . The results show that the solution of Poisson's equation with the SOR algorithm shows negligible deviations from the reference solution obtained with the SuperLU package. Moreover, the long-term stability of the simulation was preserved. The main drawback of the method is execution time, as the SOR solver was roughly 40 times slower than the reference solver for sequential execution. This is expected from theory, because for ideal  $\omega$  the algorithm scales  $\sim N^3$ , where  $N$  is the total number of mesh points in the simulation domain. For SuperLU, the worst-case scaling for the actual solve phase, i.e. the solve time without the creation of the LU decomposition, is a scaling  $\sim N^2$  which is actually closer to a scaling  $\sim N$  in HEMP-T simulations [74]. As a result, the SOR algorithm should only be used as a solver for eq. 2.3 in the scope of a fluid model, where the benefits of the increased spatial and temporal scales outweigh the decrease in solver performance compared to the reference implementation.

First attempts of using a hybrid PIC approach in HEMP-T simulations were carried out in Ref. [75]. There, the non-quasineutral electron fluid model outlined above was applied to the full HEMP-T thruster and the plume of a converged fully kinetic HEMP-T simulation. A collision model based on a steady state approximation was used, where the steady state electron distribution function was used in the collision algorithms. This is a crude approximation, but including collisional terms in fluid models is difficult if isotropic pressure and heat flux are assumed [76]. When applied to the whole thruster, the model showed strong deviations from the fully kinetic PIC solution. With this model, the plasma densities in the channel increased significantly. Plasma-wall contact increased, and the classical

sheath which builds up at the magnetic cusp of the HEMP-T was not preserved because no additional sheath model was included. The highest axial electric field moved further downstream from the thruster exit. As a result, the ion emission shifted to higher emission angles with a pronounced annular beam shape. The results confirmed the suspicion that this fluid model could not be applied to the simulation of the HEMP-T discharge channel. The most important aspect for electron confinement there is the influence of the magnetic field, which was neglected entirely in the applied electron fluid model. Furthermore, an additional plasma-wall model is necessary, especially at the magnetic cusp where a classical sheath forms. However, even more sophisticated fluid models are not capable of reproducing the physics in the channel, because magnetic field strengths vary substantially within the channel and the confinement and distribution of electrons in the channel relies heavily on kinetic effects such as mirroring of electrons at the cusps. Therefore, the model was also applied only to the plume. For this purpose, the ions in the plume were injected from a given axial position according to their distribution function measured in the fully kinetic simulation. The charge densities in the thruster channel were kept constant to provide the correct potential decay in the plume. With this approach the influence of the fluid electron model on the ion beam expansion was rather low and yielded results almost equal to those obtained with a straight line ion motion. This was likely the result of the low electron densities in the plume region and the high non-neutrality due to the applied similarity scaling. Because of these results, a more sophisticated fluid model was used for the simulation of a HEMP-T plume expansion in the scope of this work.

For this purpose, the hybrid 3D PIC code EP2PLUS [76, 77] can be used for the simulation of a HEMP-T plume. It uses a more sophisticated electron fluid model which still relies on a Maxwellian electron energy distribution. Again, the magnetic field, electron collisions and electron inertia are neglected and the electron pressure is approximately constant. For the electron density, quasineutrality is assumed. However, the electron temperature is approximated with a polytropic law,

$$T_e = T_{e,0} \left( \frac{n_e}{n_{e,0}} \right)^{\gamma-1}, \quad (2.11)$$

with the polytropic coefficient  $\gamma \geq 1$ . If  $\gamma = 1$ , the isothermal case is preserved. For  $\gamma > 1$ , the electron temperature decreases with decreasing density, which was shown to result in a realistic plume expansion which was confirmed with experiments and fully kinetic PIC

simulations [31, 78]. The electric potential is then calculated with the polytropic relation

$$\Phi(n_e) = -\frac{T_{e,0}}{e} \frac{\gamma}{\gamma-1} \left[ 1 - \left( \frac{n_e}{n_{e,0}} \right)^{\gamma-1} \right], \quad (2.12)$$

in a straightforward manner.

Because of the kinetic single particle effects and the important role of the high energy tail in the EEDF for ionization in the channel, such a hybrid model is not well-suited for the simulation of the discharge channel. In the plume, however, the influence of the EEDF is reduced because of the low plasma density and long mean-free-paths, which makes the hybrid model well equipped for the simulation of ion thruster plumes. However, it is not capable of simulating the coupled problem of discharge channel and plume, which makes a combination of such a fluid model for the plume together with a fully kinetic PIC model for the discharge channel very attractive. There, the particle distributions of the near-field plume from the PIC simulation are used as an input for the fluid model, which is then used to compute the plume expansion. In the next chapter, the simulation tools described here are used to investigate the research questions outlined in chapter 1.



## 3 Simulation results

In this chapter the research questions outlined in chapter 1 are investigated by applying the fully kinetic and hybrid PIC models discussed in chapter 2 to the HEMP-T. With regards to the first question, the coupling between channel and plume plasmas and effects arising from the coupling are investigated in the HEMP-T DM3a thruster model. To understand the coupling between channel and plume, the channel physics are first discussed in section 3.1. In section 3.2, the focus lies on the near-field plume, which is the plume region close to the thruster exit. There the ion emission characteristics is a result of the coupled channel-plume dynamics. An effect arising from this coupling is the breathing mode oscillation, which is observed in all plasma quantities in the thruster exit region. The oscillation will be discussed in section 3.3.

After the first question, the second research question regarding suitable simulation models for the plume simulation in HEMP-Ts is considered. For this purpose, a combined model of fully kinetic PIC and hybrid PIC models was used to study the plume expansion of the HEMP-T DP1 thruster in section 3.4. The fully kinetic PIC model is responsible for the simulation of the discharge channel and near-field plume while the hybrid 3D PIC model was applied to simulate the plume expansion several meters downstream from the thruster exit. Both models are coupled explicitly, which means that the ion distribution in the near-field plume obtained with the fully kinetic PIC model was used as an input to the hybrid PIC model. Therefore, this approach is not suitable for the simulation of the coupled problem of channel and plume plasmas. For this purpose, an approach is proposed in section 3.5 which can overcome some of the limits presented by the fully kinetic PIC simulation and help to make computations of the coupled problem feasible.

## 3.1 Discharge channel

For the simulation of the HEMP-T discharge channel the DM3a model with one central magnetic cusp was used [39]. This section summarizes some of the results of publication [P1] in the appendix where the simulation parameters are discussed. All relevant time scales of the system were covered in the simulation.

### 3.1.1 Electrons

In the discharge channel the electrons will be considered first. Figure 3.1 shows the electron number density in the HEMP-T DM3a. To emulate the experimental neutralizer and to fuel the plasma discharge in the channel, the electrons are injected outside the discharge channel. They are guided towards the channel exit by following the electric and magnetic fields but only enter the channel near the symmetry axis because the magnetic exit cusp reflects most electrons at higher radii. Because of the high electric field at the thruster exit the electrons which enter the channel have high energies, which results in high ionization rates close to the symmetry axis.

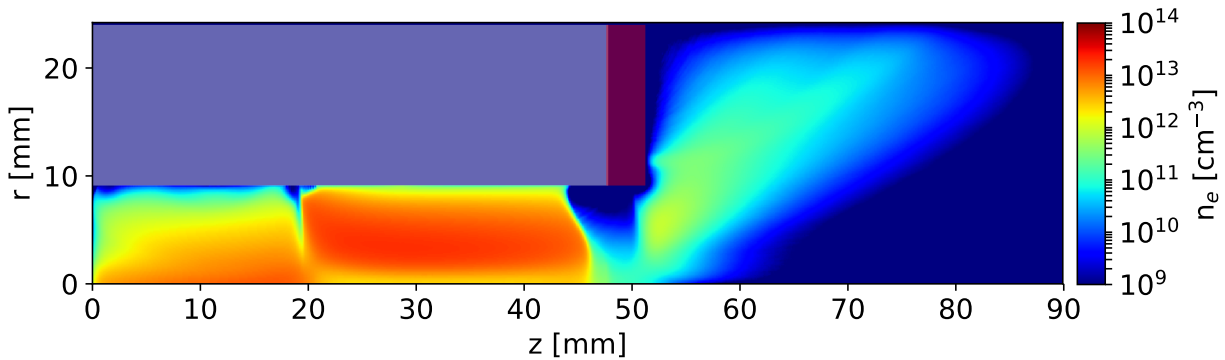


Figure 3.1: Electron number density in the HEMP-T DM3a. The dielectric (white) and grounded metal parts (red) are indicated ([P1]).

In the channel between the cusps, the magnetized electrons follow the magnetic field lines which have an orientation parallel to the symmetry axis. The electrons are guided towards the spatially confined central magnetic cusp, where the magnetic field orientation becomes mostly radial and the field strength at the symmetry axis vanishes, while it is very high near the channel wall, resembling a magnetic mirror. At the cusps the electrons are reflected because of the combination of this magnetic mirror structure and the plasma-wall sheath. The reflected electrons then again follow the parallel magnetic field which guides them

towards the next cusp where they can be reflected again. This results in a pendulum motion of the electrons between the cusps, which increases their lifetime and mean-free paths as a result of the thrusters' cusp geometry. The good electron trapping increases the electron utilization in terms of ionization probability because the effective travel length of an electron is higher than the mean-free-path of single electron impact ionization of neutral xenon atoms, which is the most important ionization process in the system.

The regions with a parallel magnetic field outweigh the cusp regions and thus the electron transport occurs predominantly parallel to the symmetry axis. As a result, the plasma-wall sheath is reduced to the scale of the electron gyro radius and no classical plasma-wall sheath builds up in the regions with a parallel magnetic field [40]. Because the electron gyro radius in the channel is generally smaller than the Debye scale, this reduced sheath cannot be observed in the simulation. However, at the cusps the situation is different. There, the electrons are directly guided towards the wall and losses of high energy electrons occur despite the magnetic mirror structure, which leads to a plasma-wall sheath building up. Secondary electron emission occurs at higher rates there and thus reduces the drop from plasma potential towards the wall. In figure 3.2, the radial profiles of charged particle

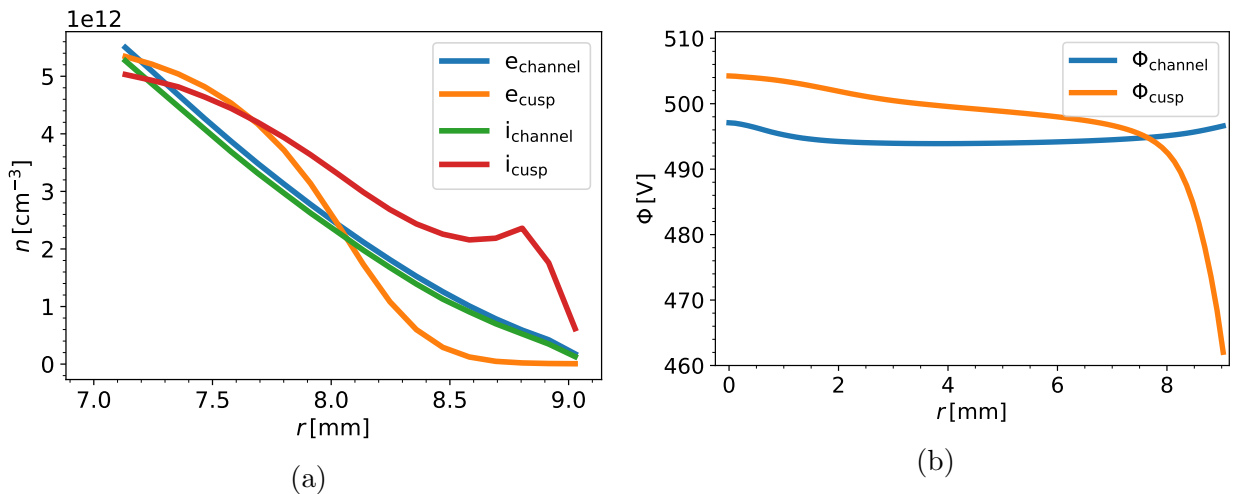


Figure 3.2: Radial profiles of (a) charged particle densities ( $e$  denotes the electrons,  $i$  the sum of  $\text{Xe}^+$  and  $\text{Xe}^{2+}$  ions) and (b) electric potential at a cusp ( $z = 19.5$  mm) and non-cusp location ( $z = 33.4$  mm) of the HEMP-T DM3a. The data was axially averaged for 2 mm around each location. The particle density data is zoomed into the near-wall region to emphasize the features of the plasma-wall sheath.

densities and the electric potential are shown. The data show a classical sheath at the cusp. Charge separation between electrons and ions occurs and the electric potential drops by 42 V from plasma to wall potential, respectively. At the non-cusp location, no charge separation or potential drop is observed because of the lower electron wall fluxes which are a result

of the reduced sheath size. In sum, the sheath at the cusps leads to improved reflection of electrons, thus improving the thrusters' electron confinement and utilization.

The magnetic cusp also broadens the ionization profile in the discharge channel. With a strong radial magnetic field near the wall, the magnetic field topology is similar to HETs, where such a structure exists throughout the channel. In HETs, the transport of electrons across magnetic field lines is several orders of magnitude higher than expected in classical electron diffusion theories based on electron-neutral or electron-ion collisions, especially at low plasma densities [79–81]. This additional electron transport results in higher measured discharge currents and is commonly referred to as anomalous electron transport in HET physics. Because of the perpendicular electric and magnetic fields in the discharge channel, an azimuthal electron Hall current increases the travel length of the electrons in the channel and leads to efficient ionization of the propellant. The large azimuthal electron current drives a high-amplitude instability in azimuthal direction. Fluctuations of the plasma quantities such as the azimuthal electric field and electron and ion densities are observed [82, 83]. The occurrence of this instability is directly related to the anomalously increased electron mobility [84].

Because of a similar magnetic field structure and plasma discharge characteristics, the anomalous electron transport was also observed in the cusp region of a 3D simulation of the HEMP-T [30]. However, in an axisymmetric 2D simulation in the  $(r, z)$ –plane, azimuthal instabilities are naturally suppressed because the azimuthal particle motion is not resolved. The anomalous transport is therefore included parametrically in the simulation model described in section 2.2.1. It is implemented as a rotation of the particle velocity with a rotation angle proportional to  $|\mathbf{B}|$ . The hot electrons, which enter the channel near the symmetry axis, are guided towards the central cusp by the magnetic field geometry. At this location, where the magnetic field topology is similar to HETs, the anomalous transport spreads the highly energetic electrons across the magnetic field lines. These electrons are then reflected because of the combined effects of the magnetic mirror and plasma-wall sheath. After the reflection, the high energy electrons then drift along a different magnetic field line in the discharge channel. This broadens the distribution of hot electrons, which are mostly located near the symmetry axis, towards higher radii. As a result the ionization profile broadens and increases the total propellant utilization. It also leads to a non-Maxwellian EEDF throughout the channel.

### 3.1.2 Ions

In figure 3.3 the ion number density is shown. It resembles the electron density shown in figure 3.1 in the channel, because the ions are not magnetized and therefore follow the electric fields created by the magnetized electrons. Small deviations between these two densities can appear in the plasma bulk due to the  $\text{Xe}^{2+}$  ions, which contribute about 7% to the total number of ions, which are not shown. Because the parallel transport of electrons along the

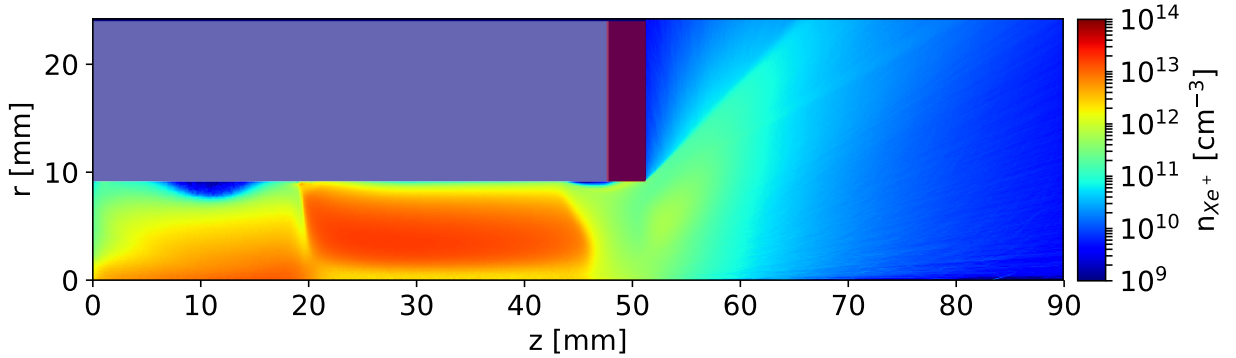


Figure 3.3:  $\text{Xe}^+$  ion number density in the HEMP-T DM3a. The dielectric (white) and grounded metal parts (red) are indicated ([P1]).

magnetic field lines dominates while the ions follow, a flat potential structure builds up in the channel which is shown in figure 3.4. The plasma potential is in the range of the applied anode voltage of 500 V. Therefore the electric fields in the channel are small, and ions are accelerated only in the thruster exit region, where potential and particle densities drop because of the lost plasma confinement.

Only at the cusp, ion and electron densities deviate significantly because the electrons are guided towards the wall there and a classical plasma-wall sheath develops. The potential drops by 42 V from the plasma toward the wall, which is shown in figure 3.2. It accelerates the ions towards the channel wall which results in energies of impinging ions  $\mathcal{E}_i \lesssim 50$  eV. However, this energy is still smaller than the sputtering threshold of boron nitride for impinging xenon ions of about 60 eV [85, 86]. In the other channel regions, the energies of impinging ions are much lower because of the reduced plasma-wall sheath discussed in section 3.1.1. This results in small electron fluxes towards the dielectric wall, which results in a smaller potential drop compared to the classical plasma-wall sheath at the cusp in figure 3.2. The ion fluxes towards the wall are therefore small, and ions still impinging the wall have energies well below the sputtering threshold. Therefore sputtering in the discharge channel occurs almost exclusively in the spatially confined region of the magnetic cusp and even there on a relatively low level because of the still low ion energies. Specifically, the wall

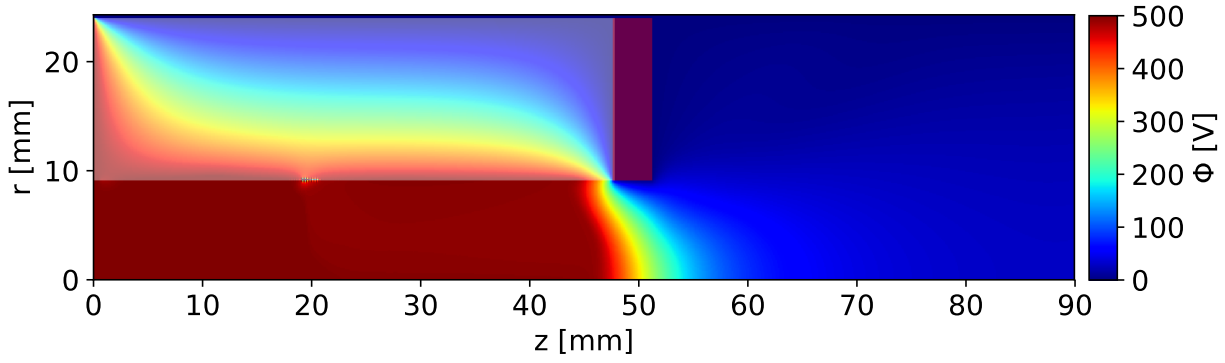


Figure 3.4: Electric potential in HEMP-T DM3a. The dielectric (white) and grounded metal parts (red) are indicated ([P1]).

erosion in most channel regions is smaller than HETs, resulting in long thruster lifetimes [23, 28].

### 3.1.3 Neutrals

In figure 3.5 the neutral densities are shown. The density is highest near the nozzle which is centered around the symmetry axis at the anode. The neutrals quickly relax after injection due to elastic neutral-neutral collisions. A decay of the density is observed downstream from the axial cusp position where the densities near the symmetry axis are generally lower than at higher radii. Despite the distribution of hot electrons throughout the channel because of

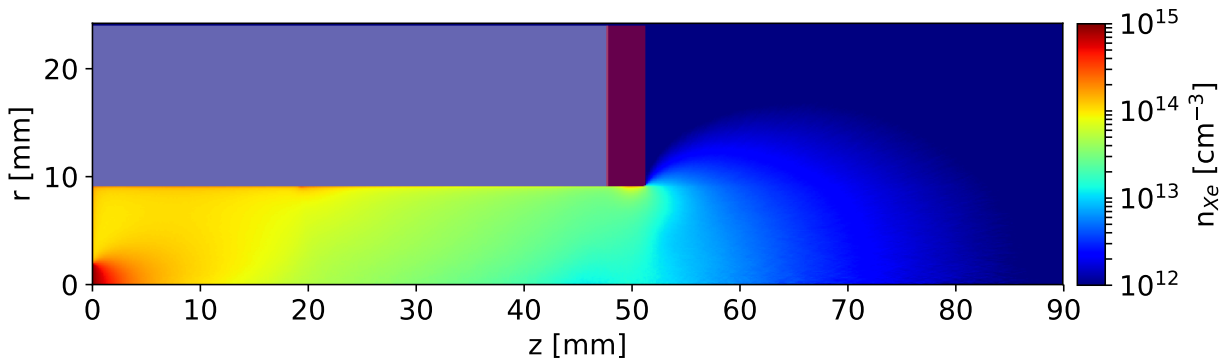


Figure 3.5: Xe neutral number density in the HEMP-T DM3a. The dielectric (white) and grounded metal parts (red) are indicated ([P1]).

the cusp physics outlined above, the channel electrons have the highest energies near the axis where they enter the channel from the plume. This leads to higher ionization rates and hence lower neutral densities there. Upstream from the channel exit, the electrons are cooled because of the influence of collisions. The high neutral densities at the wall are a result of the thermal recombination of ions to neutrals.

### 3.1.4 Comparison to experiments and limits of the simulation

In the simulation, the discharge current, i.e. the net current measured at the anode, is  $I_A = 613 \text{ mA}$  and the emitted ion beam current is  $I_B = 356 \text{ mA}$ . This results in an ionization efficiency of  $\eta_i = I_B m_{Xe} / (e \Gamma_{Xe}) = 39.5\%$ , with the neutral xenon mass flow rate  $\Gamma_{Xe} = 1.22 \text{ mg/s}$  (12.5 sccm) used here. It measures how much ion beam current is produced from the neutral flow rate at the anode. The ionization efficiency is lower compared to the efficiencies of 70% – 90% reported from experiments [39, 87]. As a result, the total thrust  $T = T_{Xe^+} + T_{Xe^{2+}} = 5.53 \text{ mN} + 1.57 \text{ mN} = 7.10 \text{ mN}$  is also lower than in experiments, where for comparable parameters (anode voltage and neutral gas flow) thrusts in the range of 12.5 – 15 mN were reported [39]. There are several possible explanations for this behavior. One is an overestimation of plasma wall losses because of the applied similarity scaling scheme. Because the ratio of electron Debye length and system length is not preserved, the sheath size and thus plasma-wall losses increase. They lead to a decreased plasma density, discharge current, beam current and thrust. This results in a deteriorated thruster performance which is shown in publication [P5] in the appendix where the high wall losses in the small scale  $\mu\text{HEMP-T}$  result in a reduced thruster performance. A similarly contributing mechanism is the influence of the boundary conditions on the electric potential, notably of the grounded pole piece at the thruster exit. It is the result of the similarity scaling scheme which alters the relative length scales between real and down-scaled system [88]. The distorted potential structure affects the electron transport from the plume into the discharge channel, which results in changed plasma discharge characteristics. Moreover, the distorted potential changes the ion emission characteristics and contributes to the deviations between simulation and experiments. Another aspect is the influence of the suppressed anomalous transport in the axisymmetric 2D model. Instabilities in the thruster exit region could increase the transport of hot electrons from the injection region in the plume into the channel. This would lead to a higher number of high-energy electrons in the channel and would further increase the ionization rates and propellant utilization. The azimuthal electron drift stability could also increase the electron energies in the cusp region because of the large electric field fluctuations, which can be on the scale of the present electric field in HETs [84]. Because a combination of these factors is likely responsible, further investigation is necessary to identify the cause for the differences between simulation model and experiment.

A physical reason for the lower observed thrust, but not for the reduced ion beam current, are the higher ion emission angles observed in most simulations compared to experiments

which is discussed in publication [P3] in the appendix. A high ion beam divergence results in a lower thrust obtained from the emitted ions, making thruster operation more inefficient despite a high ionization efficiency. However, the shape of the ion beam is determined by the potential structure in the near-field plume. This in turn is determined by the discharge conditions in the channel. It is further affected by the boundary conditions for the electric potential which present only an approximation to the real system. Their influence depends on the similarity scaling factor, and it increases with higher scaling factors. Together with relative increase of the Debye scale compared to the system size for higher scaling factors, this results in altered electric fields in the near-field plume which lead to higher ion emission angles. To obtain a more realistic model, the distance between thruster exit and boundaries should be as high and the similarity scaling factor as low as possible. The electric field structure in the near-field plume is determined by the coupling between channel and plume plasmas, which is investigated in the next section.

## 3.2 Near-field plume

In the near-field plume, the shaping of the ion emission characteristic takes place. The structure of the electric field there, which is the result of the channel to plume transition of the plasma, determines the ion emission characteristics of a HEMP-T. In general, the thrust contribution of species  $s$  is calculated as

$$T_s = \int dE_s \int d\theta \sqrt{\frac{2E_s(\theta)}{m_s}} \cos(\theta) \frac{m_s I_s(E_s, \theta)}{q_s}, \quad (3.1)$$

with the angular energy and current distributions  $E_s(\theta)$  and  $I_s(E_s, \theta)$ , respectively. The angle  $\theta$  is the beam divergence angle measured from the symmetry axis in the thruster exit plane. Eq. 3.1 shows that to achieve a high thrust for a fixed ion beam current, the ion emission angle must be minimized, while the ion energies should be maximized towards  $q_s \Phi_{plasma}$ . In figure 3.6,  $I_{Xe^+}(E_s, \theta)$  of the HEMP-T simulations discussed in section 3.1 from publication [P1] is shown. Experimentally, the ion current and energy distributions are measured with retarding-potential analyzers (RPA) which cover the angular bins in the plume during thruster operation tests in vacuum chambers [20]. The distance between thruster exit and RPA can vary but is on a scale of about one meter. In figure 3.6 one can see that close to the symmetry axis for angles of up to  $50^\circ$ , the main ion energies are near the plasma potential and anode voltage of 500 V. Higher angle contributions show a gradually decreasing ion energy. In experiments, a contributing factor is the influence of  $Xe^+ - Xe$  charge exchange and momentum transfer collisions. As a result of these collisions the charge can be transferred from the fast ion to a slow neutral which is detected at energies below anode voltage. The influence of charge exchange collisions is only relevant on a scale of more than one meter because of their high mean-free-path. Therefore, their influence in the simulation with a total domain size of under 10 cm is negligible.

In publication [P3] in the appendix, the origin of the low energy ion current contributions at emission angles above  $50^\circ$  in the HEMP-T DM3a is investigated. It was found that these low energy, high angle contributions are related to the origin of the ions, i.e. the location where the ions are generated by an ionization collision. For the diagnostic, this origin location was stored for each ion in the simulation. The spatial ionization distribution could then be analyzed for each angle bin in the plume. For emission angles between  $30^\circ$  and  $50^\circ$  the emitted ions are mostly generated inside the discharge channel and near the symmetry axis. From there, they drift slowly towards the thruster exit where they are accelerated from plasma to vacuum potential, resulting in the high ion energies at low

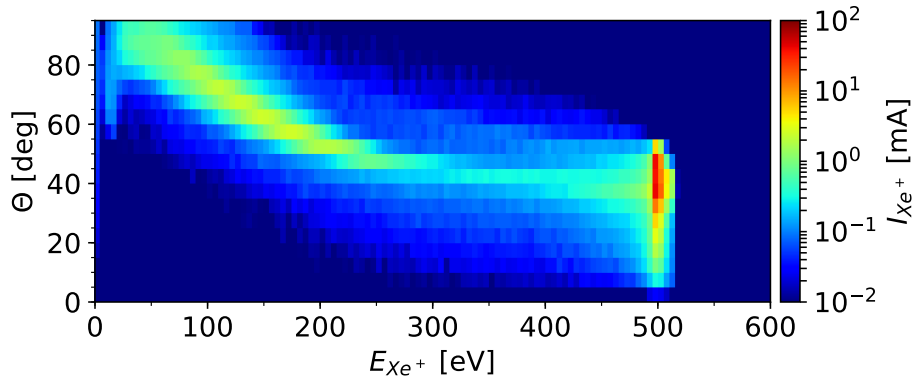


Figure 3.6: Angular energy distribution of emitted  $\text{Xe}^+$  ions in the simulation, measured at the domain boundary. The ion energies are corrected for the residual potential at the right domain boundary ([P1]).

emission angles observed in figure 3.6. For higher angles, the ions were mostly generated in the thruster exit region and at higher radii. There, the plasma potential has already decayed towards vacuum potential and the fraction of the radial to axial electric field components increases and accelerates the ions towards higher angles at lower energies. These findings were confirmed in the simulations of the S1 thruster carried out in publication [P7] in the appendix. The results show that at low emission angles, the ions are generated closer to the symmetry axis compared to higher ion emission angles near the channel wall. Ions created at higher radii in the thruster exit region experience a more radially oriented electric field, which accelerates them towards higher emission angles. Thus, to reduce the high angle, low energy ion current contributions in the simulation, the density of residual neutrals in the near-field plume must be decreased. This can be achieved with a higher ionization efficiency in the channel, leading to higher ionization of neutrals upstream which reduces the residual neutral density and therefore the ionization rates in the near-field plume.

The second important aspect of the ion emission characteristic is the ion emission angle of ions with high energies. In figure 3.6 one can see that the highest ion currents are reached at emission angles of about  $40^\circ$ . This agrees well with experiments, but in most HEMP-T simulations the emission angle is higher than in experimental measurements as discussed in publication [P3]. From eq. 3.1 one can see that the thrust contribution of the ion current scales with  $\cos(\theta)$ . As a result, the ion current with a maximum at  $40^\circ$  contributes about 25% less to the thrust than the same current with an emission angle of  $0^\circ$  would.

In general, the emission angle of high energy ions is determined by the electric field structure at the thruster exit. Unlike the low energy ions which are generated in the thruster exit region, the high energy ions experience the full drop from plasma to vacuum potential.

---

Their angular distribution is mostly determined by the ratio of radial and axial electric field components in the channel exit region. The electric potential, however, is affected by the plasma discharge conditions where higher plasma densities (and therefore discharge and beam currents) correspond to a decay from plasma to vacuum potential further downstream from the exit plane. Because there is no confinement from the channel walls in the vacuum, the radial electric field components increase, which leads to an increased ion emission angle. Lower plasma densities lead to the opposite effect such that the highest electric fields are shifted towards the channel which leads to a mostly axially oriented electric field and hence a low ion beam divergence. Another contributing aspect is the origin of ion generation. Although these general trends can be identified, the electric field structure is also strongly influenced by the thruster geometry. The length of the discharge channel in relation to the exit cusp or a grounded pole piece at the thruster exit (such as the one in the HEMP-T DM3a) are the most important parameters. The former determines the position and structure of the potential drop at the exit because of its confinement while the latter acts as a lens for the ion beam [89].

Besides physical effects, simulation artifacts can influence the ion emission characteristics. The boundary conditions at the top and right domain boundary influence the structure of the electric potential in the plume because of the limited size of the simulation domain. To guarantee independence of the potential from the boundary conditions, the simulation domain would have to be impractically large [74]. The injection of electrons to fuel the plasma discharge presents another artificial influence on the ion emission characteristics in the simulation. In experiments, a hollow cathode neutralizer provides electrons for the plasma discharge and plume neutralization. The exact electron currents provided for the discharge are unknown. This is in part due to the influence of electron emission caused by ions impinging on walls of the vacuum vessel in which the thruster is tested. Also unlike in the experiments, an axisymmetric 2D simulation can only model an axisymmetric injection scheme. Commonly, electron injection occurs either in a small region of the plume or along the right domain boundary in the simulation. In the publication [P4] in the appendix, the influence of the location of the electron source on the angular ion current distribution is investigated. There the position of the electron source affects the angular ion distribution. The effect is small for thermal electron injection but increases for higher injection currents and drift velocities. Because the experimental electron currents are unknown, the electron sources used in the simulations are only approximations to the real-life system. All these influences demonstrate the non-linear coupling of channel and plume plasmas. Because the plume influences the plasma discharge in the channel and vice versa, the entire coupled

system has to be considered for a realistic thruster model.

### 3.3 Breathing mode oscillations

One of the research questions formulated in chapter 1 concerned the investigation of physical phenomena arising from the coupling of channel and plume plasmas which was described in section 3.2. Such an effect is the breathing mode oscillation which can be observed in all plasma quantities. It was first observed in a PIC simulation of the HEMP-T in publication [P2] in the appendix. The oscillations were first observed during the stable operation of HETs and have been investigated experimentally [90–96] and theoretically [97–105]. They are determined by the coupled dynamics of ions, electrons and neutrals where the latter are ionized and subsequently repopulate the oscillation region. In HETs the observed oscillation frequencies are in the range of 10 – 30 kHz with oscillation amplitudes of the discharge current ranging from 10 – 100%. Because of their high amplitudes, control of the breathing mode oscillations is important for stable operation of HETs. In HEMP-Ts breathing mode oscillations are also observed experimentally during thruster operation. The reported frequencies are in the range of 100 – 300 kHz with discharge current oscillation amplitudes of up to 30 % [51]. For HEMP-Ts, however, theoretical and experimental investigation was largely lacking.

A simple description of the breathing mode oscillations is obtained with a 0D predator-prey model [99, 104]. There, the oscillation is a result of a local imbalance between the replenishment of neutrals acting as prey and the ions and electrons acting as predators. The oscillation frequency can then be estimated as

$$\omega = \frac{(u_i u_n)^{1/2}}{L} \quad (3.2)$$

with the oscillation length scale  $L$  and the replenishment velocities  $u_i$  and  $u_n$  of ions and neutrals, respectively. This approximation agrees well with experimental data [104]. However, the electron temperature, which is assumed to be constant in eq. 3.2, is expected to play an important role in the development of breathing oscillations [102] and recent measurements suggest that the predator-prey model is unrealistic for HETs [95].

The model used for the investigation of the breathing mode in HEMP-Ts is the PIC model described in section 2.2.1. Again the HEMP-T DM3a thruster model is considered and

the detailed simulation parameters can be found in publication [P2]. Note that a feedback electron injection scheme is used to keep the plasma densities near  $10^{13} \text{ cm}^{-3}$ . Because this leads to fluctuations of the injection current, all modes in the plasma are excited and only the main mode is amplified from the excitation spectrum, which results in the observed breathing oscillations. As is the case in experiments, the oscillation can be observed in the discharge current in the simulation. The emitted ion beam current and thus the generated thrust also oscillate with the same frequency. The oscillation of those quantities is shown in figure 3.7. An amplitude of 15% from the mean current discharge current of 84 mA

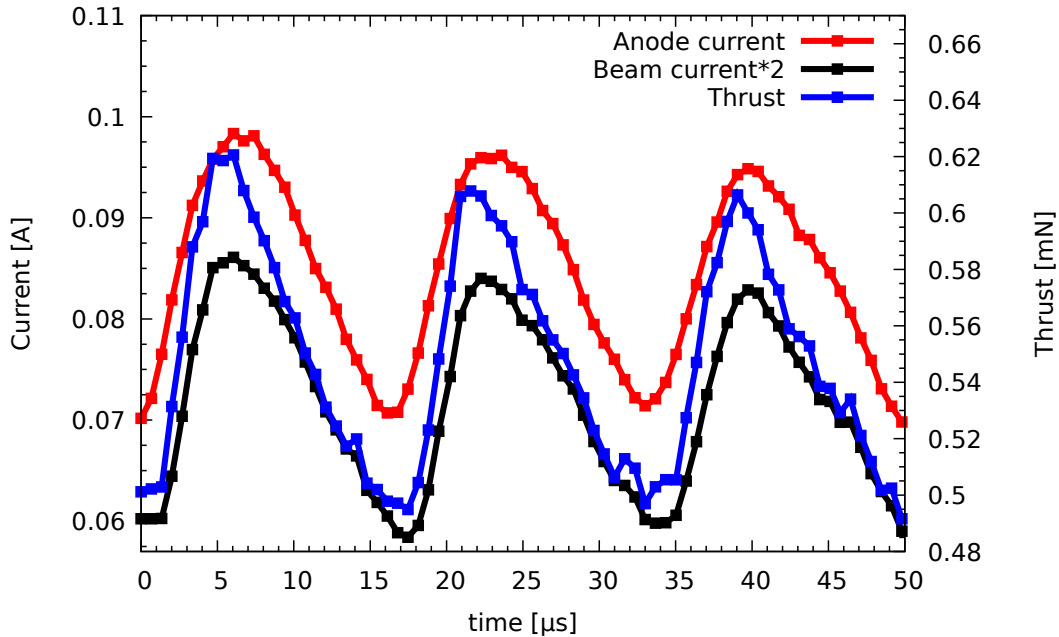


Figure 3.7: Anode and net beam currents along with the net thrust over the course of the breathing oscillation ([P1]).

is observed, with similar amplitudes for the ion beam current and thrust. The oscillation frequency is 60 kHz, which is within a factor of two from the lower end of the reported frequencies of 100 – 300 kHz in HEMP-Ts [51]. This frequency is in good agreement with the predator-prey estimate of 75 kHz, which was obtained with ion and neutral velocity data from the PIC simulation. In publication [P2], a comparison with an experimental measurement is also presented. The experimentally measured frequency, however, is much higher at 313 kHz. This can be attributed to very disparate discharge characteristics between the simulation and the experiment, as the experimental mean discharge current of 390 mA was higher by a factor of about five. Further research is necessary to investigate the influence of the plasma discharge conditions on the breathing oscillation in the HEMP-T.

Together with the global parameters, the oscillation can be observed in the plasma discharge. The oscillation is located near the thruster exit plane around  $z = 50 \text{ mm}$ . Figure 3.8 shows

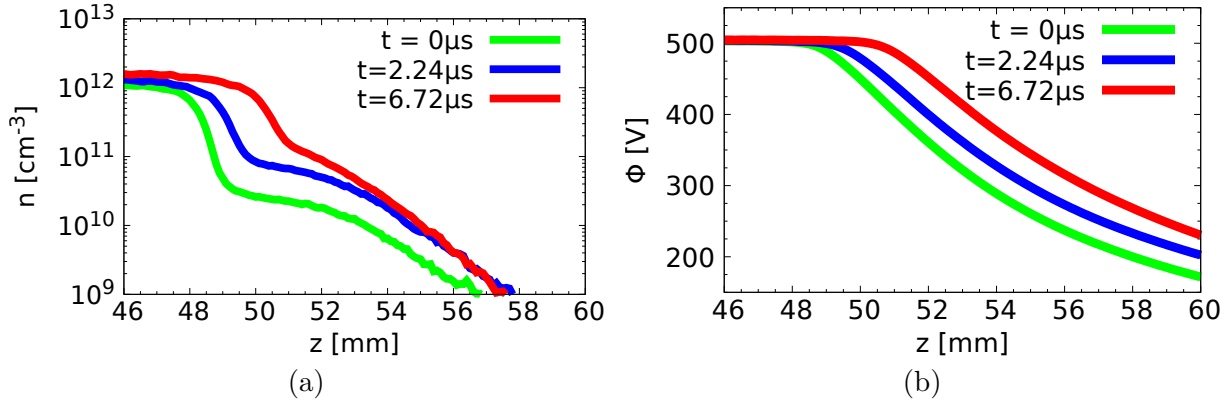


Figure 3.8: Axial (a) electron and (b) electric potential profiles at  $r = 1$  mm in the thruster exit region ([P1]).

the axial fluctuation of the electron density and the electric potential in the oscillation region  $48 \text{ mm} \leq z \leq 52 \text{ mm}$ . One can see that the drop from channel plasma to vacuum is shifted downstream at the discharge current maximum ( $t = 6.72 \mu\text{s}$ ) while at the minimum ( $t = 0 \mu\text{s}$ ) it moves further into the discharge channel. In the channel, the electron densities at the oscillation maximum are slightly higher than at the minimum, which agrees with the higher discharge currents observed at that time. The ions show an analogous behavior. For the electron temperature, however, the behavior is inverse. At the oscillation minimum, the average electron temperature in the oscillation region is at its maximum at 168 eV and at the oscillation maximum it is the lowest with 78 eV. This is the result of the potential drop moving into the discharge channel into the area of the exit cusp at the oscillation minimum, which produces high temperature electrons in the oscillation region. These high energy electrons then lead to an increased ionization, which increases the charged particle densities and pushes the potential drop downstream out of the discharge channel which decreases electron temperatures again. As a result, plasma densities drop and the strong electric field moves into the discharge channel again, restarting the oscillation. This is represented by the oscillation of the potential drop which is shown in figure 3.8. There, it is defined as the axial location where the radially averaged potential drops to the  $e$ -th fraction of the anode voltage. In sum, the electron temperature plays an important role in the breathing oscillation in HEMP-Ts.

Figure 3.9 shows the oscillation of the potential drop and hence the electric field together with the mean  $\text{Xe}^+$  ion emission angle. One can see the correlation between the potential drop and the ion emission angle which shows the coupling between both quantities. The phase shift between both quantities occurs because of the ion flight time from the exit region to the diagnostic surface at the simulation domain boundary. A potential drop further

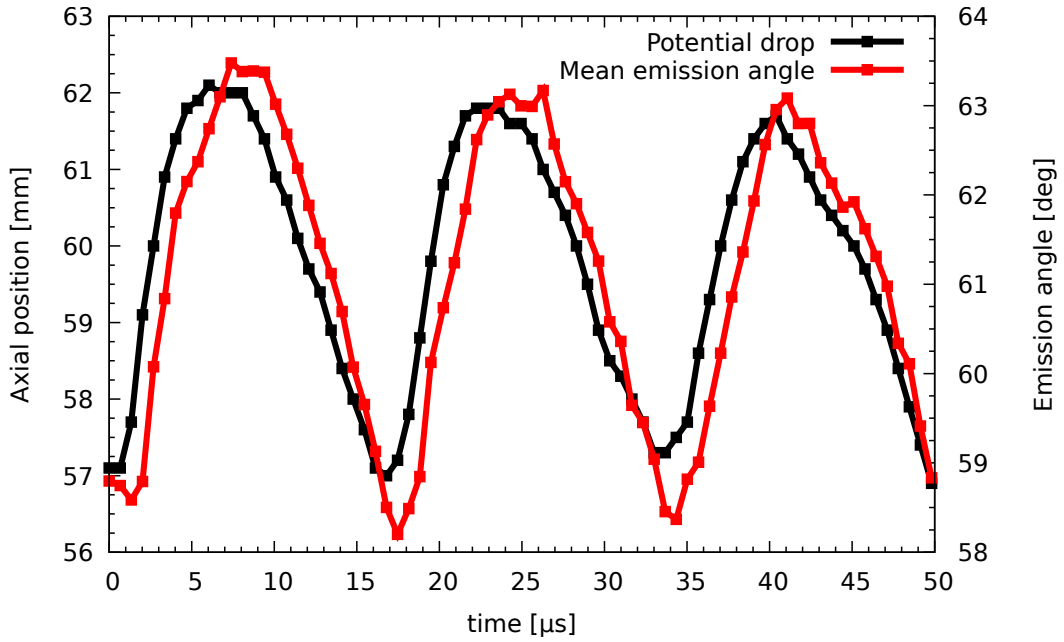


Figure 3.9: Axial position of the potential drop and mean ion emission angle. A potential drop further downstream results in higher ion emission angles ([P1]).

downstream results in higher radial electric fields because the radial confinement from the dielectric walls is lost. The ions are then accelerated towards higher emission angles which results in a lower thrust contribution, which was discussed in section 3.2. Thus, the position of the potential drop is an important quantity for optimization of the ion emission angle and hence for the optimization of HEMP-Ts in general.

Due to the variation of the number density and energies of the charged particles, the oscillation can also be observed in the collision rates measured in the simulation. The most important collision process is the single electron-xenon impact ionization collision, which produces a  $\text{Xe}^+$  ion and an electron from a neutral due to electron impact. At the oscillation maximum, the ionization collision rates are at their maximum throughout the channel. This is the result of the hot electrons entering the channel at the oscillation minimum, which increases ionization rates in the whole channel, as discussed in section 3.1, and moves the plasma towards the oscillation maximum again. The collision rates of the inelastic electron-neutral excitation collisions oscillate analogous to the ionization collisions. These collision rates present a good approximation to the light emission of the excited neutrals in the thruster. This allows for a simple experimental diagnostic based on optical emissions where the breathing oscillations are indeed observed experimentally via optical emission [106].

In summary, the breathing mode demonstrates the coupling between channel and plume plasma which affects the emission characteristics of a HEMP-T. The simulation of a plume

expansion extending several meters downstream with a fully kinetic PIC model, however, is too costly computationally and other simulation methods are required.

### 3.4 Plume expansion

To investigate the question of simulation models suitable for the simulation of a coupled thruster channel and plume outlined in chapter 1, a coupled model of fully kinetic and hybrid PIC is investigated. Such a combined model can overcome the computational constraints imposed by the fully kinetic model. To achieve such a plume model, the kinetic method discussed in section 2.2.1 is coupled with the hybrid PIC model from section 2.2.2. In the plume the influence of the non-Maxwellian EEDF is small because of the low densities and energies of the plume plasma. Moreover, kinetic boundary or magnetic field effects play only a minor role in the plume. As a result, the electrons can be successfully approximated as a fluid in that region. This relaxes the spatial and temporal resolution of the simulation from the electron Debye length and plasma frequency to the ion quantities, respectively and offers a decrease in computational costs.

For the coupling of both models, the fully kinetic PIC model is used for the simulation of the thruster channel and near-field plume of a HEMP-T. The ion and neutral fluxes then serve as the input for the hybrid PIC plume simulation which allows for the computation of a large scale plume expansion. However, kinetic and fluid models can only be combined explicitly (i.e. one-way, from the channel to the plume) in ion thruster simulations because an implicit (two-way) coupling can introduce numerical instabilities. Although an implicit coupling model has been applied successfully, it relied on an implicit PIC formulation with equal grid resolutions and time steps in both kinetic and fluid models, which makes it inadequate for the reduction of the computational effort [107]. An explicit coupling, however, does not provide a solution to the combined channel-plume problem, but rather an approximation of the plume expansion for a given thruster channel configuration. In the following, such an explicit combination of fully kinetic PIC-MCC and hybrid PIC models is discussed. The simulations were carried out in Ref. [108]. The HEMP-T DP1 thruster model introduced in section 2.1 was used for the investigations.

The fully kinetic axisymmetric 2D3v PIC-MCC simulation described in section 2.2.1 is used for the simulation of the DP1 channel and near-field plume. From there the ion and neutral distributions serve as an input to the 3D hybrid PIC code EP2PLUS [76, 77] whose main

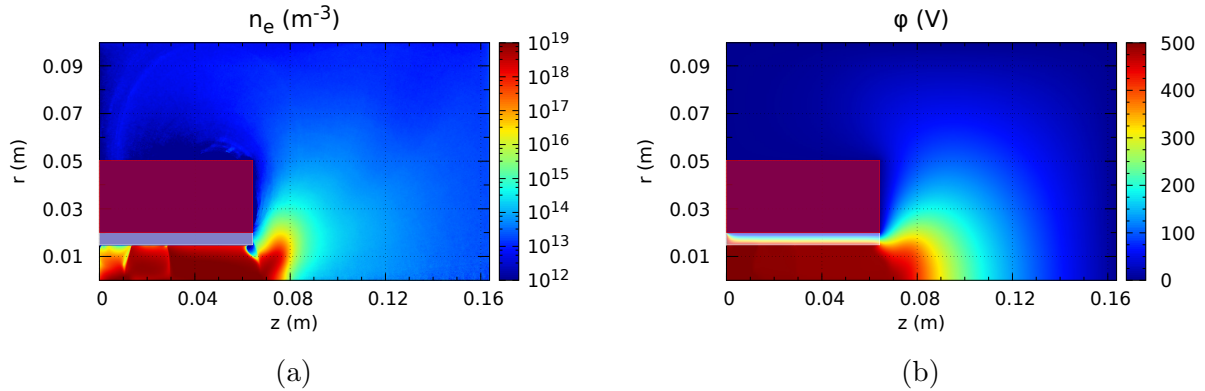


Figure 3.10: Electron number density (a) and electric potential (b) in the HEMP-T DP1. The dielectric (white) and grounded metal parts (red) are indicated [108].

features were described in section 2.2.2. The simulation of the HEMP-T DP1 discharge channel with the fully kinetic PIC simulation reproduce the typical physics of HEMP-Ts which were identified in section 3.1. In the channel, the electrons are magnetized and the characteristic magnetic cusp structure with the two intermediate cusps of the DP1 thruster is visible in figure 3.10. The electron distribution is similar to the DM3a model in figure 3.1. An equal oscillatory motion of the electrons between the cusps results in the flat electric potential structure in the channel, also shown in figure 3.10. The ion density again resembles the electron density in the channel. The doubly charged  $\text{Xe}^{2+}$  ions make up about 10% of the total number of ions. The number densities of both species are shown in figure 3.11. In the thruster exit region, the plasma densities drop because of the lost confinement from

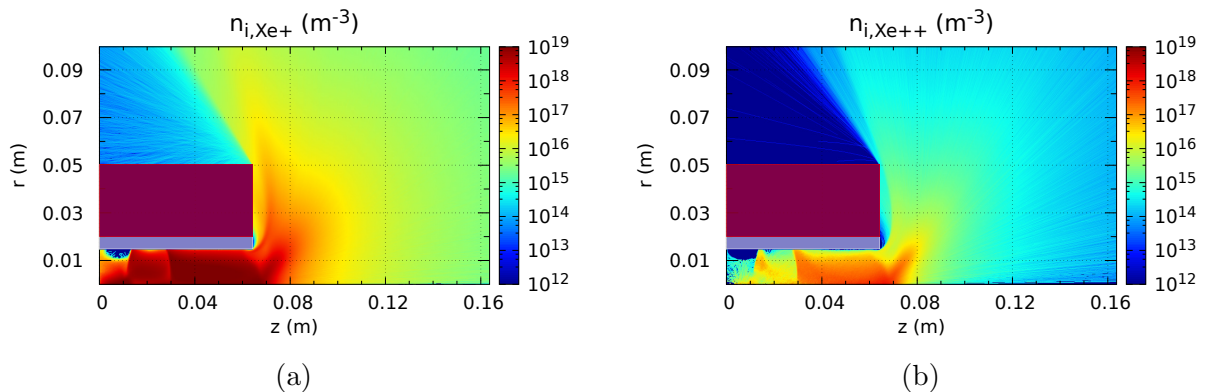


Figure 3.11:  $\text{Xe}^+$  (a) and  $\text{Xe}^{2+}$  (b) ion number densities in the HEMP-T DP1. The dielectric (white) and grounded metal parts (red) are indicated [108].

the channel walls. The electric potential begins to drop towards vacuum potential, but the highest electric fields can be observed outside the discharge channel which results in a very high beam divergence of the emitted ions with a maximum current at an angle of  $85^\circ$ . Similar to the discussion of the potential drop in section 3.2, this is a result of the very high

plasma densities of up to  $10^{14} \text{ cm}^{-3}$ , which were chosen to emphasize the plume features but are unpractical for actual thruster operation. In the near-field plume of figure 3.10 and figure 3.11 one can see that the ion densities are higher than the electron densities, by almost two orders of magnitude which should result in very high potential gradients which are not observed. This is the result of the high similarity scaling factor of 60 which was used for this simulation. As discussed in section 2.2.1, high similarity scaling factors result in an increased ratio of electron Debye scale to system size. In the plume it leads to regions where quasineutrality is seemingly violated after interpolation from the down-scaled to the real-life system. Hence, a realistic plume description is difficult to achieve with a fully kinetic PIC simulation using a high similarity scaling factor. To use the ion distribution as an input to the hybrid PIC code, the scaling has to be accounted for.

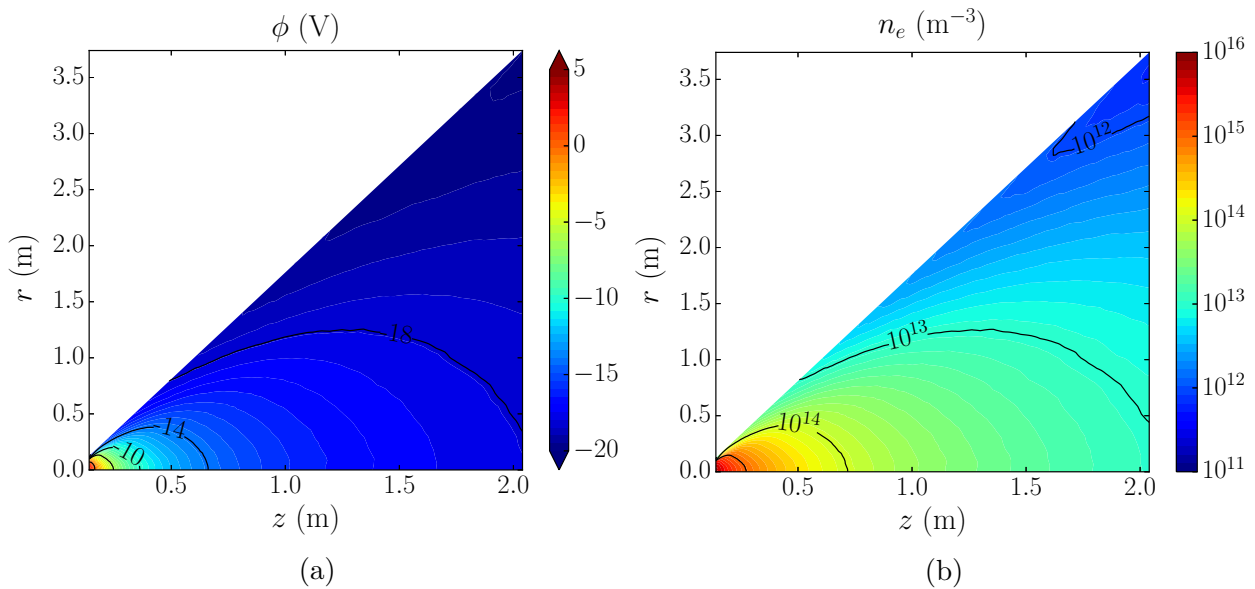


Figure 3.12: Electric potential (a) and electron number density (b) in the HEMP-T DP1 plume. The initial plane is located at  $z = 0.14 \text{ m}$  and the colored part of the plots indicates the conical simulation domain [108].

For the computation of the plume expansion with the EP2PLUS 3D hybrid PIC code, the neutral and ion densities and velocity distributions from the results of the 2D3v PIC code along the line  $z_0 = 0.14 \text{ m}$  were used as input. The reference electron temperature chosen arbitrarily in the ion injection plane at  $r = 0 \text{ m}$  was  $5 \text{ eV}$ . Quasineutrality was assumed for the electron number density in the domain. Electron collisions, electron inertia and magnetic field effects were neglected and the electric potential was calculated with the polytropic relation in eq. 2.12 with the coefficient  $\gamma = 1.3$ . Both the electron temperature and the polytropic coefficient present typical values for ion thruster plumes which can reproduce major plume features which was shown in comparison with experiments and fully kinetic simulations [31, 78]. The electric potential was set to zero at the reference point. The

simulation domain is conical and extends 2 m axially and 3.5 m radially from the injection plane. The total simulated time for the plume expansion was 2.5 ms, which is enough to reach convergence. In figure 3.12, the electric potential and electron number density are shown in the plume. The electron density decreases monotonically during the expansion by about two orders of magnitude. Likewise, the potential decreases monotonically and tends asymptotically towards  $\phi_\infty = -\gamma T_{e0}/(e(\gamma - 1)) \approx -22$  V. The ion density shown in figure 3.13 shows the expansion of the  $\text{Xe}^+$  ions in the plume which are of the highest interest. About 0.7 m downstream the ion density drops by one order of magnitude, and drops by one more order near the right domain boundary after an expansion of nearly 2 m. The ion expansion is conical and no pronounced beam shape can be observed. This is

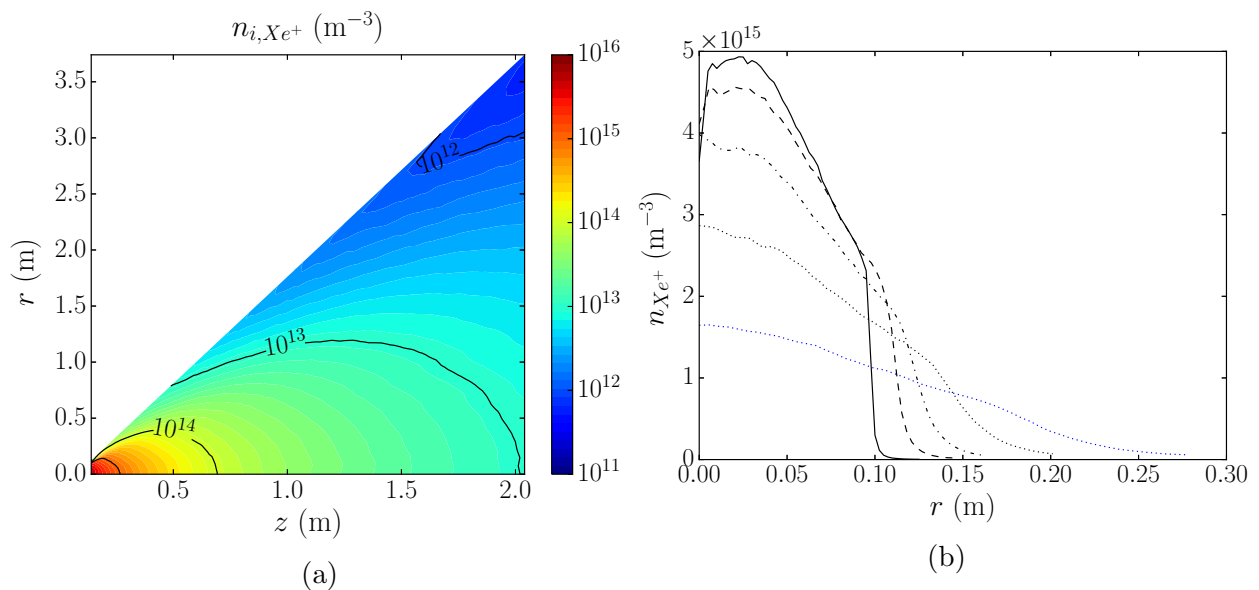


Figure 3.13: Ion number density map (a) and radial profiles (b) in the HEMP-T DP1 plume. The initial plane is located at  $z_0 = 0.14$  m. In plot (a) the coloured part indicates the conical simulation domain. In plot (b) the black solid line refers to  $z = z_0$ , the black dashed line to  $z = z_0 + 0.01$  m, the black dash-dotline to  $z = z_0 + 0.02$  m, the black dotted line to  $z = z_0 + 0.04$  m and the blue dotted line to  $z = z_0 + 0.08$  m [108].

the result of a gradually decreasing electron pressure which results in a small ambipolar electric field which is not strong enough to significantly influence the ion trajectories. As was the case in the discharge channel simulation, the doubly charged  $\text{Xe}^{2+}$  show a behavior analogous to the singly charged ions and their fraction of about 10% of the total ion number is retained. Figure 3.13 also shows the development of the radial ion profile at several axial positions near the injection plane. In the injection plane, the ion emission was very pronounced with a hollow density profile. However, this shape is rapidly lost during the expansion after 2 – 4 cm because of the ambipolar electric field such that the ion emission has a conical shape further downstream.

In summary, the method of combining kinetic and hybrid PIC methods to compute the plume expansion in a combined numerical model is suitable to achieve a plume simulation of an originally fully kinetic model to overcome length limits. Even with the approximations imposed by the electron fluid model the plume expansion produces results which have been validated by experiments and fully kinetic PIC models. Although the actual electron energy distribution is influenced by the plasma in the discharge channel, its influence on the plume expansion itself is probably low because of the low collision rates and long mean-free paths. However, a fully kinetic simulation covering the discharge channel and the whole plume is required to resolve the coupling. In the following section, a method is presented which can help to overcome the computational limits of the fully kinetic PIC simulation to make a combined model feasible.

### 3.5 Kinetic plume simulation

In this section a method to reduce the computation time of the fully kinetic PIC model from section 2.2.1 for the simulation of the coupled channel-plume plasma is introduced. If the plume and thruster channel are considered in a single PIC model, a large simulation domain which has to resolve the smallest length scale, the electron Debye length in the channel, is required which leads to a very high computational cost. Furthermore, the total number of super-particles in the simulation increases because of the long length scales of the small density plume plasma. The domain decomposition parallelization outlined in section 2.2.1 already reduces the computational cost for the particle mover and the collisions substantially. As a result, the most computing time goes into the Poisson-solver module, especially for the large simulation domains for the coupled channel-plume simulation.

The first approach to a reduction in computation time for a large simulation domain is called mesh coarsening (MC). It aims to reduce the overall number of mesh points  $N$  to reduce the computation time of the Poisson-solver module, whose execution time increases with some function of  $N$ , depending on the specific solver. This reduction in  $N$  is achieved by increasing the (so far uniform) grid spacing  $\Delta r$  between mesh points. It can be applied in regions with low plasma densities to avoid the finite-grid instability such as the HEMP-T thruster plumes. However, because of the symmetric difference scheme for the computation of the electric field, self-forces arise at the interface between regions with different grid spacing. These self-forces artificially alter the energy of charged particles crossing the interface which leads to physically incorrect results. This can be overcome with a correction for the electric

field, which was derived in Ref. [109]. If this correction is applied in the calculation of the electric field, no self-forces arise and a non-uniform grid spacing can be used.

In Ref. [74], the MC algorithm was generalized to 2D grids and applied to the axisymmetric 2D3v PIC-MCC simulation of the HEMP-T DM3a described in section 2.2.1. The solution of the electric potential calculated with the MC method showed only small deviations compared to the one calculated completely on the fine mesh in the HEMP-T DM3a. The number of mesh points was drastically reduced for large simulation domains, which resulted in performance increases of the solver compared to the unmodified case. The stability of the method was proven with a long-term continuation of a converged run, which aside from statistical noise showed no meaningful deviation. So far, the implementation of this algorithm is static, i.e. the regions with larger grid spacing must be supplied by hand, but a dynamic algorithm which tailors the grid spacing to the plasma density in an adaptive MC algorithm is conceivable. Therefore, the MC method can substantially reduce the computational costs of PIC simulations with large domains and unevenly balanced plasma densities.

The above approach can be coupled with another method which aims to reduce the time scales encountered in the plume. There, the plasma particles must be tracked for paths of several meters but with a time step chosen to resolve the much higher electron plasma frequency in the discharge channel. This results in a very small displacement per particle push and time step in the plume, which makes the particle mover inefficient there. Sub-cycling, which was introduced in section 2.2.1, can be used to overcome this limit. The technical implementation treats plasma particles in the plume as separate species, each with their own sub-cycling interval. Each such particle is then moved only after a number of time steps and experiences the average electric field during the sub-cycling interval which results in a higher particle displacement per particle push. However, the PIC stability criteria must still be satisfied to avoid numerical instabilities. On average, a particle's travel distance during one particle push should not surpass the length of a single cell. If both approaches are combined, this requirement is weak because the effective cell size in the plume increases and thus higher sub-cycling factors can be applied. Furthermore, the matter of bad statistics in the plume due to low plasma densities relaxes because the number of particles in the larger cells increases. In the following, this method will be called sub-cycling mesh-coarsening (SMC) algorithm, and a proof-of-principle simulation with the PIC model from section 2.2.1 of the HEMP-T DP1 is carried out.

The total size of the simulation domain is  $r \times z = 80.45 \text{ mm} \times 150 \text{ mm}$  with a grid spacing

of  $\Delta r = 0.223$  mm and a time step of  $\Delta t = 1.68 \cdot 10^{-11}$  s. A similarity scaling factor of 60 is used. Neutrals are injected half-Maxwellian with a drift energy of 0.03 eV and a temperature of 0.017 eV with a flow rate of 15 sccm (1.48 mg/s) at the anode ( $z = 0$ ) in the range  $0 \leq r \leq 5$  mm. Electron injection occurs thermally with an energy of 1 eV at the right domain boundary with a current of 360 mA. The other simulation parameters are equal to the ones used in the publication [P1]. With the MC algorithm, the grid spacing is doubled in the region  $(20 \text{ mm}, 80 \text{ mm}) \leq (r, z) \leq (30 \text{ mm}, 100 \text{ mm})$  and increased by a factor of four in the region  $(30 \text{ mm}, 100 \text{ mm}) \leq (r, z)$ , respectively. For this proof-of-principle simulation, only the electrons in the plume are treated as a separate species in the region  $(25 \text{ mm}, 90 \text{ mm}) \leq (r, z)$ . In general, however, several electron and ion species can be used with this approach. The reference run also uses the mesh coarsening algorithm with the

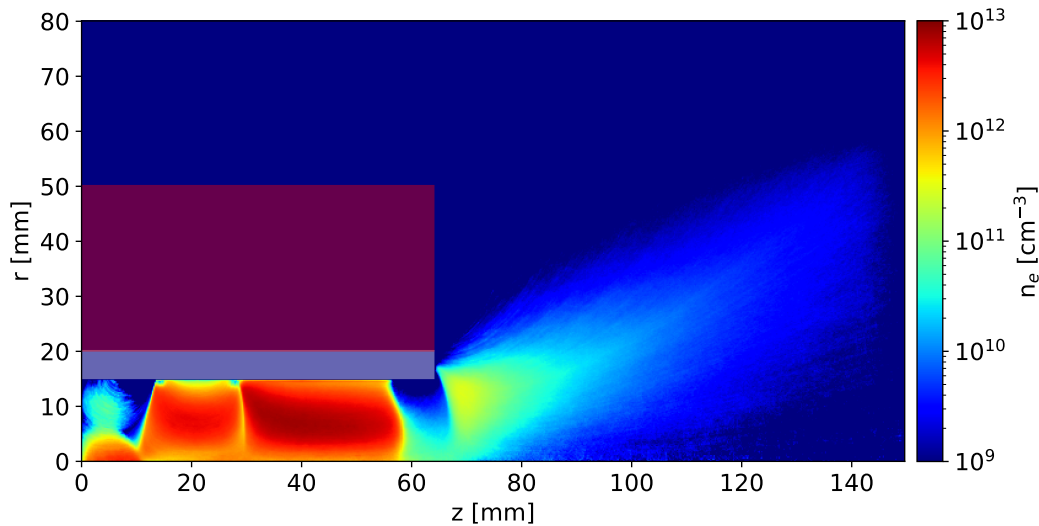


Figure 3.14: Electron number density calculated with the SMC algorithm in the HEMP-T DP1. The dielectric (white) and grounded metal parts (red) are indicated.

same grid spacing as above because its stability was already shown without the electron sub-cycling [74]. Both simulations started from a converged run of the HEMP-T DP1 with a run time of  $3 \cdot 10^6$  time steps which covers all relevant time scales of the system. The simulation results were averaged for  $10^4$  time steps at the end of the total simulation time.

The electron number density of the proof-of-principle simulation is shown in figure 3.14. It is lower than the one in figure 3.10 because of the lower neutral flux rate, but both show the same characteristic features such as the two intermediate cusps of the DP1. In figure 3.15, the absolute difference of the electron number densities between the proof-of-principle run with the SMC algorithm and the reference case is shown. One can see that the deviations between both simulations are very small compared to the total number density shown in figure 3.14. The largest differences are observed in the discharge channel, which only show

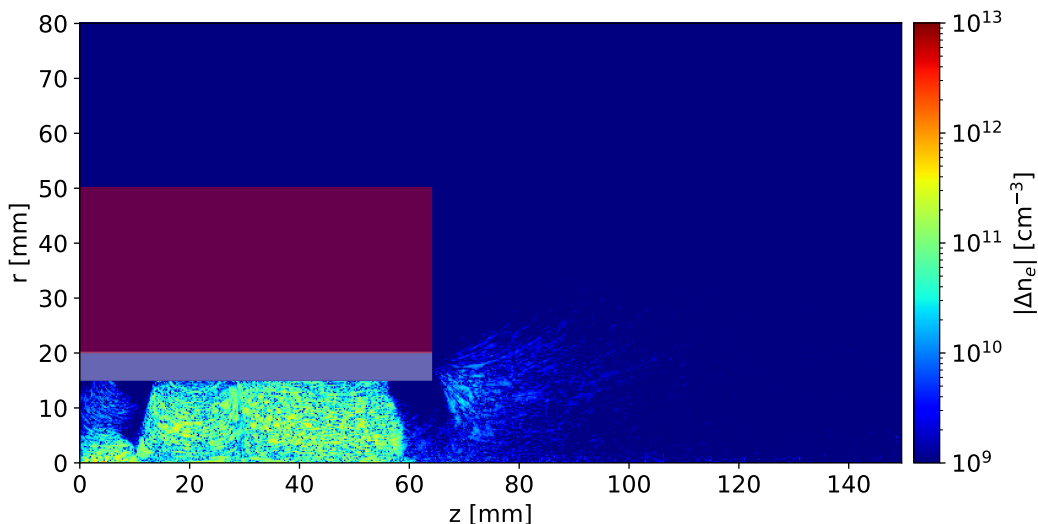


Figure 3.15: Absolute difference of the electron number densities of the reference case and the SMC-PIC simulation of the HEMP-T DP1. The dielectric (white) and grounded metal parts (red) are indicated.

statistical fluctuations which are below 10% of the reference value. The number densities of the other species show a similar behavior and no difference can be observed in the electric potential. Because of the long total simulation time, the results are not expected to change appreciably for longer simulation times. In all, one can see that the proposed method is stable and can be applied to make the simulation of the coupled channel and plume plasmas in the HEMP-T feasible.

The results show that the SMC method, which combines the mesh-coarsening and the sub-cycling for electrons and ions, can potentially reduce the computational cost for fully kinetic simulations of the combined channel and plume system significantly. However, further research is necessary to investigate the limits of this method and possible stability concerns as well as to carry out actual scaling measurements to estimate the savings in computational costs. After these questions are answered, a large scale plasma model which combines channel and plume plasmas is feasible.



## 4 Conclusions

Numerical modeling offers great opportunities for the optimization of ion thrusters. It serves as a tool to increase the understanding of the underlying thruster physics which can be applied for thruster optimization. This potentially reduces the number of required prototypes and testing cycles. For a predictive ion thruster model both the thruster discharge channel and the plume must be considered in a self-consistent approach. However, because of the different length and time scales in the discharge channel and the plume, most thruster simulations treat both regions separately and disregard their coupling. Therefore, the aim of this work was the investigation of the coupling between channel and plume plasmas with effects arising from the coupling and how they influence the ion thruster performance. Furthermore, simulation models which are suitable for the simulation of the coupled system of discharge channel and plume were investigated. For this purpose, the HEMP-T ion thruster was considered. The simulation models for the investigation of the research objectives were an axisymmetric 2D3v PIC-MCC and a 3D fluid-electron hybrid PIC model.

The coupling between the channel and plume plasmas can be observed in the near field plume region. This is the region close to the thruster exit where the transition from the channel into the plume takes place. Because there is no confinement from the channel walls, the plasma expands with gradually decreasing densities. The electric potential drops from the plasma potential in the range of the applied anode voltage towards vacuum potential. The electric field as the gradient of the potential determines the ion emission characteristics. A low ratio of radial to axial electric field components results in smaller ion emission angles and increases the generated thrust which is determined by the axial ion velocity. In the simulations the high angle emissions are related to the region where the ions were generated and a high fraction of the ions emitted at a high angle was generated in the near-field plume and at high radii. The channel plasma determines the emission characteristics because it shapes the electric potential in the near-field plume and determines the number density of residual neutrals required for ionization there. It was observed that high plasma densities result in a potential decay further downstream from the thruster exit, which generally increases the

radial electric field components and results in higher emission angles. The plume expansion, however, influences the plasma discharge in the channel because it determines the electron characteristics for the plasma discharge. To feed the discharge the electrons are injected in the plume and accelerated towards the channel by the electric field in the near-field plume. The combination of electric and magnetic fields in the near-field plumes thus determines the amount and energy of electrons entering the channel, which determines most of the plasma discharge characteristics.

Regarding the question of effects arising from this coupling, the breathing mode oscillation, which was first observed in a simulation of a HEMP-T was identified and discussed. This oscillation is present in all plasma quantities as well as the operational parameters of the thruster, i.e. discharge current, beam current and thrust. The coupling of channel and plume plasmas was shown from the oscillation of the potential drop, mean ion emission angle and thrust. A high plasma density corresponds to a downstream shift of the potential drop, which increases the mean ion emission angle and vice versa. At the oscillation maximum, the electron temperature in the oscillation region is minimal which contributes to the consequent reduction of the plasma density. At the minimum, the high electron energies lead to the reversal of the oscillation towards the maximum again. The measured oscillation frequency was compared to a predator-prey estimate and showed good agreement. However, the deviations from an experimental measurement are very high for very disparate plasma discharge conditions between the simulation and the experiment. Further research is necessary here to investigate the origin of the deviations.

Regarding the question of models suitable for the simulation of the plume, two methods were discussed. For the simulation of the plume of a HEMP-T, the fully kinetic, axisymmetric 2D3v PIC-MCC simulation provided the input to the 3D fluid-electron hybrid PIC code EP2PLUS with the measured ion distribution function. The fully kinetic PIC simulation only covered an axial domain length of about 16 cm which was extended by 2 m with the hybrid PIC model. In the plume, the ions showed an initial hollow shape which was rapidly lost and turned into a conical expansion downstream. The electron and ion densities gradually decreased by two orders of magnitude downstream from the injection plane. The drop of the electric potential towards vacuum potential in the plume is small compared to the drop in the near-field plume. Such a combination of models is well suited for the investigation of ion thruster plumes, but they are only coupled explicitly without feedback between the two approaches. Therefore, the plume physics does not affect the plasma discharge in the thruster channel. To surpass this shortcoming, a novel method which combines the mesh

---

coarsening algorithm with sub-cycling of the plume plasma species in a fully kinetic PIC simulation was proposed. It offers the means to vastly reduce the high computational costs of the plume region to make a simulation feasible. A proof-of-principle simulation was carried out and the simulation results showed nearly no deviations from the reference solution. Therefore, this method is well suited for the combined simulation of an ion thruster and its plume to correctly model the full system.

Some focal points for future research remain. The first is the clarification of the remaining differences between the simulation and experimental results, which are observed in the operational parameters of a HEMP-T such as the discharge current, beam current, ionization efficiency and thrust. This difference is likely the result of a combination of simulation artifacts caused by the similarity scaling and the 2D axisymmetric approximation which suppresses azimuthal turbulences. An investigation of the influence of similarity scaling factors and a full 3D simulation of a thruster would provide more insight to advance the numerical model even further towards a predictive model. In the plume, the deviations between the experimentally and numerically observed breathing oscillations have to be investigated, which requires a matching set of discharge conditions for both the simulation and experiment. Moreover, the influence of the similarity scaling scheme appears in the near-field plume in non-quasineutral regions because of the artificially increased Debye scale relative to the system size. This casts doubts on the quality of predictions in the plume of the fully kinetic PIC model. The proposed method for the reduction of the computational effort for large simulation domains was confirmed in this thesis in a proof-of-principle test. Future research has to investigate the limits and stability, as well as the scaling of this method to enable a large scale, fully kinetic channel-plume plasma model.



## 5 Bibliography

- [1] J. Spilker Jr., *Digital Communication by Satellite*. Upper Saddle River, NJ, USA: Prentice Hall PTR, 1977, ISBN: 0132141558.
- [2] R. Gopal and N. BenAmmar, „Framework for Unifying 5G and Next Generation Satellite Communications“, *IEEE Network*, vol. 32, no. 5, pp. 16–24, Sep. 2018, ISSN: 0890-8044. DOI: 10.1109/MNET.2018.1800045.
- [3] J. J. Spilker Jr., P. Axelrad, B. W. Parkinson, *et al.*, „Overview Of GPS Operation And Design“, in *Global Positioning System: Theory and Applications, Volume I*, ser. Progress in Astronautics and Aeronautics, 0, American Institute of Aeronautics and Astronautics, Jan. 1996, pp. 29–55, ISBN: 978-1-56347-106-3. DOI: 10.2514/5.9781600866388.0029.0055.
- [4] A. S. Belward and J. O. Skøien, „Who launched what, when and why; trends in global land-cover observation capacity from civilian earth observation satellites“, *ISPRS Journal of Photogrammetry and Remote Sensing*, vol. 103, pp. 115–128, 2015, Global Land Cover Mapping and Monitoring, ISSN: 0924-2716. DOI: <https://doi.org/10.1016/j.isprsjprs.2014.03.009>.
- [5] N. Gorelick, M. Hancher, M. Dixon, *et al.*, „Google Earth Engine: Planetary-scale geospatial analysis for everyone“, *Remote Sensing of Environment*, vol. 202, pp. 18–27, Dec. 2017. DOI: 10.1016/j.rse.2017.06.031.
- [6] K. Danzmann, „LISA mission overview“, *Advances in Space Research*, vol. 25, no. 6, pp. 1129–1136, Jan. 2000. DOI: 10.1016/s0273-1177(99)00973-4.
- [7] W. J. Borucki, „KEPLERMission: development and overview“, *Reports on Progress in Physics*, vol. 79, no. 3, p. 036 901, Feb. 2016. DOI: 10.1088/0034-4885/79/3/036901.
- [8] J. Polk, R. Yakuda, D. Brinza, *et al.*, „Demonstration of the NSTAR Ion Propulsion System on the Deep Space One mission“, in *Proceedings of the 27th International Electric Propulsion Conference*, IEPC-2001-075, 2001.

- [9] C. T. Russell and C. A. Raymond, „The Dawn Mission to Vesta and Ceres“, in *The Dawn Mission to Minor Planets 4 Vesta and 1 Ceres*, Springer New York, 2011, pp. 3–23. DOI: 10.1007/978-1-4614-4903-4\_2.
- [10] S.-i. Watanabe, Y. Tsuda, M. Yoshikawa, *et al.*, „Hayabusa2 Mission Overview“, *Space Science Reviews*, vol. 208, no. 1-4, pp. 3–16, Jun. 2017. DOI: 10.1007/s11214-017-0377-1.
- [11] I. Levchenko, M. Keidar, J. Cantrell, *et al.*, „Explore space using swarms of tiny satellites“, *Nature*, vol. 562, no. 7726, pp. 185–187, Oct. 2018. DOI: 10.1038/d41586-018-06957-2.
- [12] I. Levchenko, S. Xu, S. Mazouffre, *et al.*, „Mars Colonization: Beyond Getting There“, *Global Challenges*, vol. 3, no. 1, p. 1800062, Oct. 2018. DOI: 10.1002/gch2.201800062.
- [13] S. Do, A. Owens, K. Ho, *et al.*, „An independent assessment of the technical feasibility of the Mars One mission plan – Updated analysis“, *Acta Astronautica*, vol. 120, pp. 192–228, Mar. 2016. DOI: 10.1016/j.actaastro.2015.11.025.
- [14] I. Levchenko, K. Bazaka, Y. Ding, *et al.*, „Space micropropulsion systems for Cube-sats and small satellites: From proximate targets to furthestmost frontiers“, *Applied Physics Reviews*, vol. 5, no. 1, p. 011104, Feb. 2018. DOI: 10.1063/1.5007734.
- [15] E. Seedhouse, *SpaceX: Making Commercial Spaceflight a Reality*. Springer Praxis Books, 2013, ISBN: 978-1-4614-5514-1.
- [16] B. Lal, E. de la Rosa Blanco, J. A. Behrens, *et al.*, *Global Trends in Small Satellites*. Science & Technology Policy Institute, Dec. 2017.
- [17] J. R. Wertz and W. Larson, Eds., *Reducing Space Mission Cost*. Springer, 1996, ISBN: 0792340213.
- [18] D. M. Goebel and I. Katz, *Fundamentals of Electric Propulsion: Ion and Hall Thrusters*. Wiley, 2008, ISBN: 0470429275.
- [19] D. Lev, R. M. Myers, K. M. Lemmer, *et al.*, „The Technological and Commercial Expansion of Electric Propulsion in the Past 24 Years“, in *Proceedings of the 35th International Electric Propulsion Conference, IEPC-2017-242*, 2017.
- [20] A. Lazurenko, B. van Reijen, N. Koch, *et al.*, „Overview on Testing Infrastructures and Diagnostic Tools for HEMPT based Ion Propulsion Systems“, in *Proceedings of the 32nd International Electric Propulsion Conference, IEPC-2011-146*, 2011.

- 
- [21] A. Genovese, A. Lazurenko, N. Koch, *et al.*, „Endurance Testing of HEMPT-based Ion Propulsion Modules for SmallGEO“, in *Proceedings of the 32nd International Electric Propulsion Conference*, IEPC-2011-141, 2011.
- [22] F. Moneti, E. Bonelli, F. Pulcinelli, *et al.*, „Performance of Aerospazio Lifetest Facilities and Diagnostic Tools for the HEMPT Qualification Programme“, in *Proceedings of the 35th International Electric Propulsion Conference*, IEPC-2017-483, 2017.
- [23] K. Matyash, R. Schneider, A. Mutzke, *et al.*, „Comparison of SPT and HEMP thruster concepts from kinetic simulations“, in *Proceedings of the 31st International Electric Propulsion Conference*, IEPC-2009-159, 2009.
- [24] C. Birdsall and A. Langdon, *Plasma Physics via Computer Simulation*. CRC Press, 2004, ISBN: 9780750310253.
- [25] R. Hockney, *Computer Simulation Using Particles*. Routledge, 1989, ISBN: 0852743920.
- [26] K. Matyash, „Kinetic Modeling of Multi-Component Edge Plasmas“, PhD Thesis, University of Greifswald, 2003.
- [27] F. X. Bronold, K. Matyash, D. Tskhakaya, *et al.*, „Radio-frequency discharges in oxygen: I. Particle-based modelling“, *Journal of Physics D: Applied Physics*, vol. 40, no. 21, p. 6583, 2007.
- [28] K. Matyash, R. Schneider, A. Mutzke, *et al.*, „Kinetic Simulations of SPT and HEMP Thrusters Including the Near-Field Plume Region“, *IEEE Transactions on Plasma Science*, vol. 38, no. 9, pp. 2274–2280, Sep. 2010, ISSN: 0093-3813. DOI: 10.1109/TPS.2010.2056936.
- [29] K. Matyash, O. Kalentev, R. Schneider, *et al.*, „Kinetic simulation of the stationary HEMP thruster including the near-field plume region“, in *Proceedings of the 31st International Electric Propulsion Conference*, IEPC-2009-110, 2009.
- [30] O. Kalentev, K. Matyash, J. Duras, *et al.*, „Electrostatic Ion Thrusters - Towards Predictive Modeling“, *Contributions to Plasma Physics*, vol. 54, no. 2, pp. 235–248, Feb. 2014. DOI: 10.1002/ctpp.201300038.
- [31] K. Dannenmayer, S. Mazouffre, M. Merino-Martinez, *et al.*, „Hall Effect Thruster Plasma Plume Characterization with Probe Measurements and Self-Similar Fluid Models“, in *48th AIAA/ASME/SAE/ASEE Joint Propulsion Conference & Exhibit*, American Institute of Aeronautics and Astronautics, Jul. 2012. DOI: 10.2514/6.2012-4117.

- [32] F. Cichocki, M. Merino, E. Ahedo, *et al.*, „Fluid vs PIC Modeling of a Plasma Plume Expansion“, in *Proceedings of the 34th International Electric Propulsion Conference*, IEPC-2015-420, Jul. 2015.
- [33] V. Kim, G. Popov, B. Arkhipov, *et al.*, „Electric Propulsion Activity in Russia“, in *Proceedings of the 27th International Electric Propulsion Conference*, IEPC-2001-005, 2001.
- [34] C. Garner, J. Brophy, J. Polk, *et al.*, „Cyclic endurance test of a SPT-100 stationary plasma thruster“, in *30th Joint Propulsion Conference and Exhibit*, American Institute of Aeronautics and Astronautics, Jun. 1994. DOI: 10.2514/6.1994-2856.
- [35] I. G. Mikellides, I. Katz, R. R. Hofer, *et al.*, „Magnetic shielding of the channel walls in a Hall plasma accelerator“, *Physics of Plasmas*, vol. 18, no. 3, p. 033 501, Mar. 2011. DOI: 10.1063/1.3551583.
- [36] I. G. Mikellides, I. Katz, R. R. Hofer, *et al.*, „Magnetic shielding of a laboratory Hall thruster. I. Theory and validation“, *Journal of Applied Physics*, vol. 115, no. 4, p. 043 303, Jan. 2014. DOI: 10.1063/1.4862313.
- [37] R. R. Hofer, D. M. Goebel, I. G. Mikellides, *et al.*, „Magnetic shielding of a laboratory Hall thruster. II. Experiments“, *Journal of Applied Physics*, vol. 115, no. 4, p. 043 304, Jan. 2014. DOI: 10.1063/1.4862314.
- [38] G. Kornfeld, H. Seidel, and J. Wegener, *Plasma Accelerator Arrangement, Germany Patent No. 198 28 704.6, PCT/DE99/01708*.
- [39] G. Kornfeld, N. Koch, and G. Coustou, „First Test Results of the HEMP Thruster Concept“, in *Proceedings of the 28th International Electric Propulsion Conference*, IEPC-2003-212, 2003.
- [40] R. Chodura, „Plasma–wall transition in an oblique magnetic field“, *Physics of Fluids*, vol. 25, no. 9, p. 1628, 1982. DOI: 10.1063/1.863955.
- [41] A. Keller, P. Köhler, W. Gärtner, *et al.*, „Feasibility of a down-scaled HEMP-Thruster“, in *Proceedings of the 32nd International Electric Propulsion Conference*, IEPC-2011-138, 2011.
- [42] A. Keller, P. Köhler, F. G. Hey, *et al.*, „Parametric Study of HEMP-Thruster, Down-scaling to  $\mu\text{N}$  Thrust Levels“, in *Proceedings of the 33rd International Electric Propulsion Conference*, IEPC-2013-269, 2013.

- 
- [43] F. G. Hey, T. Brandt, G. Kornfeld, *et al.*, „Downscaling a HEMPT to micro-Newton Thrust levels: current status and latest results“, in *Proceedings of the 34th International Electric Propulsion Conference*, IEPC-2013-377, 2015.
- [44] N. Koch, H. P. Harmann, and G. Kornfeld, „Development & Test Status Of The THALES High Efficiency Multistage Plasma (HEMP) Thruster Family“, in *Proceedings of the 29th International Electric Propulsion Conference*, IEPC-2005-297, 2005.
- [45] N. Koch, H. P. Harmann, and G. Kornfeld, „Status of the THALES High Efficiency Multi Stage Plasma Thruster Development for HEMP-T 3050 and HEMP-T 30250“, in *Proceedings of the 30th International Electric Propulsion Conference*, IEPC-2007-110, 2007.
- [46] J. Duras, O. Kalentev, R. Schneider, *et al.*, „Electrostatic Ion Thrusters - Towards Predictive Modeling“, *Acta Polytechnica*, vol. 55, no. 1, pp. 7–13, Feb. 2015. DOI: 10.14311/ap.2015.55.0007.
- [47] N. Koch, J. Duras, D. Kahnfeld, *et al.*, „Particle-in-Cell Simulation of a HEMP Thruster Digital Prototype Optimized for Future Satellite Applications“, in *Proceedings of the 35th International Electric Propulsion Conference*, IEPC-2017-329, Atlanta, USA, Oct. 2017.
- [48] D. Meeker, *Finite Element Method Magnetics, v4.2*, Mar. 2017. [Online]. Available: <http://www.femm.info>.
- [49] T. Fahey, A. Muffatti, and H. Ogawa, „High Fidelity Multi-Objective Design Optimization of a Downscaled Cusped Field Thruster“, *Aerospace*, vol. 4, no. 4, p. 55, Nov. 2017. DOI: 10.3390/aerospace4040055.
- [50] S. Yeo, T. Fahey, H. Ogawa, *et al.*, „Multi-Objective Optimization and Particle-In-Cell Simulation of Cusped Field Thruster for Micro-Satellites Platform“, *AIAA Science and Technology Forum and Exposition 2019*, 2019.
- [51] G. Kornfeld, N. Koch, and H.-P. Harmann, „Physics and Evolution of HEMP thrusters“, in *Proceedings of the 30th International Electric Propulsion Conference*, IEPC-2007-108, 2007.
- [52] P. R. C. Neumann, M. Bilek, and D. R. McKenzie, „Optimising Ion Production in Pulsed Refractory and Non-Refractory Cathodic Arcs“, in *Proceedings of the 12th Asia Pacific Physics Conference (APPC12)*. JPS Conference Proceedings, 2014, vol. 1, p. 015 059. DOI: 10.7566/JPSCP.1.015059.

- [53] P. R. C. Neumann, M. Bilek, and D. R. McKenzie, „A centre-triggered magnesium fuelled cathodic arc thruster uses sublimation to deliver a record high specific impulse“, *Applied Physics Letters*, vol. 109, no. 9, p. 094101, 2016. DOI: 10.1063/1.4962124.
- [54] C. K. Birdsall and D. Fuss, „Clouds-in-clouds, clouds-in-cells physics for many-body plasma simulation“, *Journal of Computational Physics*, vol. 3, no. 4, pp. 494–511, Apr. 1969. DOI: 10.1016/0021-9991(69)90058-8.
- [55] A. Langdon, „Effects of the spatial grid in simulation plasmas“, *Journal of Computational Physics*, vol. 6, no. 2, pp. 247–267, Oct. 1970. DOI: 10.1016/0021-9991(70)90024-0.
- [56] C. K. Birdsall and N. Maron, „Plasma self-heating and saturation due to numerical instabilities“, *Journal of Computational Physics*, vol. 36, no. 1, pp. 1–19, Jun. 1980. DOI: 10.1016/0021-9991(80)90171-0.
- [57] H. Ueda, Y. Omura, H. Matsumoto, *et al.*, „A study of the numerical heating in electrostatic particle simulations“, *Computer Physics Communications*, vol. 79, no. 2, pp. 249–259, Apr. 1994. DOI: 10.1016/0010-4655(94)90071-x.
- [58] J. Stoer and R. Bulirsch, *Numerische Mathematik 2*. Springer-Verlag, 2005, p. 394. DOI: 10.1007/b137272.
- [59] J. W. Demmel, S. C. Eisenstat, J. R. Gilbert, *et al.*, „A supernodal approach to sparse partial pivoting“, *SIAM J. Matrix Analysis and Applications*, vol. 20, no. 3, pp. 720–755, 1999.
- [60] X. Li, J. Demmel, J. Gilbert, *et al.*, „SuperLU Users’ Guide“, Lawrence Berkeley National Laboratory, Tech. Rep. LBNL-44289, Sep. 1999.
- [61] X. S. Li, „An overview of SuperLU: Algorithms, implementation, and user interface“, *ACM Trans. Mathematical Software*, vol. 31, pp. 302–325, Sep. 2005.
- [62] J. P. Boris, „Relativistic plasma simulation-optimization of a hybrid code“, *Proceeding of Fourth Conference on Numerical Simulations of Plasmas*, Nov. 1970.
- [63] H. Qin, S. Zhang, J. Xiao, *et al.*, „Why is Boris algorithm so good?“, *Physics of Plasmas*, vol. 20, no. 8, p. 84503, Aug. 2013. DOI: 10.1063/1.4818428.
- [64] D. Tskhakaya, K. Matyash, R. Schneider, *et al.*, „The Particle-In-Cell Method“, *Contributions to Plasma Physics*, vol. 47, no. 8-9, pp. 563–594, 2007.
- [65] A. Dunaevsky, Y. Raitses, and N. J. Fisch, „Secondary electron emission from dielectric materials of a Hall thruster with segmented electrodes“, *Physics of Plasmas*, vol. 10, no. 6, pp. 2574–2577, Jun. 2003. DOI: 10.1063/1.1568344.

- 
- [66] F. Taccogna, S. Longo, M. Capitelli, *et al.*, „Particle-in-Cell Simulation of Stationary Plasma Thruster“, *Contributions to Plasma Physics*, vol. 47, no. 8-9, pp. 635–656, Dec. 2007. DOI: 10.1002/ctpp.200710074.
- [67] T. Takizuka and H. Abe, „A binary collision model for plasma simulation with a particle code“, *Journal of Computational Physics*, vol. 25, no. 3, pp. 205–219, 1977.
- [68] V. Vahedi, G. DiPeso, C. K. Birdsall, *et al.*, „Capacitive RF Discharges modelled by Particle-In-Cell Monte Carlo simulation. I. Analysis of numerical techniques“, *Plasma Sources Science and Technology*, vol. 2, no. 4, p. 261, 1993.
- [69] M. Hayashi, „Bibliography of Electron and Photon Cross Sections with Atoms and Molecules Published in the 20th Century - Xenon“, NIFS, Tech. Rep. NIFS-DATA-79, 2003.
- [70] J. Lacina, „Similarity rules in plasma physics“, *Plasma Physics*, vol. 13, no. 4, pp. 303–312, Apr. 1971. DOI: 10.1088/0032-1028/13/4/003.
- [71] L. Clarke, I. Glendinning, and R. Hempel, „The MPI Message Passing Interface Standard“, in *Programming Environments for Massively Parallel Distributed Systems*, Birkhäuser Basel, 1994, pp. 213–218. DOI: 10.1007/978-3-0348-8534-8\_21.
- [72] S. I. Braginskii, „Transport Processes in a Plasma“, *Reviews of Plasma Physics*, vol. 1, p. 205, Jan. 1965.
- [73] D. Kahnfeld, R. Schneider, K. Matyash, *et al.*, „Solution of Poisson’s Equation in Electrostatic Particle-In-Cell Simulations“, *Plasma Physics and Technology*, vol. 3, pp. 66–71, 2016.
- [74] P. Arlinghaus, „Application of advanced solvers for PIC“, Master’s Thesis, University of Greifswald, Greifswald, Germany, Sep. 2018.
- [75] D. Kahnfeld, „Hybrid plume modeling“, Master’s Thesis, University of Greifswald, Greifswald, Germany, Aug. 2015.
- [76] F. Cichocki, A. Domínguez-Vázquez, M. Merino, *et al.*, „Hybrid 3D model for the interaction of plasma thruster plumes with nearby objects“, *Plasma Sources Science and Technology*, vol. 26, no. 12, p. 125 008, Nov. 2017. DOI: 10.1088/1361-6595/aa986e.
- [77] F. Cichocki, A. Domínguez, M. Merino, *et al.*, „A 3D hybrid code to study electric thruster plumes“, in *Proceedings of Space Propulsion Conference*, May 2016.

- [78] M. Merino, J. Mauriño, and E. Ahedo, „Direct-Vlasov Study of Electron Cooling Mechanisms in Paraxial, Unmagnetized Plasma Thruster Plumes“, in *Proceedings of the 35th International Electric Propulsion Conference*, IEPC-2017-104, 2017.
- [79] A. I. Morozov and V. V. Savelyev, „Fundamentals of Stationary Plasma Thruster Theory“, in *Reviews of Plasma Physics*, Springer US, 2000, pp. 203–391. DOI: 10.1007/978-1-4615-4309-1\_2.
- [80] N. B. Meezan, W. A. Hargus, and M. A. Cappelli, „Anomalous electron mobility in a coaxial Hall discharge plasma“, *Physical Review E*, vol. 63, no. 2, Jan. 2001. DOI: 10.1103/physreve.63.026410.
- [81] J. C. Adam, J. P. Boeuf, N. Dubuit, *et al.*, „Physics, simulation and diagnostics of Hall effect thrusters“, *Plasma Physics and Controlled Fusion*, vol. 50, no. 12, p. 124 041, Nov. 2008. DOI: 10.1088/0741-3335/50/12/124041.
- [82] A. Ducrocq, J. C. Adam, A. Héron, *et al.*, „High-frequency electron drift instability in the cross-field configuration of Hall thrusters“, *Physics of Plasmas*, vol. 13, no. 10, p. 102 111, Oct. 2006. DOI: 10.1063/1.2359718.
- [83] J. Cavalier, N. Lemoine, G. Bonhomme, *et al.*, „Hall thruster plasma fluctuations identified as the ExB electron drift instability: Modeling and fitting on experimental data“, *Physics of Plasmas*, vol. 20, no. 8, p. 082 107, Aug. 2013. DOI: 10.1063/1.4817743.
- [84] T. Lafleur, S. D. Baalrud, and P. Chabert, „Theory for the anomalous electron transport in Hall effect thrusters. I. Insights from particle-in-cell simulations“, *Physics of Plasmas*, vol. 23, no. 5, p. 053 502, May 2016. DOI: 10.1063/1.4948495.
- [85] A. Yalin, B. Rubin, S. Domingue, *et al.*, „Differential Sputter Yields Of Boron Nitride, Quartz, and Kapton Due to Low Energy Xe+ Bombardment“, in *43rd AIAA/ASME/SAE/ASEE Joint Propulsion Conference & Exhibit*, American Institute of Aeronautics and Astronautics, Jul. 2007. DOI: 10.2514/6.2007-5314.
- [86] B. Rubin, J. L. Topper, and A. P. Yalin, „Total and differential sputter yields of boron nitride measured by quartz crystal microbalance“, *Journal of Physics D: Applied Physics*, vol. 42, no. 20, p. 205 205, Sep. 2009. DOI: 10.1088/0022-3727/42/20/205205.
- [87] N. Koch, M. Schirra, S. Weis, *et al.*, „The HEMP-T Concept - A Survey on Theoretical Considerations and Experimental Evidences“, in *Proceedings of the 32nd International Electric Propulsion Conference*, IEPC-2011-236, 2011.

- 
- [88] P. Matthias, D. Kahnfeld, R. Schneider, *et al.*, „Particle-in-cell simulation of an optimized high-efficiency multistage plasma thruster“, *Contributions to Plasma Physics*, e201900028, Aug. 2019. DOI: 10.1002/ctpp.201900028.
- [89] J. Duras, „Kinetic Simulation of Ion Propulsion Systems“, PhD Thesis, University of Greifswald, Apr. 2018.
- [90] E. Y. Choueiri, „Plasma oscillations in Hall thrusters“, *Physics of Plasmas*, vol. 8, no. 4, pp. 1411–1426, 2001. DOI: 10.1063/1.1354644.
- [91] N. Gascon, M. Dudeck, and S. Barral, „Wall material effects in stationary plasma thrusters. I. Parametric studies of an SPT-100“, *Physics of Plasmas*, vol. 10, no. 10, pp. 4123–4136, 2003. DOI: 10.1063/1.1611880.
- [92] R. B. Lobbia and A. D. Gallimore, „Two-dimensional Time-resolved Breathing Mode Plasma Fluctuation Variation with Hall Thruster Discharge Settings“, in *Proceedings of the 31st International Electric Propulsion Conference*, IEPC-2009-106, 2009.
- [93] R. B. Lobbia, M. J. Sekerak, R. Liang, *et al.*, „High-speed Dual Langmuir Probe Measurements of the Plasma Properties and EEDFs in a HET plume“, in *Proceedings of the 32nd International Electric Propulsion Conference*, IEPC-2011-168, 2011.
- [94] M. J. Sekerak, A. D. Gallimore, D. L. Brown, *et al.*, „Mode Transitions in Hall-Effect Thrusters Induced by Variable Magnetic Field Strength“, *Journal of Propulsion and Power*, vol. 32, no. 4, pp. 903–917, 2016. DOI: 10.2514/1.B35709.
- [95] E. T. Dale and B. A. Jorns, „Non-Invasive Characterization of the Ionization Region of a Hall Effect Thruster“, in *2018 Joint Propulsion Conference, AIAA Propulsion and Energy Forum*, 2008.
- [96] I. Romadanov, Y. Raitses, A. Diallo, *et al.*, „On limitations of laser-induced fluorescence diagnostics for xenon ion velocity distribution function measurements in Hall thrusters“, *Physics of Plasmas*, vol. 25, no. 3, p. 033501, 2018. DOI: 10.1063/1.5020749.
- [97] J. P. Boeuf and L. Garrigues, „Low frequency oscillations in a stationary plasma thruster“, *Journal of Applied Physics*, vol. 84, no. 7, pp. 3541–3554, 1998. DOI: 10.1063/1.368529.
- [98] N. Yamamoto, K. Komurasaki, and Y. Arakawa, „Discharge Current Oscillation in Hall Thrusters“, *Journal of Propulsion and Power*, vol. 21, no. 5, pp. 870–876, 2005. DOI: 10.2514/1.12759.

- [99] S. Barral and E. Ahedo, „Theoretical Study of the Breathing Mode in Hall Thrusters“, in *42nd AIAA/ASME/SAE/ASEE Joint Propulsion Conference and Exhibit*, 2006.
- [100] S. Barral and E. Ahedo, „Low-frequency model of breathing oscillations in Hall discharges“, *Phys. Rev. E*, vol. 79, p. 046 401, 4 Apr. 2009. DOI: 10.1103/PhysRevE.79.046401.
- [101] S. Barral and Z. Peradzyński, „Ionization oscillations in Hall accelerators“, *Physics of Plasmas*, vol. 17, no. 1, p. 014 505, 2010. DOI: 10.1063/1.3292645.
- [102] K. Hara, M. J. Sekerak, I. D. Boyd, *et al.*, „Perturbation analysis of ionization oscillations in Hall effect thrusters“, *Physics of Plasmas*, vol. 21, no. 12, p. 122 103, 2014. DOI: 10.1063/1.4903843.
- [103] K. Hara, M. J. Sekerak, I. D. Boyd, *et al.*, „Mode transition of a Hall thruster discharge plasma“, *Journal of Applied Physics*, vol. 115, no. 20, p. 203 304, 2014. DOI: 10.1063/1.4879896.
- [104] K. Hara, I. D. Boyd, M. J. Sekerak, *et al.*, „Breathing mode in Hall effect thrusters“, in *Joint Conference of 30th ISTS, 34th IEPC and 6th NSAT*, 2015.
- [105] E. T. Dale, B. Jorns, and K. Hara, „Numerical investigation of the stability criteria for the breathing mode in Hall Effect Thrusters“, in *Proceedings of the 35th International Electric Propulsion Conference*, IEPC-2017-265, 2017.
- [106] R. Heidemann, private communication, Nov. 2015.
- [107] L. K. Daldorff, G. Tóth, T. I. Gombosi, *et al.*, „Two-way coupling of a global Hall magnetohydrodynamics model with a local implicit particle-in-cell model“, *Journal of Computational Physics*, vol. 268, pp. 236–254, Jul. 2014. DOI: 10.1016/j.jcp.2014.03.009.
- [108] D. Kahnfeld, R. Schneider, F. Cichocki, *et al.*, „HEMPT thruster discharge and plume simulation with a 2D3v-PIC-MCC and a 3D hybrid fluid-PIC code“, in *Proceedings of the 35th International Electric Propulsion Conference*, IEPC-2017-309, Atlanta, USA, Oct. 2017.
- [109] J. Duras, K. Matyash, D. Tskhakaya, *et al.*, „Self-Force in 1D Electrostatic Particle-in-Cell Codes for NonEquidistant Grids“, *Contributions to Plasma Physics*, vol. 54, no. 8, pp. 697–711, Feb. 2014. DOI: 10.1002/ctpp.201300060.

## 6 Cumulative thesis articles

### Author Contributions

**Article [P1]:** "Numerical modeling of high efficiency multistage plasma thrusters for space applications", D. Kahnfeld, J. Duras, P. Matthias, S. Kemnitz, P. Arlinghaus, G. Bandelow, K. Matyash, N. Koch and R. Schneider, *Reviews of Modern Plasma Physics* **3**(1): 11 (2019). All authors carved out the problem, outlined the calculation, and determined the scope of the article. D. Kahnfeld performed the analytic and numerical calculations, based on numerical developments by S. Kemnitz, J. Duras, P. Matthias, K. Matyash, G. Bandelow and P. Arlinghaus. The manuscript was written by D. Kahnfeld, R. Schneider and N. Koch and was edited by all authors.

**Article [P2]:** "Breathing modes in HEMP thrusters", D. Kahnfeld, R. Heidemann, J. Duras, P. Matthias, G. Bandelow, K.F. Lüskow, S. Kemnitz, K. Matyash and R. Schneider, *Plasma Sources Science and Technology* **27**(12): 124002 (2018). All authors carved out the problem, outlined the calculation, and determined the scope of the article. D. Kahnfeld performed the analytic and numerical calculations, based on numerical developments by S. Kemnitz J. Duras, P. Matthias, K. Matyash, G. Bandelow, and K.F. Lüskow. R. Heidemann performed the experimental measurement. The manuscript was written by D. Kahnfeld and R. Schneider and was edited by all authors.

**Article [P3]:** "Ion angular distribution simulation of the Highly Efficient Multistage Plasma Thruster", J. Duras, D. Kahnfeld, G. Bandelow, S. Kemnitz, K.F. Lüskow, P. Matthias, N. Koch and R. Schneider, *Journal of Plasma Physics* **83**(1): 595830107 (2017). All authors carved out the problem, outlined the calculation, and determined the scope of the article. D. Kahnfeld performed the analytic calculation. J. Duras performed the numerical calculation, based on numerical developments by D. Kahnfeld, G. Bandelow, S. Kemnitz,

K.F. Lüskow and P. Matthias. The manuscript was written by J. Duras, D. Kahnfeld, N. Koch and R. Schneider and was edited by all authors.

**Article [P4]:** "Influence of electron sources on the near-field plume in a multistage plasma thruster", J. Duras, R. Schneider, O. Kalentev, S. Kemnitz, K. Matyash, N. Koch, K.F. Lüskow, D. Kahnfeld and G. Bandelow, *Plasma Physics and Technology* **3**(3): 126–130 (2016).

All authors carved out the problem, outlined the calculation, and determined the scope of the article. J. Duras performed the numerical calculation, based on numerical developments by O. Kalentev, S. Kemnitz, K. Matyash, K.F. Lüskow, D. Kahnfeld and G. Bandelow. The manuscript was written by J. Duras, R. Schneider and N. Koch and was edited by all authors.

**Article [P5]:** "Particle-in-cell simulation of a down-scaled hemp thruster", T. Brandt, R. Schneider, J. Duras, D. Kahnfeld, F.G. Hay, H. Kersten, J. Jensen and C. Braxmaier, *Transaction of the Japan Society for Aeronautical and Space Sciences, Aerospace Technology Japan* **14**(ists30): Pb.235–Pb.242 (2016).

All authors carved out the problem, outlined the calculation, and determined the scope of the article. T. Brandt performed the analytic calculation. T. Brandt, D. Kahnfeld and J.Duras performed the numerical calculation. The manuscript was written by T. Brandt and R. Schneider and was edited by all authors.

**Article [P6]:** "Particle-in-cell simulation of the cathodic arc thruster", K.F. Lüskow, P.R.C. Neumann, G. Bandelow, J. Duras, D. Kahnfeld, S. Kemnitz, P. Matthias, K. Matyash and R. Schneider, *Physics of Plasmas* **25**(1): 013508 (2018).

All authors carved out the problem, outlined the calculation, and determined the scope of the article. K.F. Lüskow and R. Schneider performed the analytic calculation. K.F. Lüskow performed the numerical calculation, based on numerical developments by S. Kemnitz, G. Bandelow, J. Duras and D. Kahnfeld. The manuscript was written by K.F. Lüskow, R. Schneider and D. Konigorski and was edited by all authors.

---

**Article [P7]:** "Particle-in-cell simulation of an optimized High Efficiency Multistage Plasma Thruster", P. Matthias, D. Kahnfeld, R. Schneider, S.H. Yeo and H. Ogawa, *Contributions to Plasma Physics*: e201900028.

All authors carved out the problem, outlined the calculation, and determined the scope of the article. P. Matthias performed the analytic and numerical calculations based on numerical developments by D. Kahnfeld. S.H. Yeo and H. Ogawa developed the design of the ion thruster. The manuscript was written by P. Matthias and R. Schneider and was edited by all authors.

Confirmed:

---

(Prof. Dr. Ralf Schneider)

Greifswald, September 26, 2019

---

(Daniel Lars Kahnfeld)

Greifswald, September 26, 2019





## Numerical modeling of high efficiency multistage plasma thrusters for space applications

Daniel Kahnfeld, et al. [*full author details at the end of the article*]

Received: 3 January 2019 / Accepted: 27 May 2019

© Division of Plasma Physics, Association of Asia Pacific Physical Societies 2019

### Abstract

The high efficiency multistage plasma-thruster (HEMP-T) represents an ion thruster technology that was developed by Thales Deutschland GmbH beginning in the early 2000s. It features a dielectric-coated discharge channel with an anode at the channel bottom. A magnetic field is applied by periodic permanent magnets (PPMs) that is mostly axially oriented in most channel regions, with radial orientation only at spatially confined magnetic cusps resulting in low particle fluxes towards the dielectric wall. The typical length scales in the description of the HEMP-T plasma range from microscopic over mesoscopic to macroscopic. Microscopic effects are introduced, e.g., by atomic interactions and surface interactions. Mesoscopic scales appear by the gyro radius of particles in the magnetic field and the formation of a transition zone between plasmas and walls on the length scale of some Debye lengths, respectively. Large-scale macroscopic length scales are introduced, e.g., by the plume expansion and interaction with test vessel walls. For a correct description of both thruster and plume plasma, one has to solve a kinetic problem for the whole region of interest, including all significant physical processes. This review offers an overview of modeling strategies and their results for the HEMP thruster. The axisymmetric 2D3v Particle-in-Cell (PIC) simulation method is used to identify the basic physics of the acceleration channel and the near-field plume region. Direct comparison with the observed plasma radiation and angular ion energy distributions, both for stationary and dynamic modes, is also presented. While good qualitative agreement with experimental data is achieved, even better agreement with experiments is necessary to predict thruster performance via numerical models in the future. The limited size of the simulation domain restricts the study of the coupled thruster-plume dynamics, which is an important aspect for the interaction of ion thruster and carrier spacecraft. Improvements in computer technology, the use of hierarchical models and the multigrid method discussed in this review can help overcome these limits and improve the quality of predictive thruster modeling.

**Keywords** Electric propulsion · HEMP-T · Particle-in-cell · PIC · Plasma simulation · Thruster modeling

## 1 Introduction

Low earth orbit satellites play an important role in many aspects of science and everyday life, ranging from telecommunications (Spilker 1977), to earth imaging (Belward and Skøyen 2015) and navigation purposes (Spilker et al. 1996). With the continued improvement in technologies (Gopal and BenAmmar 2018) and the rise of new players in the space sector, private (Seedhouse 2013) or national, the demand for satellites is expected to grow in the coming years (Kishi 2017; Lal et al. 2017). For the launch of new satellites, mass efficiency and longevity play an important role to cost efficiency (Wertz and Larson 1996). Often, this can be achieved using ion propulsion devices instead of conventional chemical propulsion, which offers a specific impulse (ISP) that is higher by up to a factor of ten (Goebel and Katz 2008). Also in deep space (Levchenko et al. 2018c; Polk et al. 2001) and interplanetary (Do et al. 2016; Levchenko et al. 2018d) missions, ion thrusters offer great benefits due to their very high efficiency.

The basic mechanism of ion propulsion is the ionization of a neutral gas inside a discharge channel. The heavy ions are then accelerated into the vacuum of space downstream from the channel to generate thrust. Although thrust levels are lower than for chemical propulsion devices, the integral  $\Delta v$  per propellant mass unit is much higher. The devices longest in use commercially using this operational principle are gridded ion thrusters (GITs) (Goebel and Katz 2008). There, a plasma is generated in the discharge channel, and the heavy ions are accelerated by a grid with an applied voltage at the thruster exit. These thrusters reach very high propellant utilization efficiencies and ISPs typically in the range of 3000–4000 s which can reach up to 10,000 s (Goebel and Katz 2008). However, device and system complexity are cost drivers, making cheaper alternatives attractive.

Another common system is the Hall-effect thruster (HET, also including the stationary plasma thruster SPT), which has first been used on Soviet satellites since the 1970s (Kim et al. 2001) and is commonly used as an alternative to GITs today. It features a less complex device and system architecture compared to GIT systems (Goebel and Katz 2008), because an electron Hall current generated by a perpendicular structure of electric and magnetic fields leads to good electron confinement and efficient propellant ionization in the discharge channel. The electric field at the thruster exit is mainly axially oriented, and no grid is necessary for acceleration of the heavy propellant ions. A disadvantage of the concept is relatively high wall erosion caused by impinging ions on the discharge channel wall due to the magnetic field structure. Together, HETs and GITs are mounted on over 70% of all GEO satellites (Lev et al. 2017).

The high efficiency multistage plasma-thruster (HEMP-T) offers a recently developed, alternative concept to the established GITs and HETs. It is developed since the early 2000s by Thales Deutschland GmbH, with a first patent registered in 1998 (Kornfeld et al. 1998, 1999). The first measurements were published in 2003 (Kornfeld et al. 2003). Reported thrusts were in a range of 1–43 mN with ISPs between 1700 and 3500 s and input power levels of up to 1.4 kW. The design is outlined in more detail in Kornfeld et al. (2007). As thruster development

continued, net thrusts of up to 250 mN and discharge powers of 7.5 kW were reached with the development of the HEMP-T 3050 and HEMP-T 30250 (Koch et al. 2005, 2007). Based on a 250 h operation test at a thrust level of 57 mN, the total lifetime of the HEMP-T 3050 is estimated to reach at least 18,000 h (Koch et al. 2005). Since then, the HEMP thruster has proven reliable operation and low erosion in endurance tests of 4000 h of thruster operation (Genovese et al. 2011). Along with the endurance tests, the thruster has undergone several qualification stages in the frame of the SmallGEO project (Koch et al. 2011b; Lazurenko et al. 2015; Weis et al. 2011, 2013, 2015, 2017). Additionally, a down-scaled HEMP-T concept, called the  $\mu$ HEMP-T, was developed specifically for low thrust ranges in the  $\mu$ N range (Hey et al. 2015; Keller et al. 2011, 2013), which are necessary for the development of smaller satellites (Levchenko et al. 2018b).

The discharge channel of ion propulsion devices is difficult to access experimentally due to the plasma discharge conditions. Hence, the plasma parameters in the discharge channel are often unknown. Most of the time only macroscopic plasma quantities or plume diagnostics are measured in experiments (Lazurenko et al. 2011). This makes optimization of ion thrusters difficult without additional tools. Numerical plasma models offer the means to understand the physics of the plasma discharge in ion thrusters for optimization of such devices. The first simulations of the HEMP-T were carried out in 2009 (Koch et al. 2011a; Matyash et al. 2009, 2010), resulting in an improved understanding of operational characteristics and the plasma physics in the discharge channel. Also, the difference in operational characteristics from HETs was investigated and the small, low energy ion fluxes of the HEMP-T compared to the SPT100 ML thruster were shown in simulations carried out in Matyash et al. (2009). Today, even the numerical development of thruster models is possible, as applied in the development of the HEMP-T DP1 (Koch et al. 2017) and the HEMP-T S1 (Fahey et al. 2017) both of which have been designed using only numerical modeling.

The purpose of this work is to give an overview of recent developments in HEMP thruster modeling and to describe the advances in the understanding of the underlying physics of the channel and near field plume plasmas. In Sect. 2, the HEMP-T concept is explained in detail, with a focus on the DM3a model (Kornfeld et al. 2003). The basic physical mechanisms encountered in the HEMP-T discharge channel are explained there. In the following Sect. 3, the Particle-in-Cell method, which is used for numerical modeling of the thruster, is discussed. It is explained why a fully kinetic model is necessary and what tools are used to make such a simulation feasible. This model is then used to describe the physics by firstly focusing on the discharge channel, and then moving to the near-field plume and plasma effects observed in that region. The work is concluded with a summary and outlook in Sect. 5.

## 2 Physics of the HEMP-T

The HEMP-T concept is based on plasma confinement by several permanent periodic magnets (PPMs) of pairwise opposite magnetization directions. These magnets surround a discharge channel of cylindrical symmetry containing a plasma. Typically,

the length of the channel is three to six times larger than the channel radius, depending on the number of magnets chosen. The channel structure can be flat or consist of a more complicated design, i.e., containing slanted walls or other features. It is covered with a dielectric layer, preventing direct contact between PPMs and plasma, making the inside of the channel non-conducting. The latter is an important aspect for stable thruster operation (Kalentev et al. 2014). A material with a high sputtering threshold energy is chosen to ensure a long lifetime of the thruster. Commonly, boron nitride is chosen (Yalin et al. 2007; Yim et al. 2008), but other materials with improved characteristics could become available in the near future (Levchenko et al. 2018a, e; Lin et al. 2017). An anode is placed at the channel bottom and a constant discharge voltage between 300 and 2000 V is applied. The neutral gas inlet, providing the fuel for the propulsion device, is also placed at the channel bottom. It can be centered around the channel's symmetry axis, but other positions are also possible, usually with radial symmetry of the inlet. For high thrust efficiency, a gas with high molecular mass is chosen. Xenon is a common choice, because it has a high molecular mass, is non-hazardous and has simple plasma discharge characteristics due to its low reactivity and the absence of molecular reactions (Goebel and Katz 2008). Outside of the discharge channel, a cathode provides electrons as primary source for the plasma discharge and neutralizes the ions expelled from the thruster to avoid charging of the satellites.

The magnetic field structure created by the PPMs is such that the magnetic field lines are parallel to the symmetry axis in most regions of the discharge channel. Only at the magnetic cusps one gets radially directed field lines connecting the plasma to the dielectric walls. The cusps develop at the interface of the oppositely magnetized PPMs and due to the rotational symmetry at both ends of the set of PPMs. In the cusp regions, the magnetic field strength is zero at the symmetry axis and reaches its highest strengths near the channel wall. Hence, the field lines have a mostly radial orientation there. Typically, the anode is placed inside the first cusp, which reduces plasma discharge losses at the channel bottom because of the nearly perpendicular alignment of electric and magnetic field lines. Also, the thruster exit is often chosen to coincide with the last (exit) cusp. This leads to trapping of the electrons inside the discharge channel while ions are accelerated outward from the thruster exit plane. The magnetic and strong axial electric field in this (acceleration) region then guide the plasma away from the channel walls, limiting channel erosion.

The magnetic field strength must be high enough to magnetize the electrons while leaving the ions almost unaffected. In the HEMP-T DP1, it reaches 0.1–0.5 T in the channel (Koch et al. 2017). In Fig. 1, the HEMP-T DM3a model, which is mostly considered in this work, is outlined. It consists of two PPMs, which results in three magnetic cusps: one at the anode position, one intermediate cusp and one at the thruster exit. It also features a grounded metal pole piece that is placed at the thruster exit with no additional dielectric coating of the channel wall.

The electrons emitted from the cathode are guided into the thruster channel by the external magnetic fields from the magnets and internal electric fields resulting from the anode and the plasma discharge. Inside the discharge channel, electrons are magnetized and follow the magnetic field lines close to the axis with a

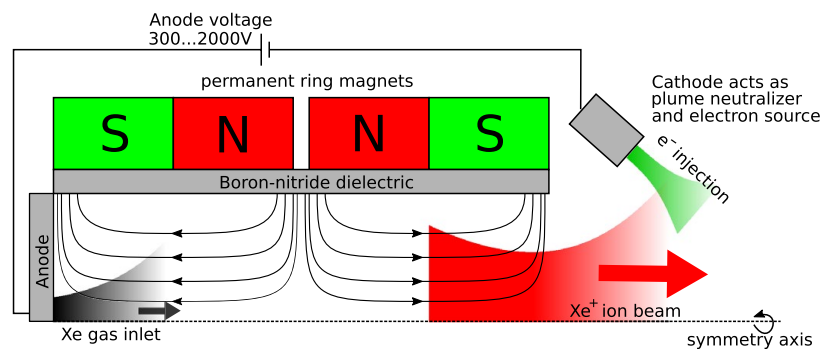


**Fig. 1** Sketch of the HEMP-T DM3a

predominantly axial orientation. At the cusps, electrons move radially towards the wall and are reflected due to a combination of the magnetic field structure forming a magnetic mirror and the plasma–wall sheath. For the magnetic mirror, a high magnetic field gradient towards the wall is vital for electron trapping. Electrons still impinging on the walls cause secondary electron emission (SEE). In summary, electrons are trapped and well confined to guarantee long lifetimes inside the discharge channel to increase the ionization efficiency of the xenon gas. One should note that the mean-free paths of single electron-xenon single impact ionization collisions is typically larger than the channel length.

In the discharge channel, the ion density follows the electron density due to the quasi-neutrality constraint for the plasma. This region is dominated by the parallel axial electron transport along the magnetic field lines, especially close to the axis. In combination with the dielectric wall, which builds up a potential near anode voltage, this results in a flat potential structure. Only at the cusps plasma–wall contact establishes and forms a classical Debye sheath, whereas in the rest of the acceleration channel there are practically no radial plasma fluxes towards the wall and the potential drop from plasma to wall potential is small. This results in only small losses of low energy ions towards the channel wall. At the thruster exit, a drop from plasma potential to vacuum potential occurs due to the large radial losses, because there is no confinement from the magnetic field structure anymore. These high density gradients result in high axial electric fields. The ions in the exit region are accelerated outwards, generating the thrust because they are not magnetized and, therefore, not affected by the magnetic field in the exit region. This results in a low divergence of the emitted ion beam, with high thrust and small plasma–spacecraft interaction caused by the thruster. The electrons follow the ions and expand into the forming plume.

The potential structure is axially nearly constant in the discharge channel, with a steep drop at the exit resembling a gridded ion thruster (Koch et al. 2011a). There, the ions are accelerated at the channel exit by a charged grid. This grid is exposed to impinging ions of high energy and thus sputtering erosion, limiting the lifetime of such a device. In the HEMP-T, the same potential structure appears as for a grid thruster, but without grid. The concept offers rather small erosion and long lifetime.

The operational principle of the HEMP-T is also very different from the HET. This popular design uses magnetic fields perpendicular to the symmetry axis, guiding electrons towards the channel wall. A high axial electric field in the exit region, along with the magnetic field structure, is then responsible for a Hall current in the channel exit plane (Goebel and Katz 2008). This leads to electrons that are trapped at high energies which causes ionization. Due to the magnetic field structure, wall processes, such as SEE, are also very important for the operation of HETs (Ahedo and Parra 2005; Raiteses et al. 2006). In the HEMP-T, however, the situation is different, as outlined in Matyash et al. (2009). The regions with high magnetic field strengths, between the cusps with a parallel field and at the cusp near the dielectric wall with a predominantly radial field, lie inside the discharge channel. There, the electric fields are very small due to the flat potential structure, which results in small Hall currents. The only region with a high electric field is the thruster exit region, where the plasma potential drops to vacuum potential. This drop occurs behind the exit cusp and electric and magnetic fields have an almost parallel alignment. Therefore, in the HEMP-T the Hall currents are very small and the operational principle is different from HETs, which will be shown in Sect. 4.1.

The channel plasma of ion propulsion devices is often difficult to access although some measurements exist (Reid and Gallimore 2008). Often, only integral spectroscopy data or retarding potential analyzer (RPA) diagnostics of the emitted ions are available (Kornfeld et al. 2003; Lazurenko et al. 2011). Therefore, plasma simulations provide a valuable method to improve the understanding of the physical processes in an ion thruster, which will be discussed in the next section.

### 3 PIC simulation of HEMP thrusters

Modeling a whole HEMP thruster is challenging due to the large length and time scales that need to be covered. The non-linear coupling of the channel plasma and the near-field plume in the thruster exit region must be resolved by the model while correctly treating the physics in the discharge channel. There, the electron distribution is dominated by kinetic effects, such as mirroring and heating at the cusps, ultimately resulting in a non-Maxwellian distribution with a high-energy tail responsible for ionization in the discharge channel, as discussed in Sect. 2. Plasma-sheath effects and wall processes need to be considered as well.

Electron fluid models are inadequate for correctly modeling the physics in the discharge channel, as the electron distribution is often assumed as a Maxwellian for the closure of the fluid equations (Chen 2015). Kinetic effects cannot be modeled correctly in this way. However, such hybrid models can be applied for the simulation of the thruster plume, where mean-free-paths of collisions are high enough to diminish the effect of an assumed electron distribution while the ions are still treated kinetically. Electron driftkinetic and gyrokinetic models (Littlejohn 1983, 1984) are also not suitable due to the variation of the channel magnetic field, with near-zero field regions and the magnetic mirrors in the cusp region. Only a fully kinetic model correctly resembles the physics inside the HEMP thruster, where no preliminary assumptions about the plasma distribution function have to be made.

### 3.1 The particle-in-cell method

One of the most prominent kinetic simulation methods is the Particle-in-Cell (PIC) method (Birdsall and Langdon 2004; Hockney 1989). First PIC calculations were carried out by hand in the 1940s, modeling the interaction of several electrons (Birdsall and Langdon 2004). PIC simulations with computers started in the 1950s (Evans et al. 1957; Harlow 1957) for hydrodynamic calculations. With the observation of the only theoretically predicted Landau damping in plasma simulations (Dawson 1962), the method became increasingly popular for the investigation of plasmas (Dawson 1964; Hockney 1966; Morse 1969) and was aided by improved understanding of the numerical techniques (Birdsall and Fuss 1969; Langdon 1970a, b). With increasing computational capacities, the simulations grew more complex, with increasing numbers of simulated particles and increases in spatial dimensions to 2D and 3D simulations. Today, PIC simulations present a reliable tool for fully kinetic plasma description with a wide variety of applications. In the following, the basic principle of the PIC method is discussed.

To fully characterize a plasma, the plasma distribution function  $f_s(\mathbf{x}_s, \mathbf{v}_s, t)$  must be known for all species  $s$ . Its time evolution is determined by the Boltzmann equation

$$\left. \frac{\partial f}{\partial t} \right|_{\text{coll}} = \frac{\partial f}{\partial t} + \mathbf{v}_s \frac{\partial f}{\partial \mathbf{x}_s} + \frac{\mathbf{F}_s}{m_s} \frac{\partial f}{\partial \mathbf{v}_s}, \quad (1)$$

with the force  $\mathbf{F}_s$  acting on the particles of a species with mass  $m_s$  (Chen 2015). If the left hand side of Eq. 1, summarizing collision effects, is zero, it is equivalent to the Vlasov equation for collisionless plasmas (Chen 2015). In low-temperature plasmas, the force acting on the particles with charge  $q_s$  is the Lorentz force

$$\mathbf{F}_{L,s} = q_s(\mathbf{v}_s \times \mathbf{B} + \mathbf{E}), \quad (2)$$

with the electric field  $\mathbf{E}$  and magnetic field  $\mathbf{B}$ . This set of coupled differential equations cannot be solved directly for most realistic systems, making other solution methods necessary. A straightforward ansatz is the linearization of Eq. 1 for small advances in time from  $t$  to  $t + \Delta t$ . The operator form of Eq. 1

$$\hat{J}f = \frac{\partial f}{\partial t} - \hat{D}f, \quad (3)$$

is used and the approximation

$$f(t + \Delta t) = f(t) + \frac{\partial f}{\partial t} \Delta t + \mathcal{O}(\Delta t^2) \quad (4)$$

is substituted at the time  $t + \Delta t$ . Rearranging of the coefficients then yields the linearized form

$$f(t + \Delta t) = (1 + \Delta t \hat{J} + \Delta t \hat{D})f(t) + \mathcal{O}(\Delta t^2). \quad (5)$$

The distribution  $f(t + \Delta t)$  can, therefore, be calculated from the distribution  $f(t)$  by separate application of the operator for collisionless plasma movement  $\hat{D}$  and collisional processes  $\hat{J}$ , respectively. Numerically, this enables the separation of

collective particle movement and close-range collisional effects and both can be treated separately. The PIC method takes advantage of this separation.

In PIC simulations, instead of physical particles, the so-called super-particles, each representing a large number of the former, are moved according to the Lorentz force in Eq. 2. Since the charge-to-mass ratio is the same for super-particles and real particles, both experience the same acceleration  $\mathbf{a}_{L,s} = \mathbf{F}_{L,s}/m_s$  and thus follow the same trajectories in an electromagnetic field. To avoid the calculation of the  $N^2$  Coulomb interactions of the  $N$  simulated charged super-particles, a mesh with spacing  $\Delta r$  covering the simulation domain is introduced. This approach correctly models the collective behavior, represented by the operator  $\hat{D}$  in Eq. 5, but does not take into account the short range particle interactions, i.e., collisions  $\hat{J}$  (Birdsall and Fuss 1969). Long-range particle interaction is calculated by means of macroscopic forces on the mesh, using a mapping scheme to weight charges from the super-particles onto the mesh points. The model used here is electrostatic, since the magnetic fields induced by the plasma currents in the HEMP-T are small compared to the magnetic field of the PPMs in the discharge channel. Therefore, the magnetic field  $\mathbf{B}$  is assumed to be constant in the simulation model. After calculation of the electric field  $\mathbf{E}$ , the same mapping scheme is used for the interpolation from the mesh points back to the super-particles. The particles are then moved again according to the newly calculated fields and the system time is advanced by  $\Delta t$ . A sketch of the PIC cycle is depicted in Fig. 2

To correctly model the physics, the time step must be chosen to resolve the fastest movement in the system, which in the case of HEMP thrusters is defined by the electron plasma frequency  $\omega_{p,e}$ , which is in the range of some picoseconds for the low-temperature plasmas in the thruster channel. The mesh spacing  $\Delta r$  (only equally spaced meshes are considered here) must resolve the electron Debye length  $\lambda_{D,e}$ ,

$$\Delta r \lambda_{D,e}^{-1} \lesssim 1, \quad (6)$$

where the plasma is not quasi-neutral locally. If this is not the case, a numerical heating instability can occur as quasi-neutral Debye spheres are moved due to small fluctuations of the electromagnetic field (Birdsall and Maron 1980; Langdon 1970a; Ueda et al. 1994). If stability is given, the PIC method is an exact solution to the

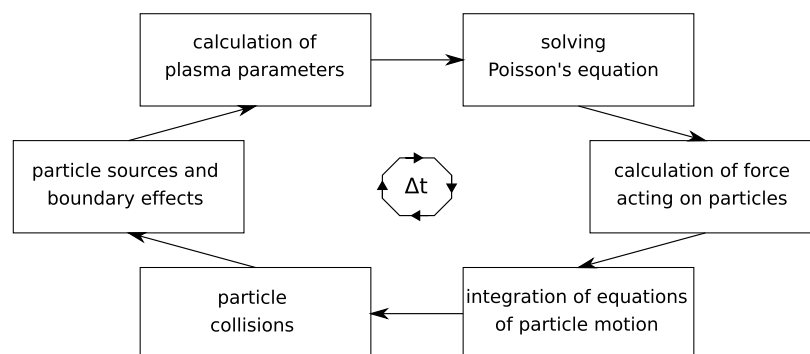


**Fig. 2** Basic scheme of the PIC method

Vlasov equation for collisionless plasmas (Hockney 1989). Additionally, collisions can be introduced with a variety of methods. One of the most common is the Monte-Carlo Collision (MCC) model, colliding super-particles randomly within each cell, providing the means to model collisional effects in plasmas as well (Matyash 2003).

An advantage of the PIC method is the ability to easily implement a variety of particle-based processes and diagnostics, such as spatially resolved wall processes for incident particles or tracing of super-particles for trajectory information. This enables the use of secondary electron emission (SEE), particle recombination or other wall models. Even the coupling of PIC and a sputtering model is possible when the plasma impurities introduced by the erosion are considered in the plasma. Almost all diagnostics desired can be performed since the full distribution function of all species is available at all time steps.

The main drawback of the PIC method is computation time, as the spatial and temporal resolution scales are often small compared to the length and time scales of the full system. This is especially true in a multiscale system like the HEMP thruster, where the spatially confined discharge channel with high plasma densities (and, therefore, high electron plasma frequencies and small electron Debye lengths) and the plume with low plasma densities that extend to several meters downstream from the thruster exit must be simulated. These challenges make special means necessary to increase computational efficiency.

### 3.2 Code history

The electrostatic Particle-in-Cell simulation code used in this work originated in the early 1980s from Chodura, who used a 1D PIC model to study plasma–wall interactions in a fusion device (Chodura 1982). In 1994, the code was expanded to a 2D3v axisymmetric PIC model for the study of Langmuir probe sheaths in an oblique magnetic field by Bergmann (1994) with a simplified collision model based on the assumption of Maxwellian background distributions. While the code at the time was very sophisticated, the collisional model was unrealistic. This was changed with the development of an MCC collision model (Matyash 2003). The code was then used to study plasma–wall sheaths mainly in fusion devices (Matyash et al. 2005; Tskhakaya et al. 2008), as well as RF discharges (Matthias et al. 2018; Matyash et al. 2004; Matyash and Schneider 2006) and re-entry simulations (Lüskow et al. 2016).

The actual PIC simulation code is written in C++ and is parallelized using the MPI protocol (Clarke et al. 1993). It is a 2D3v axisymmetric PIC code with a Monte-Carlo collision model, i.e., particle motion is tracked only in the  $(r, z)$ -plane and azimuthal forces are neglected. An extensive review of the simulation model can be found in Tskhakaya et al. (2007). For thruster simulations, the model resolves neutral xenon gas, electrons and singly and doubly charged xenon ions. For the HEMP-T DM3a, early mass spectroscopy measurements have shown that higher xenon charge states provide less than 1% of the total number of ions (Kornfeld et al. 2003) combined, which are therefore neglected.

The following sections explain most code features in detail, starting with a similarity scaling scheme designed to reduce the computational cost of the thruster simulation.

### 3.3 Similarity scaling

Two systems are called similar, if the invariants of Eq. 1, which have been derived in Lacina (1971), remain constant. In a collisional, low-temperature plasma with magnetized electrons, four of originally six invariants are required to remain constant for the scaling, while the invariance of self-induced electric and magnetic fields is neglected due to the electrostatic case considered here. Hence, the invariants to remain constant are

$$C_1 = \frac{q_s EL}{m_s v^2}, \quad (7)$$

$$C_2 = \frac{q_s BL}{m_s v}, \quad (8)$$

$$C_3 = \frac{L}{vt}, \quad (9)$$

$$C_4 = \frac{\lambda_{\text{mfp},s}}{L}, \quad (10)$$

with the system length scale  $L$ . The invariants  $C_1$  and  $C_2$  preserve the trajectories in constant electric and magnetic fields, respectively, and the latter of the two is also called the Hall parameter.  $C_3$  preserves the trajectories of force-free motion and  $C_4$ , called the Knudsen number, preserves the ratio of mean free path and system size to preserve collisional effects. These four parameters are required to remain constant to derive a scaling scheme which is designed to decrease the system size  $L$  linearly by the similarity scaling factor  $\xi$ , while also leaving the Debye length constant, to reduce the overall number of grid cells required to sufficiently resolve all plasma processes in a PIC simulation. This approach reduces the computational effort of the fully kinetic model by several orders of magnitude.

The spatial dimensions of the system are scaled down linearly with the scaling factor  $\xi$ , as is the system time, in order to satisfy Eq. 9, while the velocity  $v$  is unscaled. Because the velocity is not scaled, neither are particle energies and temperatures. As a consequence, the number densities  $n_s$  of each species are unscaled because the Debye length is constant. However, because cell volume increases by the factor  $\xi^3$  relative to the total system volume  $\sim L^3$  in the down-scaled system, the super-particle factor  $N_{\text{SP}}$ , i.e., the number of real particles per super-particle, also increases by  $\xi^3$ . From Eq. 8, it follows that  $B$  is increased by the factor  $\xi$  in the down-scaled system, while  $\lambda_{\text{mfp},s}$  scales with  $\xi^{-1}$  according to Eq. 10. Because of Eq. 7, the same is the case for the electric field, but due to the

potential calculation in the down-scaled system this is automatically ensured in the simulation. The scaling laws for all other physical quantities can be derived from these, and an overview of the most important ones is given in Table 1. All diagnostic outputs from the simulations are presented in the physical system, with similarity scaling accounted for.

The scaling exactly preserves the physics in the bulk of a plasma that is dominated by electron gyro motion (i.e., magnetized electrons) and collisional processes. However, the scheme can fail because the Debye length was required to be constant. This means that  $\lambda_D/L \neq \text{const}$ , which artificially increases the Debye scale when extrapolating the simulation results from the down-scaled system to the real life system. In regions where space charge effects are relevant, i.e., the plasma-wall sheath, or where the Debye length becomes comparable to the system size, i.e., the near field plume, this leads to an artificial overestimation of charge separation effects. Furthermore, the influence of boundaries, such as grounded metal parts or simulation domain boundaries, on the plasma solution increases with higher scaling factors. This effect is discussed in Sect. 4.2. Besides this scheme, other similarity scaling schemes exist (Battista et al. 2007; Fubiani et al. 2017).

### 3.4 Dimensionless scaling

For an optimized algorithm guaranteeing a sufficient spatial resolution and a sufficiently small time step, a dimensionless formulation is used where all physical quantities of the system are scaled in terms of the system dimensions. This reduces the number of necessary multiplications with constants. Therefore, all lengths are expressed in terms of the cell size  $\Delta r$ , and all times in terms of the PIC timestep  $\Delta t$ . From that, a set of scaling laws can be derived for all physical quantities which is carried out, e.g., in Hockney (1989). These laws must be considered together with the similarity scaling.

**Table 1** Similarity scaling laws for the most important quantities in the PIC simulation

Quantity	Scaling law
length	$L = L^* \xi$
time	$t = t^* \xi$
particle velocity	$v = v^*$
collision cross section	$\sigma = \sigma^* \xi^{-1}$
magnetic field	$B = B^* \xi^{-1}$
super particle factor	$N_{\text{sp}} = N_{\text{sp}}^* \xi^3$
number density	$n = n^*$
super particle mass	$m_{\text{sp}} = m_{\text{sp}}^* \xi^3$
super particle flux per unit area	$\Gamma_{\text{sp}} = \Gamma_{\text{sp}}^*$

A prime denotes the quantities of the down-scaled system. The similarity scaling factor is  $\xi$

### 3.5 Weighting of forces and densities

The weighting function is used for projecting the charges of the super-particles onto the mesh for the calculation of the electric field, and to map those forces back onto each individual super-particle for the particle movement. The simplest method is the nearest-grid-point (NGP) scheme, where the entire charge of a super-particle is projected onto the closest grid point. While easy to implement and cheap to compute, it was shown that the NGP method introduces substantial numerical noise in the simulation and should be avoided (Birdsall and Fuss 1969; Tskhakaya et al. 2007).

A different approach is the use of a more complicated mapping function, which is called the cloud-in-cell method (Birdsall and Fuss 1969). Each super-particle is considered to be a space charge cloud defined by a shape function. The simplest shape is a linearly decreasing shape function, with maximum at the particle's position and zero for distances greater than  $\Delta r$ . In 2D simulations, each grid point adjacent to the cell containing the current particle is awarded a charge proportional to the cell area (split by the particle's position) opposite of the grid point. This process produces much less numerical noise than the NGP method. It is vital that the same mapping routine is used for mapping of charges to the mesh, and for mapping of forces back onto the particles or else artificial self-forces arise. After computation of the Lorentz force acting on a particle, its equation of motion must be solved by the particle pusher or particle mover.

### 3.6 Particle pusher

The particle pusher is one of the most important modules of a PIC simulation, because  $10^6 \dots 10^9$  particles must be moved for up to  $10^8$  time steps. Computational efficiency is necessary because the particle pusher is one of the most time consuming code modules. Accuracy and stability, especially for long simulation times, are also very important. Furthermore, the pusher should obey the conservation laws of the system in order to yield the correct physics. The integrator for the equations of motion used in this model is the Boris leap-frog algorithm. The derivatives in the equations of single-particle motion

$$\frac{d\mathbf{x}}{dt} = \mathbf{v} \frac{d\mathbf{v}}{dt} = \frac{1}{m} \mathbf{F}_L \quad (11)$$

are discretized with finite differences and the actually implicit scheme is transformed into an explicit one (Boris 1970; Buneman 1967). As a consequence of the explicit Boris scheme, particle positions and velocities are defined a half time step apart. Therefore, momentum conservation cannot be assured (Hockney 1989). In the case of an absent electric field, the algorithm is symplectic. However, in plasma simulations this is rarely the case and assumptions about the total integration error are non trivial. However, the algorithm conserves phase space volume with a global error bound, providing the long-term accuracy necessary for simulations which require many particle push steps (Qin et al. 2013). Stability of the Boris integrator is guaranteed if the time step  $\Delta t$  satisfies the criterion

$$\omega_{p,e} \Delta t < 2, \quad (12)$$

as shown in Tskhakaya et al. (2007). To resolve fluctuations in the plasma density and hence in the plasma frequency, a stricter condition for the time step is required in practice. A time step of  $\Delta t \lesssim 0.2\omega_{pe}^{-1}$  is commonly chosen. If Eq. 12 is satisfied, the Boris leap-frog scheme is accurate and efficient.

In most cases, the electrons have much higher velocities than the charged species. For the particle mover of the heavy species, sub-cycling can then be used (Tskhakaya et al. 2007). This means that the particles are only moved after a number of electron push steps, and the particle displacement for the move grows with the sub-cycling step. Heavy ions experience the average electric field during their sub-cycling period for their movement. The sub-cycling step should be chosen low enough to conserve the order of velocities in the plasma and therefore stability. As a consequence, the computational cost of moving ions and neutrals can be drastically reduced and the most computational effort in the particle push comes from the electron movement.

Along with particle movement, other particle-based effects can easily be included. In the simulations carried out in this work, an additional anomalous cross-field electron transport in velocity space is employed, since 3D PIC simulations have shown larger transport coefficients than is the case in 2D axisymmetric simulations, which by design suppress 3D turbulence effects (Kalentev et al. 2014). This model represents a Bohm-like diffusion in velocity space, where the transport coefficient  $D$  scales with the electron temperature  $T_e$  and the inverse of the magnetic field strength  $D \sim T_e/B$ . From 3D studies, a diffusion coefficient of 0.125 was deduced (Kalentev et al. 2014). In the simulation, the transport is implemented as a Bohm-like diffusion with a rotation of each particles' velocity vector in velocity space. Along with this mechanism, it is possible to use other particle-based methods, such as an additional diffusion in real space, which was not used in this work. Another important aspect covered in the particle mover are particle boundary conditions, treating particle losses at walls in the simulation plane.

### 3.7 Boundary effects

The particle boundary conditions for thruster simulations can be implemented easily in PIC, because particle losses, emissions or recombinations/recycling are treated on a particle basis. In the simulations, the right and top domain boundaries represent vacuum boundary conditions and all particles leaving the domain are removed from the system. The bottom boundary is the symmetry axis where particle reflection occurs.

At all grounded, conducting metal parts, incident electrons are removed from the system. Neutrals are reflected thermally with a temperature of 0.04 eV. All incident ions recombine as neutrals and are reflected with the same energy. At the left domain boundary, the discharge channel bottom, the anode is placed and treated like other metal parts. The HEMP-T DM3a model also has a grounded metal pole piece at the end of the channel dielectrics. For all ion and neutral species, the boundary conditions at the boron nitride dielectrics are treated the same way as for metal, i.e., neutrals are reflected thermally and ions recombine as neutrals. Only the necessary

number of negative charges for ion recombination is removed from the surface charges in the incident dielectric cell. Incident electrons at the dielectrics cause secondary electron emission (SEE) with an emission coefficient of 0.5. If no SEE occurs, a negative space charge is added at the incident dielectric cell. The choice of the SEE coefficient is very conservative (Dunaevsky et al. 2003), even for the low electron energies of mostly below 5 eV encountered in HEMP-T discharge channels, because the influence of electron back-scattering increases for lower energies, as measurements indicate (Taccogna et al. 2007). Furthermore, for very low incident electron energies, near perfect electron reflection in the plasma–wall sheath is a possibility. Therefore, SEE is likely to be underrepresented in the current model.

### 3.8 Particle injection

The particle injection schemes are designed to represent experimental conditions as well as possible. In HEMP thrusters, neutrals are injected at the anode in the channel bottom. The propellant gas inlet can be placed near the symmetry axis or closer to the dielectric walls, depending on the thruster model. Thermalization of neutrals occurs through elastic Xe-Xe neutral collisions and wall reflection throughout the channel.

Electron injection provides electrons for the plasma in the discharge channel, but is not acting as a plume neutralizer in the simulations carried out here since injection currents are generally lower than the ion beam currents. The scheme can serve as a control mechanism to keep the plasma density in a desired range to avoid numerical artifacts, such as numerical heating, caused by higher plasma densities than targeted in the simulation setup. The injection current increases or decreases whenever plasma densities rise above or below an electron density threshold. This injection scheme is called a feedback injection. In the experiment, a similar approach is used, where the neutral flux rate is controlled for to reach a constant discharge power. Since neutral transit times are very large compared to the total simulation times, this approach is unpractical and instead the feedback electron injection can be used. The amount of electrons provided by injection has proven to be a good control parameter for the plasma parameters in ion thruster simulations.

### 3.9 Poisson solver and electric field calculation scheme

Because an electrostatic simulation is sufficient, Poisson's equation for the calculation of the electric potential from the charge density distribution must be solved at each time step. The equation is discretized on the mesh points using a five point finite difference scheme, accounting for changing dielectric permittivity for boron nitride with  $\epsilon = 4$  and channel vacuum with  $\epsilon = 1$ . No extra condition for the dielectric-vacuum transition is necessary. At the symmetry axis, the radial electric field tends to zero in the limit  $r \rightarrow 0$ . Using L'Hôpital's rule, this leads to a special discretization scheme at the axis, resulting in radial symmetry of the potential, and an additional boundary condition at the symmetry axis is not necessary (Matyash et al. 2010).

At the left domain boundary, a Dirichlet condition is applied with a constant anode voltage  $U_a$ . The top domain boundary and the metal pole piece in the simulation domain are fixed at ground potential. At the right domain boundary, a von-Neumann boundary condition sets the axial electric field to 0 V/m. The boundary conditions at the outer (top and right) domain boundary present only a crude approximation to the real system, since the influence of boundary conditions is present in the near-field plume when small domain sizes are used (Arlinghaus 2018). A sketch of the simulation domain for the HEMP-T DM3a is shown in Fig. 3.

The solution to Poisson's equation must be obtained during each time step. While charge densities change every time step, the matrix for the linear system of equations obtained from the finite difference discretization remains constant. Therefore, linear solution methods that can be split into a (possibly costly) setup phase executed only once in the beginning, and a fast solve phase that is executed at every time step, are attractive. In the simulation considered here, the direct LU decomposition (Stoer 2005) from the SuperLU 4.3 package (Demmel et al. 1999; Li et al. 1999; Li 2005) is used. The decomposition is calculated once in the beginning of code execution. At each time step, only the re-substitution is executed, providing very fast solve times. Other methods have been tested (Kahnfeld et al. 2016), but SuperLU has proven to be the fastest method for typical domain sizes encountered in HEMP thruster simulations.

The electric field at each grid point is calculated as the symmetric difference of potential values from adjacent grid points in the according spatial dimension. At the domain boundaries the electric field is calculated in the middle of the boundary point and its neighbor.

In general, the LU decomposition scales quadratically with the total number of grid points,  $\sim N^2$ , of the simulation domain (Stoer 2005). For the simulation of HEMP thrusters, the SuperLU implementation shows an almost linear scaling  $\sim N$  (Arlinghaus 2018). Thus, an increase in system size by a factor of two in each dimension of the simulation plane results in an increase of factor four in solver complexity. One method to reduce the complexity for large domain sizes is the grid jump method introduced in Duras et al. (2014). There, the grid spacing is increased at an interface that must be in a region where plasma densities are small to avoid artifacts. At the interface, a special treatment of the electric field calculation becomes necessary to ensure energy conservation for passing particles (Duras et al. 2014). Grid jumps can be made in both dimensions, and several successive increases in

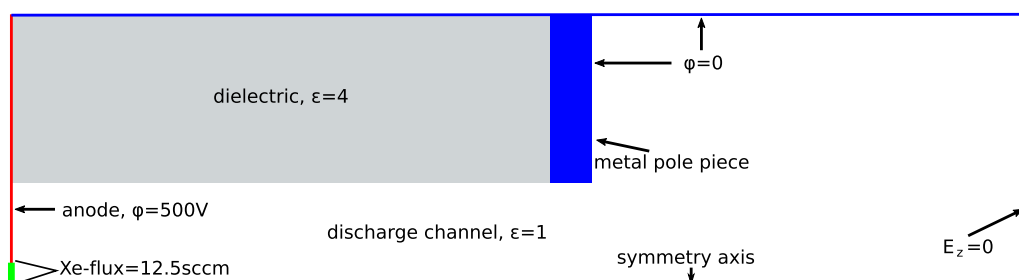


**Fig. 3** Simulation domain of the HEMP-T DM3a with potential boundary conditions

grid spacing are possible to keep solver times low. Implementation of this algorithm makes simulation of larger domain sizes feasible.

### 3.10 Binary collision model and MCC collisions

While the force calculation on the mesh correctly models the collective behavior of plasma particles, within a cell short range forces are not represented correctly (Birdsall and Fuss 1969). Therefore, an additional Coulomb collision model is necessary for the collisions of particles within a cell. Coulomb collisions play an important role in plasmas, because they lead to population of the high energy tails in the electron energy distribution, pushing the distribution towards a Maxwellian. The high energy electrons are important, as they present the main source of ionization despite their non-Maxwellian distribution in HEMP thrusters, which is discussed in Sect. 4.1. If the electron distribution is close to Maxwellian, a linearized Fokker–Planck model, which was historically used in the code (Reinmüller 1998), is applicable. However, the electron energy distribution in HEMP thrusters is expected to deviate from Maxwellian behavior due to the kinetic sheath effects and long mean-free paths for all relevant electron collisions. Therefore, a binary collision model as first proposed by Takizuka and Abe (1977) is used in the PIC simulation. In this model, randomly picked pairs of particles within a cell are collided, and their velocities after the collision are obtained using a Monte-Carlo technique. The scattering angles are chosen randomly from a certain distribution of angles. Particle coordinates are not influenced by collisions. This method is equivalent to the Coulomb integral in the Landau form as shown in Takizuka and Abe (1977), and the implementation has been tested thoroughly (Matyash 2003).

Together with electron–electron Coulomb collisions, modeling of other collision processes is necessary to self-consistently simulate a plasma discharge. Included in the model are direct single and double  $e^-$ -Xe impact ionization, single  $e^-$ -Xe<sup>+</sup> impact ionization, integral elastic Xe<sup>+</sup>-Xe collisions (including charge exchange and momentum transfer), as well as integral elastic and inelastic  $e^-$ -Xe collisions. These collisions are also modeled as a Monte-Carlo process, in an approach similar to Vahedi et al. (1993). Within a cell, particles of both collision species are randomly divided in pairs. Their collision probability

$$P = 1 - \exp[-u_r n_t \sigma_c(u) \Delta t_c], \quad (13)$$

with  $0 \leq P_{\text{coll}} < 1$ , is calculated using the relative velocity of the particle pair  $u_r$ , the target particle density  $n_t$ , the collision cross section  $\sigma_c$  and the time step for the collision process  $\Delta t_c$  (Matyash 2003). If a uniform random number  $r \in [0, 1)$  is smaller than  $P_{\text{coll}}$ , the collision takes place. In elastic collisions, the model presents a rotation of the velocity vector of the incident particle. Inelastic collisions are treated the same way and the lost energy is removed from the system. For ionization processes, the ionization energy is removed and a new particle is created at the location and with the same velocity as the target particle (in most cases a neutral particle). The incident and newly created particles then perform a Coulomb collision. This scheme strictly conserves total momentum and energy for all particles involved. For the

thruster simulations carried out in this work, xenon is used exclusively as propellant gas and cross-section data are taken from Hayashi (2003). More detailed information of the collision algorithms can be found in Bronold et al. (2007), Matyash (2003), and Tskhakaya et al. (2007).

### 3.11 Parallelization

The PIC code used in this work is parallelized using the MPI protocol (Clarke et al. 1993). The scheme is parallel only for the particle based code modules, i.e., particle mover and collision modules since the parallel SuperLU package offers no advantage for the simulation due to the non-parallel back-solve of the LU matrices (Li et al. 1999; Li 2005). Remember that only the back solve is needed, because the LU decomposition needs to be performed only once at the beginning of the run. The parallelization is designed to split the work of the particle mover among the participating MPI tasks. This tends to work well for the collisions as long as the linear approximation is valid. Starting with the entire simulation domain, it is cut in half vertically at the point where each sub-domain contains approximately half of the total simulated super-particles. To account for the reduced computational effort due to sub-cycling, heavy species are weighted with the inverse of their sub-cycling step. This procedure creates two sub-domains and is repeated for each sub-domain using horizontal cuts. This is repeated with an alternating series of horizontal and vertical cuts until the number of sub-domains matches the number of MPI tasks. Each MPI process then computes the particle push and collisions for its own patch of the domain. Sub-domains created this way can have vastly different sizes (i.e., cell counts). It is obvious that the number of MPI processes should only increase in powers of two to assure load balance between tasks. The total simulation domain is often small and each MPI task has information of the entire domain, not just its sub-domain. This reduces synchronization of particle information, which is only necessary before each call of the collision module, where all particles must be ordered in their correct cell on the correct MPI task owning the cells sub-domain. Synchronization at each time step occurs only for the exchange of charge density information before the potential calculation, which is done on the master process. After potential calculation, the potential is distributed to all tasks. A typical domain decomposition for the simulation of the HEMP-T DM3a is shown in Fig. 4.

## 4 HEMP thruster simulations

The PIC method described in the previous section is now used to model a HEMP thruster and its near field plume. In all simulations, the HEMP-T DM3a model (Kornfeld et al. 2003) is considered unless stated otherwise. The discharge channel is 51.14 mm long with a radius of 9.2 mm. The dimensions of the simulation plane are 24.4 mm  $\times$  90.0 mm, with a similarity scaling factor of 30. The time step of the simulation is  $\Delta t = 8.41 \times 10^{-12}$  s with a cell unit length  $\Delta r = 1.115 \times 10^{-1}$  mm. This results in a simulation domain of 218  $\times$  807 cells. Six super-particles are necessary

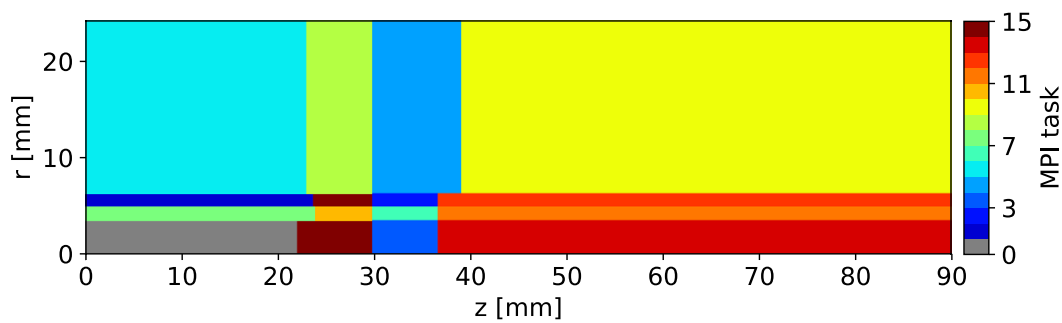


**Fig. 4** Map of the domain decomposition parallelization in a typical simulation of the HEMP-T DM3a with 16 MPI tasks. Although the size of the sub-domains is very uneven, the computational effort for the particle push is balanced

to represent the target density of  $10^{13} \text{ cm}^{-3}$  at the symmetry axis. Due to the increase in cell volume with increasing radius, this number increases linearly, e.g., to 493 at the channel wall. The super-particle factor is 537 in the down-scaled system. The simulation contains about  $4 \times 10^6$  simulated super-particles of each charged species (with a  $\text{Xe}^{2+}$  fraction of 7.3%) and  $7 \times 10^7$  neutrals, respectively.

The propellant gas inlet is placed at the anode, from the axis up to  $r = 2 \text{ mm}$ , with a xenon flow rate of 12.5 sccm (1.22 mg/s). The neutrals are injected half-Maxwellian with a drift energy of 0.03 eV and a temperature of 0.017 eV. Electron injection is performed by two injection sources. The first is located in the area of  $z \in [47.2 \text{ mm}, 47.7 \text{ mm}]$  and  $r \in [0 \text{ mm}, 2 \text{ mm}]$  injecting a current of 70 mA. The second electron source injects a current of 20 mA in the area  $z \in [69.2 \text{ mm}, 74.2 \text{ mm}]$  and  $r \in [19 \text{ mm}, 21 \text{ mm}]$ . Both sources inject thermal electrons with a temperature of 1 eV. A voltage of 500 V is applied at the anode. The total simulation time is in the range of  $10 \mu\text{s}$  to  $100 \mu\text{s}$ , covering all relevant transport times of electrons, ions and neutrals. Unless stated otherwise, results were averaged for  $5 \times 10^5$  time steps.

The results are separated into two sections. The first one is concerned with the simulation results in the HEMP-T discharge channel, while the second focuses on the plasma plume, in particular on the ion dynamics.

#### 4.1 Discharge channel

The most important aspects of the HEMP-T discharge channel physics are ionization, ion extraction and plasma–wall interaction. As will be shown within this section, the physical properties of the DM3a thruster result in an efficient electron confinement and ionization, low erosion inside the thruster channel and very good thrust production. In the discharge channel, electron motion is defined by the magnetic field structure. The magnetic field orientation between the cusps is mostly parallel to the symmetry axis and the magnetized electrons move along the magnetic field lines, resulting in a strong parallel electron transport there. At the cusps, however, the electrons are guided towards the channel wall. There, they are reflected by the magnetic field structure, acting as a magnetic mirror, and the plasma–wall sheath, leading to good electron confinement and the oscillatory electron motion between the cusps. In this near-wall cusp region, the anomalous electron transport discussed

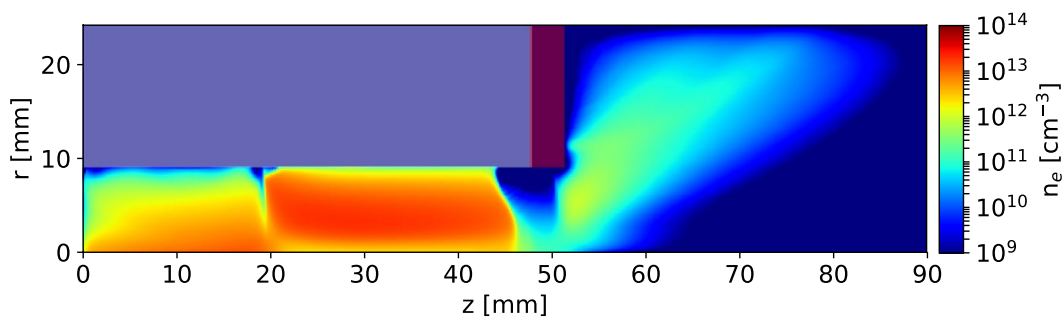


**Fig. 5** Electron density in the HEMP-T DM3a. The dielectric (white) and the metal pole piece (red) are indicated

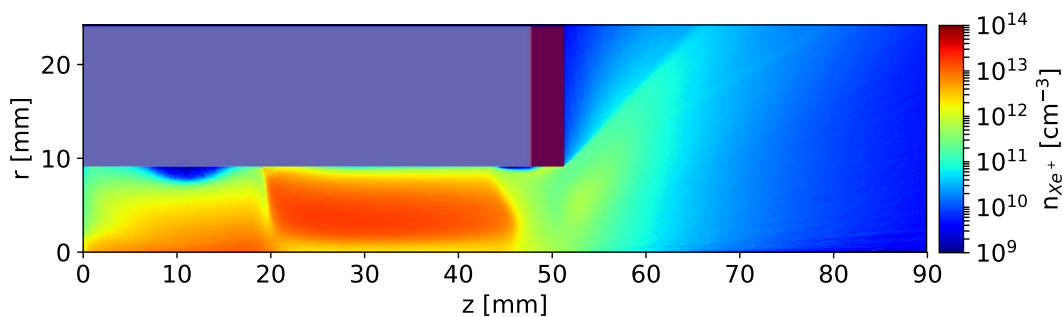


**Fig. 6**  $\text{Xe}^+$  ion density in the HEMP-T DM3a. The dielectric (white) and the metal pole piece (red) are indicated

in Sect. 3 becomes important for cross-field electron transport. This is similar to the cross-field electron transport in HETs across the radially oriented magnetic field lines. In the HEMP-T, this increased electron transport increases the amount of highly energetic electrons at higher channel radii, leading to a radial broadening of the ionization profile. Thus, the good electron confinement leads to efficient electron utilization for ionization processes.

Due to electron magnetization, the dominating electron transport is parallel to the magnetic field lines, building up a characteristic density distribution for electrons and ions, the former shown in Fig. 5. The ions follow the electron distribution in the bulk, due to the quasi-neutrality of the plasma. The  $\text{Xe}^+$  ion density is shown in Fig. 6. The neutral number densities in Fig. 7 are low in the regions of high ionization, most notably near the symmetry axis and in the channel exit region. The increased densities near the channel wall are the result of neutral recycling of impinging ions. Typically, the neutral density is reduced near the symmetry axis and in the cusps due to high ionization there.

The mainly axial magnetic field, especially close to the symmetry axis, combined with the large parallel electron transport results in a flat potential structure in the discharge channel. Only in the narrow cusp regions, where the field lines intersect the channel wall, the electron transport parallel to the magnetic field leads to plasma-wall interactions. In other regions, due to the guidance of the magnetic field, the overall electron wall contact is reduced. Therefore, impinging ions at the

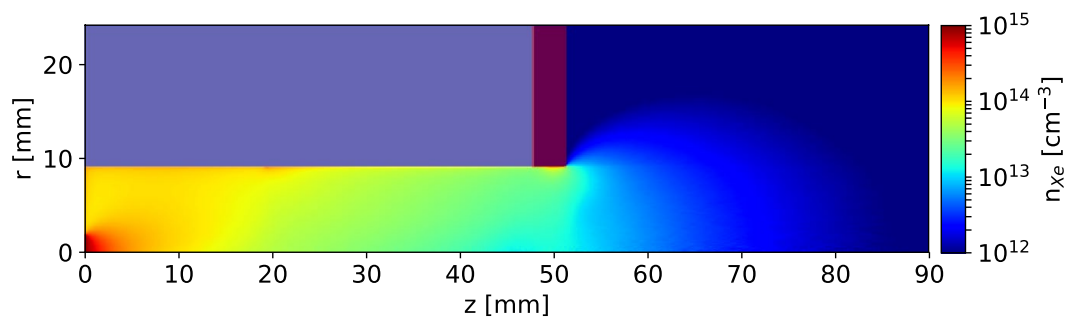


**Fig. 7** Xe neutral density in the HEMP-T DM3a. The dielectric (white) and the metal pole piece (red) are indicated

dielectric channel wall build up a positive surface charge, resulting in a potential in the range of the plasma potential and a small radial electric field. The overall channel potential is flat and its value is determined by the applied anode voltage of 500 V, as is shown in the simulation results in Fig. 8. It also shows the potential drop in the dielectric channel wall as well as the grounded pole piece mounted at the thruster exit. This grounded wall leads to a radial drop of the channel potential, which focuses the electrons at the channel axis. Therefore, no electron wall contact appears in this region despite the radial magnetic field of the exit cusp. This electron focusing also affects the ion density distribution and the electric potential in the exit region.

Overall, the channel plasma is confined by the magnetic field configuration, acting on the magnetized electrons and therefore also on the ions. It is characterized by a flat electric potential at anode voltage and the electric fields in the thruster channel are small. As a consequence, the  $\mathbf{E} \times \mathbf{B}$  vector in the cusp-regions is small, together with the resulting Hall current. Moreover, the trapping of electrons in the HEMP-T is achieved by the oscillation between and reflection at the cusp, respectively. Figure 9 shows an estimate of the Hall current in the simulation, using the ratio of the absolute values of the electric field of the simulation and the  $\Theta$  component of the equation  $\mathbf{F}_L/q_e$ , using the Lorentz force  $\mathbf{F}_L$  from Eq. 2 and the mean electron velocities measured in the simulation. This is only an approximation of the influence of the Hall effect, because the electric and magnetic fields do not have azimuthal field

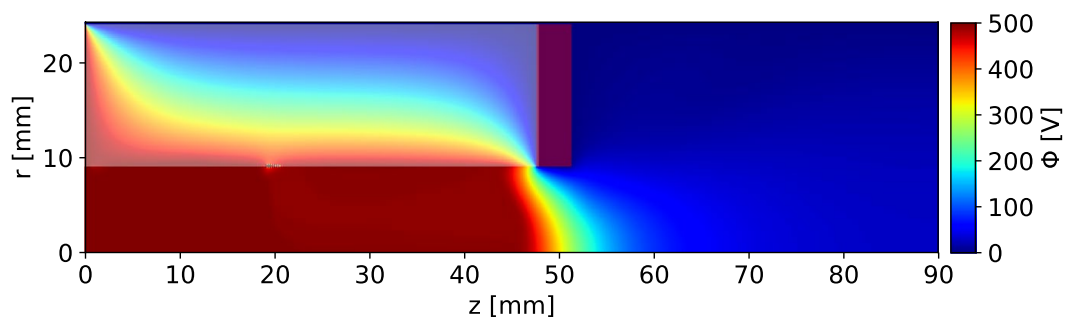


**Fig. 8** Electric potential in the HEMP-T DM3a. The dielectric (white) and the metal pole piece (red) are indicated

components in a 2D3v PIC simulation and no azimuthal forces act on the particles. One can see that only in some parts of the discharge channel, this estimate reaches the same level as the regular electric field of the 2D simulation. Moreover, this only happens in regions where the absolute values of the electric field are low. In regions with high electric fields, i.e., at the cusps and the thruster exit plane, the estimated current is almost negligible. Thus, in the HEMP-T the plasma is confined by the magnetic field structure, whereas in HETs the combination of electric and magnetic fields results in an electron Hall current which increases travel distance and ionization effectiveness of channel electrons.

Further investigation of the results gives more insight into the electron kinetics and ionization process. In Fig. 8, the potential drop at the thruster exit into the plume region is visible. This drop accelerates electrons injected by the source towards the channel. Close to the exit, where the field strength is high enough, the magnetic field configuration guides these electrons. The magnetic field at the exit cusp allows them to enter the thruster channel only close to the symmetry axis. In the mean electron energies in Fig. 10, one can see that these high energy electrons are guided by the field lines at the axis toward the central cusp region. The mean energy decreases with increasing distance to the thruster exit due to collisions. Figure 11 shows the reduction of electron energy in the channel, with mean energies in the range of 1–8 eV, while there are some regions with electron temperatures above 10 eV. These high energy electrons are mostly located near the symmetry axis and the cusp. Upstream towards the anode the mean electron energy decreases due to the influence of collisions.

In the cusp regions, the magnetic mirror effect reflects low energy electrons and the mean electron energy increases near the channel wall. Due to higher electron energies, cross-field transport increases. This spreads the distribution of hot electrons across the magnetic field lines, and after reflection near the cusp wall hot electrons populate the entire discharge channel. This increases the ionization rates at higher radii. As a result, the electron energy distribution is non-Maxwellian in the entire channel, as shown in the radially integrated electron energy distributions at different axial positions in Fig. 12. Because the mean free paths of all electron-neutral collisions are longer than the channel length, electrons are not thermalized, resulting in the nonlinear relationship in Fig. 12.

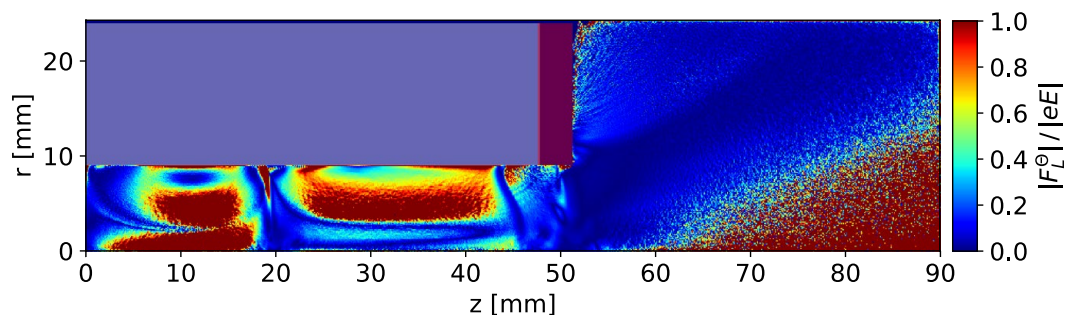


**Fig. 9** Estimate of the Hall current using the  $\theta$  component of  $\mathbf{F}_L/q_e$  relative to the regular electric field in the HEMP-T DM3a. The dielectric (white) and the metal pole piece (red) are indicated

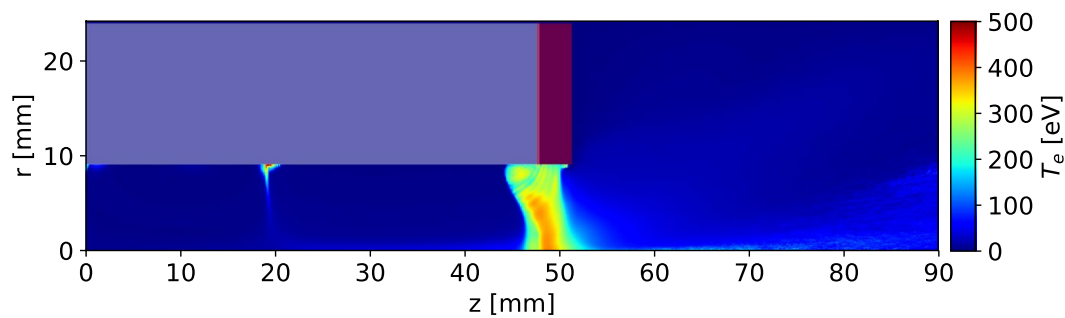


**Fig. 10** Electron temperatures in the HEMP-T DM3a. The dielectric (white) and the metal pole piece (red) are indicated. The full plot range is used to show the spatial distribution of high energy electrons

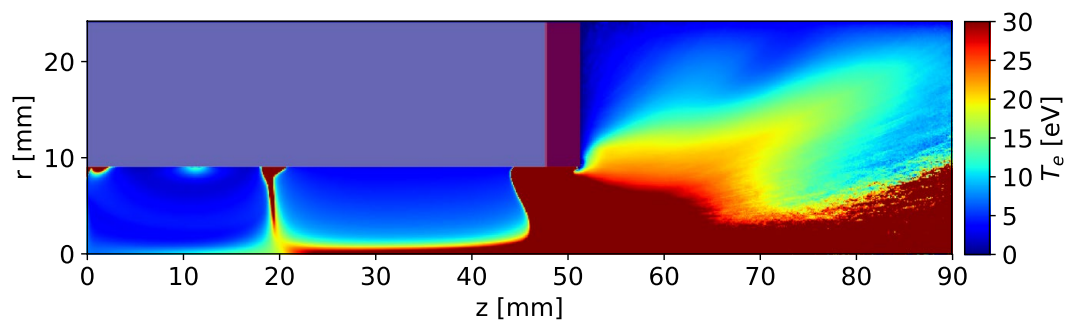


**Fig. 11** Electron temperatures in the HEMP-T DM3a. The dielectric (white) and the metal pole piece (red) are indicated. The maximum temperature is restricted to 30 eV to pronounce the temperature distribution in the discharge channel

The non-Maxwellian electron energy distribution ensures ionization in the thruster channel. The mean electron energies in the range of 1–8 eV are below the threshold energy of single electron impact ionization collisions in a xenon gas at  $\mathcal{E}_{\text{thr}}^{\text{INZ}} = 12.13$  eV (Hayashi 2003). Thus, ionization collisions are performed only by high energy electrons from the tail of the energy distribution. This is evident from the distribution of ionization collisions in Fig. 13, which correlates with the distribution of highly energetic electrons. The ionization of propellant atoms mainly takes place at the axis and in the cusp regions, where electrons have the highest energies. The limited radial extension of ionization at the exit cusp is caused by the grounded pole piece, focusing electrons at the symmetry axis. However, downstream from the exit cusp ionization takes place. Here, the neutral density is not as low as in the outer plume region and the electron energy is high due to acceleration by the potential drop. By increasing the length of the electron's paths due to the trapping of electrons between the cusps, the ionization rate is increased. Thus, the good electron confinement of the HEMP-T leads to an efficient ionization of the propellant in terms of electron utilization.

The axial velocity distributions of ions and neutral propellant atoms are discussed in Kalentev et al. (2014). For the propellant neutrals, a normal distribution around  $v_z = 0$  m/s indicates a thermal behavior. In contrast, the non-normal distribution of xenon ions demonstrates a non-Maxwellian character in the thruster channel. This again confirms the assumption that a fully kinetic method is necessary for the

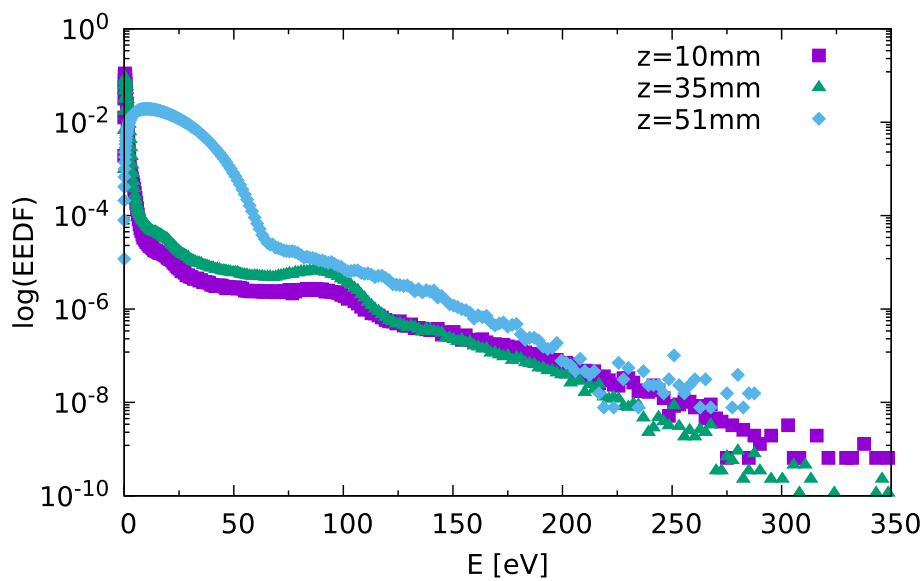


**Fig. 12** Electron energy distribution at different axial positions, averaged over the channel radius for  $10^6$  time steps

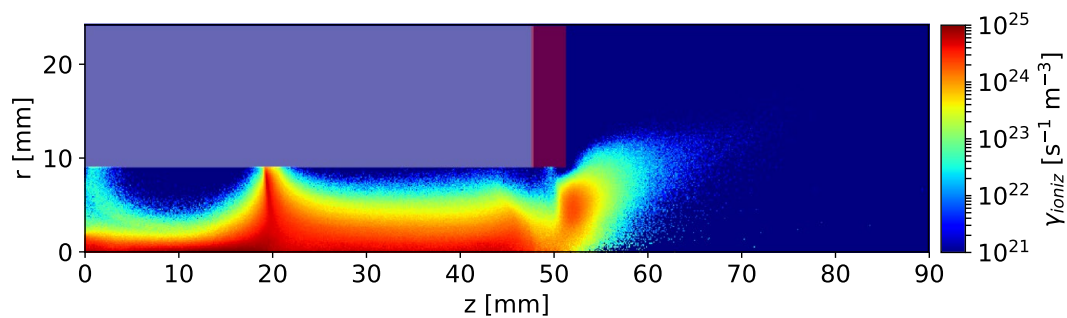


**Fig. 13** Collision rates of the main ionization source, single electron-xenon impact ionization, of the HEMP-T DM3a. The dielectric (white) and the metal pole piece (red) are indicated

simulation of the HEMP-T. For a better understanding of the small discharge losses and the low channel erosion, the plasma–wall interactions must be considered.

In the present simulation, the electron source current of 90 mA is lower than both the discharge current of 613 mA and the ion beam current of 356 mA. This shows the high amplification of source electrons within the plasma of the DM3a HEMP thruster, again due to the long electron lifetime in the discharge channel and the non-Maxwellian characteristics of the electron energy distribution. In experiments, the good electron confinement is evident by the low influence of an operating neutralizer once the plasma has stabilized (Kornfeld et al. 2003). Although the electron amplification is high, the ionization efficiency is much lower than in typical experiments (Kornfeld et al. 2003). It is calculated as  $\mu = I_{\text{plume}} / (q_e \cdot Q_{\text{prop}})$ , where  $q_e$  is the elementary charge and  $Q_{\text{prop}}$  the flux of the propellant source. In the simulation, a source of  $Q_{\text{prop}} = 12.5$  sccm was used, resulting in an efficiency of roughly  $\mu = 39.5\%$  that is low compared to the efficiencies of 70–90% reported from experiments (Koch et al. 2011a; Kornfeld et al.

2003). A detailed discussion of this discrepancy will be done later, but one possible mechanism could be an overestimation of wall losses in the simulation model due to the influence of the applied similarity scaling. Therefore, the wall processes in the discharge channel are discussed in the following.

Plasma wall contact in the channel is determined by the magnetic field configuration. The electron flux is mostly axial in the regions with a parallel magnetic field, because the magnetized electrons follow the magnetic field lines. As a result, the size of the plasma–wall sheath reduces to the scale of the electron Larmor radius, which is smaller than the cell size, so no plasma–wall sheath is observed in the non-cusp channel regions of the simulation. Due to the small sheath, the radial electron flux is reduced and is relevant only in the central cusp region (Matyash et al. 2010). There, the magnetic mirror effect reduces the flux, but highly energetic electrons overcome the barrier and reach the dielectric channel wall. Since the ions are following the electrons, a plasma sheath emerges, with equal current densities at the surface  $j_e = j_i$  and a resulting potential drop of  $\Delta\Phi \approx 35$  V towards the dielectric wall as measured in the simulation. Impinging electrons can produce secondary electron emission (SEE), cooling the channel electrons due to the low energy of the re-emitted electrons. These additional negative charges in front of the wall lead to a further reduction of the radial potential drop in the cusp region. The mean energy of impinging ions is hence reduced to  $\mathcal{E}_i < 45$  eV in the simulation. Boron nitride ceramics is used for the dielectric channel wall due to its high sputtering threshold energy of roughly 50 eV for impinging xenon ions (Gamero-Castaño and Katz 2005). The sputtering yields for ion energies larger than the threshold are small as well (Yalin et al. 2007; Yim et al. 2008). Therefore, erosion of the dielectric channel wall is very small and is not a constraint to thruster lifetime (Koch et al. 2011a; Matyash et al. 2009).

At the anode, the magnetic field configuration is similar to the cusp regions to reduce the loss of plasma electrons towards the anode. Near the symmetry axis, electron flux to the anode is strong, but with increasing radius, the flux is reduced due to the predominantly radial magnetic field. The ion flux to the anode is very small because of the applied voltage, and the flux is dominated by electrons.

In summary, the plasma wall contact of the HEMP-T is minimal, with very little erosion inside the discharge channel. Experimental measurements have shown erosion of less than 5  $\mu\text{m}$  in the cusp regions after a 1200 h test run (Koch et al. 2011a). Therefore, lifetime can be expected to surpass 10,000 h and was confirmed for 7532 h (Genovese et al. 2011). The estimated minimum lifetime is 18,000 h of operation, based on a 250 h test run of the HEMP-T 3050 with a thrust of 57 mN (Koch et al. 2005).

These considerations emphasize the importance of the channel geometry, since the plasma confinement depends on the area of intersection between channel wall and magnetic field lines. The smaller the area, the more electrons are reflected at the cusp due to the stronger magnetic field gradient causing more electron reflection. A minimized area of intersection is achieved by keeping the channel wall close to the permanent magnets, where the cusp magnetic field is the strongest.

Therefore, the HEMP-T magnetic field and channel geometry have to be optimized for ideal discharge characteristics.

The volume of the bulk plasma in the discharge channel plays a key role for the performance of a HEMP thruster. A large volume ensures a large amount of generated ions, but due to limited strength of the permanent magnets, confinement decreases with increasing channel radius. A small channel radius on the other hand increases the influence of the plasma sheath on the bulk plasma and reduces the bulk volume and, therefore, thrust and efficiency. An example of such a HEMP thruster is the  $\mu$ -HEMP-T (Hey et al. 2015; Keller et al. 2011, 2013) which has also been modeled using the fully kinetic PIC method outlined in Sect. 3 in Brandt et al. (2016). While the DM3a thruster is designed for thrusts in the range of some mN, the  $\mu$ -HEMP is designed to produce a net thrust in the range of some  $\mu$ N. Here, the plasma bulk volume is comparable to the thickness of the plasma sheath, resulting in a decrease in overall thruster performance.

## 4.2 Near-field plume

In ion thrusters, channel and plume plasma are coupled. The near-field plume is the region, where the transition from discharge channel to vacuum takes place, defining the ion emission characteristics of the device. Ions are expelled from the discharge channel into the plume, generating thrust. The angular distribution of the emitted ion current determines the efficiency of thrust generation of the propulsion device since the thrust roughly scales with the cosine of the mean ion emission angle in a simple estimate (Goebel and Katz 2008). Together with the near-field plume, the far-field plume is of interest because ion beam interaction with the spacecraft or other objects can ultimately result in damages by sputtering of impinging ions. Simulations can help to understand the physics of the plume and can ultimately be a tool for thruster optimization.

In the near-field plume, the ion trajectories are determined by the electric field, which reaches its maximum in the region just downstream from the discharge channel exit. The ions follow the strong electric field, the structure of which therefore determines the angular distribution of the emitted ion current. However, collisions in the plume change the ion emission characteristics, most notably charge-exchange and momentum transfer collisions with non-ionized neutrals in the exit region, increasing the low energy contribution in the ion emission profile. Furthermore, a change of the electron distribution in the near-field plume can modify the ionization rate and spatial distribution inside the thruster channel and hence the thruster efficiency. In the near-field plume, the electrons are affected by the potential and by the magnetic field of the thruster, resulting in a complex interaction between plasma densities, potential and magnetic field.

The angular ion current distribution is an important quantity not only because of the thrust efficiency, but also because it provides an important point of comparison between simulation and experiment. Because the plasma parameters in the discharge channel are difficult to measure experimentally, often only plume measurements are available. One of the most common experimental diagnostics is the use of retarding

potential analyzers (RPAs), which allow the measurement of the ion current and energy distribution depending on the emission angle. This is achieved by either moving a single RPA into the specified areas, or by using an array of mounted RPAs (Lazurenko et al. 2011). The distance from thruster exit to the RPA is in the range of 1 m, a length scale that is difficult to model using a fully kinetic simulation due to computational restrictions. For the definition of the emission angle, the thruster is assumed as a point source positioned at the symmetry axis in the thruster exit plane.

The energy distribution of ejected  $\text{Xe}^+$  ions at the domain boundary, shown in Fig. 14, is mainly determined by the origin of each ion in the discharge channel and the electric potential drop experienced by the ions moving out of the thruster from that location. All ion energies are corrected by the residual potential at the right domain boundary caused by the von-Neumann boundary condition applied there. Therefore, most of the detected ions have an energy close to the anode potential  $U_a = 500$  V, as most ionization takes place in the discharge channel at plasma potential in Fig. 13. This observation agrees very well with the experimental measurements (Koch et al. 2011a) and leads to the conclusion that the potential is almost flat across regions of high ionization. This agrees with the simulation results in the discharge channel in Figs. 8 and 13.

In most simulations, the feasible simulation domain is much smaller than the distance to the RPAs for angular ion measurements. Therefore, the distributions are measured in the simulation along the vacuum boundaries, at the top and right ends of the simulation domain. For a comparison to the experimentally measured distributions, the physical processes in the space between the simulation domain boundary and the RPAs must be considered. The distribution from the simulation can be mapped to the position of the RPA using a so-called transfer function (Duras et al. 2017). Especially for small domains with von-Neumann boundary conditions at the right domain boundary, the impact of this correction on the angular ion energy distribution is visible. Here, the plume potential has not yet decayed to zero at the surface of measurement, and the potential energy of the detected ions has to be taken into account. In Duras et al. (2017), a comparison of the corrected and uncorrected angular ion energy distributions is displayed for a simulation domain with a von-Neumann condition at the right domain boundary.

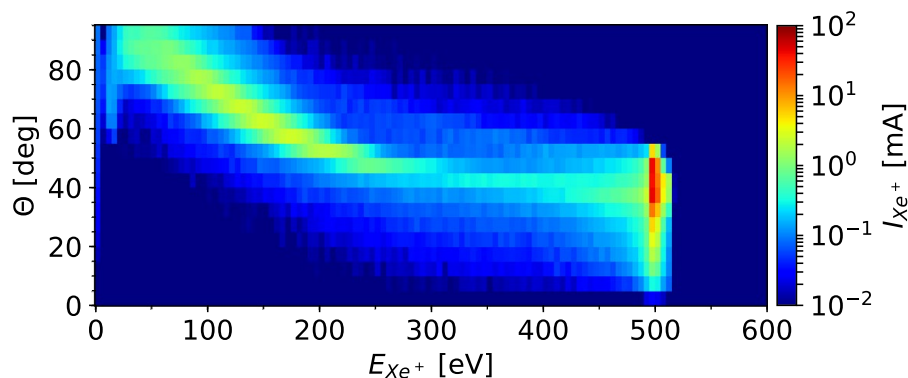


**Fig. 14** Angular energy distribution of emitted  $\text{Xe}^+$  ions in the simulation, measured at the domain boundary

Another method to overcome the simulation domain size limit is the use of the grid jump method discussed in Sect. 3. By increasing the distance between adjacent mesh points for the potential calculation, the overall solver complexity is reduced for large domains, but special treatment of the electric field calculation is necessary to avoid particle self-forces (Duras et al. 2014). Generalization to more than one dimension and for execution of several grid jumps is straightforward. Due to the small electron Debye length in the discharge channel and the stability considerations detailed in Sect. 3, grid jumps can only be applied in regions of low plasma density. The grid jumps must also be considered in the finite-difference discretization of Poisson's equation, resulting in changed matrix coefficients for the linear system of equations that is solved at every time step. The calculations for the discretization are carried out in detail in Arlinghaus (2018).

In that work, the solution method was tested and validated thoroughly for simulations of the HEMP-T DM3a in a small domain. Only the electric potential was considered, no plasma solution was calculated self-consistently. The difference in electric potential between the solutions with and without grid jump in a small domain is shown in Fig. 15. The differences arising, especially near the boundaries, can be neglected as the boundary conditions themselves are only approximations to the real system. Furthermore, the stability was also confirmed with a self-consistent plasma calculation.

For further tests, in a large DM3a simulation domain of  $r \times z = 456.5 \times 456.5 \text{ mm}^2$  (compared to the domain of  $r \times z = 24.5 \times 90.1 \text{ mm}^2$  used in the simulations in Sect. 4.1), several grid jumps were executed and compared to the solution without any jumps. The solution times with the maximum relative deviations are shown in table 2. One can see that the speedup of the potential solution is very high for the large domain, while the relative differences in the potential solution are negligible. Therefore, the grid jump method is very well suited for achieving larger simulation domains. Self-consistent plasma simulations for large domain sizes must still be carried out using this promising approach.

Furthermore, the influence of the boundary conditions on the simulation domain was investigated. This was achieved by switching the Dirichlet and von-Neumann boundary conditions at the top and right domain boundaries, respectively, and measuring the maximum deviation of the electric potential in the simulation domain. The results are shown in Table 3. The relative difference of solutions is high for the standard simulation domain used in Sect. 4.1, and is acceptably small for domains

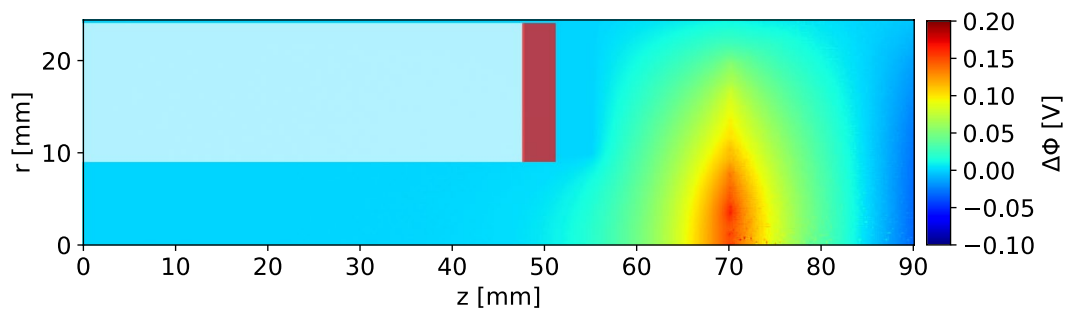


**Fig. 15** The absolute difference of the electric potential in the HEMP-T DM3a with a single axial grid jump executed at  $z = 70 \text{ mm}$

**Table 2** The number of non-zero matrix entries (nnz), the back solve time and the deviation for several grid jumps in the large  $456.5 \times 456.5 \text{ mm}^2$  domain of the HEMP-T DM3a

Grid-jumps	Width	Grid jump at (mm)	nnz	Back solve (ms)	Deviation (%)
0	1	–	83855074	9280	0%
1	2	$r = 40; z = 70$	21794340	2087	0.10
2	4	$r = 75; z = 90$	6581166	546	0.10
3	8	$r = 115; z = 120$	2912188	225	0.11
4	16	$r = 150; z = 150$	2038630	161	0.15
5	32	$r = 200; z = 200$	1842260	143	0.20

The back solve time in the  $r \times z = 24.5 \times 90.1 \text{ mm}^2$  domain is about 40 ms

as large or larger than  $r \times z = 160 \times 215 \text{ mm}^2$ . The relative difference saturates for larger domains because the absolute values of the potential become very small near the domain boundaries. Still, the absolute deviations between the largest and smallest simulation domains do not surpass 30 V, which is small compared to the anode and plasma potential of 500 V. However, this is only true for the potential calculation, since in full thruster simulations the potential expands further into the plume, modifying the overall solution. Therefore, to further investigate the influence of the boundary conditions, again a self-consistent thruster simulation featuring a large domain is necessary.

Experimental results show a fraction of low energy ions reaching the RPA that is larger than the one obtained from the simulation. While inside the thruster channel the ion-neutral charge-exchange collisions are negligible, the traveled length of an ion increases to about 1 m and thus increases the collision probability of an ion until it reaches the detector. This distance is much larger than the size of the simulated

**Table 3** The domain size, the number of grid points and the corresponding relative deviation of the electric potential in the HEMP-T DM3a

Domain size ( $\text{mm}^2$ )	Grid points	Deviation (%)
$24.4 \times 90.0$	176952	135.6
$40.0 \times 105.0$	338537	56.0
$55.0 \times 120.0$	532038	45.2
$70.0 \times 135.0$	762348	39.9
$85.0 \times 150.0$	1026998	35.7
$100.0 \times 165.0$	1329938	31.9
$130.0 \times 190.0$	1989735	24.2
$160.0 \times 215.0$	2771480	19.9
$190.0 \times 240.0$	3672570	17.3
$225.0 \times 265.0$	4801182	15.8
$260.0 \times 290.0$	6072799	15.3
$320.0 \times 320.0$	8248384	16.3
$385.0 \times 385.0$	11937025	14.7
$456.5 \times 456.5$	16785409	13.4

plume, resulting in fewer collisions compared to the experiment. This leads to the creation of highly energetic neutrals and ions of low energy that are strongly influenced by residual electric fields. Therefore, the low energetic ions are under represented in the angular ion energy distribution of the simulation, which can be fixed with a more advanced transfer function (Duras et al. 2017).

Along with the ion energy distribution, the angle at which the most high energy ions are emitted is important, due to the cosine dependence of the thrust on the emission angle (Goebel and Katz 2008). The contributions to certain angle bins of the emission profile correlate with the origin of ion creation, as shown in Duras et al. (2017). There, the different origins of the ejected ions lead to two different peaks in the angular current distribution. The ionization origins for incident ions in the 40° and 60° angle bins is shown in Duras et al. (2017). For emission, angles between 30° and 50° ions are mostly generated inside the discharge channel. Larger angle contributions of more than 55° are mainly generated by ions that were ionized in the thruster exit region. For angles below 30°, both cusp regions contribute.

The total angular current corresponding to the ion energy distribution in Fig. 14 is shown in Fig. 16. In Duras et al. (2017), this figure is compared to the experimentally measured angular current distribution from Kornfeld et al. (2003). Between the diagnostic surface in the simulation and the position of the RPA in the experiment, the plume potential can be estimated as decaying linearly. Therefore, a direct flight can be assumed for the ejected ions in the simulation, and the angular current distribution can be directly compared to the experimental data. In all, the simulated ion current distribution resembles the experimentally measured one very well, with a deviation of the mean emission angle of about 10°.

In the experiment, the thruster is mounted on a thrust balance, directly measuring the thrust  $T$ . In the simulation,  $T$  can be calculated by the angular distributions of the ejected ions. A cosine law connecting the thrust and the mean ion emission angle is only a rough approximation, because it does not take into account the energy distribution shown in Fig. 14. In the simulation, the entire kinetic information is available and, therefore, the thrust for species  $i$  can be calculated accurately via

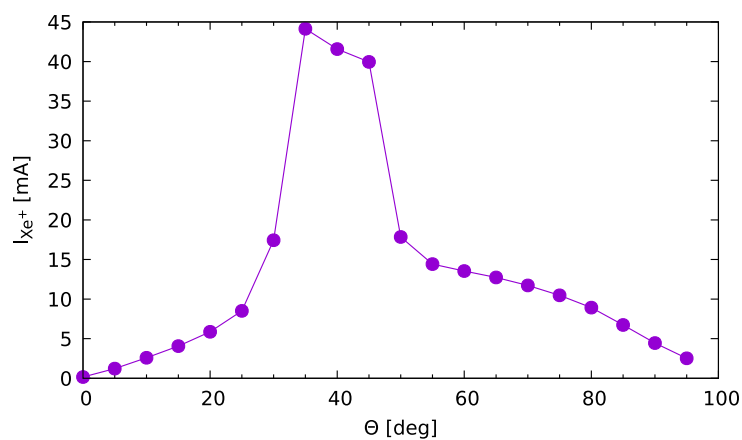


**Fig. 16** Angular current distribution of emitted  $Xe^+$  ions in the simulation, measured at the domain boundary

$$T^i = \int dE_{\text{plume}}^i \int d\theta \sqrt{\frac{2 E_{\text{plume}}^i(\theta)}{m_i}} \cos(\theta) \frac{m_i I_{\text{plume}}^i(E_{\text{plume}}^i(\theta))}{q_i}, \quad (14)$$

with the emission angle  $\theta$ , charge  $q_i$  and mass  $m_i$  of the ion species  $i$ . The total thrust obtained for this simulation is  $T = T^{Xe^+} + T^{Xe^{2+}} = 5.53 \text{ mN} + 1.57 \text{ mN} = 7.10 \text{ mN}$ . It is lower than in experiments, where thrusts of 12.5–15 mN were measured for the HEMP-T DM3a for voltages and neutral mass flow rates comparable to those in the simulation (Kornfeld et al. 2003). The main reason for this is an ionization efficiency which at roughly 39.5% is lower than in experiments, where efficiencies of up to 90% are reached (Kornfeld et al. 2003).

That could be caused by an underestimated electron transport across magnetic field lines, induced by turbulence in the electric field. The importance of this transport is indicated by measurements of HETs, e.g., in Janes (1966). This is a three-dimensional turbulence effect that does not appear in axisymmetric 2D simulations and is, therefore, neglected in the simulations carried out in Duras et al. (2017). It is only approximated by the anomalous diffusion model described in Sect. 3, which might not be accurate enough. With increased anomalous transport, the region with highly energetic electrons would extend to larger channel radii and widen the ionization profile that is observed in Fig. 13. Therefore, the total ionization rates would increase and thus the total amount of ions ejected by the channel plasma. With increasing ionization in the discharge channel, the neutral density profile in Fig. 7 would decrease more quickly, reducing the ionization in the thruster exit region. This would move the drop from plasma to vacuum potential further into the discharge channel. This results in a more axially oriented electric field, increasing the thrust contribution of the emitted ions in Eq. 14 and decreasing the high angle contributions of the ion emission, with a mean emission angle that is roughly  $10^\circ$  higher in the simulation compared to the experiment. The connection between the axial position of the potential drop and the mean ion emission angle is also observed in Fig. 20, which will be discussed in detail in the next section. However, increased ionization and radial transport also increases wall losses, which can negate the effects of the increased ionization. This was confirmed in simulations carried out for the HEMP-T 3050 model. A parameter study was conducted for an increased anomalous transport of electrons, however, not in velocity space but rather in coordinate space. Increased diffusion leads to higher discharge currents, ion beam currents and produced thrust up to diffusion coefficients of  $5 \text{ ms}^{-2}$ , due to the behavior described above. Larger transport coefficients, however, increase wall losses and a decrease in thrust production was observed.

Another aspect that can lead to different results is the influence of the similarity scaling scheme discussed in Sect. 3. Since the plasma sheath is not scaled, the influence of the relative increase of the plasma–wall sheath size can increase wall losses in the cusp region, leading to reduced ionization. To fully quantify this effect, comparative simulations with lower scaling factors would be necessary, which have not been carried out yet.

An experimental characteristic observed in HEMP thrusters during stable operation in test facilities is the formation of breathing oscillations. These are

more commonly known from HET operation and are well investigated experimentally (Choueiri 2001; Dale and Jorns 2018; Gascon et al. 2003; Lobbia and Galimire 2009; Lobbia et al. 2011; Romadanov et al. 2018; Sekerak et al. 2016) and theoretically (Barral and Ahedo 2006, 2009; Barral and Peradzyński 2010; Boeuf and Garrigues 1998; Dale et al. 2017; Hara et al. 2014a, b, 2015; Yamamoto et al. 2005) for that thruster system. Observed frequencies are in the range of 10–30 kHz, determined by the dynamics of the neutrals, which are ionized locally and then re-populate that region. Oscillation amplitudes observed in the discharge current range from 10 up to 100% of the mean current, depending on discharge parameters and thruster geometry. Due to the large oscillation amplitude, understanding the breathing oscillation is important for stable thruster operation.

Breathing mode oscillations are also observed during operation of HEMP thrusters in test facilities (Kornfeld et al. 2007). The reported frequency range is 100–500 kHz, with an amplitude modulation of the discharge current of up to 30%. In HEMP thrusters, theoretical and experimental investigation of the oscillation was largely missing, but recently published results show an investigation of a breathing mode from experimental and simulation data and is discussed here. A detailed discussion of the results and the parameters for the simulation setup can be found in Kahnfeld et al. (2018). Simulation results show an oscillation of the discharge current with a frequency of 60 kHz and an amplitude of 15%, which is shown in Fig. 17. Both values are near the lower end of the previously published results (Kornfeld et al. 2007). In Fig. 17, also the oscillations of the total beam current and the net thrust are plotted. Hence, the oscillation is not just an electron effect, but evolves from coupled plasma dynamics. Furthermore, the connection of ion beam current and thrust is evident.

The feedback electron injection scheme introduced in Sect. 3 leads to fluctuations of the injected current, exciting all modes in the plasma. From the broad excitation spectrum, the main mode then adjusts itself self-consistently. The oscillation is observed in most discharge parameters, such as electron, ion and neutral number densities, electrostatic potential and ionization collision rates. They are most easily observed in the axial profiles at different times of the oscillation in Figs. 18 and 19. The oscillation is localized in the thruster exit region from  $z = 48$  mm to  $z = 52$  mm, with a radial extension of about 4 mm from the axis into the plume. There, plasma parameters start the expansion from the high density channel plasma into the near-field plume. One can see the high ionization and consequent lack of electrons, which are then replenished at the minimum of the oscillation. This coincides with the position of the potential drop, the point in the discharge channel where the potential drops to the  $e$ -th fraction of the anode voltage, averaged over the discharge channel radius. In Figs. 19 and 20, it is apparent that the position of the potential drop is oscillating along with the other plasma parameters. Also shown is an oscillation of the mean ion emission angle. This again proves the previously discussed (4.1) dynamics between the position of the potential drop and the mean ion emission angle, i.e., that a potential drop further inside the discharge channel leads to lower emission angles, and vice versa. The phase shift is explained by the ion transit times from the exit to the location of the angular ion current measurement at the simulation boundary.

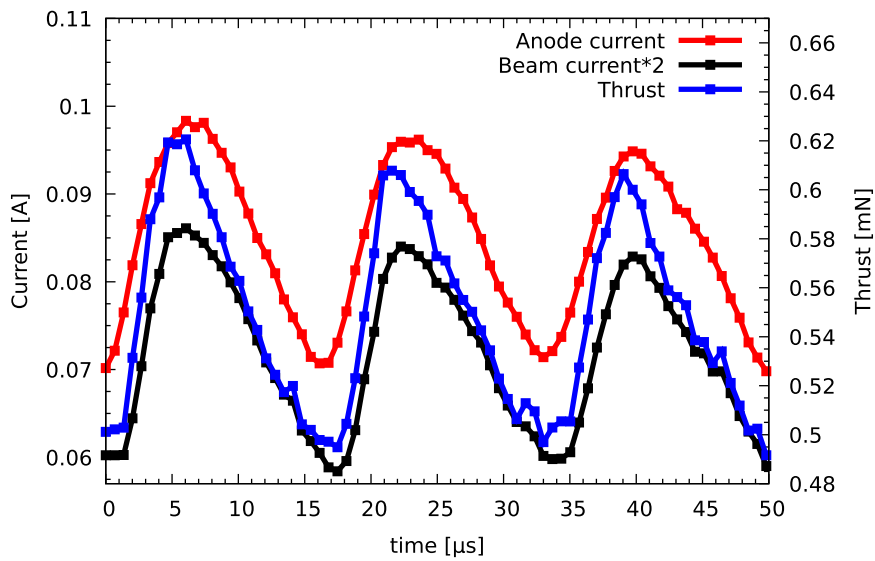


**Fig. 17** Oscillation of the anode current, ion beam current and thrust in the HEMP-T DM3a

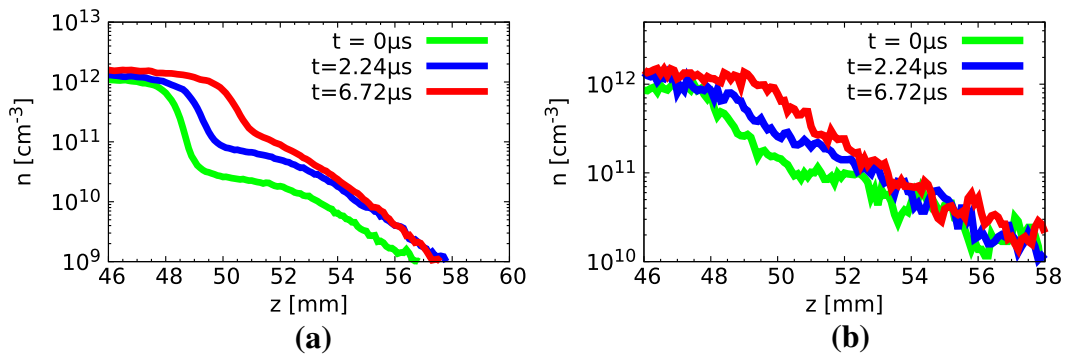


**Fig. 18** Axial **a** electron and **b** ion density profiles at  $r = 1$  mm in the thruster exit region of the HEMP-T DM3a

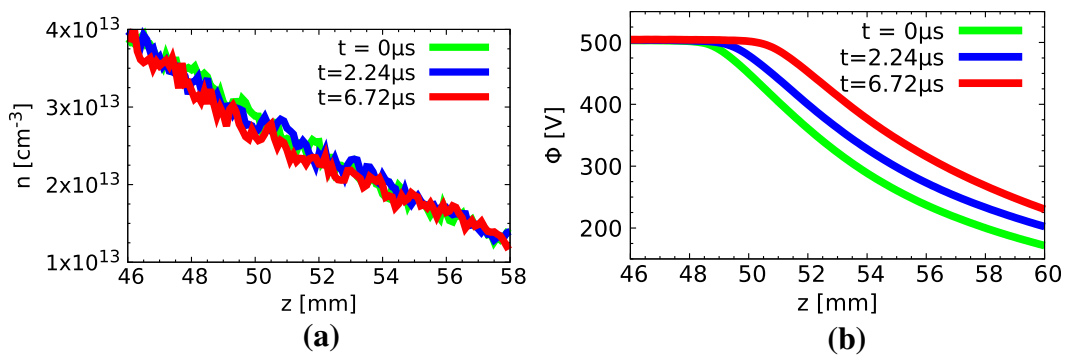


**Fig. 19** Axial **a** neutral density and **b** potential profiles at  $r = 1$  mm in the thruster exit region of the HEMP-T DM3a

The simplest breathing mode model is a 0D predator–prey ansatz, assuming constant electron temperature and neglecting its influence on the ionization and breathing oscillation (Hara et al. 2014b). Electrons and ions are acting as predators and neutrals as prey, resulting in an imbalance between replenishment and ionization of neutrals, as a result of forming the breathing mode in the area of the ionization front. The frequency of the oscillation is determined by the flight time of neutrals for replenishment within the oscillation area. A simple frequency estimate (Hara et al. 2015) of 75 kHz is obtained from the simulation results, which is in very good agreement with the measured oscillation frequency of 60 kHz in the simulation. Therefore, the ansatz is a valid first approach to the characterization of breathing modes in HEMP thrusters, although recent measurement in HETs suggests that such a model is unrealistic (Dale and Jorns 2018). In the simulation, the influence of the electron temperature is investigated, showing that electron temperatures are highest at the minimum of the oscillation, resulting in higher ionization rates and reversing the trend. The opposite is the case at the oscillation maximum.

Along with the evaluation of the simulation results, a comparison with an experimental measurement is discussed and shown in Fig. 21. It is apparent that the experimentally measured frequency of 313 kHz is much higher than the 60 kHz in the simulation. Also the amplitude of 44% of the mean current is much higher than obtained from the simulation results. This stark difference must be attributed to the very disparate discharge conditions, i.e., the neutral flow rate in the experiment of 7.5 sccm (0.7 mg/s) is lower than the 12.5 sccm in the simulation, while ionization efficiency is much higher at 75% compared to 10% in the model. While the quantitative differences between experiment and simulation must still be investigated, the qualitative characteristics of the breathing oscillations in HEMP-Ts were reproduced.

To investigate the plume of a HEMP thruster, the PIC method is not well suited, due to the high computational cost that arises due to the potential calculation, as discussed in Sect. 3, and the small time step and mesh spacing necessary to correctly

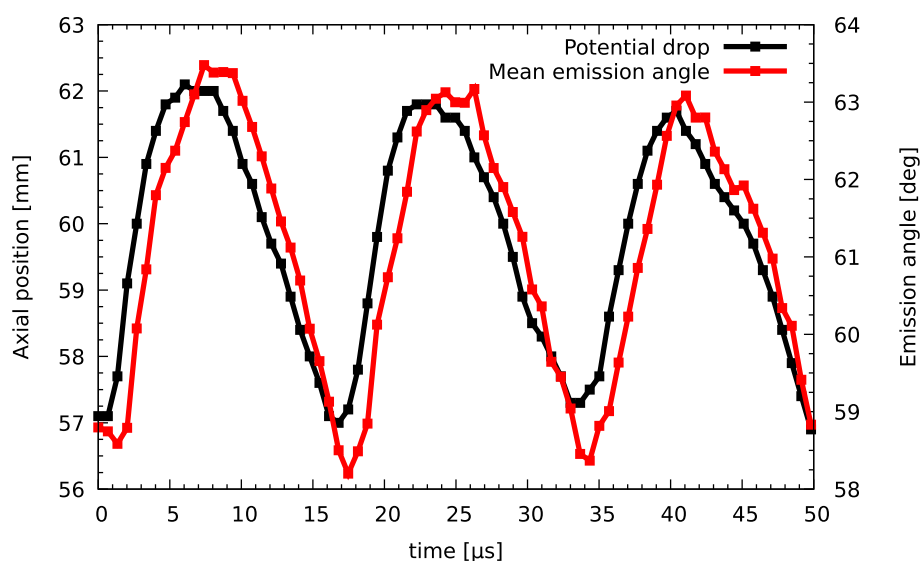


**Fig. 20** Oscillation of the potential drop and mean ion emission angle in the HEMP-T DM3a

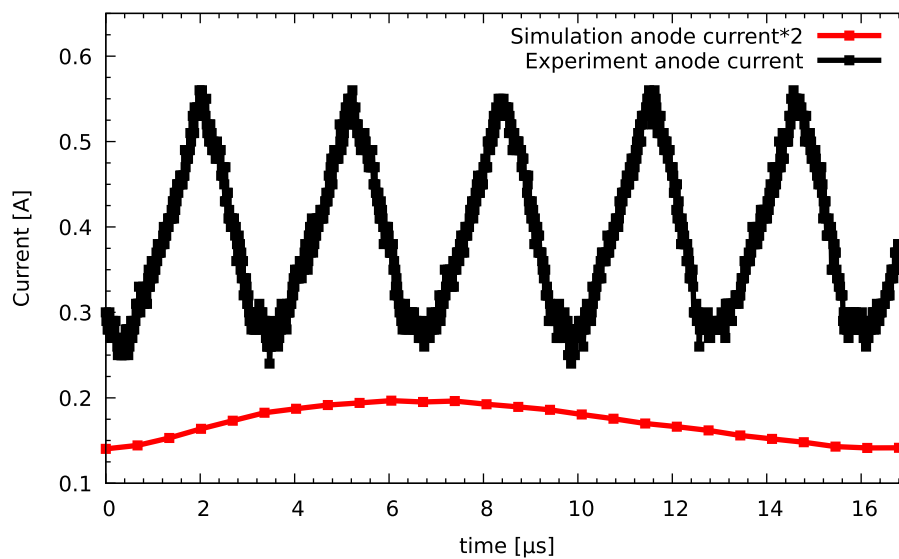


**Fig. 21** Comparison of the breathing oscillation of the anode current in the simulation and an experimental measurement in the HEMP-T

simulate the channel plasma. It is useful to investigate only the plume to decouple the different time and length scales. The particle distribution functions from the near-field plume of the fully kinetic thruster simulation can be used to investigate the expansion of the plume and possible interactions of the plume with the carrier spacecraft. To cover large simulation domains, other models have proven to be valuable, one such model being a 3D hybrid PIC model (Cichocki et al. 2016). The electrons are modeled as a fluid, while ions are treated fully kinetic. This allows to increase the time step and mesh spacing to increase from electron Debye length and plasma frequency to the ion quantities, respectively.

This approach was carried out studying the HEMP-T DP1 model developed by Koch et al. (2017). The DP1 model was developed as a digital prototype and simulations were carried out to study the effectiveness of the design before a prototype will be built. It is designed to operate with discharge currents in the range of 0.5–1.5 A and anode voltages between 200–800 V featuring a cost-effective and simple design. The thrust levels are planned to be in the range of 0.1–25 mN with ISPs between 1200 and 2700 s. In its final form, the discharge channel of the DP1 has a radius of 15.1 mm and is 64 mm long. The magnetic field was computed numerically using the FEMM code (Meeker et al. 2017) and features two inside cusps, compared to one in the DM3a model. Also, the DP1 does not feature a metal pole piece at the channel exit. First simulation results show an ISP of 1840 s with a net thrust of 2.5 mN (Koch et al. 2017). The full simulation results with a detailed description of the simulation and the thruster design can be found in Koch et al. (2017).

Ion and electron densities from a simulation of the DP1 with a similarity scaling factor  $\xi = 60$ , time step  $\Delta t = 2.8 \times 10^{-13}$  s and grid spacing  $\Delta r = 3.7 \times 10^{-3}$  mm are shown in Fig. 22 and Fig. 23. A neutral flow rate of 60 sccm (5.8 mg/s) and an electron injection current of 40 mA, injected at the right domain boundary without feedback control, were used. The other simulation parameters are the same as outlined in

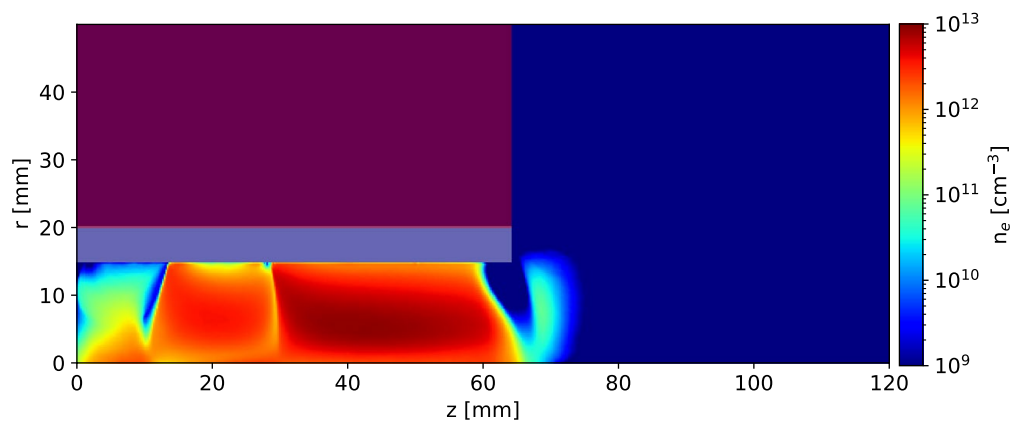


**Fig. 22** Electron density in the HEMP-T DP1. The dielectric (white) and the metal pole piece (red) are indicated. The data were averaged for  $5 \times 10^5$  time steps

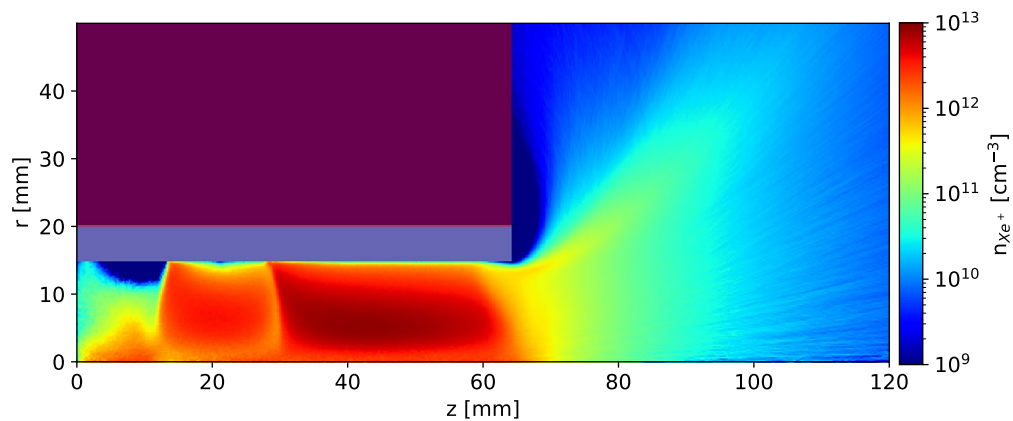


**Fig. 23**  $\text{Xe}^+$  ion density in the HEMP-T DP1. The dielectric (white) and the metal pole piece (red) are indicated. The data were averaged for  $5 \times 10^5$  time steps

Sect. 4. In Fig. 22, one can see the additional cusp compared to the electron density in the DM3a in Fig. 5. Electron densities are gradually decreasing with the passing of each cusp from the thruster exit towards the anode. The ions in Fig. 23 follow the electron distribution in the discharge channel in similar fashion to the DM3a. Plasma wall contact is still limited to the cusp regions. In the thruster exit plane at  $z = 64$  mm, the magnetic field guides the electrons towards the symmetry axis, and the acceleration of the ions occurs in this region, leading to the ion plume density observed in Fig. 23. A detailed discussion of the HEMP-T DP1 can be found in Koch et al. (2017).

A plume expansion using the 3D hybrid PIC code EP2PLUS was carried out for the HEMP-T DP1 with particle data from the fully kinetic 2D3v PIC-MCC simulation (Kahnfeld et al. 2017). A preliminary code description of the EP2PLUS code can be found in Cichocki et al. (2016) and an extensive overview is presented in Cichocki et al. (2017). Details of the simulation parameters are found in Kahnfeld et al. (2017). The point of operation was chosen to be much higher than in Koch et al. (2017) with a higher similarity scaling factor (60 compared to 30). This results in a very large ion emission angle. The ion emission characteristics of the DP1

thruster show a hollow shape that is very sharp in the thruster exit plane. This shape is rapidly lost due to the ambipolar electric fields in the plume, expanding the ion density profile radially. This results in an almost conical expansion of the plume, which is considered to be a good characteristic due to the low beam divergence.

Another aspect of the fully kinetic PIC simulation discussed in Kahnfeld et al. (2017) is the underestimation of potential gradients combined with the violation of quasi-neutrality. This is a consequence of the applied similarity scaling scheme as described in Sect. 3. When extrapolating the results from the down-scaled system to the real one, the Debye scale is artificially increased in the real system. In the plume, the Debye scale becomes very large because of the decreased number densities of charged species which is a result of the loss of plasma confinement. The Debye scale becomes comparable to the system size, resulting in areas that seemingly violate quasi-neutrality in the simulation. This is an artifact of the similarity scaling.

## 5 Conclusions and outlook

In this work, the current progress on the modeling of HEMP thrusters was discussed. The PIC model of HEMP-Ts helped to improve the physical understanding of the device. The discharge channel physics is dominated by the magnetized electrons which move along the magnetic field lines parallel to the symmetry axis in most channel regions. Only at the magnetic cusps, plasma-wall contact occurs because electrons are guided towards the wall, but are mostly reflected due to the magnetic mirror structure of the field. The hot electrons are distributed across magnetic field lines, effectively transporting high energy electrons to higher radii away from the symmetry axis, which results in a non-Maxwellian electron energy distribution in the discharge channel. The ions follow the electrons. The electric potential in the channel is flat with rather small radial variation towards the dielectric wall. Hence, the energy of ions impinging on the wall is below the sputter threshold. As a result, practically no erosion is observed. The potential drops strongly in axial direction to vacuum potential at the thruster exit, where ion acceleration occurs. Its structure in the acceleration region shapes the ion emission profile.

The ion energy distribution in the plume is easily accessible experimentally via RPA measurements. However, due to the small simulation domain, a comparison between simulation and experiment is somehow limited. A transfer function or an increased simulation domain size can improve the results. Simulations of a breathing mode in a HEMP thruster were discussed and the oscillation is observed in all plasma quantities in the thruster exit region. A 0D predator prey model shows good agreement with the simulation, but comparison to experimental results is still difficult due to disparate plasma discharge conditions. For plume simulations, coupled models offer a good trade-off between accuracy and computational effort. The results of a 2D3v PIC-MCC simulation were coupled to the 3D hybrid PIC code EP2PLUS and the calculation of the plume expansion of the HEMP-T DP1 was carried out.

In general, the simulations show a qualitative agreement with experimental data, but for a full quantitative model some aspects of the simulation need to be improved.

This is the case for the total ionization efficiency and the ion angular energy distribution. Future efforts should focus on improvement on these points to achieve better agreement with the experiment. Probably, the location of the axial potential drop at the exit is a key element here. This can be affected by different operational scenarios or additional radial transport due to turbulence. A successful prove of a simulation close to experiment will be an important step towards predictive modeling of thruster systems via computer simulations. To achieve this, 2D simulations or full 3D simulations with low similarity scaling factor are necessary, which can be achieved with the continued improvement in computer technology. This offers chances for savings in time, cost and effort for the development of new thruster models due to a smaller number of necessary prototypes and testing cycles. Another aspect where improvements are expected is the coupled simulation of thruster channel and the plume, extending several meters from the thruster exit, which is important to estimate the interaction of thruster and carrier spacecraft. Here, the multigrid method with a subcycling ansatz for the plume particles makes such a simulation feasible while using a fully kinetic model. First thruster models have already been developed with the aid of computer simulations, such as the HEMP-T DP1. One promising direction is optimized by utilization of hierarchical models for even faster optimization of thruster models. Here, optimization of a set of simplified balance equations for thruster models will decrease the computational effort. The parameters of such balance models can be derived not only from simulations, but also from experiments (Matthias et al. 2019; Yeo et al. 2019).

**Acknowledgements** The work of Daniel Kahnfeld, Paul Matthias and Gunnar Bandelow was funded by the German Space Agency DLR through project 50RS1510. The work of Norbert Koch and Julia Duras was funded by the Bavarian State Ministry of Education and Cultural Affairs, Science and the Arts in the frame of the project “ITSim - Skalierung von Ionenantrieben mittels numerischer Simulation”.

## Compliance with ethical standards

**Conflict of interest** On behalf of all authors, the corresponding author states that there is no conflict of interest.

## References

- E. Ahedo, F.I. Parra, Partial trapping of secondary-electron emission in a hall thruster plasma. *Phys. Plasmas* **12**(7), 73503 (2005). <https://doi.org/10.1063/1.1943327>
- P. Arlinghaus, Application of advanced solvers for pic. Master's thesis, University of Greifswald (2018)
- S. Barral, E. Ahedo, Theoretical study of the breathing mode in hall thrusters. in *42nd AIAA/ASME/SAE/ASEE Joint Propulsion Conference and Exhibit, AIAA 2006-5172* (2006)
- S. Barral, E. Ahedo, Low-frequency model of breathing oscillations in hall discharges. *Phys. Rev. E* **79**, 046401 (2009). <https://doi.org/10.1103/PhysRevE.79.046401>
- S. Barral, Z. Peradzyński, Ionization oscillations in hall accelerators. *Phys. Plasmas* **17**(1), 014505 (2010). <https://doi.org/10.1063/1.3292645>
- F. Battista, E.A. De Marco, T. Misuri, M. Andrenucci, A review of the hall thruster scaling methodology. in *Proceedings of the 32nd International Electric Propulsion Conference, IEPC-2007-037* (2007)
- A.S. Belward, J.O. Skøien, Who launched what, when and why; trends in global land-cover observation capacity from civilian earth observation satellites. *ISPRS J. Photogramm. Remote Sens.* **103**, 115–128 (2015). <https://doi.org/10.1016/j.isprsjprs.2014.03.009>

- A. Bergmann, Two-dimensional particle simulation of langmuir probe sheaths with oblique magnetic field. *Phys. Plasmas* **1**(11), 3598–3606 (1994). <https://doi.org/10.1063/1.870895>
- C.K. Birdsall, D. Fuss, Clouds-in-clouds, clouds-in-cells physics for many-body plasma simulation. *J. Comput. Phys.* **3**(4), 494–511 (1969). [https://doi.org/10.1016/0021-9991\(69\)90058-8](https://doi.org/10.1016/0021-9991(69)90058-8)
- C. Birdsall, A. Langdon, *Plasma Physics via Computer Simulation* (CRC Press, Boca Raton, 2004)
- C.K. Birdsall, N. Maron, Plasma self-heating and saturation due to numerical instabilities. *J. Comput. Phys.* **36**(1), 1–19 (1980). [https://doi.org/10.1016/0021-9991\(80\)90171-0](https://doi.org/10.1016/0021-9991(80)90171-0)
- J.P. Boeuf, L. Garrigues, Low frequency oscillations in a stationary plasma thruster. *J. Appl. Phys.* **84**(7), 3541–3554 (1998). <https://doi.org/10.1063/1.368529>
- J.P. Boris, Relativistic plasma simulation-optimization of a hybrid code. in *Proceeding of Fourth Conference on Numerical Simulations of Plasmas* (1970)
- T. Brandt, R. Schneider, J. Duras, D. Kahnfeld, F.G. Hey, H. Kersten, F. Jansen, C. Braxmaier, Particle-in-cell simulation of a down-scaled hemp thruster. *Trans. Jpn. Soc. Aeronaut. Space Sci. Aerosp. Technol. Jpn.* **14**(ists30), 235–242 (2016). [https://doi.org/10.2322/tastj.14.Pb\\_235](https://doi.org/10.2322/tastj.14.Pb_235)
- F.X. Bronold, K. Matyash, D. Tskhakaya, R. Schneider, H. Fehske, Radio-frequency discharges in oxygen: I. particle-based modelling. *J. Phys. D Appl. Phys.* **40**(21), 6583 (2007). <https://doi.org/10.1088/0022-3727/40/21/018>
- O. Buneman, Time-reversible difference procedures. *J. Comput. Phys.* **1**(4), 517–535 (1967). [https://doi.org/10.1016/0021-9991\(67\)90056-3](https://doi.org/10.1016/0021-9991(67)90056-3)
- F. Chen, *Introduction to Plasma Physics and Controlled Fusion* (Springer, New York, 2015)
- R. Chodura, Plasma-wall transition in an oblique magnetic field. *Phys. Fluids* **25**(9), 1628 (1982). <https://doi.org/10.1063/1.863955>
- E.Y. Choueiri, Plasma oscillations in hall thrusters. *Phys. Plasmas* **8**(4), 1411–1426 (2001). <https://doi.org/10.1063/1.1354644>
- F. Cichocki, A. Domínguez, M. Merino, E. Ahedo, A 3d hybrid code to study electric thruster plumes. in *Proceedings of Space Propulsion Conference* (2016)
- F. Cichocki, A. Domínguez-Vázquez, M. Merino, E. Ahedo, Hybrid 3d model for the interaction of plasma thruster plumes with nearby objects. *Plasma Sources Sci. Technol.* **26**(12), 125008 (2017). <https://doi.org/10.1088/1361-6595/aa986e>
- L. Clarke, I. Glendinning, R. Hempel, The MPI message passing interface standard, in *Programming environments for massively parallel distributed systems*, ed. by K.M. Decker, R.M. Rehmman (Birkhäuser, Basel, 1994), pp. 213–218. [https://doi.org/10.1007/978-3-0348-8534-8\\_21](https://doi.org/10.1007/978-3-0348-8534-8_21)
- E.T. Dale, B.A. Jorns, Non-invasive characterization of the ionization region of a hall effect thruster. in *2018 Joint Propulsion Conference, AIAA Propulsion and Energy Forum, AIAA 2018-4508* (2018)
- E.T. Dale, B. Jorns, K. Hara, Numerical investigation of the stability criteria for the breathing mode in hall effect thrusters. in *Proceedings of the 35th International Electric Propulsion Conference, IEPC-2017-265* (2017)
- J.M. Dawson, One-dimensional plasma model. *Phys. Fluids* **5**(4), 445 (1962). <https://doi.org/10.1063/1.1706638>
- J.M. Dawson, Thermal relaxation in a one-species, one-dimensional plasma. *Phys. Fluids* **7**(3), 419 (1964). <https://doi.org/10.1063/1.1711214>
- J.W. Demmel, S.C. Eisenstat, J.R. Gilbert, X.S. Li, J.W.H. Liu, A supernodal approach to sparse partial pivoting. *SIAM J. Matrix Anal. Appl.* **20**(3), 720–755 (1999)
- S. Do, A. Owens, K. Ho, S. Schreiner, O. de Weck, An independent assessment of the technical feasibility of the mars one mission plan—updated analysis. *Acta Astronaut.* **120**, 192–228 (2016). <https://doi.org/10.1016/j.actaastro.2015.11.025>
- A. Dunaevsky, Y. Raitses, N.J. Fisch, Secondary electron emission from dielectric materials of a hall thruster with segmented electrodes. *Phys. Plasmas* **10**(6), 2574–2577 (2003). <https://doi.org/10.1063/1.1568344>
- J. Duras, D. Kahnfeld, G. Bandelow, S. Kemnitz, K. Luskow, P. Matthias, N. Koch, R. Schneider, Ion angular distribution simulation of the highly efficient multistage plasma thruster. *J. Plasma Phys.* (2017). <https://doi.org/10.1017/s0022377817000125>
- J. Duras, K. Matyash, D. Tskhakaya, O. Kalentev, R. Schneider, Self-force in 1d electrostatic particle-in-cell codes for nonequidistant grids. *Contrib. Plasma Phys.* **54**(8), 697–711 (2014). <https://doi.org/10.1002/ctpp.201300060>
- M. Evans, F. Harlow, E. Bromberg, The particle-in-cell method for hydrodynamic calculations (1957). <https://fas.org/sgp/othergov/oe/lanl/dtic/ADA384618.html>

- T. Fahey, A. Muffatti, H. Ogawa, High fidelity multi-objective design optimization of a downscaled cusped field thruster. *Aerospace* **4**(4), 55 (2017). <https://doi.org/10.3390/aerospace4040055>
- G. Fubiani, L. Garrigues, G. Hagelaar, N. Kohen, J. Boeuf, Modeling of plasma transport and negative ion extraction in a magnetized radio-frequency plasma source. *New J. Phys.* **19**(1), 015002 (2017). <https://doi.org/10.1088/1367-2630/19/1/015002>
- M. Gamero-Castaño, I. Katz, Estimation of hall thruster erosion using hphall. in *Proceedings of the 29th International Electric Propulsion Conference, IEPC-2005-297* (2005)
- N. Gascon, M. Dudeck, S. Barral, Wall material effects in stationary plasma thrusters. i. parametric studies of an spt-100. *Phys. Plasmas* **10**(10), 4123–4136 (2003). <https://doi.org/10.1063/1.1611880>
- A. Genovese, A. Lazurenko, N. Koch, S.e.a. Weis, Endurance testing of hempt-based ion propulsion modules for smallgeo. in *Proceedings of the 32nd International Electric Propulsion Conference, IEPC-2011-141* (2011)
- D.M. Goebel, I. Katz, *Fundamentals of Electric Propulsion: Ion and Hall Thrusters* (Wiley, Hoboken, 2008)
- R. Gopal, N. BenAmmar, Framework for unifying 5g and next generation satellite communications. *IEEE Netw.* **32**(5), 16–24 (2018). <https://doi.org/10.1109/MNET.2018.1800045>
- K. Hara, M.J. Sekerak, I.D. Boyd, A.D. Gallimore, Mode transition of a hall thruster discharge plasma. *J. Appl. Phys.* **115**(20), 203304 (2014). <https://doi.org/10.1063/1.4879896>
- K. Hara, M.J. Sekerak, I.D. Boyd, A.D. Gallimore, Perturbation analysis of ionization oscillations in hall effect thrusters. *Phys. Plasmas* **21**(12), 122103 (2014). <https://doi.org/10.1063/1.4903843>
- K. Hara, I.D. Boyd, M.J. Sekerak, A.D. Gallimore, Breathing mode in hall effect thrusters. in *Joint Conference of 30th ISTS, 34th IEPC and 6th NSAT, IEPC-2015-283/ISTS-2015-b-283* (2015)
- F.H. Harlow, Hydrodynamic problems involving large fluid distortions. *J. ACM* **4**(2), 137–142 (1957). <https://doi.org/10.1145/320868.320871>
- M. Hayashi, Bibliography of electron and photon cross sections with atoms and molecules published in the 20th century - xenon. Tech. Rep. NIFS-DATA-79, NIFS (2003). <http://www.nifs.ac.jp/report/NIFS-DATA-079.pdf>. Accessed 3 Dec 2018
- F.G. Hey, T. Brandt, G. Kornfeld, C.e.a. Braxmaier, Downscaling a hempt to micro-newton thrust levels: current status and latest results. in *The 34th International Electric Propulsion Conference, IEPC-2013-377* (2015)
- R.W. Hockney, Computer experiment of anomalous diffusion. *Phys. Fluids* **9**(9), 1826 (1966). <https://doi.org/10.1063/1.1761939>
- R. Hockney, *Computer Simulation Using Particles* (Routledge, Abingdon, 1989)
- G.S. Janes, Anomalous electron diffusion and ion acceleration in a low-density plasma. *Phys. Fluids* **9**(6), 1115 (1966). <https://doi.org/10.1063/1.1761810>
- D. Kahnfeld, R. Heidemann, J. Duras, P. Matthias, G. Bandelow, K. Luskow, S. Kemnitz, K. Matyash, R. Schneider, Breathing modes in hempt thrusters. *Plasma Sources Sci. Technol.* **27**(12), 124002 (2018). <https://doi.org/10.1088/1361-6595/aaf29a>
- D. Kahnfeld, R. Schneider, K. Matyash, S. Kemnitz, J. Duras, K. Luskow, G. Bandelow, Solution of poisson's equation in electrostatic particle-in-cell simulations. *Plasma Phys. Technol.* **3**, 66–71 (2016)
- D. Kahnfeld, R. Schneider, F. Cichocki, M. Merino, E. Ahedo, J. Duras, N. Koch, Hempt thruster discharge and plume simulation with a 2d3v-pic-mcc and a 3d hybrid fluid-pic code. in *The 35th International Electric Propulsion Conference, IEPC-2017-309* (2017)
- O. Kalentev, K. Matyash, J. Duras, K.F. Luskow, R.E. Schneider, N. Koch, M. Schirra, Electrostatic ion thrusters—towards predictive modeling. *Contrib. Plasma Phys.* **54**(2), 235–248 (2014). <https://doi.org/10.1002/ctpp.201300038>
- A. Keller, P. Köhler, W. Gärtner, B. Lotz, D.e.a. Feili, Feasibility of a down-scaled hempt-thruster. in *The 32nd International Electric Propulsion Conference, IEPC-2011-138* (2011)
- A. Keller, P. Köhler, F.G. Hey, M. Berger, C.e.a. Braxmaier, Parametric study of hempt-thruster, downscaling to  $\mu$ n thrust levels. in *The 33rd International Electric Propulsion Conference, IEPC-2013-269* (2013)
- V. Kim, G. Popov, B. Arkhipov, V.e.a. Murashko, Electric propulsion activity in russia. in *Proceedings of the 27th International Electric Propulsion Conference, IEPC-2001-005* (2001)
- N. Kishi, Management analysis for the space industry. *Space Policy* **39–40**, 1–6 (2017). <https://doi.org/10.1016/j.spacepol.2017.03.006>
- N. Koch, J. Duras, D. Kahnfeld, P.e.a. Matthias, Particle-in-cell simulation of a hempt thruster digital prototype optimized for future satellite applications. in *Proceedings of the 35th International Electric Propulsion Conference, IEPC-2017-329* (2017)

- N. Koch, H.P. Harmann, G. Kornfeld, Development & test status of the thales high efficiency multistage plasma (hemp) thruster family. in *Proceedings of the 29th International Electric Propulsion Conference, IEPC-2005-297* (2005)
- N. Koch, H.P. Harmann, G. Kornfeld, Status of the thales high efficiency multi stage plasma thruster development for hemp-t 3050 and hemp-t 30250. in *Proceedings of the 30th International Electric Propulsion Conference, IEPC-2007-110* (2007)
- N. Koch, M. Schirra, S. Weis, A. Lazurenko, B. van Reijen, J. Haderspeck, A. Genovese, P. Holtmann, R. Schneider, K. Matyash, et al.: The hemp-t concept—a survey on theoretical considerations and experimental evidences. in *Proceedings of the 32nd International Electric Propulsion Conference, IEPC-2011-236* (2011)
- N. Koch, S. Weis, M. Schirra, A.e.a. Lazurenko, Development, qualification and delivery status of the hemp based ion propulsion system for smallgeo. in *Proceedings of the 32nd International Electric Propulsion Conference, IEPC-2011-148* (2011)
- G. Kornfeld, N. Koch, G. Coustou, First test results of the hemp thruster concept. in *The 28th International Electric Propulsion Conference, IEPC-2003-212* (2003)
- G. Kornfeld, N. Koch, H.P. Harmann, Physics and evolution of hemp thrusters. in *The 30th International Electric Propulsion Conference, IEPC-2007-108* (2007)
- G. Kornfeld, H. Seidel, J. Wegener, Plasma accelerator arrangement, U.S. Patent, number 198 28 704.6, 26 June 1998. <https://register.dpma.de/DPMAREGISTER/pat/register?AKZ=198287046>
- G. Kornfeld, H. Seidel, J. Wegener, Plasma accelerator arrangement, U.S. Patent, number PCT/DE99/01708, 11 June 1999. <https://patentscope.wipo.int/search/en/detail.jsf?docId=WO2000001206>
- J. Lacina, Similarity rules in plasma physics. *Plasma Phys.* **13**(4), 303–312 (1971). <https://doi.org/10.1088/0032-1028/13/4/003>
- B. Lal, E. de la Rosa Blanco, J.A. Behrens, B.A. Corbin, E.K. Green, A.J. Picard, A. Balakrishnan, *Global Trends in Small Satellites* (Science & Technology Policy Institute, Washington, D.C., 2017)
- A. Langdon, Effects of the spatial grid in simulation plasmas. *J. Comput. Phys.* **6**(2), 247–267 (1970). [https://doi.org/10.1016/0021-9991\(70\)90024-0](https://doi.org/10.1016/0021-9991(70)90024-0)
- A.B. Langdon, Theory of plasma simulation using finite-size particles. *Phys. Fluids* **13**(8), 2115 (1970). <https://doi.org/10.1063/1.1693209>
- A. Lazurenko, A. Genovese, R. Heidemann, J.e.a. Haderspeck, Qualification test results of hemp thruster modules. in *The 34th International Electric Propulsion Conference, IEPC-2015-347* (2015)
- A. Lazurenko, B. van Reijen, N. Koch, S.e.a. Weist, Overview on testing infrastructures and diagnostic tools for hemp based ion propulsion systems. in *The 32nd International Electric Propulsion Conference, IEPC-2011-146* (2011)
- I. Levchenko, K. Bazaka, T. Belmonte, M. Keidar, S. Xu, Advanced materials for next-generation spacecraft. *Adv. Mater.* **30**(50), 1802201 (2018a). <https://doi.org/10.1002/adma.201802201>
- I. Levchenko, K. Bazaka, Y. Ding, Y. Raitses, S. Mazouffre, T. Henning, P.J. Klar, S. Shinohara, J. Schein, L. Garrigues, M. Kim, D. Lev, F. Taccogna, R.W. Boswell, C. Charles, H. Koizumi, Y. Shen, C. Scharlemann, M. Keidar, S. Xu, Space micropropulsion systems for cubesats and small satellites: From proximate targets to furthestmost frontiers. *Appl. Phys. Rev.* **5**(1), 011104 (2018b). <https://doi.org/10.1063/1.5007734>
- I. Levchenko, M. Keidar, J. Cantrell, Y.L. Wu, H. Kuninaka, K. Bazaka, S. Xu, Explore space using swarms of tiny satellites. *Nature* **562**(7726), 185–187 (2018c). <https://doi.org/10.1038/d41586-018-06957-2>
- I. Levchenko, S. Xu, S. Mazouffre, M. Keidar, K. Bazaka, Mars colonization: beyond getting there. *Global Chall.* **3**(1), 1800062 (2018d). <https://doi.org/10.1002/gch2.201800062>
- I. Levchenko, S. Xu, G. Teel, D. Mariotti, M.L.R. Walker, M. Keidar, Recent progress and perspectives of space electric propulsion systems based on smart nanomaterials. *Nat. Commun.* (2018). <https://doi.org/10.1038/s41467-017-02269-7>
- D. Lev, R.M. Myers, K.M.e.a. Lemmer, The technological and commercial expansion of electric propulsion in the past 24 years. in *Proceedings of the 35th International Electric Propulsion Conference, IEPC-2017-242* (2017)
- X.S. Li, An overview of SuperLU: algorithms, implementation, and user interface. *ACM Trans. Math. Softw.* **31**, 302–325 (2005)
- X. Li, J. Demmel, J. Gilbert, iL. Grigori, M. Shao, I. Yamazaki, SuperLU Users' Guide. Tech. Rep. LBNL-44289, Lawrence Berkeley National Laboratory (1999). <http://crd.lbl.gov/~xiaoye/SuperLU/>. Last update: August 2011. Accessed 23 Nov 2018

- Y.H. Lin, P. Pattanasattayavong, T.D. Anthopoulos, Metal-halide perovskite transistors for printed electronics: challenges and opportunities. *Adv. Mater.* **29**(46), 1702838 (2017). <https://doi.org/10.1002/adma.201702838>
- R.G. Littlejohn, Variational principles of guiding centre motion. *J. Plasma Phys.* **29**(1), 111 (1983). <https://doi.org/10.1017/s002237780000060x>
- R.B. Lobbia, A.D. Gallimore, Two-dimensional time-resolved breathing mode plasma fluctuation variation with hall thruster discharge settings. in *The 31st International Electric Propulsion Conference, IEPC-2009-106* (2009)
- R.B. Lobbia, M.J. Sekerak, R. Liang, A.D. Gallimore, High-speed dual langmuir probe measurements of the plasma properties and eedfs in a het plume. in *The 32nd International Electric Propulsion Conference, IEPC-2011-168* (2011)
- R.G. Littlejohn, Linear relativistic gyrokinetic equation. *Phys. Fluids* **27**(4), 976 (1984). <https://doi.org/10.1063/1.864688>
- K.F. Luskow, S. Kemnitz, G. Bandelow, J. Duras, D. Kahnfeld, P. Matthias, R. Schneider, D. Konigorski, Electrostatic particle-in-cell simulation of heat flux mitigation using magnetic fields. *J. Plasma Phys.* (2016). <https://doi.org/10.1017/s0022377816000829>
- P. Matthias, G. Bandelow, K. Matyash, J. Duras, P. Hacker, D. Kahnfeld, S. Kemnitz, L. Lewerentz, K.F. Luskow, J. Meichsner, R. Schneider, Pic simulations of capacitively coupled oxygen rf discharges. *Eur. Phys. J. D* **72**(5), 86 (2018). <https://doi.org/10.1140/epjd/e2017-80565-y>
- P. Matthias, D. Kahnfeld, R. Schneider, S.H. Yeo, H. Ogawa, Particle-in-cell simulation of an optimized High Efficiency Multistage Plasma Thruster. *Contrib. Plasma Phys.* (2019). <https://doi.org/10.1002/ctpp.201900028>
- K. Matyash, Kinetic modeling of multi-component edge plasmas. Ph.D. thesis, University of Greifswald (2003)
- K. Matyash, M. Fröhlich, H. Kersten, G. Thieme, R. Schneider, M. Hannemann, R. Hippler, Rotating dust ring in an rf discharge coupled with a dc-magnetron sputter source. experiment and simulation. *J. Phys. D Appl. Phys.* **37**(19), 2703–2708 (2004). <https://doi.org/10.1088/0022-3727/37/19/013>
- K. Matyash, O. Kalentev, R. Schneider, F. Taccogna, N. Koch, M. Schirra, Kinetic simulation of the stationary hemp thruster including the near-field plume region. in *Proceedings of the 31st International Electric Propulsion Conference, IEPC-2009-110* (2009)
- K. Matyash, R. Schneider, Finite size effects on charging in dusty plasmas. *J. Plasma Phys.* **72**(6), 809 (2006). <https://doi.org/10.1017/s0022377806004910>
- K. Matyash, R. Schneider, X. Bonnin, D. Coster, V. Rohde, H. Kersten, Modeling of parasitic plasma under the divertor roof baffle. *J. Nuclear Mater.* **337–339**, 237–240 (2005). <https://doi.org/10.1016/j.jnucmat.2004.10.113>
- K. Matyash, R. Schneider, A. Mutzke, O. Kalentev, F. Taccogna, N. Koch, M. Schirra, Kinetic simulations of spt and hemp thrusters including the near-field plume region. *IEEE Trans. Plasma Sci.* **38**(9), 2274–2280 (2010). <https://doi.org/10.1109/TPS.2010.2056936>
- K. Matyash, R. Schneider, A. Mutzke, O. Kalentev, F. Taccogna, N. Koch, M. Schirra, Comparison of spt and hemp thruster concepts from kinetic simulations. in *Proceedings of the 31st International Electric Propulsion Conference, IEPC-2009-159* (2009)
- D. Meeker, Finite element method magnetics, v4.2 (2017). <http://www.femm.info>. Accessed 1 Mar 2017
- R.L. Morse, Numerical simulation of warm two-beam plasma. *Phys. Fluids* **12**(11), 2418 (1969). <https://doi.org/10.1063/1.1692361>
- J. Polk, R. Yakuda, D. Brinza, I. Katz, J.e.a. Anderson, Demonstration of the nstar ion propulsion system on the deep space one mission. in *Proceedings of the 27th International Electric Propulsion Conference, IEPC-2001-075* (2001)
- H. Qin, S. Zhang, J. Xiao, J. Liu, Y. Sun, W.M. Tang, Why is boris algorithm so good? *Phys. Plasmas* **20**(8), 84503 (2013). <https://doi.org/10.1063/1.4818428>
- Y. Raitses, A. Smirnov, D. Staack, N.J. Fisch, Measurements of secondary electron emission effects in the hall thruster discharge. *Phys. Plasmas* **13**(1), 14502 (2006). <https://doi.org/10.1063/1.2162809>
- B. Reid, A. Gallimore, Langmuir probe measurements in the discharge channel of a 6-kw hall thruster. in *44th AIAA/ASME/SAE/ASEE Joint Propulsion Conference & Exhibit. American Institute of Aeronautics and Astronautics* (2008). <https://doi.org/10.2514/6.2008-4920>
- K. Reinmüller, Determination of the plasma potential using emissive probes—implications from pic simulations. *Contrib. Plasma Phys.* **38**(S1), 7–12 (1998). <https://doi.org/10.1002/ctpp.19980380106>

- I. Romadanov, Y. Raitses, A. Diallo, K. Hara, I.D. Kaganovich, A. Smolyakov, On limitations of laser-induced fluorescence diagnostics for xenon ion velocity distribution function measurements in hall thrusters. *Phys. Plasmas* **25**(3), 033501 (2018). <https://doi.org/10.1063/1.5020749>
- E. Seedhouse, *SpaceX: Making Commercial Spaceflight a Reality* (Springer Praxis Books, New York, 2013)
- M.J. Sekerak, A.D. Gallimore, D.L. Brown, R.R. Hofer, J.E. Polk, Mode transitions in hall-effect thrusters induced by variable magnetic field strength. *J. Propuls. Power* **32**(4), 903–917 (2016). <https://doi.org/10.2514/1.B35709>
- J. Spilker Jr., *Digital Communication by Satellite* (Prentice Hall PTR, Upper Saddle River, 1977)
- J.J. Spilker Jr., P. Axelrad, B.W. Parkinson, P. Enge, Overview of gps operation and design, in *Global Positioning System: Theory and Applications, Volume I, Progress in Astronautics and Aeronautics*, (American Institute of Aeronautics and Astronautics, DO, 1996), pp. 29–55. <https://doi.org/10.2514/5.9781600866388.0029.0055.0>
- J. Stoer, *Numerische Mathematik I*, 9th edn. (Springer Verlag, New York, 2005)
- F. Taccogna, S. Longo, M. Capitelli, R. Schneider, Particle-in-cell simulation of stationary plasma thruster. *Contrib. Plasma Phys.* **47**(8–9), 635–656 (2007). <https://doi.org/10.1002/ctpp.200710074>
- T. Takizuka, H. Abe, A binary collision model for plasma simulation with a particle code. *J. Comput. Phys.* **25**(3), 205–219 (1977)
- D. Tskhakaya, S. Kuhn, Y. Tomita, K. Matyash, R. Schneider, F. Taccogna, Self-consistent simulations of the plasma-wall transition layer. *Contrib. Plasma Phys.* **48**(1–3), 121–125 (2008). <https://doi.org/10.1002/ctpp.200810021>
- D. Tskhakaya, K. Matyash, R. Schneider, F. Taccogna, The particle-in-cell method. *Contrib. Plasma Phys.* **47**(8–9), 563–594 (2007)
- H. Ueda, Y. Omura, H. Matsumoto, T. Okuzawa, A study of the numerical heating in electrostatic particle simulations. *Comput. Phys. Commun.* **79**(2), 249–259 (1994). [https://doi.org/10.1016/0010-4655\(94\)90071-x](https://doi.org/10.1016/0010-4655(94)90071-x)
- V. Vahedi, G. DiPeso, C.K. Birdsall, M.A. Lieberman, T.D. Rognlien, Capacitive RF Discharges modelled by Particle-In-Cell Monte Carlo simulation. I. Analysis of numerical techniques. *Plasma Sour. Sci. Technol.* **2**(4), 261 (1993). <https://doi.org/10.1088/0963-0252/2/4/006>
- S. Weis, N. Koch, M. Schirra, A. Lazurenko, B. van Reijen, J.e.a. Haderspeck, Architecture, functional features and operational characteristics of the hempt based ion propulsion system for smallgeo. in *The 32nd International Electric Propulsion Conference, IEPC-2011-223* (2011)
- S. Weis, A. Lazurenko, A. Genovese, R. Heidemann, P. Holtmann, H. Stalzer, N. Püttmann, T. Wolf, B. Wollenhaupt, Overview, qualification and delivery status of the hempt-thruster based ion propulsion system for smallgeo. in *The 35th International Electric Propulsion Conference, IEPC-2017-197* (2017)
- S. Weis, A. Lazurenko, B. van Reijen, J.e.a. Haderspeck, Overview, qualification and delivery status of the hempt based ion propulsion system for smallgeo. in *The 33rd International Electric Propulsion Conference, IEPC-2013-299* (2013)
- S. Weis, A. Lazurenko, B. van Reijen, J.e.a. Haderspeck, Overview, qualification and delivery status of the hempt based ion propulsion system for smallgeo. in *The 34th International Electric Propulsion Conference, IEPC-2015-345* (2015)
- J.R. Wertz, W. Larson (eds.), *Reducing Space Mission Cost* (Springer, New York, 1996)
- A. Yalin, B. Rubin, S. Domingue, Z. Glueckert, J. Williams, Differential sputter yields of boron nitride, quartz, and kapton due to low energy xe+ bombardment. in *43rd AIAA/ASME/SAE/ASEE Joint Propulsion Conference & Exhibit. American Institute of Aeronautics and Astronautics* (2007). <https://doi.org/10.2514/6.2007-5314>
- N. Yamamoto, K. Komurasaki, Y. Arakawa, Discharge current oscillation in hall thrusters. *J. Propuls. Power* **21**(5), 870–876 (2005). <https://doi.org/10.2514/1.12759>
- S.H. Yeo, T. Fahey, H. Ogawa, A. Muffatti, P. Matthias, D. Kahnfeld, N.M. Padivattathumana, R. Schneider, Multi-objective optimization and particle-in-cell simulation of cusped field thruster for micro-satellites platform. in *AIAA Scitech 2019 Forum. American Institute of Aeronautics and Astronautics* (2019). <https://doi.org/10.2514/6.2019-1245>
- J.T. Yim, M.L. Falk, I.D. Boyd, Modeling low energy sputtering of hexagonal boron nitride by xenon ions. *J. Appl. Phys.* **104**(12), 123507 (2008). <https://doi.org/10.1063/1.2987090>

**Publisher's Note** Springer Nature remains neutral with regard to jurisdictional claims in published maps and institutional affiliations.

## Affiliations

Daniel Kahnfeld<sup>1</sup>  · Julia Duras<sup>2</sup> · Paul Matthias<sup>1</sup> · Stefan Kemnitz<sup>3</sup> · Peter Arlinghaus<sup>4</sup> · Gunnar Bandelow<sup>1</sup> · Konstantin Matyash<sup>3</sup> · Norbert Koch<sup>5</sup> · Ralf Schneider<sup>1,3</sup>

✉ Daniel Kahnfeld  
kahnfeldd@uni-greifswald.de

- <sup>1</sup> Institute of Physics, University of Greifswald, Felix-Hausdorff-Str. 6, 17489 Greifswald, Germany
- <sup>2</sup> Department Application Software, German Climate Computing Centre, 20146 Hamburg, Germany
- <sup>3</sup> Computing Centre, University of Greifswald, Felix-Hausdorff-Str. 12, 17489 Greifswald, Germany
- <sup>4</sup> Institute of Coastal Research, Helmholtz-Zentrum Geesthacht, Max-Planck-Str. 1, 21502 Geesthacht, Germany
- <sup>5</sup> Department of Applied Mathematics, Physics and Humanities, Nuremberg Institute of Technology, 90489 Nuremberg, Germany

# Breathing modes in HEMP thrusters

D Kahnfeld<sup>1</sup> , R Heidemann<sup>2</sup>, J Duras<sup>1</sup>, P Matthias<sup>1</sup>, G Bandelow<sup>1</sup>,  
K Luskow<sup>1</sup>, S Kemnitz<sup>3</sup>, K Matyash<sup>3</sup>  and R Schneider<sup>1,3</sup>

<sup>1</sup>Institute of Physics, University of Greifswald, Felix-Hausdorff-Str. 6, D-17491 Greifswald, Germany

<sup>2</sup>Thales Deutschland GmbH, Söflinger Str. 100, D-89077 Ulm, Germany

<sup>3</sup>Computing Centre, University of Greifswald, Felix-Hausdorff-Str. 12, D-17491 Greifswald, Germany

E-mail: [kahnfeld@uni-greifswald.de](mailto:kahnfeld@uni-greifswald.de)

Received 30 June 2018, revised 25 October 2018

Accepted for publication 21 November 2018

Published 24 December 2018



CrossMark

## Abstract

HEMP thrusters develop breathing mode oscillations with frequencies in the 100 kHz range during stable operation in test facilities. The mechanism of those oscillations in the HEMP-T DM3a model, developed by Thales Deutschland GmbH, is investigated using a fully kinetic PIC-MCC simulation model. The formation and time evolution of a breathing mode are discussed. The consequences for stable thruster operation are outlined and the oscillation frequency is compared to a 0D predator–prey oscillation frequency estimate. A comparison with an experimental discharge current measurement of a breathing mode is discussed.

Keywords: electric propulsion, HEMP-T, particle-in-cell, PIC, plasma simulation, breathing mode, plasma instability

## 1. Physics of breathing mode oscillations

Breathing mode oscillations are plasma instabilities observed during operation of a variety of electric propulsion devices. In Hall-effect thrusters (HETs), they have been well investigated experimentally [1–7] and theoretically [8–16]. The leading theory is that these oscillations originate from the coupled dynamics of neutrals and plasma particles, triggered by high ionization within the discharge channel. They result in oscillatory behaviours of plasma density, neutral density, and ionization fronts, with frequencies in the range of 10–30 kHz, determined by the dynamics of the neutrals, which are ionized locally and then repopulate that region. Notably, the instability can be observed in the discharge current, where oscillation amplitudes can range from 10% up to 100% of the mean current, depending on discharge parameters and thruster geometry. In HETs, they are the largest oscillations and play an important role in stable thruster operation [1].

For a better understanding of the fluctuation mechanisms, numerical simulations can be used. The most simple breathing mode simulation model is a 0D fluid model combined with a predator–prey ansatz, as published in [10, 15]. Using that interpretation, an imbalance between the replenishment and ionization of neutrals, with electrons/ions acting as predators and neutrals as prey, forms the breathing mode in the area of the ionization front. The frequency of the oscillation is determined by the flight time of neutrals for replenishment

within the oscillation area. With a first-order perturbation ansatz, the frequency estimate [15] is obtained in the form of

$$\omega = \frac{(u_i u_0)^{1/2}}{L} \quad (1)$$

with ion and neutral velocities  $u_i$  and  $u_0$ , respectively.  $L$  is the characteristic length scale of the oscillation of the ionization front. This model assumes constant electron temperature, neglecting its influence on ionization rates during the oscillation, as suggested in [13]. The frequency predictions of these models agree well with experimental data [15], but recent experimental measurements revealed that such a 0D model is unrealistic for real HETs [6].

Similar to HETs, high-efficiency multistage plasma (HEMP) thrusters also form breathing mode oscillations during stable operation, but in a frequency range of 100 kHz to 500 kHz, with an amplitude modulation of the discharge current of up to 30% [17]. Experimental and theoretical investigations of the instability in HEMP-like thruster models is so far largely missing.

In this work, the breathing oscillations in the HEMP-T model DM3a are investigated, using a self-consistent, fully kinetic 2D3v particle-in-cell (PIC) simulation. Firstly, the basic concept of the HEMP-T is introduced. Then, a description of the simulation used to model the plasma discharge in the ion thruster is given. The results will characterize the plasma and neutral distribution within the system.

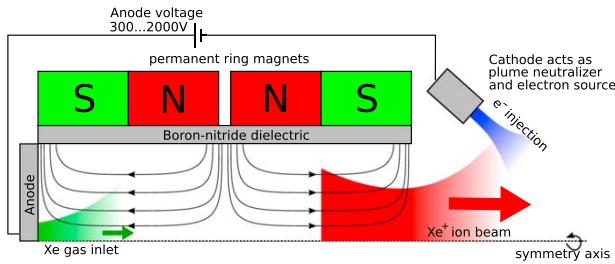


Figure 1. Sketch of a HEMP-T.

Afterwards, the focus will be on the influence of the breathing mode oscillations on the discharge. A frequency estimate of the instability is presented, and the influence on the discharge parameters, such as discharge and ion beam currents, thrust, and the ion emission angle, is discussed. The resulting discharge current from the simulation is compared to an experimental measurement of such an oscillation. The spatial distribution of electron-neutral excitation collisions is also discussed. This is an important quantity, to be directly compared with visual experimental observations of radiation emission from the thruster. Finally, a summary and an outlook on further work are given.

## 2. HEMP thruster

The high-efficiency multistage plasma thruster (HEMP-T) was developed by Thales Deutschland GmbH in the early 2000s; a sketch of the system is shown in figure 1. It is a gridless thruster concept consisting of a discharge channel coated with a dielectric material that has a high sputtering threshold, such as boron nitride, and a metal anode with a neutral gas inlet at the channel bottom. Several ring magnets, with pairwise opposite magnetization directions, impose a magnetic field structure inside the discharge channel that is characterized by a flat magnetic field near the channel axis and magnetic cusps at the interface of the ring magnets. In the regions with a flat magnetic field, the magnetic flux density reaches up to 0.4 T, while it is zero at the cusps near the symmetry axis. The detailed magnetic field structure has been patented by Thales Deutschland GmbH. Electrons are injected by a cathode neutralizer outside the thruster and are accelerated into the discharge channel by the electric field building up from the positive anode and plasma potential. Inside the channel, electrons are magnetized, with strong electron transport parallel to the symmetry axis due to an axial magnetic field in between the cusps. This results in a flat electrostatic potential inside the discharge channel. At the cusps, with a radial magnetic field, electrons are reflected and heated, with minimal wall losses. This leads to good trapping of electrons and thus results in high ionization rates. As a result, the electron distribution is non-Maxwellian, with a high energy tail that is responsible for ionization in the discharge channel [28]. Ions are non-magnetized and follow the

electron dynamics in the channel, again with the wall contact of high-energy ions limited to the cusp regions, but with energies below the sputtering threshold. Acceleration of ions occurs only in the exit region, where the plasma potential drops to vacuum potential, generating thrust. In the HEMP-T, wall losses and sputtering erosion are minimized, while reliably providing specific impulses of more than 2000 s with thrust in the range of 1–100 mN, making the concept attractive for long-term space missions [18].

Xenon is commonly used as the propellant and will be considered in this work. It is injected with influx rates in the range of 1–100 sccm at the anode. Anode voltages vary between 100 V and 1000 V. A neutralizer is placed at the thruster exit. Beside its main task of neutralizing the plume, it also provides electrons to ignite the channel plasma and compensate discharge losses. These electrons are accelerated into the discharge channel and ionize the neutral gas, with the dominant charge contribution being by singly- and doubly-charged xenon ions ( $\text{Xe}^+$ ,  $\text{Xe}^{2+}$ ). The magnetic field is strong enough for electrons to be magnetized, while ions are mostly unaffected by the magnetic field. Its structure leads to good electron confinement while reducing plasma-wall contact to the magnetic cusp regions. Most electrons entering a cusp are reflected at the magnetic mirror, and heated due to the combination of mirroring and sheath interaction. The resulting potential structure is flat at anode voltage and the drop to vacuum potential occurs at the thruster exit. Here, ions are accelerated, generating thrust in the range of 1–100 mN, depending on the propellant flux and the thruster model.

In this work, the HEMP-T DM3a model is simulated for the study of the breathing oscillations. It has a channel radius of 9.2 mm and a channel length of 51.1 mm. It also features a thin metal plate at the thruster exit. More information on HEMP thrusters and the DM3a model can be found in [19–21].

Similarly to HETs, HEMP-Ts develop breathing mode oscillations during stable operation, with frequencies in the range of 100 kHz to 500 kHz [17]. Through numerical modeling, the understanding of the physics of the instability and its implications on thruster performance are investigated.

## 3. Simulation model

In the simulation model, the entire thruster discharge channel and part of the near-field plume are considered; a sketch of the simulation domain is shown in figure 2. Since the mean-free paths of electrons are comparable to the system size and their distribution is non-Maxwellian, a fully kinetic simulation model is necessary [28]. Therefore, a PIC model is used in combination with a Monte Carlo collision (MCC) model [23]. The dynamics of neutral propellant atoms (Xe), electrons ( $e^-$ ), and  $\text{Xe}^+$  and  $\text{Xe}^{2+}$  ions are followed as super-particles. Early mass spectroscopy measurements of the ion beam emitted by the HEMP-T DM3a model have shown that  $\text{Xe}^+$  and  $\text{Xe}^{2+}$  ions contribute about 90% and 10%, respectively,

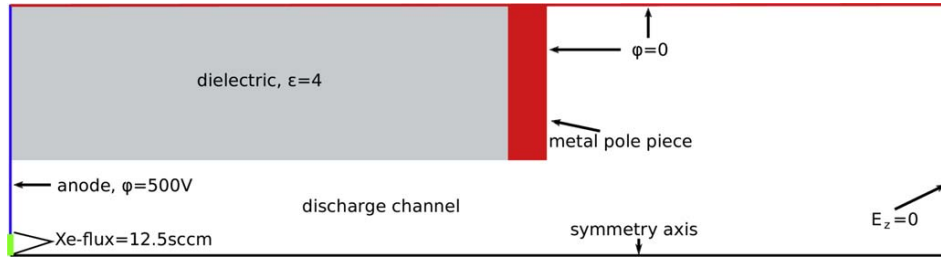


**Figure 2.** Sketch of the simulation domain and boundary conditions used for this work.

to the emitted ion counts [18]. Higher charge states contribute less than 1% combined, and are therefore neglected in the simulation.

In the MCC model, the super-particles of each species are collided in a cell using a binary collision approximation. Electron–electron Coulomb collisions are simulated directly, using the Takizuka–Abe algorithm [24], while other collisions are performed as a series of one or more binary collisions using experimentally measured collision cross-sections [25]. Detailed information on the collision algorithms can be found in [26, 27]. Thus, the simulation includes direct single and double  $e^-$ -Xe impact ionization, single  $e^-$ -Xe<sup>+</sup> impact ionization, integral elastic Xe<sup>+</sup>-Xe collisions (including charge exchange and momentum transfer), as well as integral elastic and inelastic  $e^-$ -Xe collisions. Since the thruster is axisymmetric, the simulation domain is reduced to a 2D axisymmetric  $r$ - $z$ -plane, while the velocity space is 3D to ensure energy conservation for the collisions [28].

An electrostatic model is used, since the magnetic field contribution from the plasma currents can be neglected. Poisson’s equation is solved on the mesh points of the cell grid, using a finite difference scheme [29], with a cloud-in-cell algorithm for weighting of particle densities and forces, respectively [23]. At the symmetry axis, the radial electric field tends to zero in the limit  $r \rightarrow 0$ . By using L’Hôpital’s rule, this leads to a special discretization scheme at the axis, resulting in radial symmetry of the electrostatic potential [29]. At the left boundary of the simulation domain, a constant potential boundary condition at anode voltage is applied. The top boundary is at ground potential, and at the right boundary the axial electric field is zero. The dielectric permittivity is set to  $\epsilon = 4$  for boron nitride and the metal plate at the thruster exit is grounded. The boundary condition for the normal electric field at the dielectric–plasma interface is automatically fulfilled by the discretization scheme and does not need to be implemented additionally.

Regarding the particle boundary conditions, the top and right domain boundaries represent vacuum boundary conditions. Hence, all particles leaving the domain are removed from the system. For thrust measurement, the ion energies are corrected by the residual potential at the right domain boundary. At the anode and dielectric, electrons are removed with a secondary electron emission coefficient of 0.5 at the dielectric. All incident neutrals are reflected thermally with a temperature of 0.04 eV, and all incident ions recycle into neutrals and are reflected with the same energy as neutrals.

To make the simulation of the system feasible, similarity scaling is used. This scheme is designed to leave unchanged the physical behaviour within the thruster channel (where electrons are magnetized). Therefore, the ratio of the Hall parameter and Knudsen number is kept constant, preserving the length of electron gyro motion and collision mean free paths relative to the system size. As a result, system size and time are scaled down, while magnetic flux density and collision cross-sections are linearly scaled up. Particle velocities and number densities remain unscaled. In a plasma regime where electrons are magnetized, the application of this similarity scaling is limited by an increase in the ratio of the plasma–wall sheath thickness to plasma bulk volume, which is not conserved. However, as long as the influence of wall processes is small, even high similarity scaling factors can be applied. In regions with a weak magnetic field, e.g. the plume, the assumptions of the similarity scaling fail and quasi-neutrality can be violated [30]. A more detailed description of similarity scaling schemes can be found in [29, 31, 32].

Electron injection is implemented in the model by an electron source, using a feedback control. The feedback control increases the injection current when plasma density decreases, and vice versa, with a target density of  $10^{13} \text{ cm}^{-3}$ . A similar control is used in the experiment, where the neutral flux is controlled to keep the discharge power (and therefore the anode current) constant. Since controlling neutral flux is impractical in the simulation due to the very long neutral transit times, electron injection is controlled in order to reach a constant mode of operation. Such an injection scheme leads to fluctuations of the injected current, exciting all modes in the plasma. The main mode is then amplified out of the broad excitation spectrum and adjusts itself self-consistently. This results in an observable breathing oscillation, as discussed in the results. The source is located near the axis in the ranges of  $z \in [85 \text{ mm}, 87 \text{ mm}]$  and  $r \in [0 \text{ mm}, 20 \text{ mm}]$ . The base injection current is 0.3 mA and increases to 4.2 mA during the running time of the simulation.

For the simulation, a time step of  $\Delta t = 1.12 \cdot 10^{-12} \text{ s}$  and a cell unit length of  $\Delta r = 1 \cdot 10^{-2} \text{ mm}$  are used. The discharge channel is 51.14 mm long, with a radius of 9.2 mm. The dimensions of the simulation plane are 24.4 mm  $\times$  90.0 mm, with a similarity scaling factor of 10. This results in a simulation domain of 244  $\times$  900 cells. The super-particle factor is  $1.05 \cdot 10^4$ , and six super-particles are necessary to represent the target density of  $10^{19} \text{ m}^{-3}$  at the symmetry axis. Due to the increase in cell volume with

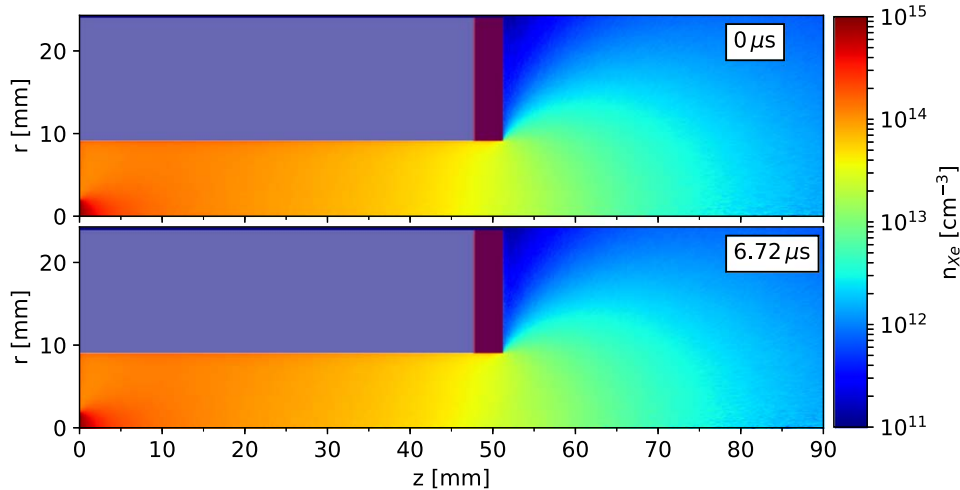


**Figure 3.** Neutral Xe densities at the minimum ( $t = 0 \mu\text{s}$ ) and maximum ( $t = 6.72 \mu\text{s}$ ) of the oscillation. The dielectric wall (white) and metal plate (red) are indicated.

increasing radius, the necessary number increases linearly, e.g. to 552 at the channel wall. This results in about  $10^6$  simulated super-particles for the charged species, and about  $1.4 \cdot 10^8$  for the neutrals. The propellant gas influx is placed at the anode, from the axis up to  $r = 2 \text{ mm}$ , with a xenon flow rate of  $12.5 \text{ sccm}$  ( $1.22 \text{ mg s}^{-1}$ ). The neutrals are injected half-Maxwellian with a drift energy of  $0.3 \text{ eV}$  and a temperature of  $0.17 \text{ eV}$ . A voltage of  $500 \text{ V}$  is applied at the anode. The total simulation time is in the range of  $10 \mu\text{s}$  to  $100 \mu\text{s}$ , covering all relevant transport times of electrons, ions and neutrals. All simulation results were averaged for  $6 \cdot 10^4$  time steps ( $6.72 \cdot 10^{-7} \text{ s}$  with similarity scaling accounted for), in order to reduce statistical noise, while still resolving the system dynamics.

#### 4. Simulation results

The simulation results in figure 3 show the particle densities of neutral xenon in the discharge channel and the near-field plume, at the minimum and maximum of the breathing mode. The xenon particles are thermalized within the channel, with the influence of electron ionization slightly visible near the symmetry axis. The ionization efficiency, which is the fraction of the ion current expelled by the thruster divided by the product of the neutral flow rate and elementary charge, is low at about 10%. So the influence of the plasma on the neutral density is small, and therefore its influence on the breathing mode as well. A mode of operation with low plasma density was chosen by using a low target density for the feedback injection, in order to reduce computation time.

The electrons, shown in figure 4, are magnetized inside the discharge channel and follow the magnetic field lines, resembling the magnetic field structure indicated in figure 1, along with the inside and exit cusps of the field. Thus, wall contact by the electrons is limited to the magnetic cusp region. Otherwise, a plasma-wall sheath is built up near the dielectric wall, leading to minimal plasma-wall contact. The

anode cusp shows smaller electron densities due to increased electron loss at the anode.

The  $\text{Xe}^+$  ions in figure 5 are the dominant positively charged species, with the fraction of  $\text{Xe}^{2+}$  ions below 10%. The ions follow the electrons inside the discharge channel, with wall contact also reduced to the magnetic cusp. When comparing ion densities with electron densities in figure 4, the ion densities in the plume are much higher. This can be attributed to the electron injection source, which does not act as a plume neutralizer as in the experiment, with injected currents being smaller than the ion beam current. The high space charge building up in the plume as a consequence is an artifact of the similarity scaling used here. The resulting electrostatic potential (figure 6), is flat inside the discharge channel. The plasma potential is at anode potential of  $500 \text{ V}$ . At the thruster exit, the potential drops to vacuum potential. Ions reaching the exit area are then accelerated, generating the thrust, with small beam divergence contributing to a higher net thrust. The position of the potential drop has a large influence on the ion emission angle.

The dominant ionization source is the electron-Xe impact ionization, with the spatially resolved collision rates depicted in figure 7. One can see the regions with increased electron energy, mainly in the cusp and along the symmetry axis and thruster exit regions, where neutral densities are high as well, showing coupling of plasma and neutrals.

The time evolution of the discharge current in the simulation, measured as anode current, is plotted in figure 8, with a mean current of  $84 \text{ mA}$ . There is an oscillation of the anode current with an amplitude of about 15% of the mean value. In the simulation, the frequency of the oscillation is measured to be  $60 \text{ kHz}$ , which is within a factor of two from the reported experimental results, suggesting oscillation frequencies in the  $100 \text{ kHz}$  range [17].

To investigate whether a predator-prey ansatz is a valid assumption for the physics involved, the predator-prey frequency estimate in (1) is compared to the oscillation frequency in the simulation. Replenishment velocities of neutrals

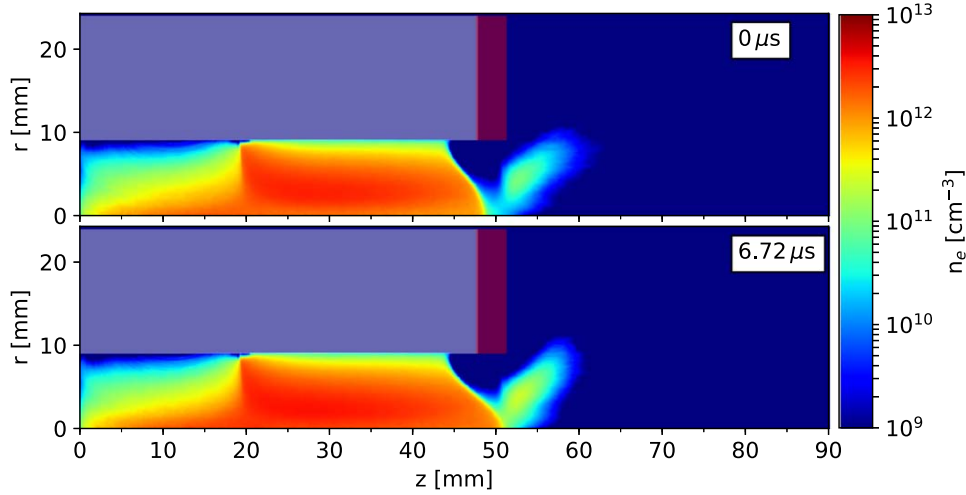


**Figure 4.** Electron densities at the minimum ( $t = 0 \mu\text{s}$ ) and maximum ( $t = 6.72 \mu\text{s}$ ) of the oscillation. The dielectric wall (white) and metal plate (red) are indicated.

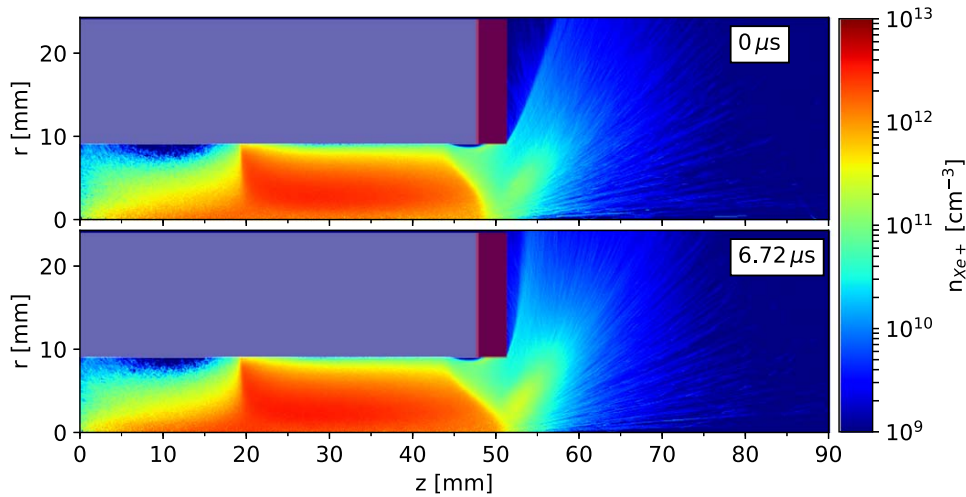


**Figure 5.**  $\text{Xe}^+$  ion densities at the minimum ( $t = 0 \mu\text{s}$ ) and maximum ( $t = 6.72 \mu\text{s}$ ) of the oscillation. The dielectric wall (white) and metal plate (red) are indicated.

and ions are taken as the  $z$ -components of the super-particle velocities measured and averaged in the region of the oscillating ionization front, extending axially from  $z = 48 \text{ mm}$  to  $z = 52 \text{ mm}$  in figure 9. The front extends about 4 mm from the axis into the plume, as is evident in figures 5 and 6. The velocities are averaged in that region for the first half-period of the oscillation, resulting in ion and neutral velocities of  $5.01 \cdot 10^3 \text{ m s}^{-1}$  and  $7.07 \cdot 10^2 \text{ m s}^{-1}$ , respectively. Hence, one obtains an oscillation frequency estimate of  $4.71 \cdot 10^5 \text{ rad s}^{-1} \approx 75 \text{ kHz}$ . This agrees very well with the oscillation frequency of 60 kHz obtained from the simulation, hence justifying a predator-prey ansatz for the given operational parameters.

The variation of the electron temperature can significantly influence the breathing oscillation, as suggested in more sophisticated models [13]. At the minimum of the oscillation (at  $t = 0 \mu\text{s}$ ), the average electron temperature in the oscillation region specified above reaches its maximum at

168 eV. At the maximum of the oscillation (at  $t = 6.72 \mu\text{s}$ ) the inverse is the case, with an average temperature of 78 eV. This can be attributed to the strong axial electric field, whose maximum moves slightly into the discharge channel in the area of the exit cusp, producing high-temperature electrons in the oscillation region. Starting at the minimum, the high-temperature electrons increase ionization in that region, due to the strong dependence of the ionization rates on the electron temperature [33]. This consequently increases ionization inside the channel. Ions are then replenished in the exit region, pushing the strong axial electric field outside the exit cusp, and reducing electron temperature in the oscillation region again. Varying electron temperature is therefore an important aspect in the formation of breathing modes in HEMP thrusters.

Along with the anode current, figure 8 also depicts the beam current, which corresponds to the total ion current expelled at the top and right domain boundary in the

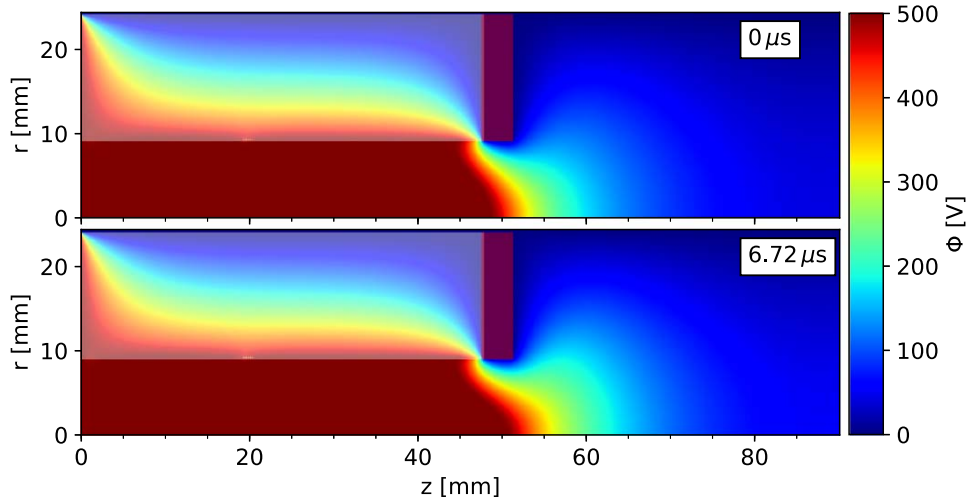


**Figure 6.** Electric potential at the minimum ( $t = 0 \mu\text{s}$ ) and maximum ( $t = 6.72 \mu\text{s}$ ) of the oscillation. The dielectric wall (white) and metal plate (red) are indicated.

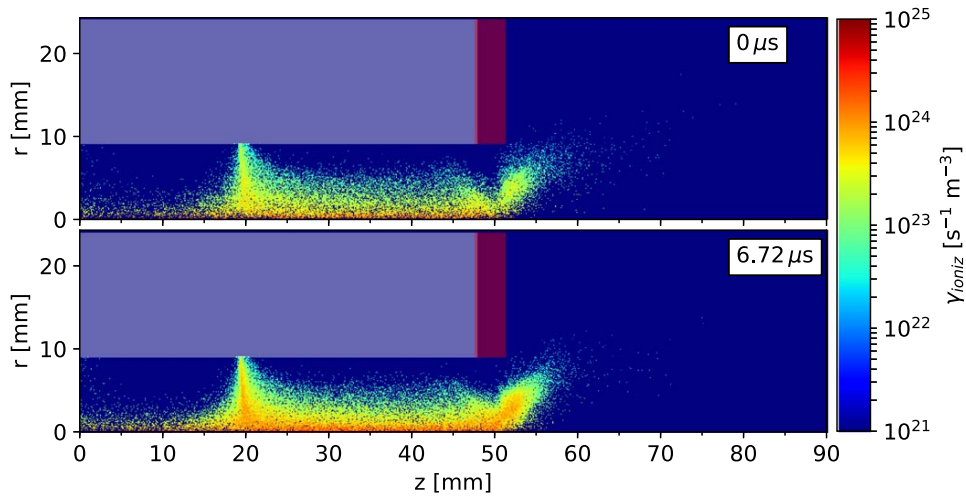


**Figure 7.** Single electron-xenon impact ionization collision rates at the minimum ( $t = 0 \mu\text{s}$ ) and maximum ( $t = 6.72 \mu\text{s}$ ) of the oscillation. The dielectric wall (white) and metal plate (red) are indicated.

simulation. The beam current shows a behavior similar to the anode current, oscillating with the same frequency and with an amplitude roughly 15% above the mean current, which at 35 mA is lower than the anode current. This discrepancy can be attributed to the point of operation chosen for the simulation, with a low ionization efficiency of just under 10%. This results in a large fraction of ionization at the thruster exit, evolving a plasma and therefore a high potential in this area. In combination with the grounded metal plate, this low ionization efficiency leads to a high loss of ions at the thruster exit, which is not observed in experiment. Therefore, the amount of ion current ejected into the plume is lower than the anode current.

Figure 10 shows a comparison of the discharge currents obtained from the simulation and from thruster performance tests of the HEMP-T DM3a performed by Thales Deutschland GmbH. During the experiment, the thruster operated with a neutral influx rate of  $7.2 \text{ sccm}$  ( $0.7 \text{ mg s}^{-1}$ ) and an anode

voltage of 495 V. The experimental mean current is 0.39 A and therefore higher by a factor of roughly 4.6 than the simulation current. This is due to the much higher ionization efficiency during the experiment, which at 75% is closer to realistic operating conditions than the simulation ionization efficiency of about 10%. Furthermore, the experimentally measured frequency of 313 kHz is roughly five times higher than the 60 kHz obtained from the simulation. The experimental oscillation amplitude of 44% of the mean current is also much higher than the 15% from the simulation. The deviation between simulation and experiment could be caused by the different set of operational parameters, most notably the xenon influx and ionization rate. More research is necessary to investigate the influence of discharge parameters on the breathing mode.

In order to further investigate the influence of the breathing mode on the plasma discharge and the resulting macroscopic thruster parameters, the ions are inspected more

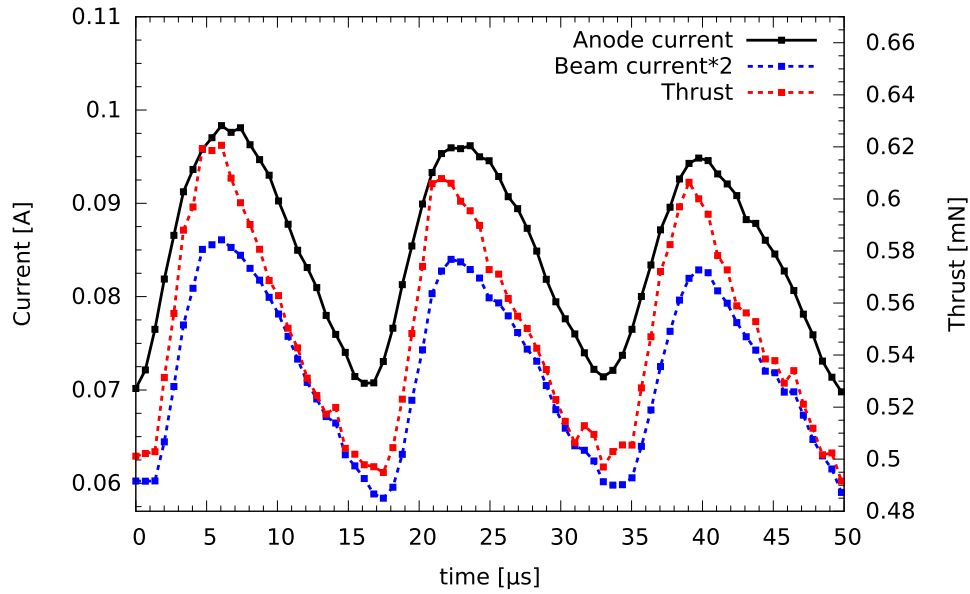


Figure 8. Anode and net beam currents along with the net thrust over the course of the breathing oscillation.

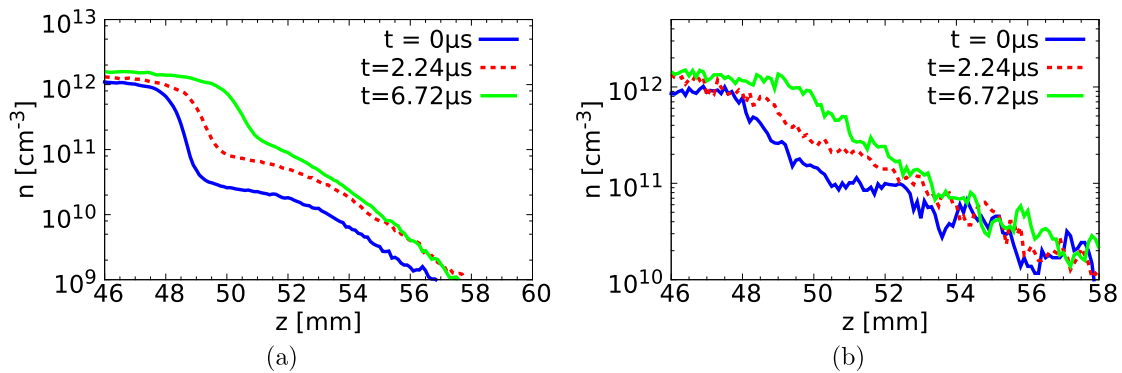


Figure 9. Axial (a) electron and (b) ion density profiles at  $r = 1$  mm in the thruster exit region.

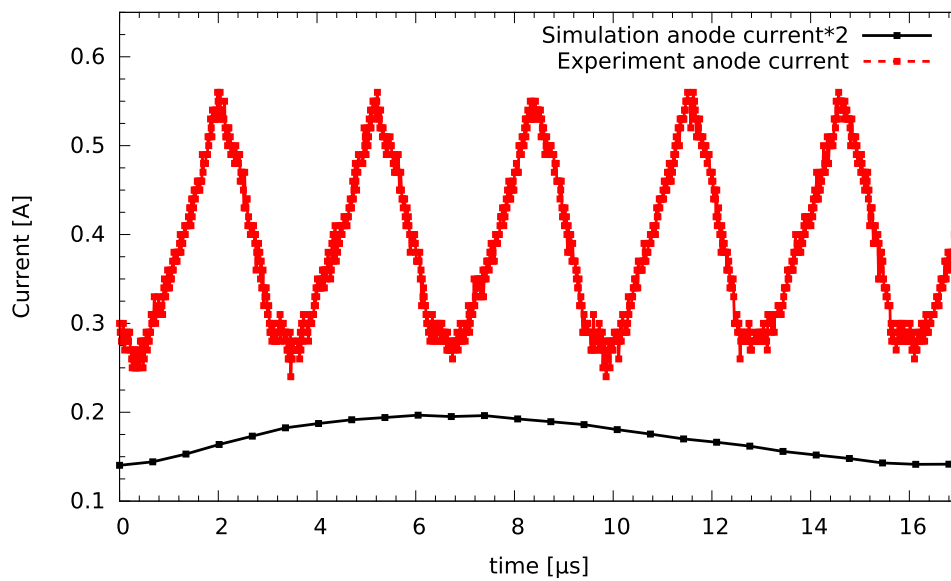
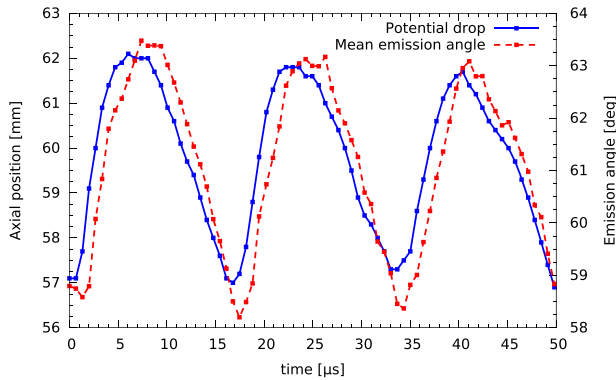


Figure 10. Comparison of anode currents from simulation and experiment, during the first oscillation of the simulation.



**Figure 11.** Axial position of the potential drop and mean ion emission angle. A potential drop further downstream results in higher ion emission angles.

closely. Ion densities are shown at the minimum and consequent maximum of the oscillation in figure 5. The density is fluctuating slightly during the oscillation, with the strongest variation at the thruster exit and in the plume. The higher plasma density at the maximum of the oscillation corresponds to higher ion emission angles. This can be attributed to the oscillation of the ionization front, influencing the position of the drop in electric potential at the thruster exit.

A potential drop inside the discharge channel leads to a more axially oriented electric field, resulting in a better focus of the emitted ion beam, and thus in a higher thrust contribution by the emitted ions. On the other hand, if the potential drop is positioned further downstream, the potential structure widens, resulting in a larger mean emission angle of the ions. This effect is clearly observed in the ion densities.

Figure 11 shows the oscillation of the position of the potential drop, defined as the point along the  $z$ -axis where the potential drops to the  $\epsilon$ th fraction of the anode potential, with the mode, along with the time variation of the thrust. The according mean emission angle of  $\text{Xe}^+$  ions is also plotted in figure 11. It can be seen that a downstream position of the potential drop coincides with larger mean emission angles of the ions. The potential drop itself is, in turn, determined by the position of the plasma edge. This explains the time evolution of the thrust, as shown in figure 8. While the oscillation frequency is the same as for the anode current and other parameters, the amplitude of 12% is lower than the amplitude variation of the beam current, at 17%. Some of the thrust difference implied by the beam current oscillation is compensated by the lower ion emission angle.

The oscillation of the ionization front becomes clearer when looking at the density profiles of electrons and  $\text{Xe}^+$  ions in figure 9. Profiles are plotted at the minimum and maximum and intermediate points in time of the oscillation. The oscillation of the edge of the plasma bulk is clearly visible and more pronounced in the electron density, due to potential and magnetic field structures in that area. The effect is smaller for ions, due to the ion emission in the exit region, but still clear.

The axial profiles of  $\text{Xe}$  neutrals and the electrical potential are shown in figure 12. Due to the low ionization efficiency, the oscillatory effect on the neutral densities is

almost negligible. The shift in the potential drop is very pronounced, showing the oscillation of the plasma edge, leading to the changed ion emission characteristics discussed above.

Optical emission during thruster operation is an easily accessible, non-invasive diagnostic that can be performed during standard thruster testing. Experimental data shows that the breathing is visible in optical emission measurements, along with an oscillation of the mean ion emission angle [34]. Measurements performed by Thales Deutschland GmbH show that this behavior is observed in the HEMP-T as well [35] and is characteristic for breathing modes. While the simulation does not contain an optical emission diagnostic, inelastic  $e^-$ -Xe collisions are simulated and the lost energy is removed from the system. In the real system, most of that energy is dissipated by radiation, so the collision rates in figure 13 provide a useful approximation to the optical emission observed in the experiment. It is apparent that the collision rates at the maximum of the oscillation are higher than at the minimum, most notably along the axis and in the thruster exit area. This corresponds to the optical breathing observed in experimental measurements, in agreement with the experimental data. The simulation is able to reproduce this important feature of the breathing oscillation.

## 5. Conclusions and outlook

In this work, a 2D3v PIC-MCC simulation was used to investigate breathing modes in HEMP thrusters. The resulting oscillation frequency of 60 kHz is close to the lower end of previously reported experimental oscillation frequencies in the range of 100 kHz. The oscillation amplitude of the discharge current is about 15% higher than its mean value, with the emitted ion current in the same range.

The oscillation of the plasma edge was clearly visible in the density profiles of the charged species and the profile of the electrostatic potential. The resulting thrust shows a slightly different behavior, as the compensation of the lowered thrust due to a reduced ion emission angle leads to an amplitude of only 12% of the mean value, three percentage points below the beam current oscillation.

Oscillations of optical emissions are characteristic in experimental measurements of breathing mode oscillations and were observed in the simulation, as estimated by the integral inelastic electron–neutral collisions. The according oscillation of the mean ion emission angle was observed as well. A comparison of the simulation results with experimental measurements of the thruster model shows large differences in the breathing frequency and amplitude. One reason could be the differing sets of operating parameters used in the simulation and experiment. The influence of the operating conditions on the breathing oscillations is an interesting topic for future research, especially in a regime with higher plasma densities and ionization efficiencies.

The frequency estimate of the 0D predator–prey model shows very good agreement with the oscillation frequency obtained from the simulation. This similarity can be expected to

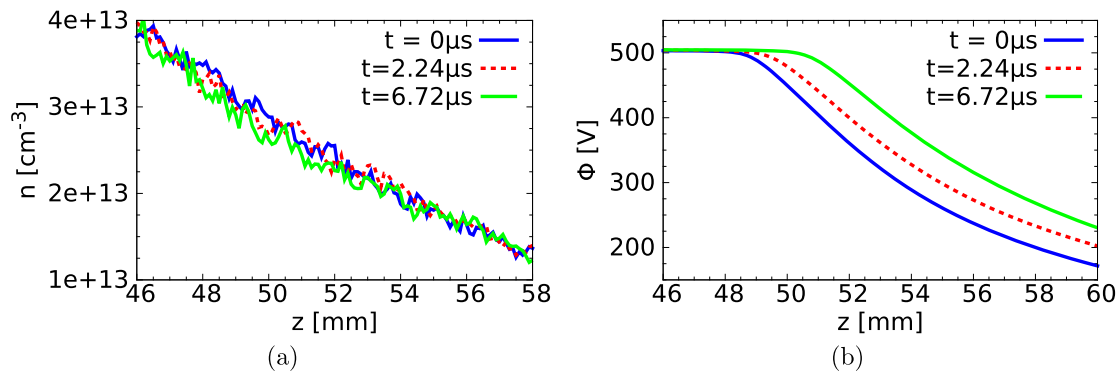


**Figure 12.** Axial (a) neutral density and (b) potential profiles at  $r = 1$  mm in the thruster exit region.

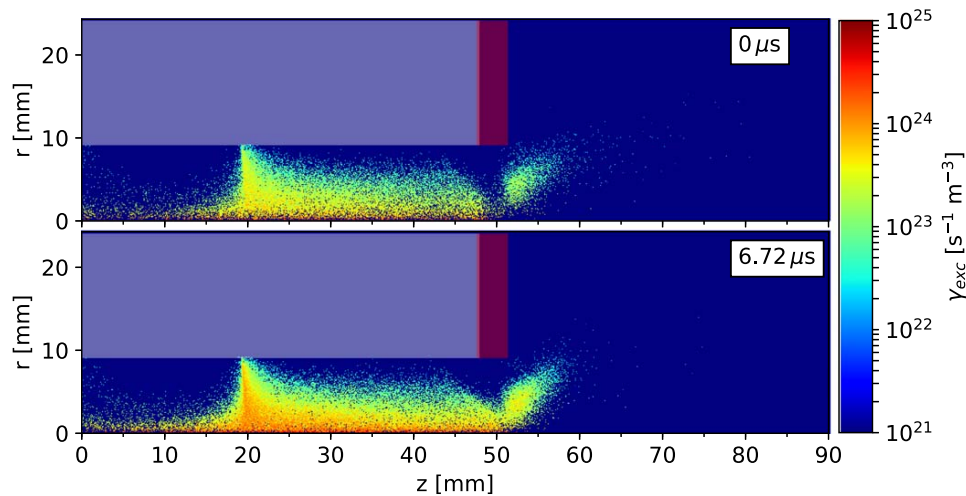


**Figure 13.** Inelastic excitation collision density at the minimum ( $t = 0 \mu\text{s}$ ) and maximum ( $t = 6.72 \mu\text{s}$ ) of the oscillation. The dielectric wall (white) and metal plate (red) are indicated.

hold as long as the breathing amplitude is small, when the linearization ansatz is still applicable. For larger amplitudes of the mode, a more complex approach, incorporating higher-order perturbation terms, may be necessary. A fully kinetic simulation could then provide a useful point of comparison for such models.

### Acknowledgments

This work was funded by the German Space Agency DLR through project 50RS1510.

### ORCID iDs

D Kahnfeld <https://orcid.org/0000-0002-5900-4423>

K Matyash <https://orcid.org/0000-0002-9453-8105>

### References

- [1] Choueiri E Y 2001 *Phys. Plasmas* **8** 1411–26
- [2] Gascon N, Dudeck M and Barral S 2003 *Phys. Plasmas* **10** 4123–36
- [3] Lobbia R B and Gallimore A D 2009 Two-dimensional time-resolved breathing mode plasma fluctuation variation with Hall thruster discharge settings *31st International Electric Propulsion Conf. IEPC-2009-106*
- [4] Lobbia R B, Sekerak M J, Liang R and Gallimore A D 2011 High-speed dual Langmuir probe measurements of the plasma properties and EEDFs in a HET plume *The XXXII International Electric Propulsion Conf. IEPC-2011-168*
- [5] Sekerak M J, Gallimore A D, Brown D L, Hofer R R and Polk J E 2016 *Journal of Propulsion and Power* **32** 903–17
- [6] Dale E T and Jorns B A 2008 Non-invasive characterization of the ionization region of a Hall-effect thruster *2018 Joint Propulsion Conf., AIAA Propulsion and Energy Forum AIAA 2018-4508*
- [7] Romadanov I, Raitses Y, Diallo A, Hara K, Kaganovich I D and Smolyakov A 2018 *Phys. Plasmas* **25** 033501
- [8] Boeuf J P and Garrigues L 1998 *J. Appl. Phys.* **84** 3541–54
- [9] Yamamoto N, Komurasaki K and Arakawa Y 2005 *J. Propul. Power* **21** 870–6
- [10] Barral S and Ahedo E 2006 Theoretical study of the breathing mode in Hall thrusters *42nd AIAA/ASME/SAE/ASEE Joint Propulsion Conf. and Exhibit AIAA 2006-5172*
- [11] Barral S and Ahedo E 2009 *Phys. Rev. E* **79** 046401
- [12] Barral S and Peradzyński Z 2010 *Phys. Plasmas* **17** 014505
- [13] Hara K, Sekerak M J, Boyd I D and Gallimore A D 2014 *Phys. Plasmas* **21** 122103

- [14] Hara K, Sekerak M J, Boyd I D and Gallimore A D 2014 *J. Appl. Phys.* **115** 203304
- [15] Hara K, Boyd I D, Sekerak M J and Gallimore A D 2015 Breathing mode in Hall-effect thrusters *Joint Conf. of 30th ISTS, 34th IEPC and VI NSAT IEPC-2015-283/ISTS-2015-b-283*
- [16] Dale E T, Jorns B and Hara K 2017 Numerical investigation of the stability criteria for the breathing mode in Hall-effect thrusters *Proc. of the 35th International Electric Propulsion Conf.* IEPC-2017-265
- [17] Kornfeld G, Koch N and Harmann H P 2007 Physics and evolution of HEMP thrusters *The 30th International Electric Propulsion Conf.* IEPC-2007-108
- [18] Kornfeld G, Koch N and Coustou G 2003 First test results of the HEMP thruster concept *The 28th International Electric Propulsion Conf.* IEPC-2003-212
- [19] Koch N, Harmann H P and Kornfeld G 2007 Status of the Thales high efficiency multi stage plasma thruster development for HEMP-T 3050 and HEMP-T 30250 *Proc. of the 30th International Electric Propulsion Conf.* IEPC-2007-110
- [20] Koch N et al 2011 The HEMP-T concept—a survey on theoretical considerations and experimental evidences *Proc. of the 32nd International Electric Propulsion Conf.* IEPC-2011-236
- [21] Weis S, Lazurenko A, Genovese A, Heidemann R, Holtmann P, Stalzer H, Püttmann N, Wolf T and Wollenhaupt B 2017 Overview, qualification and delivery status of the HEMP-thruster based ion propulsion system for SmallGEO *The 35th International Electric Propulsion Conf.* IEPC-2017-197
- [22] Matyash K, Kalentev O, Schneider R, Taccogna F, Koch N and Schirra M 2009 Kinetic simulation of the stationary HEMP thruster including the near-field plume region *Proc. of the 31st International Electric Propulsion Conf.* IEPC-2009-110
- [23] Tskhakaya D, Matyash K, Schneider R and Taccogna F 2007 *Contrib. Plasma Phys.* **47** 563–94
- [24] Takizuka T and Abe H 1977 *J. Comput. Phys.* **25** 205–19
- [25] Hayashi M 2003 Bibliography of electron and photon cross-sections with atoms and molecules published in the 20th century—xenon *Tech. Rep. NIFS-DATA-79 NIFS* URL <http://nifs.ac.jp/report/NIFS-DATA-079.pdf>
- [26] Matyash K 2003 Kinetic Modeling of Multi-Component Edge Plasmas *Ph.D. Thesis* University of Greifswald
- [27] Bronold F X, Matyash K, Tskhakaya D, Schneider R and Fehske H 2007 *J. Phys. D: Appl. Phys.* **40** 6583
- [28] Kalentev O, Matyash K, Duras J, Luskow K F, Schneider R E, Koch N and Schirra M 2014 *Contrib. Plasma Phys.* **54** 235–48
- [29] Matyash K, Schneider R, Mutzke A, Kalentev O, Taccogna F, Koch N and Schirra M 2010 *IEEE Trans. Plasma Sci.* **38** 2274–80
- [30] Kahnfeld D, Schneider R, Cichocki F, Merino M, Ahedo E, Duras J and Koch N 2017 HEMP-T thruster discharge and plume simulation with a 2d3v-PIC-MCC and a 3d hybrid fluid-PIC code *The 35th International Electric Propulsion Conf.* IEPC-2017-309
- [31] Battista F, De Marco E A, Misuri T and Andrenucci M 2007 A review of the Hall thruster scaling methodology *Proc. of the 32nd International Electric Propulsion Conf.* IEPC-2007-037
- [32] Fubiani G, Garrigues L, Hagelaar G, Kohen N and Boeuf J 2017 *New J. Phys.* **19** 015002
- [33] Goebel D M and Katz I 2008 *Fundamentals of Electric Propulsion: Ion and Hall Thrusters* vol 1 (New York: Wiley)
- [34] Vial V, Mazouffre S, Prioul M, Pagnon D and Bouchoule A 2005 *IEEE Trans. Plasma Sci.* **33** 524–5
- [35] Heidemann R private communication

# Ion angular distribution simulation of the Highly Efficient Multistage Plasma Thruster

J. Duras<sup>1,2,†</sup>, D. Kahnfeld<sup>2</sup>, G. Bandelow<sup>2</sup>, S. Kemnitz<sup>3</sup>, K. Luskow<sup>2</sup>,  
P. Matthias<sup>2</sup>, N. Koch<sup>1</sup> and R. Schneider<sup>2</sup>

<sup>1</sup>Nuremberg Institute of Technology, D-90489 Nuremberg, Germany

<sup>2</sup>Institute of Physics, University of Greifswald, D-17498 Greifswald, Germany

<sup>3</sup>Institute of Computer Science, University of Rostock, D-18059 Rostock, Germany

(Received 18 July 2016; revised 16 January 2017; accepted 16 January 2017)

Ion angular current and energy distributions are important parameters for ion thrusters, which are typically measured at a few tens of centimetres to a few metres distance from the thruster exit. However, fully kinetic particle-in-cell (PIC) simulations are not able to simulate such domain sizes due to high computational costs. Therefore, a parallelisation strategy of the code is presented to reduce computational time. The calculated ion beam angular distributions in the plume region are quite sensitive to boundary conditions of the potential, possible additional source contributions (e.g. from secondary electron emission at vessel walls) and charge exchange collisions. Within this work a model for secondary electrons emitted from the vessel wall is included. In order to account for limits of the model due to its limited domain size, a correction of the simulated angular ion energy distribution by the potential boundary is presented to represent the conditions at the location of the experimental measurement in 1 m distance. In addition, a post-processing procedure is suggested to include charge exchange collisions in the plume region not covered by the original PIC simulation domain for the simulation of ion angular distributions measured at 1 m distance.

**Key words:** plasma applications, plasma simulation

---

## 1. Motivation

For ion thrusters, the angular ion distribution in terms of ion current, charge state and energy is an important parameter since it determines the thrust efficiency of the propulsion system. It is also one of the few thruster characteristics that can be accessed experimentally to validate numerical plasma simulations.

In the present study, numerical simulations are performed for the Highly Efficient Multistage Plasma Thruster (HEMP-T), patented by the THALES group in 1998 (Kornfeld, Seidel & Wegener 1998). As described in Koch, Harmann & Kornfeld (2007), HEMP-Ts consist of a dielectric, rotationally symmetric discharge channel with an anode and a propellant inlet located at the upstream end and a hollow cathode neutraliser placed at the thruster exit. The discharge channel is surrounded

† Email address for correspondence: [julia.duras@th-nuernberg.de](mailto:julia.duras@th-nuernberg.de)

by a system of axially magnetised permanent magnet rings in opposite magnetisation, forming a multi-cusp structure. The level of magnetic induction at any position within the thruster channel is chosen such that the Larmor radius of the electrons is much smaller than the geometrical dimensions of the discharge channel. While the propellant ions are hardly affected by the magnetic field due to their much higher mass, electrons are efficiently confined and only few electrons are lost to the wall, mostly at the cusps. In this work an older prototype model named DM3a is discussed. It has three cusps, the anode, the central and the exit cusp and is described in Kornfeld, Koch & Harmann (2007). An anode potential of  $U_a = 500$  V is applied.

Numerical simulations show a typical neutral particle density in the channel is  $n_n = 10^{20} \text{ m}^{-3}$  with a neutral temperature of  $T_n = 700$  K. Typical plasma parameters are a plasma particle density of  $n_{e,i} = 10^{18} \text{ m}^{-3}$ , with a temperature of approximately  $T_e = 4$  eV and  $T_i = 1$  eV. While the ions in the channel are nearly thermalised, the electrons have an additional drift velocity of approximately  $10^4 \text{ m s}^{-1}$  towards the anode. Inside the thruster channel the electron Debye length is  $\lambda_{D_e} = 7.4 \text{ }\mu\text{m}$ , the electron plasma frequency is  $\omega_{p,e} = 1.8 \times 10^{11} \text{ Hz}$  and the electron mean free path is in the range of the channel length of 50 mm. This motivates kinetic simulations rather than a fluid approach for the electrons. The electrostatic approximation can be used, because the magnetic fields connected with the internal plasma currents are negligible compared to the static magnetic fields from the magnets. A strong coupling of the channel and plume plasma requires a simulation of both regions. In the plume, the plasma densities are decreased by at least 4 orders of magnitudes and the ion kinetic energy is increased to  $E_{kin,i} = 500$  eV, as a consequence of the accelerating potential drop close to the exit.

A widely applied kinetic method is the particle-in-cell (PIC) scheme with Monte Carlo collisions (PIC-MCC), simulating the trajectories of super-particles consisting of many real particles. It requires the resolution of the smallest length scale of the system, usually the Debye scale, and the shortest time scale of the system, usually the plasma frequency, resulting in small domain sizes in the mm range and short simulated run times of approximately some  $\mu\text{s}$ . Since angular ion distributions are typically measured at a distance of tens of centimetres to some metres from the thruster exit, it is necessary to introduce proper mapping functions to transfer the results of the kinetic model to these positions. The computational requirements for such a fully kinetic model are quite demanding in memory and run time. Therefore, after a short description of the PIC-MCC code, a possible parallelisation strategy is discussed in § 2. Afterwards, the simulated angular distribution of ion current and energy is described in detail in § 3 and compared with experimental data.

## 2. Code description and parallelisation strategy

The non-Maxwellian characteristics of the electron distribution function in the thruster requires a kinetic method (Kalentev *et al.* 2014). Due to the rotational symmetry of the system, the spatial domain was reduced to  $r$ - $z$  (radial and axial coordinate) and an electrostatic 2d3v PIC code (2-D in position space and 3-D in velocity space) with Monte Carlo collisions (Matyash *et al.* 2010; Kalentev *et al.* 2014) was used. In this PIC-MCC simulation we follow the kinetics of so-called super-particles (each of them representing many real particles), moving in the self-consistent electric field calculated on a spatial grid by solving Poisson's equation

$$\Delta\Phi = -\frac{\rho}{\epsilon}. \quad (2.1)$$

Here,  $\Phi$  indicates the electric potential,  $\rho$  the plasma density and  $\varepsilon$  the absolute permittivity. The relevant collisions: electron–electron Coulomb, electron–neutral elastic, ionisation and excitation collisions, ion–neutral momentum transfer and charge exchange collisions are included. For Coulomb collisions a binary collision routine, as suggested by Takizuka & Abe (1977), is used. Collisions with neutrals are simulated by a Monte Carlo routine similar to Vahedi *et al.* (1993), using cross-sections for xenon from Hayashi (2003), Phelps (2000) and Phelps (2002). A detailed description of the applied collision models can be found in Tskhakaya *et al.* (2007). The dynamics of the background neutral gas is self-consistently resolved by Direct Simulation Monte Carlo (Procassini *et al.* 1987). As can be seen from three-dimensional (3-D) simulations of a similar HEMP thruster model, classical transport along magnetic field lines is dominant (Kalentev *et al.* 2014). Only in the narrow cusp regions, where  $\mathbf{B}$  turns from the axial to radial direction, fluctuations of the azimuthal electric field allow the electrons to overcome. In the 3-D simulations the anomalous fluxes are calculated self-consistently (Kalentev *et al.* 2014). Using these results, an effective anomalous transport coefficient of  $D_{\perp} \propto 0.4 \times k_B T / eB$  following Bohm, Burhop & Massey (1949) can be determined. This coefficient is then used in the 2-D model, which does not allow us to calculate electrostatic turbulence self-consistently. The anomalous transport fluxes are implemented by a diffusive model using the calibrated transport coefficient deduced from the 3-D simulation for a random walk model in velocity space in all three velocity components (radial, axial and poloidal). Information of all three velocity components exists in the 2-D code due to the Monte Carlo collisions (Bronold *et al.* 2007; Tskhakaya *et al.* 2007). The isotropic characteristics of turbulence is well represented by this procedure. Dominant transport contributions in two dimensions will be perpendicular to the magnetic field lines, as discussed previously. With respect to the channel plasma parameters, an equidistant grid with a spacing of  $\Delta r = \Delta z = 1.3 \lambda_{D,e} = 0.01$  mm is used, including both the thruster channel and the near-field plume. In order to reduce the computational time, a similarity scaling is applied with a factor of 10 (Taccogna *et al.* 2005). For the time resolution a time step of  $\Delta t = 0.2 \omega_{p,e}^{-1} = 1$  ps is chosen. In the channel around the propulsion exhaust, the neutral particle density is two orders of magnitude higher than for the plasma particles. For a correct treatment of MCC of neutrals with plasma particles, the same weighting of plasma and neutral super-particles is required. This results in a number of simulated super-particles which is 100 times higher than for ions and electrons. In total, the high resolution in space, time and particles results in a long run time. For the serial PIC-MCC code, typically one month of calculation is needed on a desktop system in order to simulate a run time in the range of some micro seconds. With access to parallel computing clusters, the best chance of gaining a speed up of the simulation is an efficient parallelisation.

Dependent on the simulated system, a domain decomposition according to number of particles in each subdomain is applied; collision probability or grid cells per rank. In this work, a domain decomposition according to number of particles was used. With the help of the Message Passing Interface (MPI), particle arrays as well as the electric field computed on the grid are distributed to the different subdomains. Each subdomain is either located at different nodes or cores. This allows the parallel execution of the particle pusher. In a second step, the MC collisions routine is planned to be parallelised by using the Open Multi-Processing (OpenMP), suitable for shared memory parallelisation on a single node.

To calculate the electric field on the grid, Poisson's equation (2.1) is solved using a finite difference scheme for the spatial second-order derivatives creating a system of

linear equations

$$\mathbf{A}\Phi = \mathbf{b}. \quad (2.2)$$

Here, the vector  $\Phi$  and  $\mathbf{b}$  indicate the electric potential  $\phi$  and the plasma density  $-\rho/\varepsilon$  respectively, on the grid points. For a two-dimensional  $M \times N$  grid, this gives a matrix  $\mathbf{A}$  of dimension  $(M \cdot N) \times (M \cdot N)$ . In order to reach reasonably low computing time, the calculation of  $\Phi$  within one time step has to be faster than one second  $t_{max} \leq 1$  s.

A standard sparse matrix solver is the LU decomposition. The matrix is decomposed into a product of an upper triangular matrix  $\mathbf{U}$  and a lower triangular matrix  $\mathbf{L}$ . By this, in each time step the calculation of  $\mathbf{L}(\mathbf{U}\Phi) = \mathbf{b}$  can be done easily. While the decomposition is rather time consuming, the so-called back solve has a complexity of  $\sim(M \cdot N)^2/2$  (Stoer 2005a), making it very efficient. Therefore, the decomposition is calculated only at the beginning of the simulation, as the matrix does not change throughout the execution of the code, and only the back solve has to be computed every PIC cycle, hence giving a complexity of  $\sim(M \cdot N)^2$  per PIC cycle. A parallelisation of this method is problematic, as each line within a back-solve step depends on the results of the previous lines, limiting its application to one computational core. Parallel methods are only available for the calculation of the LU decomposition but not for the back solve (Li 2005).

In order to reduce the number of grid points, a ‘matryoska-like’ hierarchy of equidistant grids can be used for the simulation of the HEMP thruster (Kalentev *et al.* 2014). The hierarchy is constructed such that a coarse grid, given by the electron Debye length in the plume, covers the whole domain, while a fine grid with a mesh spacing of  $\lambda_{D,e}$  in the channel, covers in addition the channel and the near-field plume. The solution of Poisson’s equation (2.1) is obtained by first solving the equation on the coarse grid and then using the interpolated coarse grid values as boundary values for the fine grid solution. This approach appears to be not only accurate enough, but also remarkably fast compared with the solution for a single equidistant mesh. Alternatively, non-equidistant meshes could be used, but these suffer from artefacts (Tskhakaya *et al.* 2007), such as self-forces, and corrections to minimise such errors are needed. A reduction can be achieved by a modified two point central difference scheme for calculation of the electric field on a non-equidistant grid (Duras *et al.* 2014). In the case of thruster simulations, a transition from a fine to a coarser grid can be done in the plume region, since here the coupling with the channel plasma is lower and the influence of artificial forces is reduced.

Instead of using the fast, but serial back solve, the advantage of a slower but parallelisable method can be facilitated (Kahnfeld *et al.* 2016). A standard iterative solver is the successive over-relaxation (SOR) method which is often applied to solve the finite difference discretisation of the Poisson equation (2.1). It is a variation of the Gauss–Seidel algorithm with a relaxation factor  $\omega > 1$ . The matrix  $\mathbf{A}$  is represented by the sum of  $\mathbf{A}$ ’s diagonal matrix  $\mathbf{D}$  (with  $a_{ii} \neq 0$  for all  $i$ ) and its strictly lower and upper triangular matrices  $\mathbf{L}$  and  $\mathbf{R}$  (not to be confused with the matrix used in the LU decomposition) with  $\mathbf{A} = 1/\omega(\mathbf{D} + \omega\mathbf{L}) + \mathbf{R}$ . The expected number of iteration steps is  $\sim(M \cdot N)$ , giving the entire SOR method a complexity of  $\sim(M \cdot N)^3$  (Stoer 2005b). This is much higher compared to the back solve of the LU decomposition which scales quadratically, however the algorithm allows for easy parallelisation as the calculation of each point’s iterate depends only on the surrounding points. Only the boundary points have to be exchanged during each iteration step.

In this work, compared to a serial run, parallelisation of the particle pusher gained a speed up of 2.6, running on 2 nodes with 4 cores each node. Here, mainly the serial solver limits the total simulation speed up.

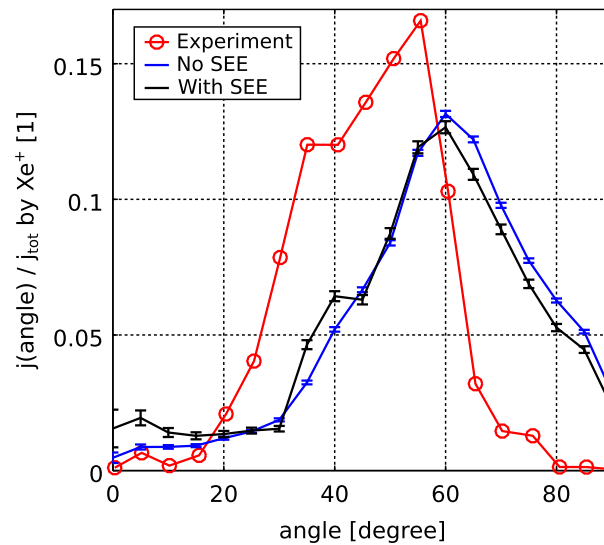


FIGURE 1. Angular ion current distribution with respect to the thruster exit at  $r=0$  mm, measured in experiment (Matyash *et al.* 2009) and simulated with SEE and without. Simulation results are given with statistic error bars.

### 3. Ion angular distributions

The angular distributions of ion current and energy are among the key parameters of an ion thruster and are also directly accessible to experiments. Within experiments, ion angular distributions are typically measured with a Retarding Potential Analyzer (RPA) at approximately 1 m distance from the thruster exit (van Reijen *et al.* 2013). In the PIC simulation, the simulated plume has a size of several centimetres, limited by the high computational costs. In the plume, the potential distribution and ion–neutral collisions are the important physical mechanisms for current and energy distribution of the ions. Also, secondary electron emission (SEE) at vessel walls, generated by accelerated ions, influences the potential at the thruster exit. These low energetic electrons are magnetised in the thruster near-field plume and follow the magnetic field lines.

In the following the angular ion current distribution, as well as the angular energy distribution, will be discussed in detail. Within the simulation, these distribution functions are diagnosed along a diagnostic surface at the plume domain boundary. The angle is defined with respect to the thruster exit at the symmetry axis ( $r=0$  mm), assuming a point source. In experimental measurements the same assumption is applied. The angular resolution is chosen to be  $5^\circ$ . For the current diagnostics, the current passing the diagnostic surface is calculated and for the energy distribution, the kinetic energy of the ions crossing this surface is detected.

#### 3.1. Angular ion current distribution

In figure 1, the calculated angular ion current distribution is given in blue. It shows contributions for all angles with a maximum current at  $60^\circ$ . In the same figure a measured angular ion current distribution for the DM3a HEMP model is given in red. It shows two maximums at  $35^\circ$  and  $55^\circ$ , respectively. For a better understanding, the origin of the detected ions was diagnosed and analysed with respect to the angle. It indicates a correlation of the respective cusp, in which an ion is generated, and the

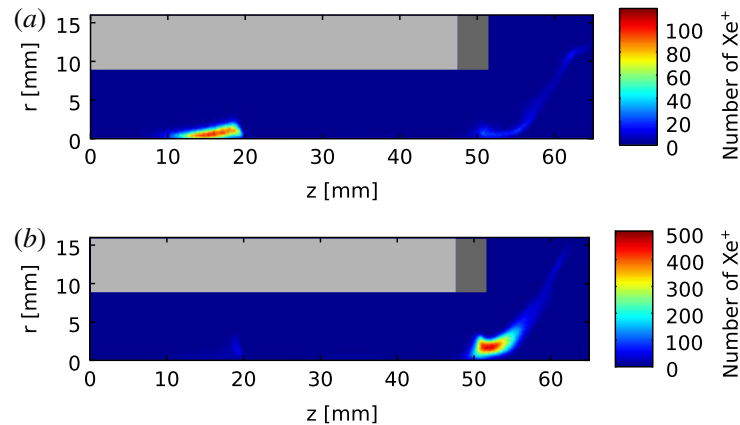


FIGURE 2. Ionisation distribution for ions detected at the diagnostic surface at  $40 \pm 2.5^\circ$  (a) and  $60 \pm 2.5^\circ$  (b). The dielectric channel wall is shown in light grey and the grounded pole piece is shown in dark grey.

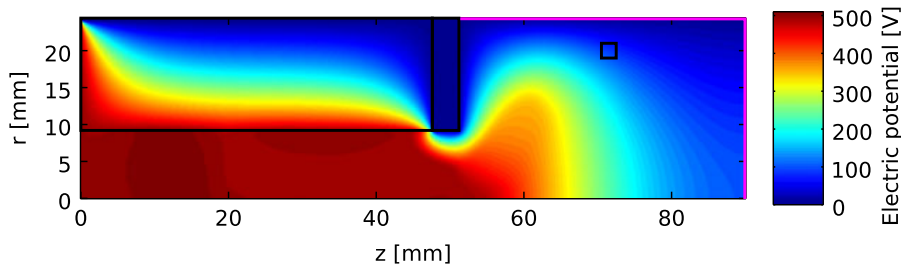


FIGURE 3. Potential of thruster channel and plume, given in V. In magenta, the diagnostic surface for the ion angular distributions is given at the plume domain boundary. The small black box in the plume indicates the position of the electron source.

angle into which it is emitted, as can be seen in figure 2, which shows the ionisation distribution for ions detected at  $40^\circ$  and  $60^\circ$ . While for angles between  $30^\circ$  and  $50^\circ$ , ions are mainly generated in the central cusp, for angles larger than  $55^\circ$  the exit cusp apparently is the place of origin. Due to a low contribution of the ionisation in the central cusp, the second maximum around  $40^\circ$  is not well accentuated. Therefore, the simulated ion angular current distribution can be seen as qualitatively matching the experimental data, shifted by  $5^\circ$  towards higher angles.

An important effect on the angular ion distribution is the potential drop in the plume, accelerating the ions towards different angles. In the simulation, it is also sensitive to the potential at the boundary of the simulation domain due to its limited size. In figure 3, the resulting potential is shown and in magenta, the diagnostic surface is indicated. The black rectangle at  $r = 20$  mm and  $z = 75$  mm indicates the position of the primary electron source with a source current of  $I_{src,1} = 0.3$  mA. It represents the real neutraliser, which is located outside the computational domain. The position was chosen in order to provide sufficient starter electrons for the thruster channel. In experiments, the HEMP-T can operate even without the neutraliser because even a very small amount of free electrons are sufficient for successful start up. Corresponding ion and electrons distributions can be found in Duras *et al.* (2016). For the boundary condition at the right-hand side of the domain  $E_z = 0$  is chosen. The potential at the left-hand side is fixed to the anode potential  $U_a$ . At the

upper boundary  $\Phi = 0$  V is used. This fixed potential can squeeze or stretch the potential solution in the radial direction, which results in shifted angular distributions. To prevent this, it is reasonable to use, for the area of the simulated plume, a similar aspect ratio as the vessel in which the experiments were taking place. What constitutes a sufficient domain size to reduce the influence of this defined potential boundary remains to be investigated.

An indirect influence on the potential is induced by the emission of secondary electrons from the vessel walls. These low energetic electrons are attracted by the anode potential and become magnetised by the magnetic field of the thruster acting as additional primary source of electrons. A study of different external electron sources and their positions showed strong influence of the magnetic field on the near-field plume (Duras *et al.* 2016). To represent the possible contributions of secondary electrons created by ions at the vessel walls, an electron source is placed close to the symmetry axis. This changes the potential distribution in the channel, while external electron sources at other places in the plume hardly influence the potential structure. The main reason for this is that the magnetic field, close to the symmetry axis, points directly into the thruster. At other radial positions the field lines are curved and electrons are trapped between a magnetic mirror movement, pushing them away from the thruster, and the potential drop forcing them towards the exit. Electrons emitted close to the symmetry axis have higher energies due to the direct guidance into the channel. This increases the probability of ionisation which expands the potential drop out of the thruster channel.

SEE at the aluminium vessel walls can act as an additional electron source. Secondary electrons created at the vessel walls by impinging ions fly towards the thruster. Rosenberg & Wehner (1962) measured sputter yields for singly charged ions impinging on aluminium which have been published for ion energies of 100, 200, 300 and 600 eV. With the help of an empirical fitting formula by Yamamura, Matsunami & Itoh (1983), an emission coefficient of  $\gamma = 0.6$  can be approximated for singly charged xenon ions impinging with an energy of 500 eV.

Approaching the thruster entrance such electrons experience an increasing magnetic field, which directs them mostly towards the axis. In the small simulation domain of this work, the electron influx from this process is parametrised as an additional surface source close to the axis. Electrons are injected at the right domain boundary close to the symmetry axis at  $r \in (0; 2 \text{ mm})$  and  $z \in (88 \text{ mm}; 90 \text{ mm})$ , with a directed drift velocity towards the thruster based on an energy of 100 eV corresponding to the potential at this location and a thermal broadening of the source distribution assuming a temperature of 0.45 eV. Of the total emitted ion current of  $I_{tot} = 142 \text{ mA}$ , 10% were chosen as an effective electron source close to the axis, representing SEE. This contribution is a factor of approximately 5 times higher than the primary electron source. This value was chosen because it induced a visible effect in the solution without affecting strongly the integral ion current.

The resulting angular current distribution with SEE can be seen in black in figure 1. It shows a higher ion contribution close to the symmetry axis ( $0^\circ$ ), which is the direct effect of the additional electron source in this region. At approximately  $40^\circ$  the second ion beam becomes more pronounced, which is in qualitative agreement with the experimental data.

### 3.2. Angular ion energy distribution

The simulated angular ion energy distribution calculated at the domain boundary is shown in figure 4. At the left-hand side the calculated ion flux is colour coded in

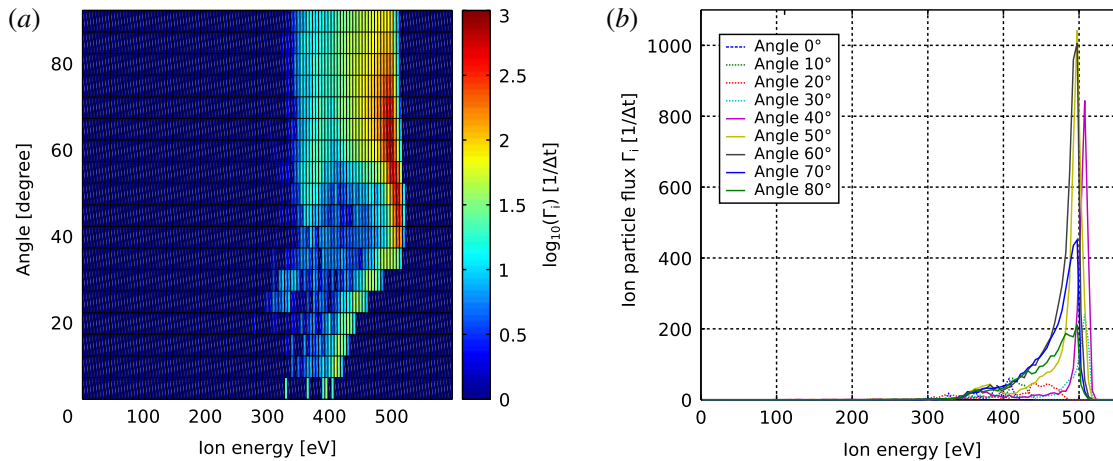


FIGURE 4. Angular ion energy distribution at the domain boundary. (a) Contour plot of the ion particle flux  $\Gamma_i$  in logarithmic scale as a function of angle and ion energy. (b)  $\Gamma_i$  in linear scale as a function of ion energy shown for nine angles.

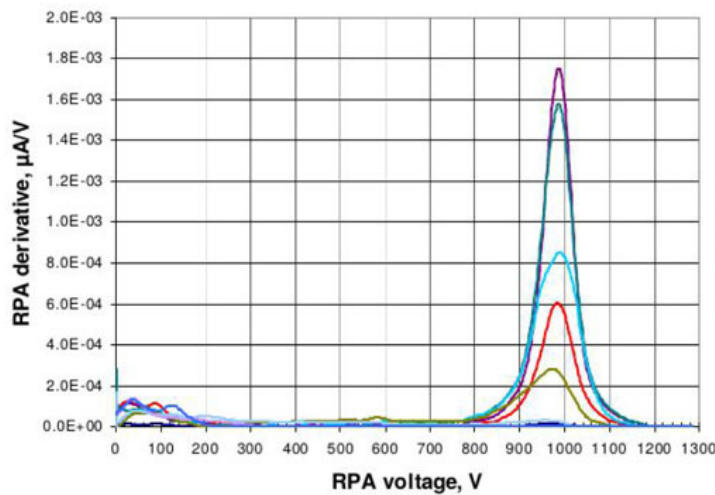


FIGURE 5. Angular ion energy distribution for the HEMP thruster model HEMPT 3050, derived from RPA measurements. The applied thruster anode voltage was  $U_a = 1000$  V (Koch *et al.* 2011).

logarithmic scale and the angle is defined with respect to the thruster exit at the symmetry axis. The right-hand side of figure 4 shows the same result in linear scale as line plots for nine angles. As expected, the maximum ion energy is 500 eV, given by the anode potential. The dominant contribution of ions originates from ions at approximately 60°.

An experimentally measured energy distribution for the HEMP thruster model HEMPT 3050 is shown in figure 5 for nine different angles (Koch *et al.* 2011). It is characterised by a maximum close to the anode potential  $U_a = 1000$  V, with an opening angle of 20°. While the simulated energy distribution shows a peak, smeared out to lower energies, the measured data show a Gaussian distribution around  $U_a$ .

In the numerical diagnostic, the limited domain size causes differences between the simulated and measured ion energy distributions. In order to make the simulated ion distribution comparable to the experimentally measured one, a transfer function  $g(f)$ ,

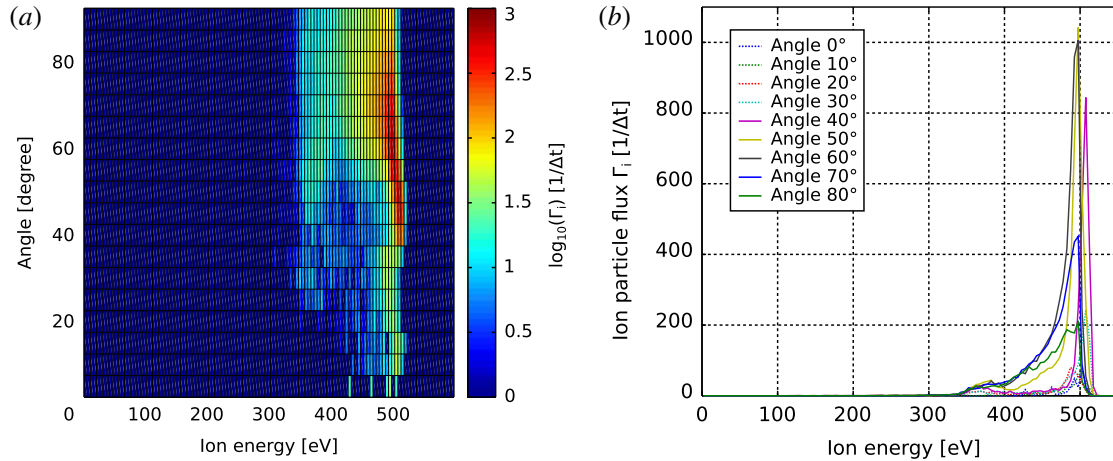


FIGURE 6. Mapped angular ion energy distribution to the location of the experimental detector position. (a) Contour plot of the ion particle flux  $\Gamma_i$  in logarithmic scale as a function of angle and ion energy. (b)  $\Gamma_i$  in linear scale as a function of ion energy shown for nine angles.

similar to the detector function in Reiter (2009), is used to transfer information from the domain boundary to the detector position in the experiment

$$g : f(\text{domain boundary}) \mapsto f(\text{detector position}). \quad (3.1)$$

Here  $f$  stands for the angular ion energy distribution. This correction is used to represent effects which are not included in the current PIC simulation. One artefact caused by the limited domain size originates from the von Neumann boundary condition at the right-hand side of the domain. Ions reaching the diagnostic surface at this location have not yet reached the maximum kinetic energy of  $U_a$ . For small angles, 0°–30°, one can clearly see in figure 4 a reduction of the maximum energy, which is decreasing with the angle. At the detector position 1 m distant from the thruster exit, the potential will have relaxed to values close to ground potential and the additional acceleration by this potential drop has to be taken into account. Therefore, the transfer function  $g(f)$  of the angular ion energy distribution corrects the ion energies of the detected ions by adding the additional potential at the domain boundary

$$f(\text{detector position}) = f(\text{domain boundary}) + q_i \Phi(\text{domain boundary}), \quad (3.2)$$

with the ion charge  $q_i$ . In figure 6, the corrected angular ion energy distribution can be seen. For angles  $< 35^\circ$ , the correction results in a shift to higher energies, so that for all angular bins the maximum energy corresponds to the anode potential  $U_a$ . This improves the qualitative agreement between simulation and measured ion energy distribution (see figure 5).

Another discrepancy between experiment and simulation are the missing ion charge exchange (CX) collisions during the 1 m of flight within the plume. Within the PIC simulation, domain charge exchange collisions between ions and neutrals are fully included. While within the acceleration channel the mean free path of these collisions is smaller than the channel length, the decreasing neutral density increases this mean free path to approximately 1 m, which is larger than the simulated domain size. Therefore, CX collisions appearing between the domain boundary of the simulation

and the position of the experimental measurement of the ion energy distribution are not represented within this simulation due to the latter's limited domain size and require special corrections. This is visible in the missing low energetic part of the ion energy distribution of the simulation (figure 4), which clearly appear in the experimental measurements at about 0–200 eV (figure 5). Here the idea of the transfer function, trying to map the information from the boundary of the simulated domain to the location of the experimental measurement, can be improved using a Monte Carlo post-processing procedure including CX collisions for a pre-defined neutral background gas density in the vessel.

#### 4. Conclusions

Although angular ion distributions are important parameters in experiments and the validation of ion thruster simulations, measurements and simulations are difficult to compare. Especially for PIC simulations, the measurement distance of these distributions is much larger than the possible domain size. Therefore, a parallelisation strategy is necessary in order to increase the domain size. With a parallel particle pusher, using a particle weighted domain decomposition, a speed up of a factor 2.6 was achieved for 2 nodes with 4 cores, compared to a serial simulation.

Ion angular distributions are sensitive to the plume potential. Secondary electron emission at vessel walls due to impinging fast ions can modify the potential structure in the near-field region of the plume and by this the ion angular distributions. As shown in previous studies (Duras *et al.* 2016), only near-axis electron sources are able to change the plume potential. In addition the magnetic field of the thruster guides most of the emitted secondary electrons towards the channel axis. Therefore a near-axis surface source was implemented at the domain boundary, which affects only the small angles in the ion angular current distribution as expected.

The small domain size leads to artefacts at the domain boundary, because the potential does not drop to zero within this domain size. The concept of a transfer function was introduced to map the simulated ion angular distribution from the computational boundary to the location of the experimental measurement at approximately 1 m. For this, the potential energies of the ions were corrected, shifting them by the potential at the domain boundary. This improves the qualitative agreement between simulation and measured ion energy distribution. In the future, a further improvement of the transfer function is possible including the effect of charge exchange collisions in the plume plasma by a Monte Carlo module, following the ions from the domain boundary to the location of the detector.

#### Acknowledgements

This work was supported by the Bavarian State Ministry of Education Science and the Arts and the German Space Agency DLR. We also like to thank R. Heidemann from THALES Electron Devices GmbH for interesting and stimulating discussions.

#### REFERENCES

- BOHM, D., BURHOP, E. H. S. & MASSEY, H. S. W. 1949 *The Characteristics of Electrical Discharges in Magnetic Fields*. McGraw-Hill.
- BRONOLD, F. X., MATYASH, K., TSKHAKAYA, D., SCHNEIDER, R. & FEHSKE, H. 2007 Radio-frequency discharges in oxygen: I. particle-based modelling. *J. Phys. D: Appl. Phys.* **40** (21), 6583–6592.

- DURAS, J., MATYASH, K., TSKHAKAYA, D., KALENTEV, O. & SCHNEIDER, R. 2014 Self-force in 1d electrostatic particle-in-cell codes for non-equidistant grids. *Contrib. Plasma Phys.* **54** (8), 697–711.
- DURAS, J., SCHNEIDER, R., KALENTEV, O., KEMNITZ, K., MATYASH, K., KOCH, N., LÜSKOW, K., KAHNFELD, D. & BANDELOW, G. 2016 Influence of electron sources in the near-field plume in a multistage plasma thruster. *Plasma Physics and Technology* **3** (3), 126–130.
- HAYASHI, M. 2003 Bibliography of electron and photon cross sections with atoms and molecules published in the 20th Century – Argon –. *Res. Rep. NIFS-Data Series*, NIFS-DATA-072.
- KAHNFELD, D., BANDELOW, G., DURAS, J., LÜSKOW, K., KEMNITZ, K. & SCHNEIDER, R. 2016 Solution of poisson's equation in electrostatic particle-in-cell simulations. *Acta Polytech.* (submitted).
- KALENTEV, O., MATYASH, K., DURAS, J., LÜSKOW, K. L., SCHNEIDER, R., KOCH, N. & SCHIRRA, M. 2014 Electrostatic ion thrusters – towards predictive modeling. *Contrib. Plasma Phys.* **54**, 235–248.
- KOCH, N., HARMANN, H.-P. & KORNFELD, G. 2007 Status of the THALES high efficiency multi stage plasma thruster development for HEMP-T 3050 and HEMP-T 30250. In *Proceedings of the 30th International Electric Propulsion Conference*, vol. IEPC-2007-110. Electric Rocket Propulsion Society.
- KOCH, N., SCHIRRA, M., WEIS, S., LAZURENKO, A., VAN REIJEN, B., HADERSPECK, J., GENOVESE, A., HOLTSMANN, H.-P., SCHNEIDER, R., MATYASH, K. *et al.* 2011 The hempt concept – a survey on theoretical considerations and experimental evidences. In *Proceedings of the 32nd International Electric Propulsion Conference*, vol. IEPC-2011-236. Electric Rocket Propulsion Society.
- KORNFELD, G., KOCH, N. & HARMANN, H.-P. 2007 Physics and evolution of HEMP-Thrusters. In *Proceedings of the 30th International Electric Propulsion Conference*, vol. IEPC-2007-108. Electric Rocket Propulsion Society.
- KORNFELD, G., SEIDEL, H. & WEGENER, J. 1998 Plasma accelerator arrangement. *Patent PCT/DE99/01708*.
- LI, X. S. 2005 An overview of superlu: Algorithms, implementation, and user interface. *ACM Trans. Math. Softw.* **31**, 302–325.
- MATYASH, K., KALENTEV, O., SCHNEIDER, R., TACCOGNA, F., KOCH, N. & SCHIRRA, M. 2009 Kinetic Simulation of the stationary HEMP thruster including the near-field plume region. In *Proceedings of the 31st International Electric Propulsion Conference*, vol. IEPC-2009-110. Electric Rocket Propulsion Society.
- MATYASH, K., SCHNEIDER, R., MUTZKE, A., KALENTEV, O., TACCOGNA, F., KOCH, N. & SCHIRRA, M. 2010 Kinetic simulations of SPT and HEMP thrusters including the near-field plume region. *IEEE Trans. Plasma Sci.* **38** (9, Part 1), 2274–2280.
- PHELPS, A. V. 2000 Nitrogen atoms and molecules. Retrieved from [http://jila.colorado.edu/avp/collision\\_data/neutralneutral/atomatom.txt](http://jila.colorado.edu/avp/collision_data/neutralneutral/atomatom.txt) (January 2015).
- PHELPS, A. V. 2002 Nitrogen atomic and molecular ions. Retrieved from [http://jila.colorado.edu/avp/collision\\_data/ionneutral/IONATOM.TXT](http://jila.colorado.edu/avp/collision_data/ionneutral/IONATOM.TXT) (January 2015).
- PROCASSINI, R., BIRDSALL, C., MORESE, E. & COHEN, B. 1987 A relativistic monte carlo binary collision model for use in plasma particle simulation codes. *Mem. No. UCB/ERL M87/24*, University of California, Berkeley.
- VAN REIJEN, B., WEIS, S., LAZURENKO, A., HADERSPECK, J., GENOVESE, A., HOLTSMANN, P., RUF, K. & PTTMANN, N. 2013 High precision thrust vector determination through full hemispherical rpa measurements assisted by angular mapping of energy charge state distribution. In *Proceedings of the 33rd International Electric Propulsion Conference*, vol. IEPC-2013-284. Electric Rocket Propulsion Society.
- REITER, D. 2009 The EIRENE code user manual. Retrieved from <http://www.eirene.de> (September 2016).
- ROSENBERG, D. & WEHNER, G. K. 1962 Sputtering yields for low energy He<sup>+</sup>, Kr<sup>+</sup>, and Xe<sup>+</sup>-Ion Bombardment. *J. Appl. Phys.* **33** (5), 1842–1845.
- STOER, J. 2005a *Numerische Mathematik*, vol. 1. Springer.

- STOER, J. 2005*b* *Numerische Mathematik*, vol. 2. Springer.
- TACCOGNA, F., LONGO, S., CAPITELLI, M. & SCHNEIDER, R. 2005 Self-similarity in hall plasma discharges: Applications to particle models. *Phys. Plasmas* **12**, 053502.
- TAKIZUKA, T. & ABE, H. 1977 A binary collision model for plasma simulation with a particle code. *J. Comput. Phys.* **25**, 205–219.
- TSKHAKAYA, D., MATYASH, K., SCHNEIDER, R. & TACCOGNA, F. 2007 The particle-in-cell method. *Contrib. Plasma Phys.* **47** (8–9), 563–594.
- VAHEDI, V., DIPESO, G., BIRDSALL, C. K., LIEBERMAN, M. A. & ROGNLIEN, T. D. 1993 Capacitive RF discharges modelled by particle-in-cell Monte Carlo simulation. I. Analysis of numerical techniques. *Plasma Sources Sci. Technol.* **2** (4), 261.
- YAMAMURA, Y., MATSUNAMI, N. & ITOH, N. 1983 Theoretical studies on an empirical formula for spitting yields at normal incidence. *Radiation Effects* **71**, 65–86.

## INFLUENCE OF ELECTRON SOURCES ON THE NEAR-FIELD PLUME IN A MULTISTAGE PLASMA THRUSTER

DURAS J.<sup>a,b,\*</sup>, SCHNEIDER R.<sup>a</sup>, KALENTEV O.<sup>d</sup>, KEMNITZ S.<sup>c,e</sup>, MATYASH K.<sup>c</sup>, KOCH N.<sup>b</sup>, LÜSKOW K.<sup>a</sup>, KAHNFELD D.<sup>a</sup>, BANDELOW G.<sup>a</sup>

<sup>a</sup> Institute of Physics, Ernst-Moritz-Arndt University of Greifswald, D-17498 Greifswald, Germany

<sup>b</sup> Department of Applied Mathematics, Physics and Humanities, Nürnberger Institute of Technology, D-90489 Nürnberg, Germany

<sup>c</sup> Computing Center, Ernst-Moritz-Arndt University of Greifswald, D-17498 Greifswald, Germany

<sup>d</sup> Biomedizinische NMR Forschungs GmbH am Max-Planck-Institut für biophysikalische Chemie, D-37077 Göttingen, Germany

<sup>e</sup> University Rostock, Institute of Informatics, D-18059 Rostock, Germany

\* julia.duras@uni-greifswald.de

**Abstract.** In order to obtain a better understanding of the near-field plume of a multistage plasma thruster, the influence of an external electron source is investigated by Particle-In-Cell simulations. The variation of the source position showed a strong influence of the magnetic field configuration on the electron distribution and therefore on the plume plasma. In the second part of this work, higher energetic electrons were injected in order to model collision-induced diffusion in the plume. This broadens the electron distribution, which leads to a more pronounced divergence angle in the angular ion distribution.

**Keywords:** Multistage plasma thruster, near-field plume, external electron source, Particle-In-Cell.

### 1. Motivation

Ion thrusters with magnetic plasma confinement can be optimized by modifying magnetic field configuration, anode potential, neutral gas source and neutralizer properties. In the case of neutralizer adjustment, mainly the plume behavior is influenced. For a better understanding of the near-field plume physics, the influence of an external electron source on its properties is studied. Here, position and source distribution are varied and the interaction between magnetic field, potential and plasma densities are investigated. For this purpose a multistage plasma thruster similar to the HEMP thruster [1], [2] was simulated with the Particle-In-Cell method.

### 2. Physics of a multistage plasma thruster

A multistage plasma thruster consists of a rotationally symmetric discharge channel with an anode and an inlet for the propellant at the upstream end, as shown in figure 1. The discharge channel is surrounded by axially magnetized permanent magnet rings with opposite magnetization. Inside the thruster channel a dielectric wall is facing the plasma. At the exit a grounded pole piece is placed. Outside the thruster channel a hollow cathode neutralizer is placed. It provides the thruster with starter electrons for igniting the discharge and neutralizes the out-going ion beam. The permanent magnets generate a magnetic field which points mainly in axial direction especially

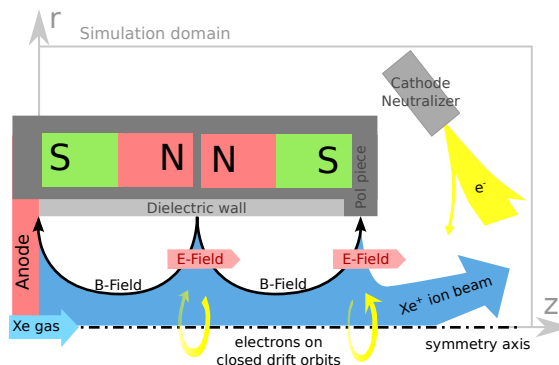


Figure 1. Scheme of HEMP-like thrusters, similar to [3].

in the channel region next to the symmetry axis. In the so-called cusp regions, the magnetic field next to the channel wall is mostly directed in radial direction. In figure 1 three cusps are shown, an anode cusp, an inner cusp and an exit cusp. The magnetic field strength  $B$  is chosen such that the Larmor radius of the electrons is much smaller than the radius of the discharge channel, while for the ions it is larger  $r_{L,e} \ll R < r_{L,i}$ . Therefore, in the thruster channel electrons are magnetized while ions are not. Electrons are created by the neutralizer acting as cathode and experience close to the axis a magnetic field nearly parallel to the axis which directs them towards the anode.

The cusp-structure of the magnetic field builds up

a magnetic mirror in front of the thruster exit. In combination with the potential drop, this magnetic mirror lets the electrons oscillate in a confined electron cloud in the plume originating from the electron source pointing towards the thruster's exit. In the cusp regions, the perpendicular electric and magnetic fields induce a  $\vec{E} \times \vec{B}$ -drift to the electrons in poloidal direction. In addition the magnetic field configuration builds up a magnetic mirror in radial direction and the electrons are reflected before they reach the channel wall. The strong radial magnetic field in these regions separate the different thruster regions. Only few electrons can overcome these regions by collisional and anomalous transport, which is caused by electrostatic turbulence [4]. By this, electron density is increased in the respective downstream cusp region and allows for efficient ionization of the propellant. In the channel regions between the cusps, the electron transport is determined in axial direction by the fields and in radial direction by collisional transport. Therefore, in the regions where no cusps are existing electron losses at the dielectric wall are low and the non-magnetized ions can generate a positive surface charge. The dominance of the axial transport along the magnetic field lines quickly compensates small perturbations of the electric potential and results in a flat potential inside the discharge channel with only small steps at the regions with large radial transport, namely at the cusps. Xenon ions follow the potential gradients and are getting accelerated mostly in the potential drop of the thruster exit. Within the acceleration channel the radial potential gradients towards the wall are rather small and the ion energies are kept below the sputter threshold, hence minimizing erosion. The different dynamics for electrons and ions lead to a spatial separation of ionization in the channel and acceleration at the thruster exit. In order to produce an ion beam with small divergence angle, a grounded magnetic pole piece is placed at the exit cusp. The magnetic field lines are focused in this region and the grounded potential produces in radial direction a large potential drop of  $\Delta\phi = eU_a$ . This guides the electrons to enter the thruster channel and get confined only close to the symmetry axis, which creates an ion lens. The resulting ion beam is strongly affected by the potential structure in this region as well as in the near-field plume region. Here, the magnetized electrons are determining the potential and therefore influencing the ion trajectories.

Therefore, the thruster magnetic field topology and the potential in the plume are important for optimization of the ion beam divergence. Different external electron source positions might change the electron distribution in the plume and therefore potential and angular ion distribution.

### 3. Code description and simulation set-up

The non-Maxwellian characteristics of the electron distribution function in the thruster requires a kinetic method [5]. Due to the rotational symmetry of the system, the spatial domain was reduced to r-z and an electrostatic 2d3v Particle-In-Cell code with Monte Carlo collisions (PIC MCC) [6], [4] was used. In this PIC-MCC simulation we follow the kinetics of so-called Super Particles (each of them representing many real particles), moving in the self-consistent electric field calculated on a spatial grid by solving Poisson's equation. The particle collisions are treated by Monte Carlo Collision (MCC) routines. All relevant collisions are included in the model: electron-electron Coulomb, electron-neutral elastic, ionization and excitation collisions, ion-neutral momentum transfer and charge exchange collisions. The dynamics of the background neutral gas is self-consistently resolved by Direct Simulation Monte Carlo [7]. Plasma surface interactions are provided by a Monte Carlo erosion module. For electrons an anomalous transport model is applied [8]. In order to reduce the computational time a similarity scaling is applied with a factor of 10 [9].

In figure 1, the simulation domain and the thruster geometry are shown. The thruster has a channel radius of  $R = 9$  mm and length of  $L = 51$  mm. The main part of the channel wall is dielectric, at the exit a grounded magnetic pole piece terminates the thruster channel. At the anode a potential of  $U_a = 500$  V is applied. The simulated domain consists of a fine grid of  $890 \times 240$  cells with a grid spacing of  $\Delta r = \Delta z = 0.5\lambda_{D,e} = 0.01$  mm containing the thruster channel and the near field plume. It is overlaid by a courser grid of four times larger cell size, covering the whole domain. The potential boundary condition at the symmetry axis and at the right hand side of the domain is set to zero radial electric field, while at other domain boundaries Dirichlet boundary conditions with  $\phi = 0$  V or  $\phi = U_a$  are applied. For the grounded magnetic pole piece the potential is set to zero. The solution at the domain boundary between fine and coarse mesh is transferred explicitly by boundary conditions between the two meshes.

## 4. Results

### 4.1. Influence of the electron source position

Within PIC ion thruster simulations, the resolved domain is usually too small to simulate the neutralizer at the position of the experiment. Due to the magnetization of the electrons the usage of an effective source, placed at the same magnetic field line as the neutralizer is used. The external source is simulated as a volume source of size  $4$  mm  $\times$   $4$  mm with Maxwellian distributed electrons of a temperature of  $T_e = 2$  eV and a cathode current of  $I_{\text{cath}} = 1.5$  mA.

Four different source positions were chosen in order

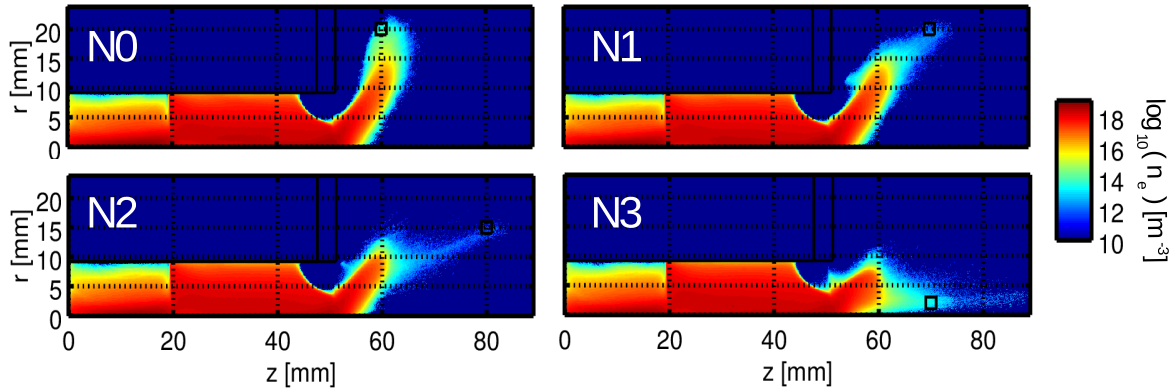


Figure 2. Electron density in logarithmic scale for different source positions.

to study its influence on the plume plasma. In figure 2 the resulting electron density is shown and the black box in the plume indicates the electron source position. The magnetic field lines where the sources N0 and N1 are located, are connected to the front of the metal cap. Sources N2 and N3 aim at the thruster exit. The positions were also chosen to represent different magnetization strengths of the source electrons. While the  $B$ -field strengths at positions N1 and N3 are similar, it is nearly doubled at N0 and nearly the half at N2.

In figure 2 the electron density for the different source position is shown in logarithmic scale. The simulated time to reach steady state was in the range of 2–6  $\mu\text{s}$ , which corresponds to a computation time of 20 up to 60 days. For the four cases the channel plasma is practically not changing. At 20 mm the central cusp is clearly visible, as well as the dominant axial transport by the magnetic field lines close to the  $z$ -axis, which produces a higher density. Due to the electron loss at the anode, the region between anode and central cusp is less filled than the region between the central and exit cusp, where both cusps act as sources of energetic electrons.

For the sources N0–N2, the electron distribution in the near-field plume and close to the exit is changing only in the low density range. The electron density in the range of  $10^{18} \text{ m}^{-3}$ , shown in red, is nearly constant. This distribution is built up by trapped electrons, oscillating between the magnetic mirror and the potential drop. For N2, with lowest magnetic field strength at its source position, electrons are getting accelerated by the potential, which results in a lower density. It increases in the region of higher  $B$  due to oscillation in the magnetic trap. In the case of N0, with highest magnetic field strength at the source position, this appears already in the source region and increases with increasing  $B$ . The electron distribution formed by source N1 shows a mixture of these two cases.

Electrons injected by source N3 fill in a wider area due to the magnetic field configuration in this region.

Since the differences of the electron distribution

generated by sources N0, N1 and N2 are only visible in the low density range, the resulting potentials are quite similar. Only the source position of N3 close to the axis shows an electron distribution expanded towards the symmetry axis. Therefore, the resulting potential, in the first row in figure 3, is given for N0 and N3. It clearly shows a flat potential in the channel, which drops in the plume. At the thruster exit the metal wall is forming a potential drop in radial direction which acts as a lens for the non-magnetized ions. For N3, in comparison to N0, the potential distribution in the plume is compressed in radial direction and stretched in axial direction. This is a result of the broader electron distribution close to the symmetry axis.

Since the ions are not magnetized they follow the potential gradient which determines their angular distribution. At the bottom row in figure 3 the corresponding ion densities for electron source N0 and N3 are shown in logarithmic scale. Within the channel the distribution satisfies very well quasi-neutrality, as expected for a plasma. At the thruster exit the potential drop accelerates the ions into the plume. Due to the different electron distributions in the plume, for N0 the distribution of higher ion density is expanding deeper into the plume than for N3. For the angular ion distribution, the influence of the different electron sources is minor, since in both cases ions show a broad distribution. Only close to the symmetry axis the contribution is higher for N3.

The magnetic field configuration in front of the thruster exit determines the distribution of electrons in the plume, whereas the source position influences the ion distribution in the plume only slightly.

#### 4.2. Thermal versus beam-like electron source

Due to the long run time of PIC simulations, it is not possible to represent the full electron dynamics. In the plume electron and neutral density are two orders lower than in the channel with a typical Coulomb collision time of about 50  $\mu\text{s}$ . Typically, for a runtime of

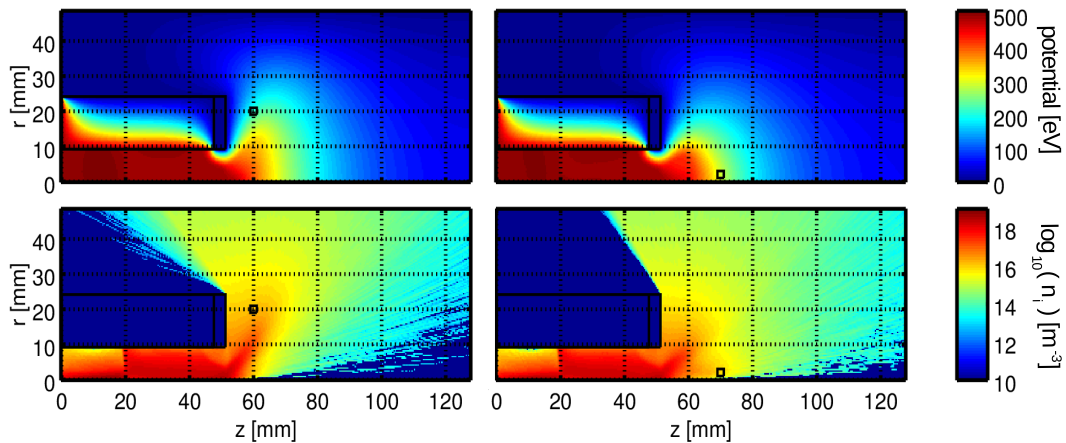


Figure 3. Potential and ion density generated by electron source N0 and N3. The ion density is given in logarithmic scale.

1 month a simulated time in the range of some micro seconds is possible, which does not resolve collision-induced electron diffusion. Therefore, the filling of the plume with electrons guaranteeing quasi-neutrality is not appearing as observed experimentally, as this happens only on the time-scale of collisional transport. In order to investigate this effect an electron beam directed away from the thruster is used as external source. Electrons with a higher velocity have a larger Larmor radius, which broadens their distribution in the plume. To further reduce the influence of the magnetic mirror the source is placed in a region of low magnetic field strength, similar to the one at the source position of N2. The injected electron beam has a thermal energy of 0.1 eV and a drift velocity of 20 eV. It is directed down-stream the thruster plume, with an angle of  $55^\circ$  with respect to the symmetry axis. As before the cathode current is set to  $I_{\text{cath}} = 1.5$  mA. The resulting electron density, potential and ion density are shown in figure 4. Densities are given in logarithmic scale. The black box in the plume indicates the electron source position.

As in the previously studied cases, the shape of the electron distribution in the plume remains very similar. But due to the higher probability to cross magnetic field lines, the distribution is broader. Since the magnetic field lines guide the plume electrons into the thruster this results in a higher density at the thruster exit, which increases the collisional rate, filling up the channel volume. As can be seen in the potential plot in figure 4, the increased electron density in the plume extends the potential drop. This affects the ions, which just follow the potential gradients, and a beam with a more pronounced shape and a dedicated peak at around  $60^\circ$  divergence angle is developing. Due to the higher electron density in the channel and close to the exit, the ionization rate increases which increases the ion density, as can be seen in the bottom plot in figure 4.

In figure 5 the angular current distribution with respect to the symmetry axis is given for the two thermal sources N0 and N3 as well as for the beam-like electron source. This distribution is calculated at the outer domain boundary and the angle vertex refers to the thruster exit  $z = 51$  mm at  $r = 0$  mm. It is given in ion current density within  $5^\circ$  normalized to the total measured ion current density. Both thermal sources produce a flat angular distribution, where for source N3, the higher ion density close to the symmetry axis contributes more at low angles. The more extended electron distribution in the plume generated by the beam-like source directed away from the thruster produces a clear ion beam. This is a characteristics which is also seen in experiments [8].

## 5. Conclusion

In this work the influence of external electron sources on the plume in a multistage plasma thruster was studied. A strong impact of the magnetic field on the electron distribution in the near field plume was observed, especially due to the magnetic mirror effect. The electron distribution was insensitive to the source position in case of a thermal electron source. Only an effective source close to the symmetry axis increases the electron density close to the axis, which leads to higher contribution in the angular current distribution at small angles. In order to overcome calculation time limits and to represent electron diffusion in the plume by collisions, a source of higher energetic electrons directed away from the source was simulated. This produces a broader distribution in the plume, its shape determined by the magnetic field lines. The broader filling produces a more extended potential drop, which generates a pronounced ion beam. In the experiment this effect might be further increased due to a higher neutral background pressure. Also, secondary electrons produced by impinging ions at the vacuum vessel walls can influence the electron

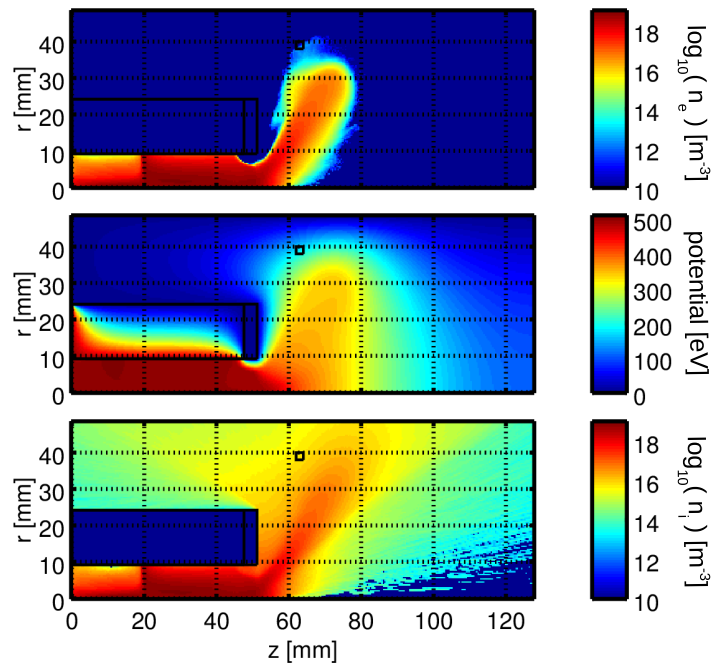


Figure 4. Electron density, potential and ion density for a beam-like electron source directed away from the thruster.

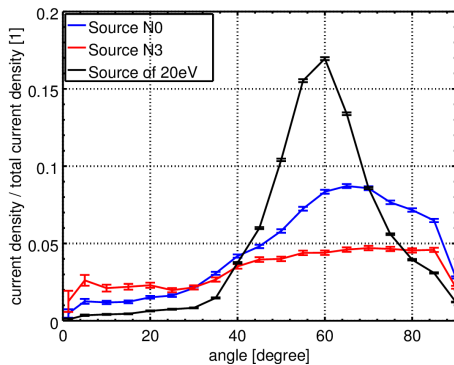


Figure 5. Angular current distribution with statistic error bars and angle given with respect to the symmetry axis.

distribution in the plume acting as additional near-axis source. Due to the magnetic field lines such electrons are guided towards the symmetry axis and would rise the angular current distribution at lower angles.

### Acknowledgements

This work was supported by the "ITSim - Skalierung von Ionentriebwerken mittels numerischer Simulation" project of the Bavarian State Ministry of Education Science and the Arts and the German Space Agency DLR.

### References

[1] G. Kornfeld, H. Seidel, and J. Wegener et al. Plasma Accelerator Arrangement, 1999. Priority: Germany No. 198 28 704.6, filed 26 June 1998.

[2] N. Koch, M. Schirra, and S. Weis et al. The HEMPT Concept - A Survey on Theoretical Considerations and Experimental Evidences . In *Proceedings of the 32nd International Electric Propulsion Conference*, number IEPC-2011-236, 2011.

[3] N. Koch, H.P. Harmann, and G. Kornfeld. Development and Testing Status of the THALES High Efficiency Multistage Plasma (HEMP) Thruster Family. In *Proceedings of the 29th International Electric Propulsion Conference*, number IEPC-2005-297, 2005.

[4] O. Kalentev, K. Matyash, and J. Duras. Electrostatic Ion Thrusters - Towards Predictive Modeling . *Contributions to Plasma Physics*, 54:235–248, 2014.

[5] Karl Felix Lüsrow. Physics of Ion Thrusters' Plumes . Master's thesis, University of Greifswald, July 2013.

[6] K. Matyash, R. Schneider, and A. Mutzke et al. Kinetic Simulations of SPT and HEMP Thrusters Including the Near-Field Plume Region. *IEEE Transactions on Plasma Science*, 38(9, Part 1):2274–2280, 2010.

[7] R. Procassini, C. Birdsall, E. Morese, and Cohen B. A relativistic monte carlo binary collision model for use in plasma particle simulation codes. *Memorandum No. UCB/ERL M87/24*, University of California, Berkeley, 1987.

[8] K. Matyash, O. Kalentev, and R. Schneider et al. Kinetic Simulation of the stationary HEMP thruster including the near-filed plume region. In *Proceedings of the 31st International Electric Propulsion Conference*, number IEPC-2009-110, September 2009.

[9] F. Taccogna, S. Longo, M. Capitelli, and R. Schneider. Self-similarity in Hall plasma discharges: Applications to particle models. *Phys. Plasmas*, 12:053502, 2005.

## Particle-in-Cell Simulation of a Down-Scaled HEMP Thruster

By Tim BRANDT,<sup>1,3,4)</sup> Ralf SCHNEIDER,<sup>2)</sup> Julia DURAS,<sup>2,6)</sup> Daniel KAHNFELD,<sup>2)</sup> Franz Georg HEY,<sup>5)</sup> Holger KERSTEN,<sup>4)</sup>  
Frank JANSEN<sup>1)</sup> and Claus BRAXMAIER<sup>1,3)</sup>

<sup>1)</sup>*DLR, Institute of Space Systems, Bremen, Germany*

<sup>2)</sup>*Institute of Physics, Ernst-Moritz-Arndt University Greifswald, Greifswald, Germany*

<sup>3)</sup>*Center of Applied Space Technology and Microgravity, University of Bremen, Bremen, Germany*

<sup>4)</sup>*Institute of Experimental and Applied Physics, University of Kiel, Kiel, Germany*

<sup>5)</sup>*Airbus Defence and Space, Claude-Dornierstraße 1, Immenstaad, Germany*

<sup>6)</sup>*Department of Applied Mathematics, Physics and Humanities, Nuremberg Institute of Technology, Nuremberg, Germany*

(Received August 8th, 2015)

We present an electrostatic Particle-in-Cell simulation of a downscaled High Efficiency Multistage Plasma Thruster (HEMPT). The purpose of downscaling the HEMPT design is to reach the requirements of missions which have a need for low thrust (0.1...150  $\mu\text{N}$ ) and low noise (root of the noise spectral density  $\leq 0.1 \mu\text{N}/\sqrt{\text{Hz}}$ ). These are upcoming formation flying space missions like eLISA (evolved Laser Interferometer Space Antenna) or NGGM (Next Generation Gravity Mission). The aim of the here presented numerical simulations is to get an improved understanding of the thruster's physics especially in its downscaled configuration, in order to reach the design goals.

**Key Words:** HEMPT, Cusped Field Thrusters, Magnetized Plasmas, Plasma Simulation, Particle-in-Cell Method

### Nomenclature

HEMPT	: High Efficiency Multistage Plasma Thruster
FEMM	: Finite Element Method Magnetics
SCCM	: Standard Cubic Centimeters per Minute
PIC	: Particle-In-Cell
MCC	: Monte-Carlo Collisions
$T_e$	: electron temperature
$k_B$	: Boltzmann constant

### 1. Introduction

Upcoming formation flying space missions like eLISA (evolved Laser Interferometer Space Antenna)<sup>1)</sup> or NGGM (Next Generation Gravity Mission)<sup>2)</sup> create a new demand for highly precise attitude control. In eLISA, three satellites form a space based interferometer. For this interferometer to work properly these satellites must keep the test masses in a drag free environment. The demands lie in the micro-Newton regime for thrust and noise levels with continued operation for several years. One promising candidate to reach these goals is the High

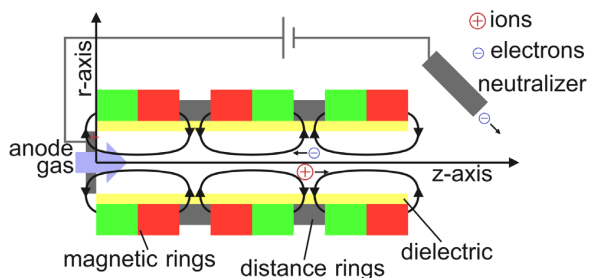


Fig. 1. HEMP thruster principle. Colors red/green to indicate the opposing polarities of the permanent magnets.

Efficiency Multistage Plasma Thruster (HEMPT). This is a new type of grid less thruster with a magnetic field topology which reduces plasma-wall contact. Both being grid less and minimising wall contact enables long live-time, which has been demonstrated in experiments.<sup>3)</sup> The latest models show stable operation over a wide range of parameters. The simple and robust design, due to the use of permanent magnets and direct current, makes it applicable to miniaturization. An effort to downscale this thruster into the demanded thrust and noise regime is undertaken in cooperation of Airbus Defence and Space, the Center of Applied Space Technology and Microgravity (ZARM) of the University Bremen, the Workgroup Plasma Technology of the University of Kiel and the German Aerospace Center (DLR). This campaign consists of a breadboard level model of the thruster,<sup>4)</sup> a highly precise thrust balance,<sup>5)</sup> and computer modeling to support the development.<sup>6)</sup> The first models of the downscaled HEMPT reach the higher  $\mu\text{N}$  regime, but in addition a better understanding of the thrusters inner working is required to reach the low thrust required for e.g. eLISA. The aim of the modeling part of the campaign is to gain this understanding. We present results of the first simulations of a downscaled HEMPT, including its discharge chamber and its near exit region.

### 2. Model Setup

The HEMPT uses a direct current discharge for ion generation, where electron confinement is improved by a static magnetic field with cusps.<sup>7)</sup> Figure 1 shows the thrusters principle. Figure 2 describes the simulation domain in the HEMPT thruster.

A typical HEMPT, like the DM3a thruster, has a discharge channel length of  $Z_{thr} = 51 \text{ mm}$  and inner radius of  $R_{thr} = 9 \text{ mm}$ . With the micro HEMPTs parameters of  $Z_{thr} = 14 \text{ mm}$

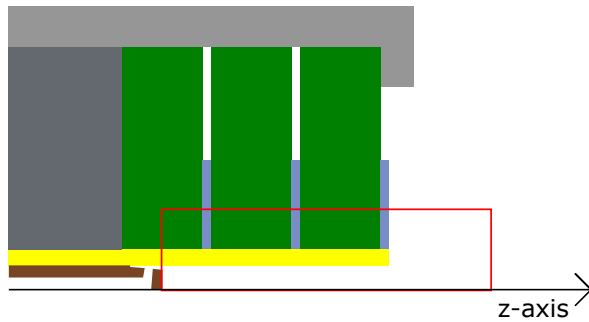


Fig. 2. Simulation domain (red) in comparison to the real thruster. Dielectric (yellow), distance rings (blue-gray), magnets (green), neutral gas inlet (brown), thruster housing (light- and dark-grey).

and  $R_{thr} = 1.5$  mm, it is build 3.6 times smaller in  $z$ -direction and 6 times smaller in  $r$ -direction. While the scaling schema shown by Taccogna et al.<sup>8)</sup> is meant for saving computational time, the idea of applying a geometrical scaling law originates from experimental efforts to miniaturize Hall thrusters.<sup>9)</sup> In principle it could be used for real word application to preserve the thrusters optimum characteristics (specific impulse and efficiency) in a downscaled configuration. Therefore the electron source strength, neutral gas source strength, and magnetic flux density should be scaled accordingly to this law. Due to the inverse dependence of the gyroradius on the strength of the magnetic field, the magnetic field must be increased by the scaling factor to obtain the same magnetization for electrons in the micro HEMPT as in the original HEMP. However, the possibilities of such an increase are limited for permanent magnets. For the same permanent magnet geometry, the maximum flux density stays the same when scaling down. The maximum flux density inside the micro HEMPTs discharge channel (e.g. at  $Z = 11$  mm,  $R = 0$  mm, with  $Z$  being counted from the anode surface) is about 0.6 T. For a 12.5 eV electron the gyroradius is 0.02 mm, which is only about 1 % of the acceleration channel radius of 1.5 mm. This indicates that the magnetic confinement is still effective even in this downscaled HEMPT. Near the magnetic cusps the flux is about 0.2 T and lower, the increase in gyration radii enables the electrons to overcome the cusp structure<sup>10)11)</sup> and reach the anode. At the exit cusp outside the channel the flux is also low (e.g. 0.05 T at  $Z = 17$  mm,  $R = 0$  mm), and the strong electric field drags the electrons inside. When entering the channel, electrons have already a significant portion of the anode potential of 400 eV by acceleration of the potential drop forming at the thruster exit.

The domain for the simulation of the downscaled thruster investigated here is a  $r-z$  plane which corresponds to a cylinder with the radius  $R = 5.12$  mm and the length  $Z = 20.48$  mm. It includes not only the thruster's discharge chamber, but also its near exit region. The  $Z = 0$  position lies at the anode surface. The discharge chamber extends beyond that into a section, which is mostly occupied by the neutral gas inlet and is not modeled in detail. The static magnetic field within this domain is imported from a finite element simulation using the software FEMM (Finite Element Method Magnetics), based on the geometric and material properties of the permanent magnet arrangement. Its  $r-z$  simulation domain consists of a triangular mesh. The resulting flux density in  $r$ - and  $z$ -direction is than

interpolated to the regular grid of the plasma simulation.

The result of a DSMC (Direct Simulation Monte Carlo)<sup>12)</sup> simulation of the neutral gas for an inflow of 0.27 SCCM (Standard Cubic Centimeters per Minute) xenon is imported to create the neutral gas distribution inside the simulation domain. The neutral gas inlet of the thruster redirects the gas so that it directly hits the interior of the discharge chamber wall. This is done to thermalize the neutral atoms. By this, their axial momentum and thus neutral thrust is reduced. Since this section is not part of the simulation, a small volume source was inserted near the place where the actual inlet is. This source inserts the neutrals with a thermal velocity according to the Maxwell-Boltzmann distribution. The neutrals are reflected at the dielectric walls of the discharge channel. In reality the way the particles are reflected depends on the surface roughness and is supposed to lie somewhere between total reflection and diffuse reflection. This value is not known by experiments and can change over time due to ion sputtering. The assumption of solely diffuse reflection gave good agreement between simulated and measured neutral gas thrust. The simulated thrust was calculated by the mass flow and the exhaust velocity, which lies roughly at the average thermal velocity of the neutrals at 500 K. The experiments showed that the overall reduction of neutral gas due to ionization was around 25 %. Considering this relatively low value, and because the timescale of the simulation is too short for significant changes in the neutral gas, it is kept as a static background.

For an average neutral gas density inside the discharge channel of about  $2 \cdot 10^{20} \text{ m}^{-3}$ , the ionization mean free path for an electron at 12.5 eV is 4.76 m. At 100 eV, which is about the energy for the maximum of the ionization cross section,<sup>13)</sup> the mean free path becomes 0.086 m, which is still several times larger than the discharge channel length (0.014 m). This shows the necessity of magnetic confinement.

For the downscaled system to stay the same as the original, additional to the magnetic field strength the neutral gas density must be increased. Only then the Knudsen number, which is the ratio of the mean free path to system length, stays constant. However, for the micro HEMPT the neutral gas flow should be kept low in order to reduce thrust fluctuations caused by non-ionized gas leaving the thruster.

For the plasma simulation, a fully self-consistent kinetic electrostatic Particle-In-Cell (PIC)<sup>14)</sup> modeling code is needed, as this enables to properly represent non-local effects and accurate energy distributions function for all plasma particles. The PIC method is combined with Monte-Carlo collisions (PIC-MCC). In plasma physics PIC is a widely accepted method to obtain a better understanding of the basic physics mechanisms in various systems, because PIC-MCC provides full insight for all (microscopic and macroscopic) parameters. A more detailed description of the PIC-MCC method itself can be found in several reviews.<sup>15)16)</sup>

The principle of PIC is to follow so-called super-particles. Each of them represents the same number of physical particles following the same trajectory as single particles due to their identical mass-to-charge ratio resulting in the same Lorentz

force.

The electric field for the Lorentz force is calculated self-consistently on a spatially equidistant grid from the Poisson equation. In the electrostatic approximation, magnetic field effects are included in the Lorentz force, but are determined just by their external sources (e.g. magnets). Corrections from plasma currents are neglected. Particles experience collisions according to Monte-Carlo collision algorithms. This allows to implement all relevant collision types. For this work electron-neutral elastic, ionisation, excitation, coulomb and charge exchange collisions are implemented. Neutrals are treated as plasma particles with zero charge.

As fully kinetic methods are computationally expensive, an efficient use of MPI (Message Passing Interface) for parallel computing was considered necessary. A number ratio of 1 : 2618 for the so-called super particles to real particles is applied to the xenon ions and electrons. This is to ensure that in the cells at the symmetry axis, for the maximum assumed plasma density, there are no less than six super particles, in order to keep numerical noise low.

Long range electrostatic interactions are resolved on the simulation grid, which has  $1024 \times 256$  cells. The volume  $0 \text{ mm} \leq z \leq 14 \text{ mm}$ ,  $2.5 \text{ mm} \leq r \leq 5.12 \text{ mm}$  is grounded, in order to represent the magnets and their distance rings. The remaining upper domain boundary ( $14 \text{ mm} \leq z \leq 20.48 \text{ mm}$ ) and the right side ( $0 \text{ mm} \leq r \leq 5.12 \text{ mm}$ ) has a potential fixed at 0 V.

The anode lies at  $z = 0 \text{ mm}$  (left side) in the range from  $0 \text{ mm} \leq r \leq 1.5 \text{ mm}$  on a potential of 400 V. It should be noted that in the real experimental setup the grounded boundaries are the walls of the vacuum vessel, which are much further away from the thrusters exit. The chosen domain size and thus the position of the boundaries is a compromise between saving computational time and simulation accuracy.

The cell size of  $\Delta r = 2 \cdot 10^{-5} \text{ m}$  and the timestep  $\Delta t = 3.17 \cdot 10^{-12} \text{ s}$  are chosen in order to resolve the Debye lengths and the electron cyclotron frequency. The spatial domain is two-dimensional (axial and radial), but due to collisions three components in velocity space need to be resolved.

The size of the domain is scaled down by a factor of four to overcome spatial resolution limits. This further reduces the size of the discharge channel within the simulation from  $Z_{thr} = 14 \text{ mm}$  to  $3.5 \text{ mm}$  and  $R_{thr} = 1.5 \text{ mm}$  to  $0.375 \text{ mm}$ . This is done by applying a self-similarity scaling keeping the relevant non-dimensional parameters constant, namely the ratio of system length to gyroradii and to mean free path. The first represents the influence of the magnetisation by the external magnetic field, the second one the collisional effects. In order to preserve the ratio of both the charged particles mean free paths and their gyration radii to the system length, the electron source strength and neutral gas inflow is reduced by the same factor, while the magnetic field strength is increased by this factor. This ensures the physical correctness of the simulation as proven by Ref. 8). However, as soon as surface processes and sources get important the scaling derived for infinite plasmas deviates from the real solution, because the surface to volume ratio changes with system size. The results have to be evaluated carefully for possible surface-dominated effects. For the geometries, densities and currents presented in this work, their values are scaled back for the original sized system.

In order to represent anomalous electron transport caused by fluctuations of the azimuthal electric field, an anomalous transport model is applied. It allows the particles to diffuse across magnetic field lines considering a diffusion coefficient proposed by D. Bohm, E. Burhop, and H. Massey,<sup>17)</sup> using a general derivation given by L. Spitzer in 1960.<sup>18)</sup> The applied diffusion coefficient of  $D_{\perp} = 0.4 \cdot k_B T_e / eB$  is derived from a 3D simulation of a similar thruster model.<sup>19)</sup> Since a diffusion coefficient cannot be applied directly to a particle model, the particles velocity vectors are rotated, which causes their center of gyration to shift. Only the component of the velocity vector perpendicular to the local magnetic field direction is rotated, to ensure that the speed of the electrons along the magnetic field lines does not change. Based on the strength of the diffusion coefficient, a random generator selects electrons on which this procedure is applied. The higher the coefficient, the more electrons are selected. The variable within this coefficient is the local magnetic flux density. This results in the electrons having a diffuse behavior perpendicular to the magnetic field lines, which is dependent on the flux density  $B$ .

At  $r = 1.5 \text{ mm}$  over the distance  $0 \text{ mm} \leq z \leq 14 \text{ mm}$ , surface charge accumulation on the ceramic tube, that forms the discharge chamber, is taken into account. A surface with equal properties is at  $z = 14 \text{ mm}$ ,  $1.5 \text{ mm} \leq r \leq 2.5 \text{ mm}$ , which forms the top end of the ceramic tube. The accumulated charge densities are taken into account in the potential calculation. Also a simple secondary electron emission model is implemented, where 50 % of the electrons are re-emitted with 90 % of their incident energy. All other boundaries for the charged particles are that they are completely absorbed. In the real thruster, the electron source (neutralizer) is located relatively far outside, approximately  $z = 14 \text{ mm}$ ,  $r = 40 \text{ mm}$ . This is far beyond the simulation domain. Strictly following the magnetic field lines, the electrons would not reach the discharge channel from this position, yet the experiments suggest they do. The magnetic field so far outside is weak, hence the electrons gyration radii are large, therefore it is reasonable to assume that they are evenly distributed before they reach the close proximity of the discharge channel exit. Therefore, an approximation is a spatially even distributed source at the maximum  $r$  and maximum  $z$  boundary. Precisely these are the areas  $14 \text{ mm} \leq z \leq 20.48 \text{ mm}$ ,  $3.84 \text{ mm} \leq r \leq 5.12 \text{ mm}$  and  $19.2 \text{ mm} \leq z \leq 20.48 \text{ mm}$ ,  $0.01 \text{ mm} \leq r \leq 3.84 \text{ mm}$ . These two areas combined are the primary electron source of this simulation. The electrons are injected with a thermal energy of 1 eV, enough to give them some initial movement, yet negligible towards the energy they will gain from the 400 V potential drop.

In order to speed up the plasma discharge ignition, an additional electron source was inserted at the discharge channels exit. This source was shut down after  $1.5 \cdot 10^6$  time steps. The complete simulation was run over  $2.4 \cdot 10^7$  time steps.

### 3. Results

Even for larger systems a direct experimental access to the plasma parameters in a thruster is rather difficult. Due to the small size of the HEMP thruster studied in this work it is rather impossible to receive detailed experimental information about profiles inside the thruster. Here, this simulation offers the only

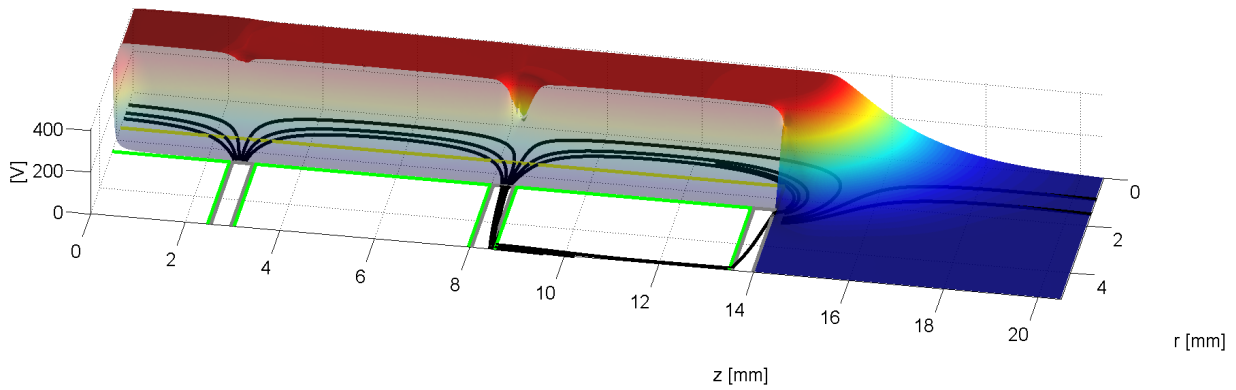


Fig. 3. Computational domain for the simulation of the micro HEMPT with a calculated electric potential profile. Dielectric surface (yellow), distance rings (gray), magnets (green), magnetic field lines (black).

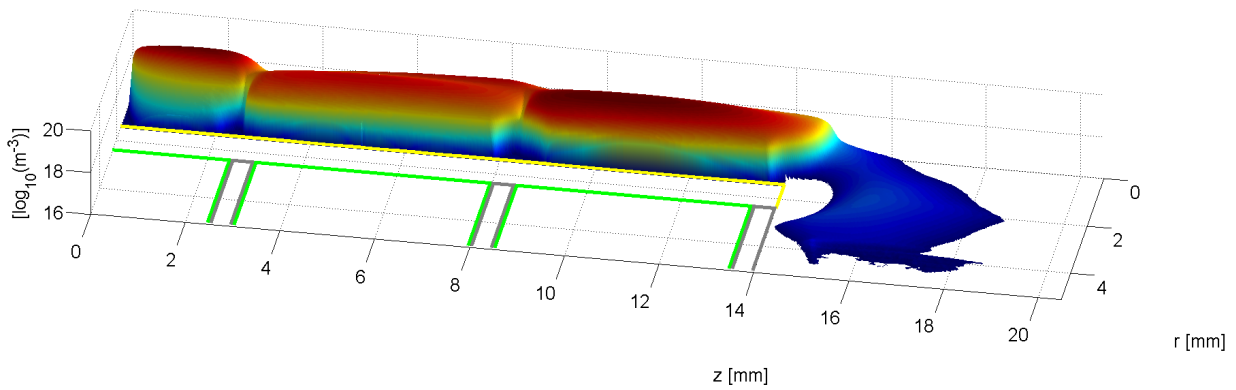


Fig. 4. Electron density profile in the micro HEMPT.

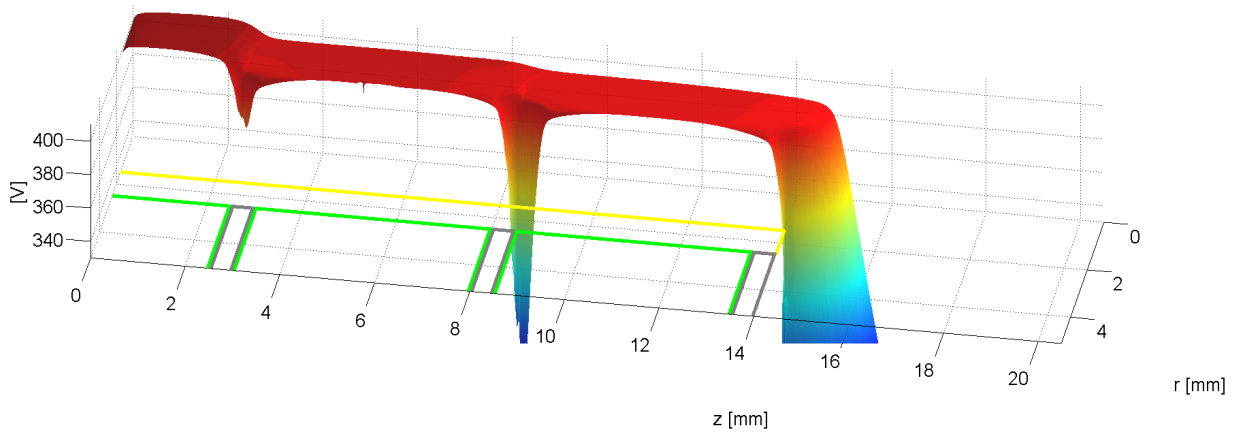


Fig. 5. Electric potential profile, 330 - 410 V, in the micro HEMPT (potential inside the dielectric not shown).

possibility to get an improved understanding of the profiles and physical principles in downscaled HEMPTs. Using the PIC-MCC code one is able to calculate all relevant parameters of the device.

Figure 3 shows the profile of the electric potential for a quasi steady-state condition after a simulated time of  $7.612 \cdot 10^{-5}$  s (averaged over  $1 \cdot 10^6$  time steps). The potential is mostly flat throughout the discharge channel, with a value close to the anode potential.

The potential is determined by the competition of parallel and perpendicular transport of the electrons. The dynamics of

the heavy ions is then a consequence of the quasi-neutrality of the plasma, that means that the overall distribution of electron and ion density minimizes charge separation. Therefore, like in the case of this device, magnetization of the electrons is already sufficient to actively control the dynamics and density of the plasma by magnetic fields. Because the ions just follow the electrons to avoid large electric fields, which anyhow would counteract charge separation on the characteristic length scales larger than a Debye length. The magnetic field structure determines then, like in the case of the larger HEMPT, the electron density, shown in Fig. 4 .

T. BRANDT et al.: Particle-in-Cell Simulation of a Down-Scaled HEMP Thruster

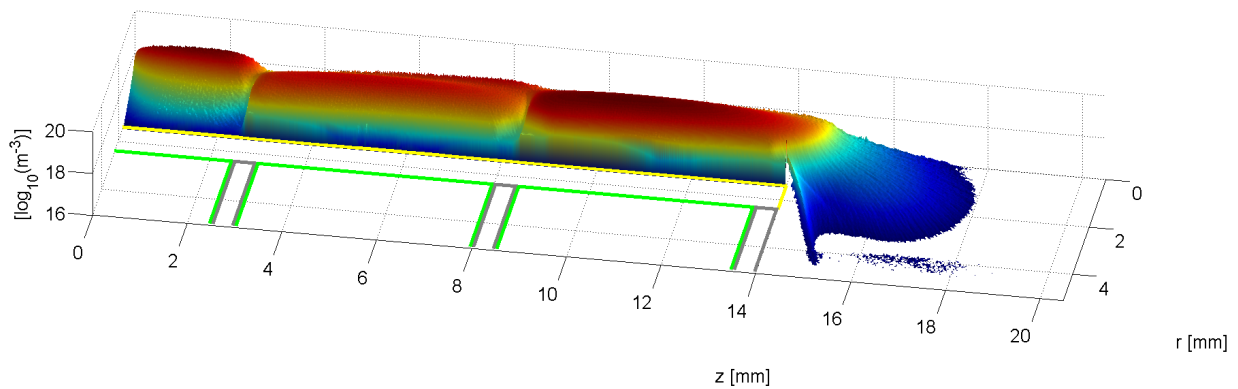


Fig. 6. Ion density profile in the micro HEMPT.

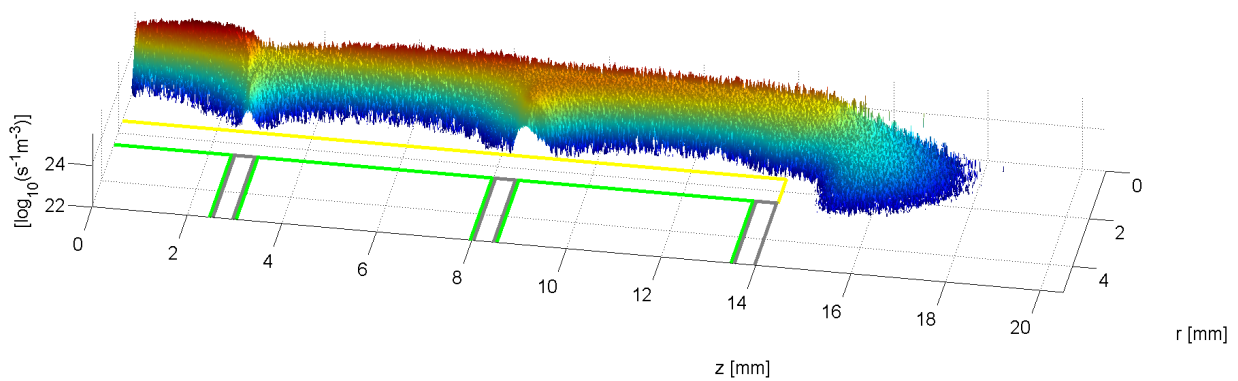


Fig. 7. Ionization rate profile in the micro HEMPT.

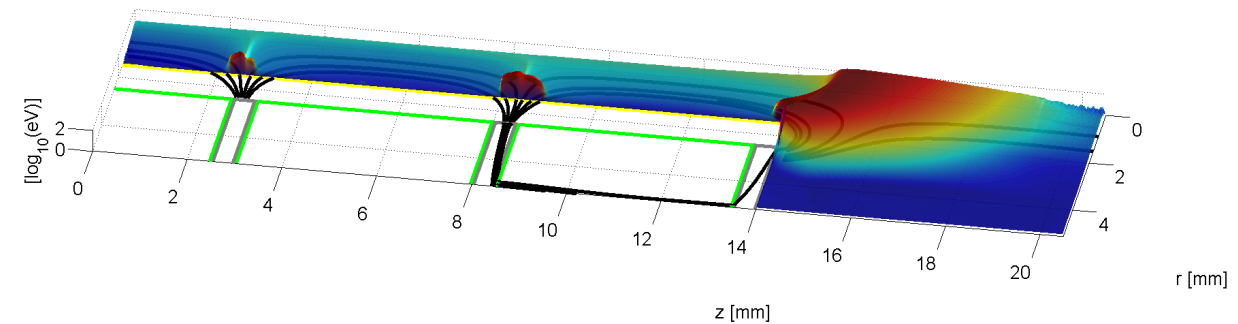


Fig. 8. Electrons energy profile in the micro HEMPT.

Close to the  $z$ -axis the magnetized electrons move practically parallel to it towards the anode and tend to create a rather smooth potential in  $z$ -direction due to the very large parallel transport. Only in the cusp regions electrons are directed towards the dielectric channel wall and produce pronounced maxima of the particle fluxes hitting the surface. In the other regions radial transport has to overcome the magnetic confinement. This is only possible by collisions<sup>20)</sup> or anomalous turbulent transport. In comparison to the larger HEMPT models the electron density fills up the acceleration channel more uniformly, which is a consequence of the larger radial transport in the smaller device studied here. The ratio of gyroradii of the electrons to discharge radius is larger in this smaller device as discussed before and this induces larger transport in radial direction.

The ions have nearly the same density distribution as the electrons to satisfy the quasi-neutrality constraint. The dielectrics produces a radial structure of the potential by the formation of a sheath, which is quite narrow as expected (typically 5 to 10 Debye lengths). In contrast to a metallic wall, the dielectrics is not enforcing a constant potential along its surface, but is determined by the surface charge collected locally, but affecting the potential non-locally as determined by the Poisson equation. The dielectrics are not requiring any explicit boundary condition in the solver, just the change of the dielectric constant and the accounting of surface charges in the boundary cell in front of the dielectrics. The dielectrics in this model is quite narrow (1 mm) and then grounded elements are forcing the potential to 0 V. Figure 5 highlights the potential at 330 – 410 V. Near the anode the plasma potential is about 5 V (relative to the

anode potential of 400 V). At the first magnetic cusp, the potential undergoes a drop of about 10 V. At the second cusp inside the channel, the potential drop is significantly lower, with only about 5 V. At the cusps, the axial movement of the electrons in regions not close to the axis is strongly hindered by the radially directed magnetic field, reducing by this their axial transport and allowing by this axial potential changes. The ions are not magnetized and just follow the electrons. The smaller drop of the potential at the second cusp can be explained, because electrons have here a higher energy and consequently higher gyration radii, which make it easier for them to overcome the cusp. The main potential drop occurs at the exit cusp, beyond the positive ‘anchor’ of the dielectric. Therefore, the overall potential structure is very similar to a grid thruster, but without the life time limitation of ion sputtering at the grid.

Retarding potential analyzer measurements for the down-scaled HEMPT that is modeled here also suggest a single, major potential drop for most of the ions.<sup>21)</sup>

The main potential drop near the thruster’s exit forms a ‘bulge’. This accelerates the ions obliquely away from the symmetry axis, showing the reason for the hollow cone shaped plume which is typical for HEMP thrusters.

The ion density of the entire simulation domain is presented in Fig. 6 (averaged over  $1 \cdot 10^6$  time steps). It illustrates, that the ions just follow the structure of the electron density. Ions have mostly a density of about  $1 \cdot 10^{19} \text{ m}^{-3}$ , which results in a Debye length in the order of magnitude of  $1 \cdot 10^{-2} \text{ mm}$ . With a typical size for a plasma sheath of ten Debye lengths, its size would be  $1 \cdot 10^{-4} \text{ m}$ . This is still significantly smaller than the channel diameter of  $1.5 \cdot 10^{-3} \text{ m}$ . Therefore, even in its down-scaled configuration, the HEMPT is still not wall-effect dominated and an application of the self-similarity is possible.

The ionization rate is shown in Fig. 7. The dominant ionization appears close to the axis and in the cusps, where the electrons are trapped, and at the thruster’s exit, where the source electrons get accelerated by the potential drop into the thruster, very similar to the larger HEMP. There is a peak in the ionization rate upstream of each cusp, which can be explained by the electrons gaining additional energy as they are kinetically heated in the cusp traps and then move towards the anode. In the simulation the electron current at the anode is 4.3 mA, which is close to the measured value of 4.5 mA. This means that in the simulation the value of ions, which are generated and not lost to the wall (‘recycled’ after wall contact as neutrals), is  $2.7 \cdot 10^{16}$  particles per second. Compared to the neutral gas influx of  $1.1 \cdot 10^{17}$  particles per second, this gives an ionization rate of 24 %, which is close to the value of 25 % derived from the measurements. The ratio of neutral to ion densities inside the channel is significantly different, with about 50 times more neutrals. This is due to the relatively slow moving neutral gas, by design of the neutral gas inlet. The primary electron source in the simulation has a value of 17.55 mA, with 11.7 mA passing the maximum- $r$  boundary. The electrons from this source do not reach the thruster. From the remaining 5,85 mA, it is estimated that a third of them reach the thruster. This gives a ratio from anode current to primary current of about 9, far lower than for non-downscaled HEMPTs, which means a more linear response to the electron source. It should be investigated by experiments, whether this results in better system control

possibilities.

The electrons energy is displayed in Fig. 8. There is a high energy region of around 200 eV near the exit cusp, where the electrons gain energy through the main potential drop. Inside the thruster the trapping of electrons in the magnetic mirror-like cusp configurations produce a kinetic heating of the electrons. By this and the trapping of electrons in between the cusps an increased ionization is obtained.

Electron trajectories in Fig. 9 show that the electrons spent a significant amount of time in the cusp outside the thruster, before they are able to enter. For electrons with higher energies their gyration radii are comparable to the cusps size, which enables them to overcome the exit cusp. If this would not be the case, filling of the thruster by source electrons would be very difficult. As the electrons enter the thruster, they have sufficient energy after being accelerated by the potential drop close to the exit to cause ionization.

For long-term operation the sputtering of the dielectrics has to be analysed. For this, the particle flux and mean energies of the ions hitting the dielectric surface is shown in Figs. 10 and 11. The maxima in particle fluxes and mean energy appear as expected at the cusp locations. The most critical area for sputtering is the cusp inside the acceleration channel close to the exit of the thruster, with ion energies up to 160 eV. For a worst case estimate experimental values for sputter yields one gets from experimental measurements a value of  $2,97 \cdot 10^{-3} \text{ mm}^3/\text{C}$ .<sup>22)</sup> At this location one gets a current flux density of  $640 \text{ A/m}^2$ . For an operation time of 100 hours that gives a maximum erosion of 0,684 mm. At all other locations the erosion is practically zero due to the much lower mean energies.

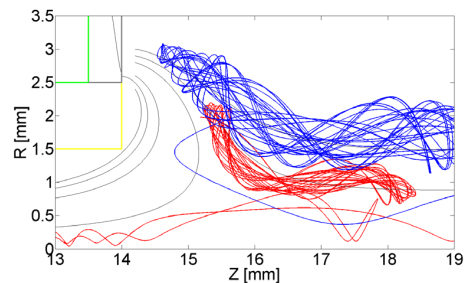


Fig. 9. Two electron particle traces (red and blue).

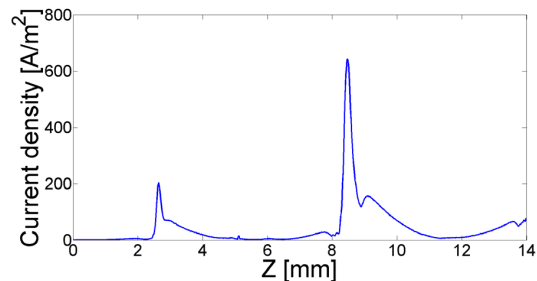


Fig. 10. Density of ion current towards the discharge channel wall.

Another important quantity for ion thrusters is the angular distribution of the ion current. For this, the boundary cells are used to count the ions reaching them. From the location of the cells the angle with respect to the axis at the thruster exit is calculated and the ion flux is determined in 5 degree steps.

T. BRANDT et al.: Particle-in-Cell Simulation of a Down-Scaled HEMP Thruster

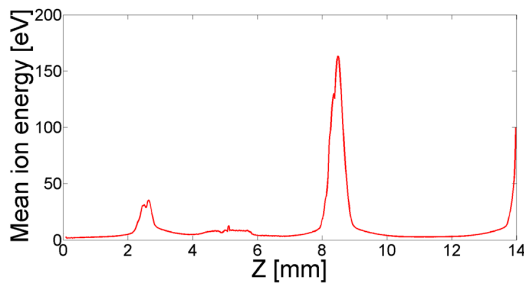


Fig. 11. Mean ion energy at the discharge channel wall.

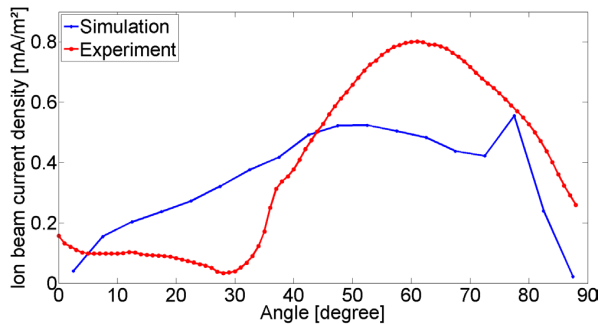


Fig. 12. Angular ion beam current distribution.

The simulated values can be compared to Faraday cup measurements.<sup>23)</sup> The Faraday cup is moved in a radius of 40 cm around the discharge chamber exit in one degree steps. Figure 12 shows the results for both measurements and simulations. The peak of the simulated ion current is about the same height, while there are deviations at lower angles, the angular profile shows similarity with the measurements at higher angles. The maximum lies at about 60 degrees in the experiment and 50 degrees in the simulation. The deviations between simulation and experiment are expected, because the outer simulation domain is still too small, as was tested changing the potential boundary conditions from Dirichlet (potential set to 0 V) to von-Neumann (electric field set to zero V/m) conditions. In case of a sufficient large domain this should not change the results, but here the potential distribution close to the boundary is still strongly affected. One should note that overall structure is not changing, but the ratio between ion currents at smaller and larger angles and the exact location of the maximum will vary. Further simulations with larger domain size will resolve this problem. From the angular distributions the overall ion beam current can be calculated, resulting in 2.5 mA, which is similar to the value of 3.1 mA<sup>23)</sup> derived from the experiment.

#### 4. Conclusions and Outlook

The electrostatic Particle-in-Cell simulation of this down-scaled HEMP thruster shows a flat potential inside the thruster, which is typical for normal sized HEMPTs, with a strong potential drop at the exit very similar to a grid thruster. The electron density distribution inside the acceleration channel is radially broader than in the normal HEMPT due to the larger ratio of gyroradii of the electrons to discharge radius, which induces larger transport in radial direction. The ion density follows the electron density due to the quasi-neutrality constraint in plas-

mas.

The angular distribution of the ion beam in the simulation reproduces the hollow cone seen in the experiment, with some deviations due to the limited size of the plume region. The simulated ion beam current value agrees quite well with experiment. As in the larger HEMPT systems erosion is minimized by the rather small mean energies of the ions reaching the di-electrics. Only at the second internal cusp close to the exit some erosion can happen, without limiting the operational scenarios. A better model will need an extension of the simulation domain including larger plume volumes. The simulation time was sufficient to reach steady state. Thrust oscillations as observed in the experiment appear on a timescale where the neutral dynamics interact with the plasma dynamics through ionization, resulting in breathing modes. To resolve this an increase of the simulation time by about one order of magnitude is needed. As an alternative the possibility will be investigated to run charged and neutral particles on alternating different time scales, in a similar fashion as it is done with the electrons and ions in the F3MPIC<sup>24)</sup> code.

#### Acknowledgments

The main author would like to thank Dr. Rodion Groll (ZARM), whose neutral gas simulation of this thruster provided a valuable reference. The authors are grateful to Dr. Thomas Trottenberg for a careful reading of the manuscript and making several useful suggestions. We also thank Dr. Ulrich Johann for stimulating discussions.

#### References

- 1) Vallisneri, M.: Low-frequency Gravitational-Wave Science with eLISA/NGO, *arXiv:1202.0839 [gr-qc]*.
- 2) Silvestrin, P., Aguirre, M., Massotti, L., and Cesare, S.: Next Generation Gravity Mission: a Step Forward in the Earth's Gravity Field Determination, Conference Paper, EGU General Assembly 2009, Volume: Vol. 11.
- 3) Kornfeld, G., Koch, N., and Coustou, G.: The Highly Efficient Multi-stage Plasma (HEMP) Thruster, A New Electric Propulsion Concept Derived from Tube Technology, 4th IEEE International Conference on Vacuum Electronics, 2003.
- 4) Keller, A., Köhler, P., Georg, F. H., Berger, M., Braxmaier, C., Feili, D., Weise, D., and Johann, U.: Parametric Study of HEMP-Thruster, Downscaling to  $\mu$ N Thrust Levels, proceeding IEP-2013-269.
- 5) Georg, F. H., Keller, A., Papendorf, D., Braxmaier, C., Tajmar, M., Johann, U., and Weise D.: Development of a Highly Precise Micro-Newton Thrust Balance, proceeding of 33rd International Electric Propulsion Conference, At The George Washington University, Washington, D.C., USA.
- 6) Brandt, T., Trottenberg, T., Groll, R., Jansen, F., Georg, F. H., Johann, U., Kersten, H., and Braxmaier, C.: Particle-in-Cell Simulation of the Plasma Properties and Ion Acceleration of a Down-Scaled HEMP-Thruster, 4th International Spacecraft Propulsion Conference, 2014, Cologne, Germany.
- 7) Leung, K. N., Hershkovitz, N., and MacKenzie, K. R.: Plasma Confinement by Localized Cusps, *Physics of Fluids*, **19** (1976), pp. 1958-1988.
- 8) Taccogna, F., Longo, S., Capitelli, M., and Schneider, R.: Self-similarity in Hall Plasma Discharges: Applications to Particle Models, *Physics of Plasmas*, **12** (1994), pp. 2005.
- 9) Khayms, V.: Ph.D. thesis, Dept. of Aeronautics and Astronautics, Massachusetts Institute of Technology, Boston, 2000.
- 10) Van Norton, R.: The motion of a Charged Particle near a Zero Field

Trans. JSASS Aerospace Tech. Japan Vol. 14, No. ists30 (2016)

- Point, New York University: Courant Institute of Mathematical Sciences, 1961.
- 11) Shinano, K. and Ito, H.: Behavior of a Charged Particle in a Cusp Field, *J. Phys. Soc. Jpn.*, **21** (1966), pp. 1822-1829.
  - 12) Spanier, J. and Gelbard, E. M.: Monte Carlo Principles and Neutron Transport Problems, Addison Wesley, 1969.
  - 13) Perkins, S. T., Cullen, D. E., and Seltzer, S. M.: Tables and Graphs of Electron-Interaction Cross Sections from 10 eV to 100 GeV Derived from the LLNL Evaluated Electron Data Library (EEDL), Z = 1 to 100, November 12, 1991.
  - 14) Hockney, R. W., and Eastwood, J. W.: Computer Simulation Using Particles, Adam Hilger, 1988.
  - 15) Birdsall, C. K., and Langdon, A. B.: Plasma Physics via Computer Simulation; Series in Plasma Physics, CRC Press, 2004.
  - 16) Tskhakaya, D., Matyash, K., Schneider, R., and Taccogna, F.: The Particle-In-Cell Method, *Contributions to Plasma Physics*, **47** (2007), pp. 563-594.
  - 17) Bohm, D., Burhop, E., and Massey, H.: The Characteristics of Electrical Discharges in Magnetic Fields, New York: McGraw-Hill, 1949.
  - 18) Spitzer, L.: *Physics of fluids*, **3** (1960), pp. 659-661.
  - 19) Kalentev et al: Electrostatic Ion Thrusters - Towards Predictive Modeling.
  - 20) Wright, J. P.: Diffusion of Charged Particles across a Magnetic Field Due to Neutral Particles, *Physics of Fluids*, **3** (1960), pp. 1958-1988.
  - 21) Keller, A., Köhler, P., Feili, D., Berger, M., Braxmaier C., Weise, D., and Johann, U.: Feasibility of a Down-Scaled HEMP-Thruster, proceeding IEPC-2011-138.
  - 22) Tartz, M., Heyn, T., Bundesmann, C., and Neumann, H.: Measuring Sputter Yields of Ceramic Materials, proceeding IEPC-2009-240.
  - 23) Keller, A., Köhler, P., Georg, F. H., Berger, M., Braxmaier, C., Feili, D., Weise, D., and Johann, U.: Parametric Study of HEMP-Thruster Downscaling to  $\mu\text{N}$  Thrust Levels, *IEEE Transactions on Plasma Science*, **43** (2014), pp. 45-53.
  - 24) Lucca, F. A., Young, C. V., Manente, M., Pavarin, D., and Cappelli, M. A.: Ion Velocimetry Measurements and Particle-In-Cell Simulation of a Cylindrical Cusped Plasma Accelerator, *IEEE Transactions on Plasma Science*, **43** (2014), pp. 54-63.



## Particle-in-cell simulation of the cathodic arc thruster

Karl Felix Lüsrow,<sup>1,a)</sup> Patrick R. C. Neumann,<sup>2,b)</sup> Gunnar Bandelow,<sup>1</sup> Julia Duras,<sup>3</sup>  
Daniel Kahfeld,<sup>1</sup> Stefan Kemnitz,<sup>4</sup> Paul Matthias,<sup>1</sup> Konstantin Matyash,<sup>1</sup>  
and Ralf Schneider<sup>1</sup>

<sup>1</sup>*Institute of Physics, Ernst-Moritz-Arndt University of Greifswald, 17489 Greifswald, Germany*

<sup>2</sup>*Neumann Space Pty Ltd., 41 Wood Avenue, Brompton 5007, South Australia, Australia*

<sup>3</sup>*Department of Applied Mathematics, Physics and Humanities, Nuremberger Institute of Technology, 90489 Nuremberg, Germany*

<sup>4</sup>*Institute of Computer Science, University of Rostock, 18059 Rostock, Germany*

(Received 7 November 2017; accepted 26 December 2017; published online 12 January 2018)

The cathodic arc thruster is a newly developed electric propulsion system. It provides a stream of ions with very high velocities from a solid conducting cathode. This high ion velocity in combination with a high ionization fraction makes the cathodic arc thruster attractive for spacecraft propulsion. In the past, a record-high specific impulse was measured for such thrusters. The thruster uses a voltage of  $-220$  V at the cathode for several microseconds, producing plasma from the cathode material which then streams out of the thruster producing thrust. In this work, a two-dimensional axial-symmetric particle-in-cell code with Monte-Carlo collisions is used to simulate the plasma of a cathodic arc thruster with a simplified wall model for the initial triggering of the arc. The work concentrates on the plasma transport and aims not at a self-consistent description of the arc, including plasma-wall interaction, e.g., description of the erosion and surface heating. The interaction of the arc beam with the background plasma results in a plasma-beam instability. Due to this instability charge separation can be detected that leads to large electric fields. By this electric field, plasma particles are accelerated and contribute to the thrust. *Published by AIP Publishing.*

<https://doi.org/10.1063/1.5012584>

### I. INTRODUCTION

Cathodic arc thrusters are a new development that could permit the delivery of far higher mass fractions to destination orbits due to their high specific impulse.<sup>1</sup> The eroded material from a conducting cathode is ejected by a striking electrical arc between the anode and cathode.<sup>2</sup> Due to its high current discharge, this material is ionized and plasma is accelerated away from the cathode surface.<sup>3</sup> Previous studies measured extremely high ion velocities for such pulsed cathodic arc thrusters. Measurements of erosion rates have confirmed that these thrusters can operate highly efficient.<sup>1,2,4,5</sup>

In order to get deeper insight into the underlying physics, simulations are perfectly suited.<sup>6</sup> Results of simulations can support the experimental development by providing a basic understanding of the system. Due to the non-Maxwellian character of cathodic arc thrusters, a fully kinetic plasma description is needed. Plasma particles have no chance to Maxwellize, due to strong magnetic fields, very fast electrons from the initial arc and, in consequence, mean free paths longer than the device dimension. Particle-In-Cell with Monte-Carlo collisions (PIC-MCC) is a widely used kinetic method to simulate a plasma and is used in this work to study the time-dependent behavior of a cathodic arc thruster.

### II. BASICS

Pulsed cathodic arcs are high current, low voltage discharges at low pressure that ablate and ionize the cathode

material and then accelerate that material away from the cathode surface in small regions known as cathode spots.<sup>7</sup> This results in a highly ionized quasi-neutral plasma being ejected from the cathode and directed downstream at high velocity.<sup>4</sup> Devices of this type are used for ion implantation and surface modification in industry, in applications ranging from the creation of hard films on the surface of tools to altering the bioactivity of polymer surfaces.<sup>5,8</sup> An application which has been of interest in recent years is that of spacecraft propulsion, where the high ion velocity implies that a flight-rated pulsed arc thruster could operate at specific impulses far greater than current technologies.<sup>1,9,10</sup> The design of experimental systems should be informed by high fidelity simulations that run at conditions experienced in laboratory experiments, so that simulation results can be verified using experimental results.<sup>6</sup> This work presents simulations of the cathodic arc plasma undertaken using PIC-MCC to guide the development of a pulsed arc thruster system.

### III. SIMULATION METHOD

The well-established electrostatic Particle-In-Cell method is combined with Monte Carlo collisions (PIC-MCC). PIC-MCC provides time-dependent information about all microscopic and macroscopic parameters of a plasma. In particular, physical entities like potential, densities of all species, temperatures, and velocity distribution functions can be calculated. For further information about the PIC-MCC method itself, several reviews can be found.<sup>11,12</sup>

The idea behind PIC is to follow the so-called super-particles where one super-particle represents a certain

<sup>a)</sup>lueskow@physik.uni-greifswald.de

<sup>b)</sup>patrick@neumannspace.com

number of physical particles. Due to the same mass-to-charge ratio as a single particle, the super-particle follows the same trajectory as the single particle. The electrostatic electric field is calculated self-consistently by using a Poisson solver on an equidistant rectangular grid. The electrostatic approximation can be used here, because the magnetic fields generated from the electric plasma currents can be neglected compared with the self-consistent electric fields or background magnetic fields (e.g., from coils) acting in the Lorentz force. Collisions between particles are simulated using Monte Carlo collision algorithms. This is valid as long as the collision term in the kinetic equation can be linearized in time, which is valid for the small time steps used in PIC. This allows implementing all relevant types of collisions like electron-neutral elastic, ionization, excitation, Coulomb collisions, neutral-neutral, and charge exchange collisions. Neutrals are treated the same way as plasma particles, but due to their zero charge they experience no electric forces. This is equivalent for the neutral transport to a DSMC (Direct Simulation Monte Carlo) description.

The two-dimensional cylinder symmetric domain used in this study consists of 150 cells in radial and 400 cells in axial direction. To resolve the collision dynamics correctly, all three dimensions in velocity space are resolved. Using a cell size of  $dr = 1$  mm leads to a domain size of  $15 \text{ cm} \times 40 \text{ cm}$ . This guarantees to resolve the shortest length-scale of the system, namely, the Debye scale. A time step of  $dt = 10^{-12}$  s is chosen in order to resolve the fastest time-scale of the system, namely the plasma frequency. Due to slower velocities of ions and neutrals compared to electrons, a sub-cycling can be used for both species. This means that neutrals and ions are pushed only every two hundredth time step. A similar ansatz can be followed for collisions. According to the collision, frequency collisions are performed only every tenth time step.

The magnetic field created by the magnetic coils is calculated using the finite element solver FEMM.<sup>13</sup> A plot of the magnetic field lines including the position of magnetic coils, anode, cathode, cathodic mount, and a trigger pin is shown in Fig. 1. To improve the numerical performance, the size of the system is scaled down by a self-similarity factor of 100 applying a scaling which preserves the ratios of length to gyroradii and mean free path. Consequently, all densities and the magnetic field are multiplied by this factor. By using this scaling, one ensures the correct physical behaviour of the scaled system compared to the real one.<sup>14</sup> The similarity scaling is motivated by the one of Taccogna *et al.*<sup>15</sup>

The potential at all outer boundaries of the domain is set to zero voltage and all particles get absorbed. Also, the anode is grounded, whereas at the cathode a pulsed potential

boundary condition is applied. For the pulse lengths of  $1.7 \mu\text{s} - 220 \text{ V}$  is set at the cathode and electrons are injected into the system at the trigger pin. The voltage of  $-220 \text{ V}$  is chosen according to the experiment of Neumann Space, but the simulation allows every other voltage as a boundary condition. When the pulse has ended there is a cool-down phase of  $0.5 \mu\text{s}$ . During this phase, the cathode is at ground potential and the electron injection is turned off. Afterwards,  $-220 \text{ V}$  is applied again and the injection source is turned on again. During the injection phase, fast electrons of about  $20 \text{ eV}$  are injected at the pin. This mimics the initial arc phase, which is not included self-consistently in the simulation. Electrons move then towards the cathode. If an electron hits the cathode, there is a probability of 1% to sputter a neutral from the cathodic surface according to the approach of Timko *et al.*<sup>16</sup>

As discussed in experimental reviews about arcs,<sup>17,18</sup> one of the most uncertain physics aspects is the triggering mechanism. Several different mechanisms had been proposed for this like thermionic electron emission, photoinduced ionization, sputtering, evaporation, and oxide removal.<sup>19-22</sup> It is still not clear which processes are active for certain conditions. Therefore, and to hold this part of the simulation as simple as possible, the approach of Timko *et al.* is used as the initial trigger for the simulations of arc discharges<sup>16</sup> in this paper. Timko *et al.*<sup>16</sup> were able to reproduce the observed currents. All plasma transport processes resulting from this initial trigger are simulated self-consistently in the code. Further effects in the cathode spot are neglected, e.g., ion emission.<sup>17</sup> Ion emission would contribute mostly to the surface heating which is not included in the model. Ions emitted from the surface will not contribute to the plasma because they experience the sheath in front of the wall and will be redeposited on the cathode delivering additional cathode heating. This paper describes the dynamics of the plasma in the thruster channel. Therefore, the approach for the physics at the cathode is chosen rather simplistic. If one wants to model the dynamics of the arc itself including effects like dynamical cathode spots, other timescales than here would be of interest and a molecular dynamic description is needed like in Ref. 23. In Ref. 17, the equilibration time for a cathodic arc is given as typically larger than  $1 \mu\text{s}$ . In the system analyzed here, the typical pulse length is a few milliseconds and the arc is not fully developed in terms of densities and currents. This dynamic behavior requires a kinetic description of the system, because equilibration is not reached. The electron density stays below  $10^{12} \text{ cm}^{-3}$ . Therefore, electrostatic Particle-in-Cell calculations are appropriate and possible for this system.

These neutrals can be ionized by other fast electrons and ions are created. Every impinging ion that reach the cathode can emit a new neutral. Neutrals that are sputtered from the surface are injected into the system with Maxwell distributed velocities, assuming room temperature.

Electrons are magnetized and stream along the magnetic field lines towards the exit of the thruster. Ions follow electrons due to quasi-neutrality in the plasma and contribute to the thrust. At the end of the pulse after  $1.7 \mu\text{s}$ , all plasma particles left the thruster producing maximum thrust. Only neutrals remain in the thruster as an inventory for higher ionization during the next pulse. After about 4–5 pulses, a

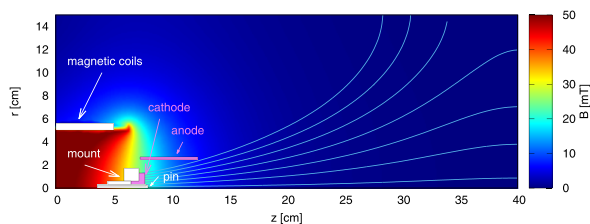


FIG. 1. Magnetic field and simulation domain.

quasi-steady state is reached, because the dynamic relaxation process of the neutrals has saturated and the whole thruster is filled up with neutrals.

#### IV. RESULTS

The large benefit of a PIC simulation is that it allows diagnosing all macroscopic and microscopic quantities time-dependently. Figure 2 shows the behavior of electron and ion densities. The number of super-particles in the system is shown at the top of this figure, left side for electrons and right side for ions. One can see that the number of electrons fluctuates strongly after a short ramp-up phase, whereas the ion number increases continuously and remains afterwards relatively constant until the end of the pulse. Electrons have a very small mass compared to ions; therefore, their dynamic response to changes is much faster. Heavy ions are slow and experience only the time-averaged electric field, like already discussed in detail for radio-frequency plasmas.<sup>24</sup>

The strong fluctuations in the number of electrons are also visible in the different snapshots of the electron density during a pulse, which are shown on the left side of Fig. 2. First, electrons starting from the pin fill up the thruster and by following the magnetic field lines they form a small plume after the exit of the thruster. Ions are created near the cathode and a small plasma builds up (a) during the first  $0.3 \mu\text{s}$ . Therefore, the number of electrons and ions increases monotonically. The plasma density inside the thruster increases especially near the cathode where ions are injected. At time (b), which is after  $0.3 \mu\text{s}$  first fluctuations in the electron density show up and a blob of electrons is separated from the bulk plasma at the thruster exit around  $z = 15 \text{ cm}$ . Afterwards, fluctuations in the electron density begin to increase. Similar to a plasma gun, regions with higher electron density form, separate and are sent out of the thruster (c). After each release of electrons, the plasma reaches a minimum in electron density, whereas the ion density increases further (d). Ions are slower and do not react as fast as electrons. Therefore, electrons are stronger influenced by fluctuations. Electron density builds up again until a critical density is reached. When this limit is reached, new blobs of electrons form and leave the thruster. The electron blobs now get so large that even ions are carried with them due to quasi-neutrality and one can detect small ion blobs (e), too. At this point, the fluctuations have grown so strong that several blobs leave close to the axis with a high frequency, visible at axial positions 20 and 28 cm. After  $1.7 \mu\text{s}$ , the end of the pulse is reached and the anode potential is set to zero Volts. In the plots of super-particle numbers at the top of Fig. 2, this is visible in a strong decrease of the particle numbers of both plasma species. The plasma collapses and only neutrals remain in the thruster channel. For the start of the next pulse, the remaining neutrals act as an inventory for ionization. Therefore, the plasma builds up faster, fluctuations are getting even stronger and the thrust is higher than in the first pulse. After about 4–5 pulses, one reaches a quasi-steady state, because the whole thruster is pre-filled with neutrals.

The fluctuations increase in size and frequency, characteristic of a plasma instability. This instability is responsible for the dynamics of the thruster described before. To identify the underlying effect responsible for these fluctuations, a phase space analysis for electrons is shown in Fig. 3. The plots show the phase space of velocity in axial direction  $v_z$  as a function of axial position  $z$ .

The six plots are snapshots of the phase space taken at the same time as the density snapshots discussed before. In the first plot (a), the thruster fills up with electrons. Beyond the exit of the thruster, which is located at  $z = 15 \text{ cm}$ , fast electrons leave the thruster with velocities larger than  $10^7 \text{ m/s}$ . At time step (b), first fluctuations occur in the density. In the phase space plot first eddies appear, characteristic of a plasma-beam instability. There are fast beam electrons with about  $1.4 \times 10^7 \text{ m/s}$  and background electrons from the plasma in the thruster channel. Considering the densities of beam and plasma electrons, following Birdsall<sup>11</sup> one can estimate the ratio  $R = n_b/n_p \propto \omega_{pb}/\omega_{pp} \approx 0.01$ . This is typical of a plasma-beam instability with a weak beam and a cold plasma.<sup>11,25,26</sup> Taking into account  $R = 0.01$  and following the calculations of Birdsall,<sup>11</sup> the instability frequency can be estimated as  $\omega = 0.93\omega_p = 0.93\sqrt{\frac{n_e e^2}{\epsilon_0 m_e}}$ . Using an average electron density near the cathode of  $n_e \approx 10^{15} \text{ m}^{-3}$ , an instability frequency of  $1.8 \times 10^9 \text{ s}^{-1}$  is obtained. This analytical result is similar to the frequency of the emitted electron blobs that one can see at time step (c), namely  $10^9 \text{ s}^{-1}$ . Three regions of trapped electrons with low energies are visible. Also, three blobs of very fast electrons appear that will leave the thruster during the next time steps. In the fourth plot (d), the instability has reached its maximum, producing also a maximum in the velocity of electrons leaving the thruster. The inventory of electrons in the thruster has to build up again, which is reached in the next time step (e). The phase space plot shows slow trapped electrons in the thruster and also some very fast blobs of electrons that leave the thruster. At timestep (f), the potential is shut down and the bulk plasma leaves the thruster, too.

After identifying the beam-plasma instability, one can explain now the electron blobs dynamics that contribute to the thrust. It is well known that the plasma-beam instability is linked with a time-varying potential, which is shown in Fig. 4. The time steps for the potential plots are the same as for density and phase space.

In the first plot (a), the potential builds up, in plot (b) first potential gradients establish beyond the exit of the thruster, which creates electric fields in the plume. These potential gradients get larger in (c), where for the first time positive potential values are detected. The steep potential gradients that are built up now enlarge the electric fields up to about  $10 \text{ kV/m}$ . Following the simple model of Birdsall,<sup>11</sup> the electric field  $E$  is calculated as

$$\frac{1}{4}\epsilon_0 E^2 = 4m_b n_b v_0 \Delta v \Rightarrow E \approx 4 \times 10^4 \text{ kV/m}. \quad (1)$$

This calculated electric field has the same order of magnitude as the electric field obtained in the simulation. In (d),

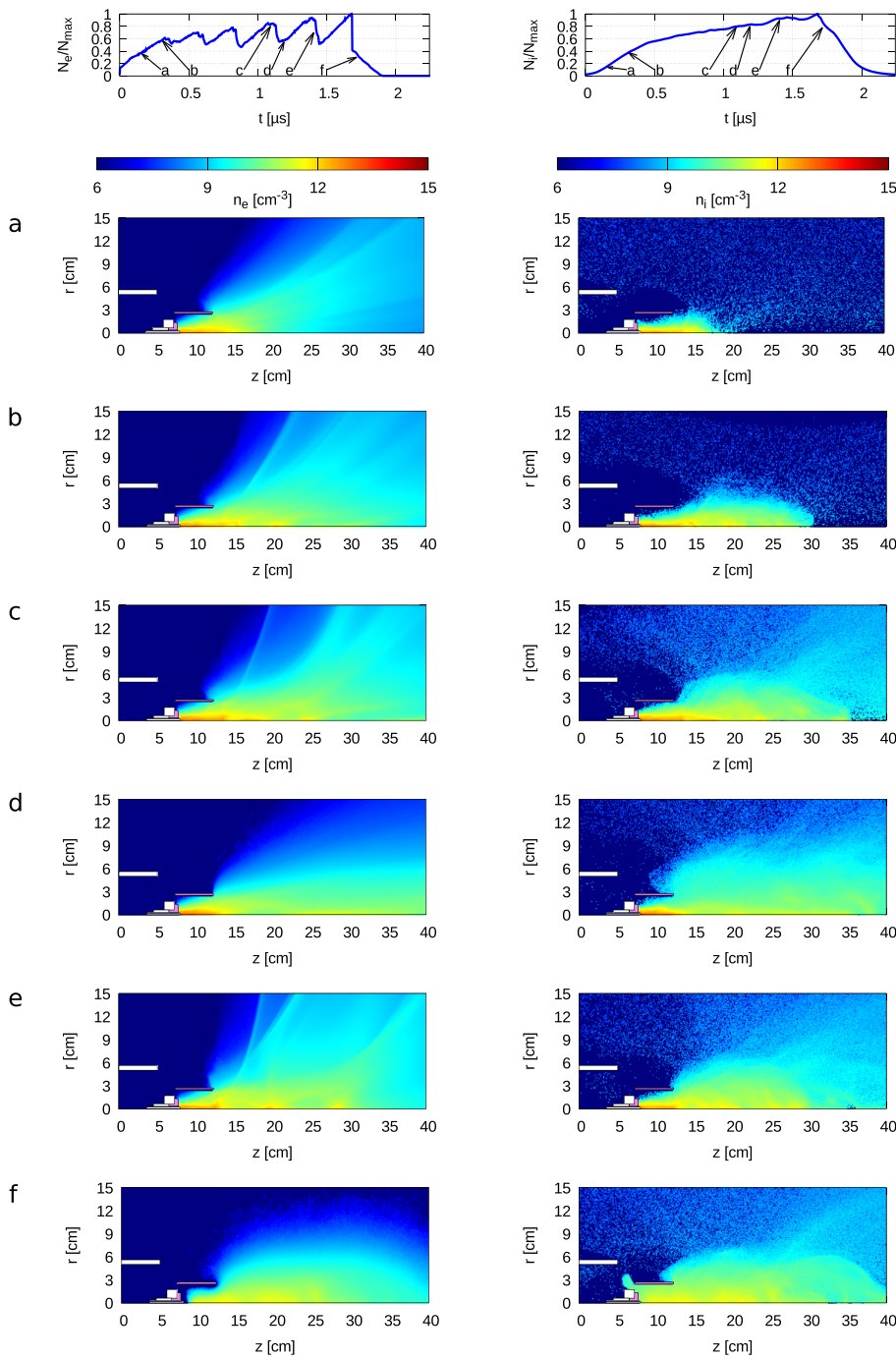


FIG. 2. Electron (left) and ion (right) densities for different time steps during a typical pulse.

the plasma loads again and the potential is again relatively constant with only small gradients. At time step (e), one large potential gradient builds up, the charge separation gets larger resulting in strong electric fields of more than 10kV/m. The dynamics in the plume region is covered by the Poisson equation. Plasma dynamics determines the charge separation and by this the creation of electric fields. Charge separation is possible due to the higher mobility of electrons compared to ions. On longer timescales, quasi-neutrality of plasma will be reached, but for short timescales very high electric fields occur. These very high electric fields accelerate electrons to high velocities, which contribute to the

thrust. In (f), the potential at the cathode is turned off, so that only a positive plasma potential remains. Very fast, all plasma particles leave the thruster and the potential approaches zero before starting with the next pulse. The resulting thrust of a complete run with four pulses is shown in Fig. 5.

The simulated thrust is diagnosed by collecting all particles leaving the thruster and their directed momentum in axial direction. This models the measurement from a pendulum thrust stand. The thrust is diagnosed at the end of the anode, where the thruster exit is located. It shows a pulsed and fluctuating characteristic as shown in Fig. 5 due to the mechanisms discussed before. The thrust in the simulation

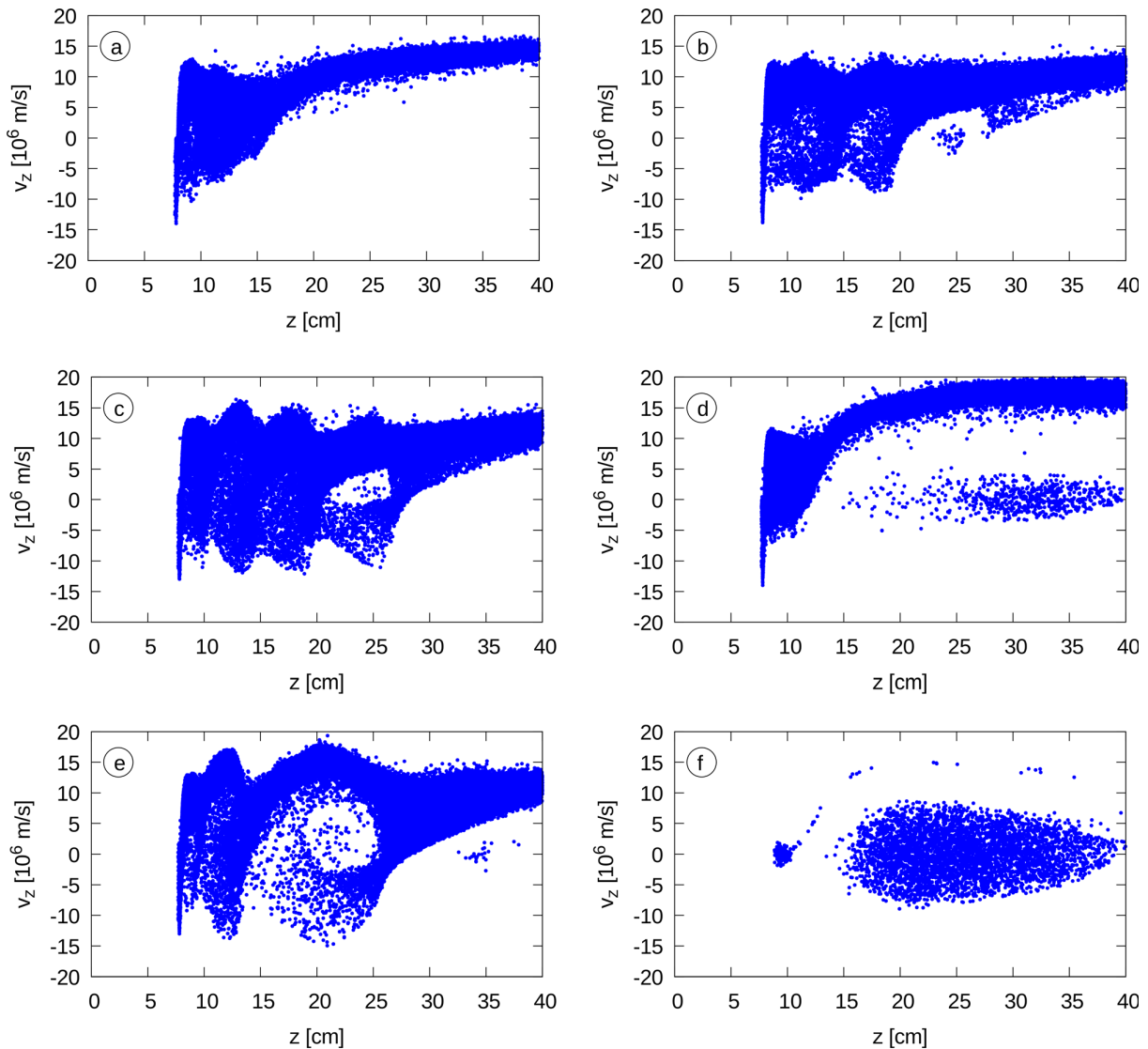


FIG. 3. Phase space of axial velocity as a function of axial position for electrons at different time steps for one pulse.

and in the experiment is of the order of 2 N. Experimentally such thrust values were reached for the same scenarios with currents of about 1 kA. This results in 0.2 mN/A.

## V. DISCUSSION

The plasma dynamics in the simulation is similar to the experimentally observed one of cathodic arcs.<sup>2,27,28</sup> In the experiments, a narrow plasma beam appears as in the simulations. A narrow beam results in a high thrust efficiency due to a better directed stream. In addition, the interaction with other spacecraft components is minimized by a narrow beam. Comparing electron and ion density in the simulation, one can see a higher electron density in the plume. This gives a net electron current as measured in the experiment, not only due to the higher density, but due to the higher electron mobility.<sup>29</sup> This electron current is necessary to sustain the arc discharge experimentally, as it creates the conductive path for the capacitors driving the arc to discharge through

the plasma, depositing energy into the plasma while generating more ionized species.<sup>7</sup> A net electron current is a helpful feature since it mitigates spacecraft charging issues due to charge expulsion.<sup>30</sup> Since ion and Hall effect thrusters are designed to extract and accelerate ions from a discharge plasma, they must also neutralize the exhaust stream; otherwise, the spacecraft would become more negatively charged until the ions return to the spacecraft, thus imparting no momentum. Since there is a net electron current, the spacecraft will gain a positive charge, which environmental electrons should be able to neutralize easily.<sup>31</sup> Thus, there is no need for charge neutralization systems, which will reduce system complexity, mass and failure modes in operational systems.

The calculated thrust in the simulation is in the region of a few Newton, due to the amount of current being modeled. As in the experiment the thrust is pulsed, with the thrust being dominated by ion production. The simulations described here simulate the action of individual cathode spots, while

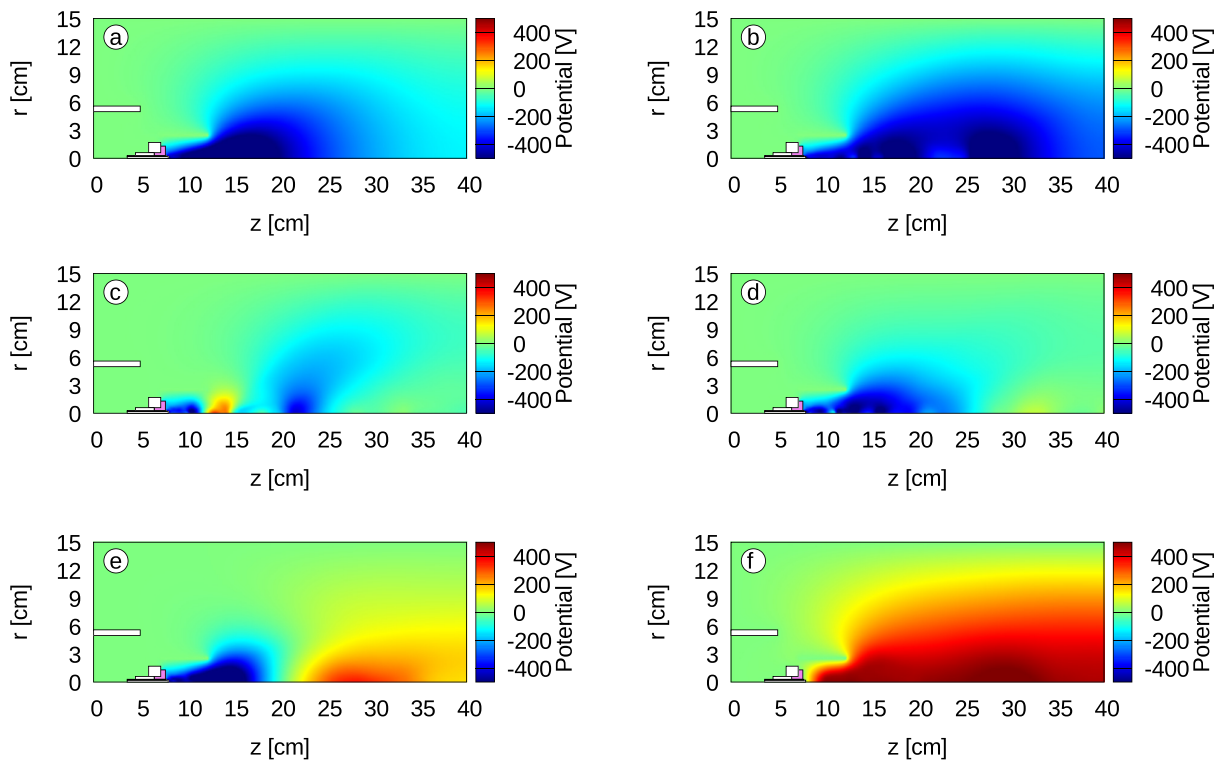


FIG. 4. Plasma potential for different time steps during a typical pulse.

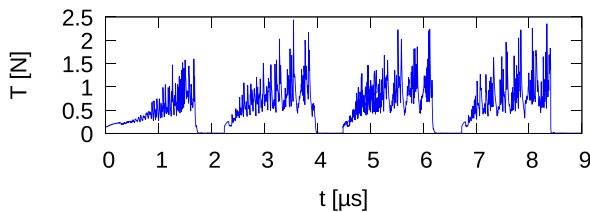


FIG. 5. Simulated thrust created by all species.

experiments with high current pulsed arcs tend to produce several tens of cathode spots; empirically, some 60...80 A of cathode current is carried by each cathode spot, and cathode current can peak at several kiloamps.<sup>7</sup> The actions of the various cathode spots reinforce each other, and so experimental generation of average thrusts on the order of Newtons is common.<sup>1,2</sup>

## VI. CONCLUSIONS AND OUTLOOK

PIC simulations are widely accepted for plasma simulations; in particular, they are well-suited for simulations of electric thrusters. In this study, the PIC method was used to simulate the plasma dynamics of a pulsed cathodic arc thruster with a simplified wall model. This pulsed cathodic arc thruster was developed by Neumann Space. The simulation is able to reproduce basic features of the plasma observed in the cathodic arc thruster. Experimental diagnostics show similar results to the simulation, especially the strongly fluctuating currents and thrust. Analyzing in the simulation the phase space of the electrons, these fluctuations

can be explained by a plasma-beam-instability. The strong fluctuations are beneficial for the operational characteristics of the arc thruster by increasing the thrust. In the future, PIC simulations can be used to study modified magnetic field configurations and their impact on the predicted performance of the arc thruster. To improve the code technically, the rather simplistic model of the surface model can be extended using a strategy as derived by Timko *et al.*<sup>23</sup>

The use of simulations to guide the experimental investigations is invaluable, as it permits a more rapid iteration and testing of prototypes while demonstrating which designs may not be worth exploring. The union of insights from simulation and data from experiment results in better science and engineering than either can do alone.

<sup>1</sup>P. R. C. Neumann, M. Bilek, and D. R. McKenzie, "A centre-triggered magnesium fuelled cathodic arc thruster uses sublimation to deliver a record high specific impulse," *Appl. Phys. Lett.* **109**, 094101 (2016).

<sup>2</sup>P. R. C. Neumann, M. M. M. Bilek, R. N. Tarrant, and D. R. McKenzie, "A pulsed cathodic arc spacecraft propulsion system," *Plasma Sources Sci. Technol.* **18**, 045005 (2009).

<sup>3</sup>J. Daalder, "Cathode spots and vacuum arcs," *Phys. B: Condens. Matter* **104**, 91–106 (1981).

<sup>4</sup>G. Y. Yushkov, A. Anders, E. M. Oks, and I. G. Brown, "Ion velocities in vacuum arc plasmas," *J. Appl. Phys.* **88**, 5618–5622 (2000).

<sup>5</sup>M. Bilek, D. McKenzie, and R. Powles, "Treatment of polymeric biomaterials by ion implantation," in *Biomaterials and Surface Modification* (Research Signpost, Kerala, 2007).

<sup>6</sup>O. Kalentev, K. Matyash, J. Duras, K. F. Luskow, R. Schneider, N. Koch, and M. Schirra, "Electrostatic ion thrusters - towards predictive modeling," *Contrib. Plasma Phys.* **54**, 235–248 (2014).

<sup>7</sup>E. Hantzschke, "Mysteries of the arc cathode spot: A retrospective glance," *IEEE Trans. Plasma Sci.* **31**, 799–808 (2003).

<sup>8</sup>R. Fu, S. Kwok, P. Chen, P. Yang, R. Ngai, X. Tian, and P. Chu, "Surface modification of cemented carbide using plasma nitriding and metal ion

- implantation," *Surf. Coat. Technol.* **196**, 150–154 (2005); in 13th International Conference on Surface Modification of Materials by Ion Beams (2005).
- <sup>9</sup>P. R. C. Neumann, M. M. M. Bilek, and D. R. Mackenzie, "Optimising ion production in pulsed refractory and non-refractory cathodic arcs," in *Proceedings of the 12th Asia Pacific Physics Conference (APPC12)* (JPS Conference Proceedings, 2014), Vol. 1, p. 015059.
- <sup>10</sup>J. E. Polk, M. J. Sekerak, J. K. Ziemer, J. Schein, N. Qi, and A. Anders, "A theoretical analysis of vacuum arc thruster and vacuum arc ion thruster performance," *IEEE Trans. Plasma Sci.* **36**, 2167–2179 (2008).
- <sup>11</sup>L. Birdsall, *Plasma Physics via Computer Simulation* (CRC Press, 2004).
- <sup>12</sup>D. Tskhakaya, K. Matyash, R. Schneider, and F. Taccogna, "The particle-in-cell method," *Contrib. Plasma Phys.* **47**, 563–594 (2007).
- <sup>13</sup>D. Meeker, "Finite element method magnetics," *FEMM* **4**, 32 (2010).
- <sup>14</sup>K. F. Lüsrow, S. Kemnitz, G. Bandelow, J. Duras, D. Kahnfeld, P. Matthias, R. Schneider, and D. Konigorski, "Electrostatic particle-in-cell simulation of heat flux mitigation using magnetic fields," *J. Plasma Phys.* **82**, 595820502 (2016).
- <sup>15</sup>F. Taccogna, S. Longo, M. Capitelli, and R. Schneider, "Self-similarity in hall plasma discharges: Applications to particle models," *Phys. Plasmas* **12**, 053502 (2005).
- <sup>16</sup>H. Timko, F. Djurabekova, K. Nordlund, L. Costelle, K. Matyash, R. Schneider, A. Toerklep, G. Arnau-Izquierdo, A. Descoeudres, S. Calatroni, M. Taborelli, and W. Wuensch, "Mechanism of surface modification in the plasma-surface interaction in electrical arcs," *Phys. Rev. B* **81**, 184109 (2010).
- <sup>17</sup>B. Jüttner, "Cathode spots of electric arcs," *J. Phys. D: Appl. Phys.* **34**, R103 (2001).
- <sup>18</sup>B. E. Djakov and R. Holmes, "Cathode spot structure and dynamics in low-current vacuum arcs," *J. Phys. D: Appl. Phys.* **7**, 569 (1974).
- <sup>19</sup>G. Mesyats, *Cathode Phenomena in a Vacuum Discharge: The Breakdown, the Spark, and the Arc* (Nauka, Moscow, 2000).
- <sup>20</sup>R. Behrisch and K. Wittmaack, *Sputtering by Particle Bombardment* (Springer, Berlin, 1981), Vol. 1.
- <sup>21</sup>J. Rager, A. Flaig, G. Schneider, T. Kaiser, F. Soldera, and F. Mücklich, "Oxidation damage of spark plug electrodes," *Adv. Eng. Mater.* **7**, 633–640 (2005).
- <sup>22</sup>A. Anders, S. Anders, M. A. Gundersen, and A. M. Martsinovskii, "Self-sustained self-sputtering: A possible mechanism for the superdense glow phase of a pseudospark," *IEEE Trans. Plasma Sci.* **23**, 275–282 (1995).
- <sup>23</sup>H. Timko, K. Ness Sjobak, L. Mether, S. Calatroni, F. Djurabekova, K. Matyash, K. Nordlund, R. Schneider, and W. Wuensch, "From field emission to vacuum arc ignition: A new tool for simulating copper vacuum arcs," *Contrib. Plasma Phys.* **55**, 299–314 (2015).
- <sup>24</sup>J. Meichsner, M. Schmidt, R. Schneider, and H.-E. Wagner, *Nonthermal Plasma Chemistry and Physics* (CRC Press, 2012).
- <sup>25</sup>A. B. Mikhailovskii, *Theory of Plasma Instabilities: Instabilities of a Homogeneous Plasma* (Consultants Bureau, 1974), Vol. 1.
- <sup>26</sup>A. Akhiezer and Y. B. Fainberg, "On the interaction of a charged particle beam with electron plasma," *Doklady Acad. Nauk SSSR* **69**, 555–556 (1949).
- <sup>27</sup>R. Sanginés, M. M. M. Bilek, and D. R. McKenzie, "Optimizing filter efficiency in pulsed cathodic vacuum arcs operating at high currents," *Plasma Sources Sci. Technol.* **18**, 045007 (2009).
- <sup>28</sup>L. Ryves, D. R. McKenzie, and M. M. M. Bilek, "Cathode-spot dynamics in a high-current pulsed arc: A noise study," *IEEE Trans. Plasma Sci.* **37**, 365–368 (2009).
- <sup>29</sup>J. Schein, N. Qi, R. Binder, M. Krishnan, J. K. Ziemer, J. E. Polk, and A. Anders, "Inductive energy storage driven vacuum arc thruster," *Rev. Sci. Instrum.* **73**, 925–927 (2002).
- <sup>30</sup>D. M. Goebel and I. Katz, *Fundamentals of Electric Propulsion: Ion and Hall Thrusters* (John Wiley & Sons, 2008), Vol. 1.
- <sup>31</sup>M. Tajmar, "Electric propulsion plasma simulations and influence on spacecraft charging," *J. Spacecr. Rockets* **39**, 886–893 (2002).

## ORIGINAL ARTICLE

# Particle-in-cell simulation of an optimized high-efficiency multistage plasma thruster

Paul Matthias<sup>1</sup>  | Daniel Kahnfeld<sup>1</sup> | Ralf Schneider<sup>1</sup> | Suk Hyun Yeo<sup>2</sup> | Hideaki Ogawa<sup>3,4</sup>

<sup>1</sup>Institute of Physics, University of Greifswald, Greifswald, Germany

<sup>2</sup>School of Engineering, RMIT University, Melbourne, Victoria, Australia

<sup>3</sup>Space Transportation Systems Engineering Laboratory, Department of Aeronautics and Astronautics, Faculty of Engineering, Kyushu University, Fukuoka, Japan

<sup>4</sup>Aerospace Engineering and Aviation, School of Engineering, RMIT University, Melbourne, Victoria, Australia

**Correspondence**

Paul Matthias, Institute of Physics, University of Greifswald, Felix-Hausdorff-Str. 6, Greifswald D-17489, Germany.  
Email: pm101481@uni-greifswald.de

**Present address**

Paul Matthias, ABS gGmbH Seniorenberatungsstelle, Trelleborger Weg 17, 17493 Greifswald, Germany.

**Funding information**

Australian Government Research Training Program; Deutsches Zentrum für Luft- und Raumfahrt, 50RS1510

**Abstract**

Electric propulsion attracts increasing attention in contemporary space missions as an interesting alternative to chemical propulsion because of the high efficiency it offers. The High-Efficiency Multistage Plasma thruster, a class of cusped field thruster, is able to operate at different anode voltages and operation points and thereby generate different levels of thrust in a stable and efficient way. Since experiments of such thrusters are inherently expensive, multi-objective design optimization (MDO) is of great interest. Several optimized thruster designs have resulted from a MDO model based on a zero-dimensional (0D) power balance model. However, the MDO solutions do not warrant self-consistency due to their dependency on estimation from empirical modelling based on former experimental studies. In this study, one of the optimized thruster designs is investigated by means of particle-in-cell (PIC) analysis to examine the predicted performance characteristics with self-consistent simulations. The 0D power balance model is used to develop additional diagnostics for the PIC simulations to improve the physics analysis. Using input parameters for the 0D power balance model from the PIC simulations allows further improvement for the design optimization.

**KEYWORDS**

cusped field thruster, electric propulsion, multi-objective design optimization, particle-in-cell, plasma simulation

## 1 | INTRODUCTION TO HEMP THRUSTERS

The high efficiency multistage plasma thruster (HEMP-T)<sup>[1]</sup> is a class of ion propulsion devices for space systems contrived by Thales Deutschland GmbH.

The HEMP-T thrusters are composed of a cylindrical discharge channel with a dielectric material at the walls. The dielectric has a high sputtering threshold, such as Boron Nitride. The source of the neutral gas is positioned at the centre of the metal anode at the channel bottom.<sup>[2]</sup> A number of ring magnets with pairwise opposite magnetization directions, force a cusp structure of the magnetic field in the discharge channel. It consists of a flat magnetic field at the symmetry axis of the channel and magnetic bottles (cusps) between the ring magnets. The general design concept of a HEMP-T is shown in Figure 1.

The discharge is fed by a cathode neutralizer, which emits electrons in the plume area outside the discharge channel. The positive anode and plasma potential create an electric field, which accelerates the electrons towards the channel. The electrons are magnetized in the channel. In the direction parallel to the symmetry axis the electron transport is strong, because of the axial magnetic field between the cusps, leading to a flat electrostatic potential stretching from the anode to the exit of the thruster.

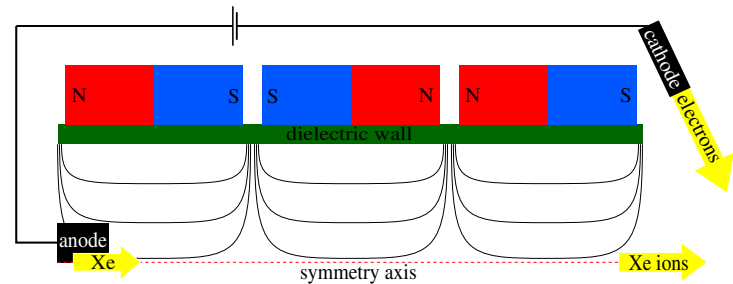


**FIGURE 1** Schematic of a HEMP thruster

The radial magnetic field at the cusps acts like a magnetic bottle. This ensures the reflection of the electrons, while keeping the wall losses to a minimum. As a consequence of the reflection of electrons, the electron temperature in the cusp rises. Only the electrons with very high energies can reach the wall, reducing in the total wall losses by the cusp. Additionally the secondary electrons emitted from the dielectric get accelerated in the sheath, resulting in a rise in electron temperature in the cusps. The confinement of the electrons results in high ionization rates. The heavier ions are non-magnetized. In the discharge channel they follow the electrons and have low energies, keeping the wall contact and therefore sputtering rates small. Only further downstream in the exit region, where the plasma potential drops to vacuum potential, the ions are accelerated and emitted. This generates the thrust. As a whole, HEMP-Ts are efficient electric propulsion devices generating thrust in a wide range of  $1 \mu\text{N} - 100 \text{mN}$  and high specific impulses of  $2000 \text{s}$ , while reducing sputtering erosion and wall losses. This makes the HEMP-T an appealing concept for long-term space missions.<sup>[3]</sup>

Xenon is commonly used as a propellant and considered in this work. It is usually injected with influx rates in the range of  $1-50 \text{sccm}$  at the anode. The applied anode voltage is in the range of  $100-2000 \text{V}$ . More information on HEMP-Ts can be found in Koch et al.<sup>[2]</sup>

Since the general design concept was established, several studies have been conducted on the scaling of the systems, aiming to serve a wide variety of space mission profiles.<sup>[3,4]</sup> These preceding studies were based on experiments, which are an inherently expensive design optimization process. Simulation serves as an affordable method for this and are used increasingly, for example, in car industry.<sup>[5,6]</sup> Kinetic simulations such as particle-in-cell (PIC) are commonly used to simulate low temperature plasmas, like they are used in ion thrusters.<sup>[7-9]</sup> The advantage of this microscopic method is the rather complete inclusion of physics, albeit considerably long run time are required for simulations. To ensure physical accuracy the smallest length and time scales of the discharge have to be resolved, which are the electron Debye length and the plasma frequency in thruster physics. The necessary scales are comparably small considering the large length and time scales, which have to be covered by the simulation. Therefore, PIC simulations are too time consuming to explore a wide variety of thruster designs and other methods are used to optimize thruster designs. Multi-objective design optimization (MDO) represents a new design approach that enables effective search in the design space to optimize the system for performance parameters of primary interest, namely thrust, specific impulse, and total efficiency. The variation parameters used as a basis for the calculation of these performance parameters are the anode voltage, the anode current, the neutral gas mass flow rate, and the inner and outer magnet radii. Each set of these basic parameters defines a different thruster design with a different performance. An MDO study was successfully conducted by coupling evolutionary algorithms with performance analysis incorporating magnetic field simulation, achieving robust global optimization to identify key design parameters and mechanism for HEMP-T scaling.<sup>[10]</sup> The performance was estimated by using a zero-dimensional (0D) power balance equation system for particles, energy, and momentum,<sup>[3]</sup> but some parameters inevitably had to rely on empirical assumptions, rendering it difficult to ensure self-consistency in the system. Empirical assumptions in this case include constant power transfer coefficients, which were originally assumed for a different HEMP-T geometry. In addition other important effects are neglected in the 0D power balance model, especially the influence of neutral gas distribution, ionization efficiency, doubly charged ions, and the details of the ion beam structure. This does not lead to self-consistent solutions of the MDO, but with the application of empiric correction terms, which take into account the neglected effects, the MDO derived several thruster designs, among which a most promising design, called the  $S_1$  thruster,<sup>[10]</sup> is considered in the present study.

In this work this optimized MDO thruster design  $S_1$  is studied with PIC simulations. Firstly, PIC is introduced, followed by the setup of the simulation for the  $S_1$ . The resulting physics characteristics of the  $S_1$  are then compared to other HEMP designs and evaluated. The 0D power balance model is employed to develop additional diagnostics modules to gain further insights to the underlying physics in the  $S_1$ . These diagnostics results are used to compare the estimated MDO input parameters to the ones obtained with the PIC simulation. Finally, the results and key findings are summarized.

## 2 | PARTICLE-IN-CELL MODEL

### 2.1 | Modelling approach

The electron mean-free paths in HEMP-Ts are of the same range as the system size and kinetic effects in the magnetic cusps create non-Maxwellian perturbations of the electron distribution function.<sup>[11]</sup> Hence, a kinetic simulation of the system is necessary for accurate analysis.<sup>[12,13]</sup> In this work an electrostatic 2D3v PIC method with a Monte Carlo Collision model<sup>[14]</sup> is applied. The simulation is electrostatic, because the internal thruster currents induce negligible magnetic fields compared to the field applied by the ring magnets. As a result of the cylindrical symmetry of the thruster the simulation uses cylindrical coordinates  $(r, z)$ . The simulation domain covers the channel and the near exit region. The velocity space is three dimensional for energy and momentum conservation of the collisions.<sup>[14]</sup> The dynamics of electrons  $e^-$ , neutrals Xe, singly charged ions  $Xe^+$ , and doubly charged ions  $Xe^{2+}$  are resolved. The density of doubly charged ions is only a small fraction ( $\approx 10\%$ ) of the singly charged ions. In typical measurements of the HEMP-T the density of higher charged xenon ions is even lower than doubly charged ions ( $<1\%$ ).<sup>[11]</sup> Therefore, higher charged xenon ions are neglected in the simulation. Because of the large number of plasma particles, super particles are introduced, each representing a large number of real particles with the same charge-to-mass ratio as the real particles, which results in identical trajectories. This reduces the computation time, owing to significant reduction of particles to be followed.

The PIC model resolves the dynamics of the particles by following the algorithm schematically shown in Figure 2.

For the PIC model a grid has to be applied to the domain. The charge density of the super particles is weighted onto the grid points with a Cloud-In-Cell (CIC) scheme.<sup>[15]</sup> Afterwards, the Poisson equation is solved on the grid using the weighted charge density with the *SuperLU* package,<sup>[16]</sup> calculating the electric potential. The Lorentz force acting on the particles is computed by weighting the fields on the particles in the cells by using the same CIC scheme to conserve energy and momentum. The particles are then moved using the Boris algorithm.<sup>[17]</sup> In comparison to the electrons, heavier particle species have much lower velocities. In this case, sub-cycling can be applied for the ions and neutrals,<sup>[14]</sup> which means that they are only moved every  $n$ th timestep. For the charged particle species the electric field is averaged between the sub-cycling steps. This leads to a decrease in computing time. Particle boundary effects are also considered in the particle mover.

After the movement the collisions are simulated using Monte Carlo Collisions. In this model direct single and double  $e^-$ -Xe impact ionization, single  $e^-$ - $Xe^+$  impact ionization, integral elastic  $Xe^+$ -Xe collisions (including charge exchange and momentum transfer), and integral elastic and inelastic  $e^-$ -Xe collisions<sup>[11]</sup> are included. Integral collisions here refer to a combined cross section for the possible elastic collisions which can occur.

The PIC algorithm guarantees a physically correct solution if the Debye length and the plasma frequency are resolved,<sup>[18]</sup> while satisfying the Courant-Friedrichs-Lewy condition.<sup>[19]</sup> Further information about the PIC method applied in this work can be found in the works of Tskhakaya et al and Kahnfeld et al.<sup>[14,20]</sup>

A way to reduce computation time for large systems is similarity scaling.<sup>[21]</sup> For kinetic systems like low temperature plasma it is derived from the Boltzmann equation, which describes the distribution function of all plasma species, and the Maxwell equations. Two systems are similar, if the physical parameters scale linearly from one system to the other, for example, the system size. Taking into account the Boltzmann and Maxwell equations, six invariants emerge. The most important invariants for the application on electrostatic systems like ion thrusters are the Hall parameter and the Knudsen number. The first one describes the effect of magnetization on the charged particles, the second one the effect of collisions, in particular ionization. For PIC simulations the system size is a limiting factor, due to higher particle numbers and larger grids. Therefore, a scaling of the system size is introduced, where the velocities and densities remain non-scaled, but the system size and the time scale down linearly. This leads to fewer cells and particles which have to be traced in comparison to the unscaled system, resulting in lower

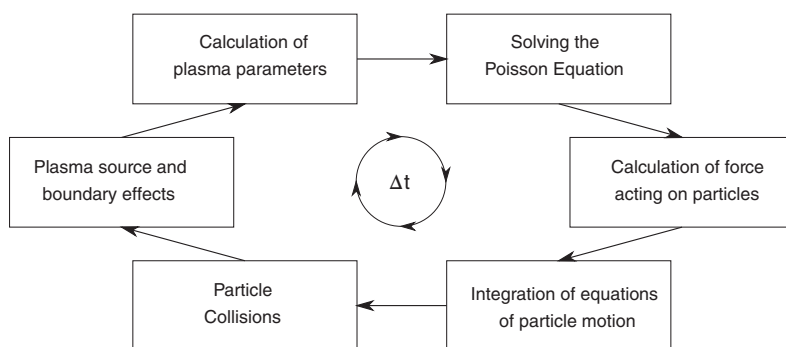


**FIGURE 2** Schematic diagram of the PIC cycle

**TABLE 1** Most important quantities in the self-similarity scaling scheme. The scaling factor is  $\xi$ 

Quantity	Scaling law
Length scale	$x = \tilde{x} \xi$
Time scale	$t = \tilde{t} \xi$
Velocity	$v = \tilde{v}$
Collision cross section	$\sigma = \tilde{\sigma} \xi^{-1}$
Magnetic field	$B = \tilde{B} \xi^{-1}$
Number density	$n = \tilde{n}$

computation time. In Table 1 the most important scalings are shown as applied in the PIC simulation. With the chosen similarity scaling, all volume processes and wall fluxes are conserved, leading to exact solutions in the plasma volume. The limit of the application is the sheath to plasma volume ratio, since the plasma sheath does not scale. If the influence of the sheath is too big, lower scaling factors have to be chosen. An detailed study of the similarity scaling, its application and limits to ion thrusters can be found in works of Lacina and Matthias et al.<sup>[22,23]</sup>

## 2.2 | Simulation setup

The  $S_1$  thruster design has an inner magnet radius of 9.91 mm, an outer magnet radius of 25.1 mm, and a channel length of 21 mm. The ring magnets lead to three cusps at the axial positions  $z = 4.5$  mm and  $z = 17$  mm and one cusp downstream from the exit plane. An electron density of  $n_e = 1 \times 10^{14} \text{ cm}^{-3}$  and a mean electron temperature of  $T_e = 10$  eV in the channel are used as reference parameters for the calculation of the Debye length and the plasma frequency which are used to calculate the grid spacing and time step, respectively. The resulting spatial resolution of the grid is  $dr = 1.76 \times 10^{-4}$  cm with a time step of  $dt = 8.9 \times 10^{-14}$  s. Taking into account the system size of the  $S_1$  design, the domain size is chosen as  $r = 20$  mm and  $z = 50$  mm to resolve the channel and the near exit region, resulting in a computational grid of  $283 \times 709$  cells ( $r, z$ ) with an applied self-similarity scaling factor of  $S_F = 40$ . The chosen similarity scaling factor ensures solutions, where the influence of the non-scaling plasma sheath is still low, so that the plasma volume solution remains close to the non-scaled system.<sup>[21]</sup> In the scaled system one super particle represents 573 real particles resulting in  $8 \times 10^6$  charged and  $20 \times 10^6$  neutral simulated particles. The anode voltage is set at  $U_a = 1000$  V at the left domain boundary according to the optimal operating parameters of  $S_1$ . The top domain boundary and the metal coating around the thruster is grounded and the right-hand side domain boundary at  $z = 50$  mm is set to a constant axial electric field  $E_z = 0$  simulating a vacuum boundary.

Particle boundary conditions are applied, including secondary electron emission with a secondary electron emission yield of 0.5 and thermal ion/neutral recycling at the dielectric, thermal ion/neutral recycling at metal boundaries and the deletion of particles leaving the computational domain. The neutral xenon propellant source is located at the center of the anode, where the neutral particles are injected into the thruster channel with a half-Maxwellian velocity distribution and a mass flow rate of  $\dot{m}_a = 50$  sccm. A neutralizer as a primary source of electrons is applied in the simulation to maintain the plasma in the channel. In the real system the mass flow rate is given as a control parameter for the system, which results in a specific anode current. The neutralizer current adapts accordingly to the same strength as the anode current to avoid electrostatic charging of the thruster. This adaption of the neutraliser current is a non-linear process and happens on a large timescale, compared to the time resolution of PIC. In the simulation it is therefore more feasible to set the electron source current of the neutralizer to match the wanted anode current. In this case, a constant electron current of 800 mA is injected over the right domain boundary. The anode current with the chosen neutralizer strength is slightly lower than the predicted current from the MDO, but with a deviation of  $<10\%$  the PIC simulation is a valid representation of the chosen operating mode. With this setup the PIC simulation is now used to investigate the physical properties of the  $S_1$ .

## 3 | RESULTS

### 3.1 | PIC analysis

Using the PIC code described before, the  $S_1$  design has been analysed and its main characteristics is discussed in this section. The electron density distribution is shown in Figure 3, which drops quickly in the plume because of the loss of confinement

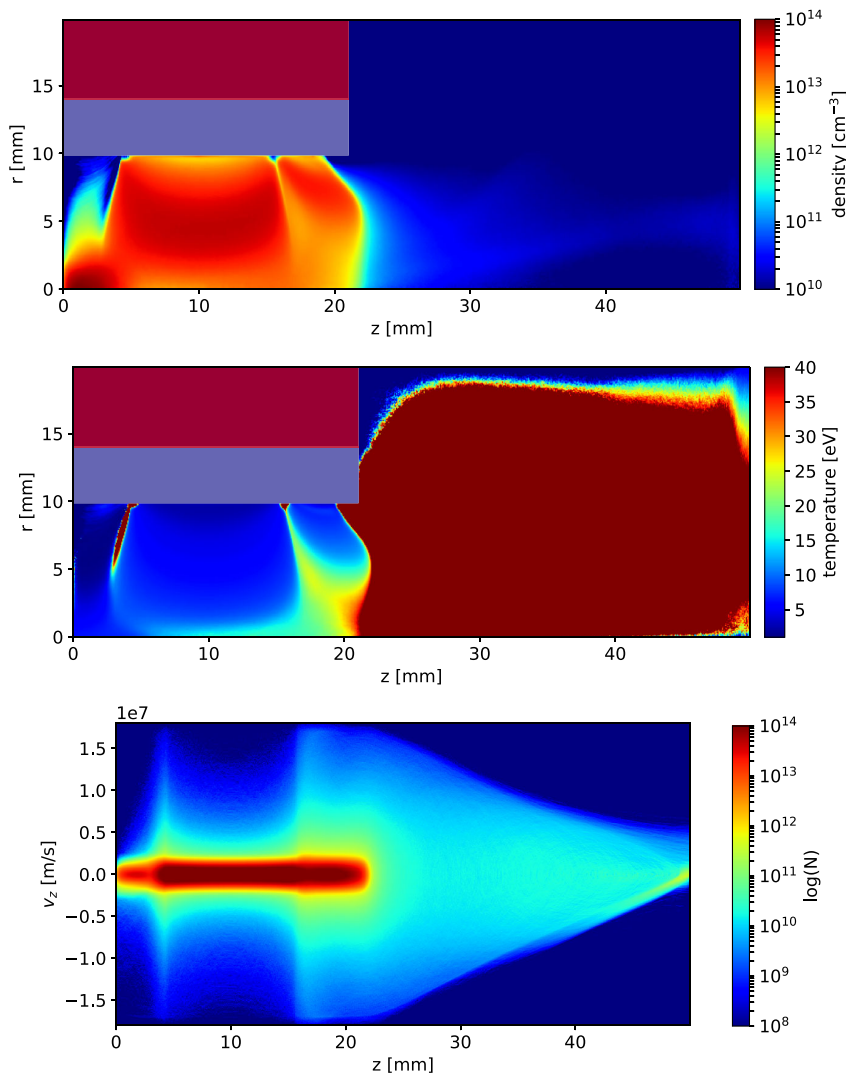


**FIGURE 3** The electron density (top), temperature (middle) and axial velocity (bottom) distribution of the  $S_1$  thruster. The electron source is located at the right domain boundary providing a constant current of electrons of  $I_e = 800$  mA. The grey box at  $r = 9.91\text{--}14$  mm represents the dielectric covering the magnets and is in direct contact to the channel plasma. The red box at the top left of the domain represents the grounded metal surrounding the thruster

for electrons and ions there. The plume electrons drift slowly from the primary source towards the channel exit and become magnetized in the magnetic field. Close to the exit the electrons are accelerated into the channel by the strong axial electric field.

By scattering collisions and anomalous diffusion, transport across magnetic field lines occurs. The anomalous transport is a 3D effect and to apply it in the 2d3v PIC-MCC model an effective anomalous transport coefficient is used for a random walk model in the velocity space.<sup>[11]</sup> This model is similar to a Bohm-like diffusion, with the transport coefficient  $D$  scaling with the electron temperature  $T_e$  and the inverse of the magnetic field  $D \propto T_e/B$ . With self-consistent 3D simulations the value of the diffusion coefficient was deduced.<sup>[11]</sup> The resulting electron energy diffusion perpendicular to the magnetic field lines increases, leading to a transport of the electrons from the outer to the inner magnetic bottle. Accordingly the anomalous transport is important in the cusp regions, where it is responsible for filling the thruster channel, since it increases the probability of electrons traversing the cusp and stream towards the anode.

Inside the thruster channel collisions lead to a decrease of the mean energy with increasing distance to the thruster exit. At the cusps, low energy electrons are reflected and the electron mean energy rises towards the channel wall. With rising mean energy of the electrons, the electron temperature rises in the cusps. Few of the high energy electrons, which are not reflected by the magnetic bottle, hit the wall and lead to secondary electron emission. By the small potential drop at the sheath of approximately 10 V the secondary electrons are accelerated towards the channel plasma, leading to an additional increase of the electron temperature in the cusp region. The total effect of the cusp heating can be seen in the electron temperature distribution in Figure 3. Figure 3 also shows the hot electrons in the plume, where they are accelerated by the strong electric field in front of the thruster exit. Additionally the cool channel area can be seen, where electrons cool down due to collisions with the neutrals and also the local heating effect at the cusp, which is a result of the magnetic mirror effect, is visible.

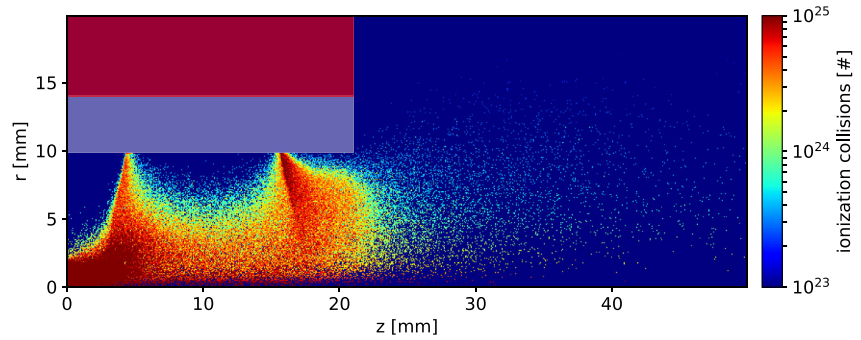


**FIGURE 4** Ionization collisions of the S1 thruster

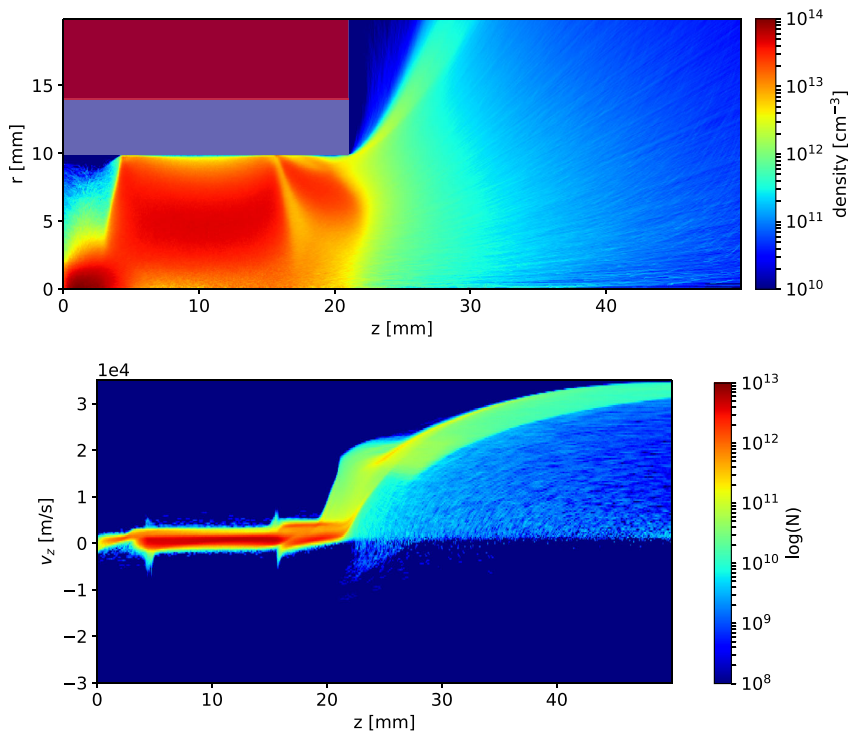
As in other laboratory low temperature plasmas, the mean electron energy (Figure 3) in the thruster channel is in the same range of 1–10 eV, while also populating the higher energy states above 10 eV. In the electron axial velocity distribution EVD in Figure 3, one can see the high energy tail of the electrons in the channel, which is mainly responsible for ionization. The mean electron energies are below the single impact ionization collision threshold energy  $E_{\text{ionize}} = 12.13$  eV of xenon.<sup>[24]</sup> It follows that only the high energy electrons of the hot tail of the energy distribution function contribute to the ionization. This can be seen when comparing the electron energy distribution in Figure 3 and the ionization collisions in Figure 4. From the data it is evident, that the ionization of xenon mainly occurs at the axis and in the cusp region, where the electrons with the highest energies are located. Additionally strong ionization occurs close to the neutral source at the anode, due to the very high neutral gas density and the therefore increased collision probability.

Because of their high energy the mean free path of the electrons is high and losses occur at the intersection of the magnetic field lines and the channel wall, that is, at the cusps. Only at the cusps in the channel the plasma connects to the wall. However, wall losses are small because the electrons are reflected by the magnetic mirror there. This results in a pendulum motion of the electrons between the cusps, where they are trapped and move along the magnetic field lines, which are mostly parallel to the symmetry axis. The symmetric axial EVD in the channel is a consequence of the electron trapping. The good electron confinement leads to an increased ionization efficiency and high ionization rates in the plasma channel.

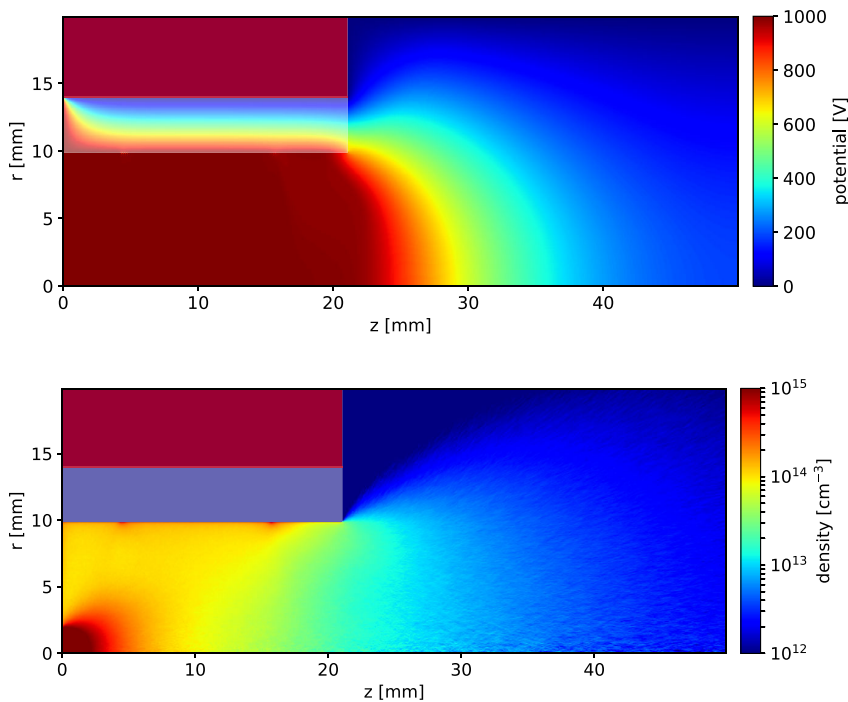
As a result of quasi-neutrality in the plasma the ion density distribution is similar to the electrons, as seen in Figure 5. The ions drift slowly in the thruster channel and are accelerated at the exit leaving the thruster with a certain angular distribution. The low energies of the ions in the channel lead to very low sputtering rates.<sup>[2]</sup> The generated thrust strongly depends on this angular ion current distribution, which will be discussed later in detail. The strong electric field at the thruster exit accelerates the ions towards the anode potential. Because of the grounded coating of the thruster the ions in the plume with high emission angles get accelerated towards the metal coating of the thruster. This is shown by the ions in the IVD with negative axial velocities downstream, as observed in the region ranging from  $z = 21$ – $26$  mm, as shown in Figure 5. The particle number of the doubly charged xenon ions is only 10.8% of that of the singly charged ions. They are emitted with the same angular profile as the singly charged ions, while they receive double the energy through the electric field at the exit. Otherwise they behave like the singly charged ions and are not considered further in the following discussions, except their contribution to the thrust.

Figure 6 displays the electric potential in the simulation of the  $S_1$ . The flat potential in the channel and the steep potential drop close to the exit region ( $z \approx 25$  mm) are present. The dominant axial transport of the electrons near the axis with a strong axial magnetic field leads to a flat potential in the thruster channel. The contact of the plasma to the wall is limited to the intersection of the magnetic field lines with the dielectric wall. In the other regions the wall contact of electrons is significantly reduced. As a result, a positive surface charge is building up at the wall contact regions from the impinging ions, which leads to a potential at the wall in the same range as the plasma potential. The applied dielectric extends to the exit of the  $S_1$  and even covers the outside surface of the thruster. Due to the magnetization and the geometry of the magnetic field lines, the electrons do not impinge on the outer surface of the dielectric. Therefore, mostly exiting ions impinge on the outer dielectric surface, lead to a positive surface charge and to an increase of the potential in the near exit region. The influence of the grounded metal coating of the thruster is rather weak, because of the larger distance away from the plasma and the compensation of the influence due to the surface charge building up at the dielectric. As a consequence the potential expands into the plume and results in a nearly isotropic potential drop outside of the thruster. At the exit the potential drops as a result of lower plasma densities until it reaches vacuum potential, which is typical of HEMP-Ts.<sup>[2]</sup> This is similar to gridded ion thrusters but without a grid at the thruster exit.

The resulting electric field accelerates the neutralizer electrons towards the thruster channel and leads to strong ionization in the exit region. The neutral density distribution drops accordingly close to the thruster exit (see Figure 7). Additionally, a higher local neutral density at the cusps in the channel can be observed. Here, the plasma wall contact produces thermal neutral xenon particles by recycling of impinging ions.



**FIGURE 5** Xe<sup>+</sup> density (top) and axial velocity (bottom) distribution of the S<sub>1</sub> thruster



**FIGURE 6** The electric potential in the channel and the near plume region in the S<sub>1</sub> thruster. The anode is located at  $z = 0$  mm and reaches from  $r = 0$ –9.91 mm

**FIGURE 7** Neutral xenon density distribution in the S<sub>1</sub> thruster. The gas inlet is located at  $r = z = 0$  mm and releases 50 sccm of neutral xenon gas in the channel with a half-Maxwellian velocity distribution

One of the most important characteristics of ion thrusters is the angular ion current distribution in Figure 8. It shows the ion current expelled by the thruster as a function of the different emission angles. Low emission angles improve the efficiency of a thruster, since they result in higher axial to radial energy ratios and minimize interaction with the satellite components. The angular current slowly rises with higher angles and peaks at 65°, which is similar to other HEMP-Ts with mean exit angles of  $\approx 60^\circ$ .<sup>[2]</sup>

To understand the composition of the angular ion current distribution, the dependency of the ion origins and emission angles must be considered. This is achieved by storing each particle's location at creation and registering the particle in the angle bin when it leaves the domain.<sup>[8]</sup> The results are visualized in Figure 8. For angle bins of 10° in the range of 0–90°, the main areas of origin per angle bin are shown with a confidence interval from 30 to 70%. The ions produced in the channel and near the

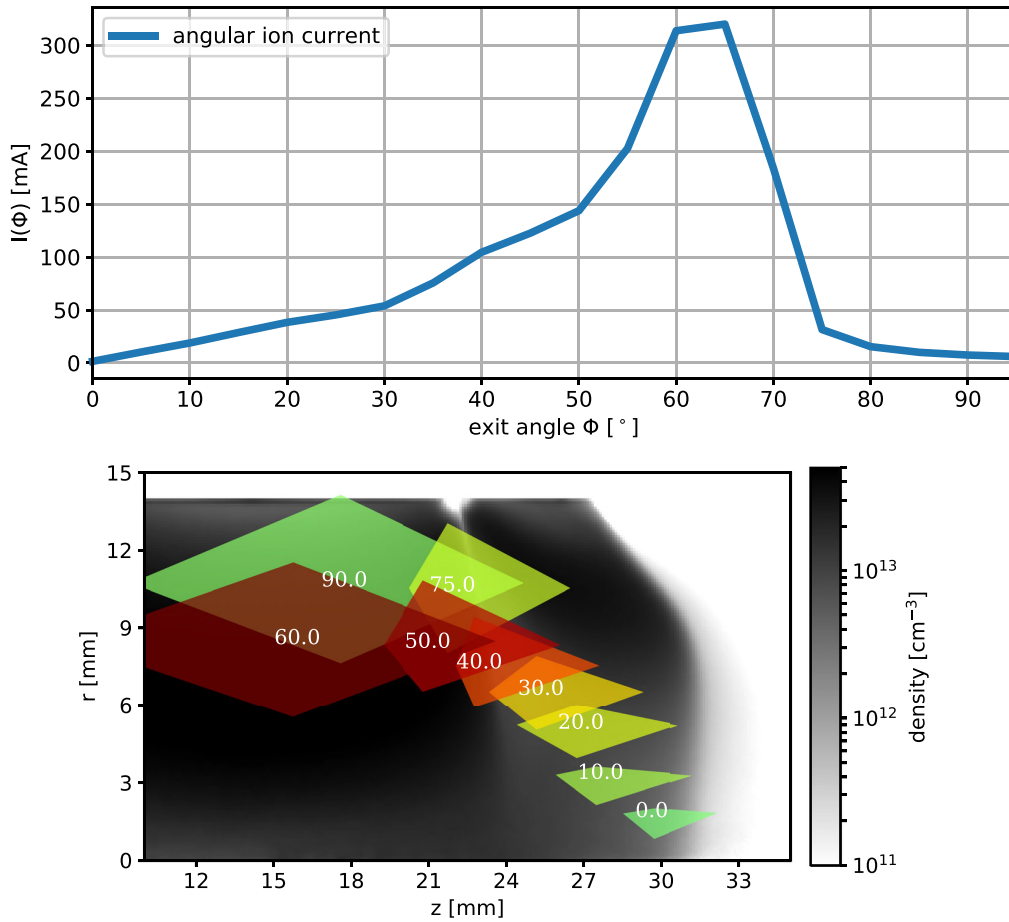


**FIGURE 8** Angular ion current distribution of the  $S_1$  thruster (top) and the mean  $\text{Xe}^+$  ionization origins for specific angles of the angular current distribution (bottom). The colour of the patches indicate the ratio from the specific angle to the total beam current, from low (green) to high (red). In the background the electron density distribution at the channel exit is shown in grayscale

symmetry axis undergo a higher axial electric field contributing to lower angles, while ions created away from the axis near the exit region experience a more radially oriented electric field (see Figure 8) populating the higher angle bins. Because of the high mass flow rate of 50 sccm leading to a high neutral density in the channel the plasma extends towards the exit, leading to an increased potential at the exit. This results in a higher ion mean emission angle and thus, as already discussed, reducing the contribution to the thrust.

To improve the emission characteristics it would be better to increase the channel length. The neutral density towards the channel exit would further decrease while the mean free path of the electrons increases. The potential would shift into the channel instead of downstream from the exit. This would result in smaller emission angles, as discussed in the study of Kahnfeld et al.<sup>[25]</sup> However, an increased channel length would result also in increased wall losses and hence in a reduction in the efficiency. Therefore, the channel length should be considered as an additional optimization parameter to identify the optimum ratio between emission angle and efficiency in the MDO.

Another way to improve the beam structure would be to opt for a lower anode current and therefore lower plasma density scenarios, while keeping the mass flow rate constant. This is realized by a lower neutralizer current in the simulation (Figure 9). Higher neutralizer currents lead to higher emission angles while increasing the beam current, too. The increased ion beam current gives higher ionization and therefore higher efficiency. The dependency of the anode current on the operating state is yet to be considered in the MDO.

To compare the PIC results to the MDO, the calculation of the performance parameters thrust  $T$ , efficiency  $\eta_t$  and specific impulse  $I_{sp}$  is required. For discrete angle bins  $i$  the thrust is calculated<sup>[26]</sup> as

$$T(\Phi) = \sum_i m_i v_{i,\text{exit}} \cdot \cos(\Phi_{i,\text{exit}}), \quad (1)$$

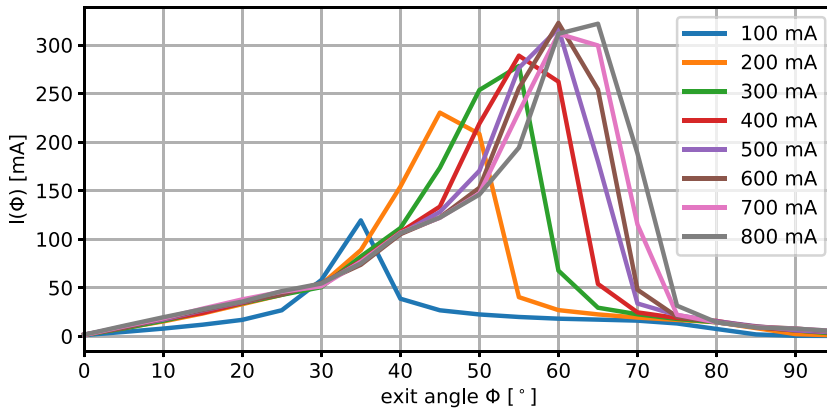


**FIGURE 9** Angular  $\text{Xe}^+$  current distribution for different neutralizer currents

with  $\dot{m}_i$  the ion mass flow leaving the the domain,  $v_{i, \text{exit}}$  the emitted ion velocity and  $\Phi_{i, \text{exit}}$  the emission angle of the ion. The potential at the simulation domain boundary is not at vacuum potential, leading to lower ion exit velocities when they leave the simulation domain. Using the potential at the domain boundary, an additional correction term for the ion velocities is applied in a postprocessing step. The corrected ion velocities are used in the calculation of the thrust. The specific impulse

$$I_{\text{sp}} = \frac{T}{\dot{m}_{\text{Xe}} g} \quad (2)$$

with  $\dot{m}_{\text{Xe}}$  the mass flow of the neutral source and  $g = 9.81 \text{ m/s}^2$ , can be calculated directly from the obtained thrust. The efficiency  $\eta_t$  in the MDO is the anode efficiency.<sup>[10]</sup>

$$\eta_t = \frac{T^2}{2\dot{m}_{\text{Xe}} U_a I_a}, \quad (3)$$

with the anode voltage  $U_a$  and the anode current  $I_a$ .

The calculated performance parameter of PIC in Table 2 show significant differences from the MDO values, even in consideration of the 10% deviation of the anode current.

In the MDO the mean ion emission angle, energy transfer coefficients and cusp arrival probabilities of the electrons, were treated as constant input parameters obtained from experimental measurements of a different HEMP-T model.<sup>[3,10]</sup> The different thruster geometry and operating conditions makes the validity of this approach uncertain. This is confirmed by the differences between the predicted performance parameters from the MDO and PIC, seen in Table 2. To investigate these differences, the input parameters from the MDO are reproduced using the kinetic information of the PIC simulation. For this reason new diagnostic routines are implemented in the PIC simulations based on the 0D power balance model.<sup>[3]</sup> Afterwards the parameters obtained are compared to the input values used in the MDO.

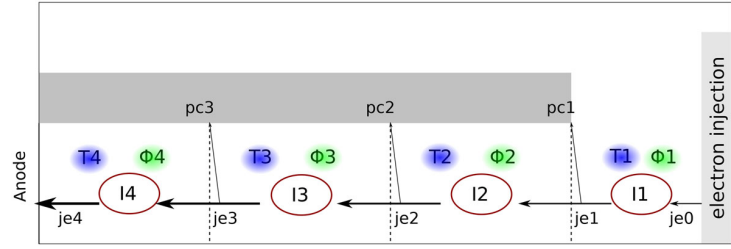
### 3.2 | 0D power balance diagnostic in PIC

The equations of the 0D power balance model, given by Kornfeld et al.<sup>[3]</sup> are outlined below. The parameters used in these equations are sketched in Figure 10. The channel of the thruster is divided into four regions between the cusps for a three ring magnet system. In these regions, constant local properties such as electron temperature  $T$ , potential  $\Phi$ , and ionization  $I$  are assumed. A constant current of electrons  $je$  and the probability for electrons to impinge on the wall  $pc$  are assumed at the interfaces of these regions.

**TABLE 2** Comparison of performance parameters between the MDO and the results based on the PIC simulation

	$I_a$ (A)	T (mN)	$\eta_t$ (%)	$I_{\text{sp}}$ (s)
MDO	2.94	102.7	36.5	2131
PIC	2.66	62.8	15.2	1333

**FIGURE 10** Schematic of a HEMP thruster with the most important quantities of the power balance model as found in Kornfeld et al.<sup>[3]</sup> The dashed lines mark the cusp positions.  $je_i$  denotes the electron current, which increases closer to the anode because of ionization. The ionization current  $I_i$ , the electron temperature  $T_i$  and the potential  $\Phi_i$  are given between the cusps



Using the anode voltage  $U_a$ , anode current  $I_a$  and an electron current from the neutralizer  $je_0$  as input parameters one can solve for the remaining properties including the cusp arrival probabilities  $pc_i$  for electrons. The following equations are derived from the power balance equations for the different cusp arrival probabilities  $pc_i$

$$pc_i = 1 - \frac{je_i - I_i}{je_{i+1}} \quad \text{for } i = 1, 2, 3. \quad (4)$$

These are the probabilities of electrons reaching the dielectric at the cusp by comparing the incoming and outgoing electron current  $je_i$  and  $je_{i+1}$  and considering the ionization current  $I_i$  as an additional electron source. These currents can be directly extracted from the PIC results by integrating electron currents and ionization rates in each region. From the PIC results the cusp arrival probabilities can be calculated and are listed in Table 3.

Of particular importance in the power balance model are empirical estimates for the global energy transfers in the system. They are given by the relative proportion of the gained electron power transferred to excitation  $CE$  and the proportions for ionization  $CI$  and thermalization  $CT$ . These transfer parameters again can be calculated self-consistently using the PIC results. From the power balance model one obtains

$$CE_i = 1 - \frac{(je_{i-1}(1 - pc_i) + I_i)T_i + I_i IE}{je_{i-1}(1 - pc_i)(\Phi_i - \Phi_{i-1} + T_{i-1})}, \quad (5)$$

$$CT_i = \frac{T_i je_i}{je_{i-1}(1 - pc_i)(\Phi_i - \Phi_{i-1} + T_{i-1})}, \quad (6)$$

$$CI_i = \frac{I_i IE}{je_{i-1}(1 - pc_i)(\Phi_i - \Phi_{i-1} + T_{i-1})}, \quad (7)$$

$$1 = CE_i + CT_i + CI_i, \quad (8)$$

for the relative energy transfer proportions, with the ionization energy of xenon  $IE = 12.1$  eV and the parameters from Figure 10. These coefficients represent the fractions of the total electron energy loss.  $CT$  is the ratio of the electron heat flux in one cell compared to the incoming total electron energy into the cell.  $CI$  is the ratio of electron energy transferred into ionization processes by multiplying the ionization number with the ionization energy. At last  $CE$  is considered as the rest of the energy losses of the electrons, coming from the excitation collisions with neutrals. For easier comparison the different proportions are summed up over the areas of the thruster and then averaged, as only global energy transfer coefficients are assumed in the MDO. The results for the proportions and calculated cusp arrival probabilities are given in Table 3.

The results in Table 3 show a significant difference in cusp arrival probabilities and in the energy transfer coefficients between the MDO input parameters<sup>[3]</sup> and the PIC simulations. The power transfer to excitation  $CE$  and ionization  $CI$  was overestimated in the MDO, whereas the thermalization  $CT$  was underestimated. The calculated cusp arrival probabilities, especially of the

**TABLE 3** Comparison of the input parameters between the MDO and self-consistently calculated coefficients based on PIC simulation

Case	CE	CI	CT	$pc_1$	$pc_2$	$pc_3$	$pc_4$
MDO	0.25	0.07	0.68	0.06	0.119	0.160	0.254
PIC	0.40	0.18	0.42	0.23	0.56	0.07	0.014

exit and the first cusps, are four to five times higher than in the empirical data while the arrival probability at the anode cusp is significantly lower. These differences can be explained by the different assumptions made for the  $S_1$  thruster in comparison to the considered thrusters used for the original 0D power balance model. There, the anode current was fixed at  $I_a = 1$  A, because no ionization cross sections and no neutral gas flow assumptions were made in the model. However, the resulting anode current of the MDO is three times higher, which extrapolated the model outside its validation range. As already discussed, the operating state, defined by the anode current, strongly influences the solution of the thruster. This changes the values of the cusp arrival probabilities and transfer coefficients.

The strong axial electric field at the exit accelerates the electrons towards the thruster channel up to anode potential. The electric fields and the magnetic field lines are nearly parallel at the exit leading to a strong magnetization of the electrons. Because of the low plasma and neutral density there, the electrons follow the magnetic field mostly undisturbed. The high parallel velocity of the electrons to the magnetic field leads to a higher probability of reaching the wall at the exit cusp  $pc_1$  and the first cusp in the channel  $pc_2$ . These cusp arrival probabilities reflect the discussion of the plasma properties from above.

In the process of this work, PIC simulations were carried out for different points of operation with constant anode voltage of 1000 V and mass flow rate of 50 sccm by varying the neutralizer and consequently the anode current. The transfer coefficients (CE, CI, and CT) from PIC simulations show little variations for different anode currents, which implies that the energy transfer coefficients can be considered nearly constant for one thruster design and different anode currents (Table A1).

Table 3 indicates that the excitation and ionization energy transfer coefficients were underestimated in the MDO model, while the thermalization was overestimated. Taking into account the higher probability of hot electrons reaching the channel wall, as the higher cusp arrival probabilities imply, it follows immediately that the coefficient of energy transfer to thermalization CT of the PIC simulation is lower.

The model from Kornfeld et al.<sup>[3]</sup> does not account for the influence of neutral gas density distribution, ionization efficiency, doubly charged ions or the details of the ion beam structure and assumes constant temperature in the considered cells. Nonetheless the 0D power balance model is a robust tool, which usefully enabled the MDO, resulting in a working HEMP-T design. The present study suggests that the approach is valid within one design where interpolation can be used across existing operational points, but it becomes inaccurate for different designs or in extrapolation mode, which therefore needs independent assessment.

## 4 | CONCLUSIONS AND OUTLOOK

In this work an optimized thruster design, the  $S_1$  thruster derived by the MDO, was investigated using the PIC method. The results of the simulation were discussed and it was found that the  $S_1$  thruster is characterized by comparable physical properties to other HEMP-Ts. With the charged particle distributions the performance parameters were calculated and compared to the predictions of the MDO, revealing considerable difference. To understand the deviation between PIC and the MDO, the fully kinetic results from PIC were used to investigate the 0D power balance model, used in the MDO. Substantial difference was found in the energy transfer properties and cusp arrival properties. Using the new physical parameters obtained with PIC, the MDO results could be improved. Further, new strategies and parameters for optimization were proposed. The results from this enhancement will be published in the future. This collaboration between PIC and the MDO paves the way for design optimization, combining optimization algorithms and fully kinetic models in conjunction with surrogate modelling.

## ACKNOWLEDGMENTS

The work of P.M. and D.K. was funded by the German Space Agency DLR through Project 50RS1510. The work of S.H.Y. was supported by the Australian Government Research Training Program (RTP) Scholarship. The authors are thankful to Angus Muffatti and Thomas Fahey for the original development of the optimization process chain incorporating the performance analysis and magnetic field simulation.

## ORCID

Paul Matthias  <https://orcid.org/0000-0002-5968-6647>

## REFERENCES

- [1] G. Kornfeld, N. Koch, G. Coustou, in *28th IEPC Electric Rocket Propulsion Society*, Toulouse, France **2003**, 1–18.

- [2] N. Koch, M. Schirra, S. Weis, A. Lazurenko, B. van Reijen, J. Haderspeck, A. Genovese, P. Holtmann, R. Schneider, K. Matyash, O. Kalentev, in *32nd IEPC*, Electric Rocket Propulsion Society, Wiesbaden, Germany **2011**, 1–8.
- [3] G. Kornfeld, N. Koch, H. Harmann, in *30th IEPC*, Vol. 108, Electric Rocket Propulsion Society, Florence, Italy **2007**, 17–20.
- [4] A. Keller, P. Köhler, F.G. Hey, M. Berger, C. Braxmaier, D. Feili, D. Weise, U. Johann, in *33rd IEPC*, IEEE, Washington, DC **2013**, 45–53.
- [5] R. Allen, D. Lee, D. Klyde, G. Howe, J. P. Chrstos, T. Rosenthal, in *1st Hum. Center. Transport. Simul. Conf.*, Iowa-City, IA **2001**, 1–14.
- [6] D. E. Smith, J. O. M. Starkey, *Veh. Syst. Dyn.* **1995**, 24(2), 163.
- [7] D. Kahnfeld, R. Schneider, F. Cichocki, M. Merino, E. Ahedo, J. Duras, N. Koch, in *35th IEPC*, Electric Rocket Propulsion Society, Atlanta, Georgia **2017**, 1–10.
- [8] J. Duras, D. Kahnfeld, G. Bandelow, S. Kemnitz, K. Lüsow, P. Matthias, N. Koch, R. Schneider, *J. Plasma Phys.* **2017**, 83, 595830107.
- [9] P. Matthias, R. Schneider, R. Heidemann, F. Holtmann, D. Kahnfeld, K.-F. Lüsow, in *35th IEPC*, Electric Rocket Propulsion Society, Atlanta, Georgia **2017**, 1–8.
- [10] T. Fahey, A. Muffatti, H. Ogawa, *Aerospace*. **2017**, 2017(4), 55.
- [11] O. Kalentev, K. Matyash, J. Duras, K.-F. Lüsow, R. Schneider, N. Koch, M. Schirra, *Contrib. Plasma Phys.* **2014**, 54(2), 235.
- [12] C. K. Birdsall, A. B. Langdon, *Plasma Physics via Computer Simulation*, CRC Press, Boca Raton, Florida **2004**.
- [13] K. Matyash, O. Kalentev, R. Schneider, F. Taccogna, N. Koch, M. Schirra, in *31st IEPC*, Vol. 110, Electric Rocket Propulsion Society, Ann Arbor, MI **2009**, 20–24.
- [14] D. Tskhakaya, K. Matyash, R. Schneider, F. Taccogna, *Contrib. Plasma Phys.* **2007**, 47(8–9), 563.
- [15] C. K. Birdsall, D. Fuss, *J. Comput. Phys.* **1969**, 3(4), 494.
- [16] S. Li Xiayoe, J.R. Gilbert, J.W. Demmel **1999**. [https://crd-legacy.lbl.gov/~xiaoye/SuperLU/superlu\\_ug.pdf](https://crd-legacy.lbl.gov/~xiaoye/SuperLU/superlu_ug.pdf).
- [17] J. P. Boris, in *Proc. Fourth Conf. Numer. Simul. Plasmas*, **1970**.
- [18] C. K. Birdsall, N. Maron, *J. Comput. Phys.* **1980**, 36(1), 1.
- [19] R. Courant, H. Lewy, K. Friedrichs, *Math. Ann.* **1928**, 100, 32–74.
- [20] D. Kahnfeld, J. Duras, P. Matthias, S. Kemnitz, P. Arlinghaus, G. Bandelow, K. Matyash, N. Koch, R. Schneider, in *t.b.p.*, **2019**.
- [21] F. Taccogna, S. Longo, M. Capitelli, R. Schneider, *Phys. Plasmas* **2005**, 12(5), 053502.
- [22] J. Lacina, *Plasma Phys.* **1971**, 13(4), 303.
- [23] P. Matthias, D. Kahnfeld, S. Kemnitz, J. Duras, N. Koch, R. Schneider, Similarity scaling - application and limits for High-Efficiency-Multistage-Plasma-Thruster PIC modeling, IOP Publishing **2019**.
- [24] M. Hayashi, in *NIFS-DATA-79*, NIFS, **2003**. <http://www.nifs.ac.jp/report/NIFS-DATA-079.pdf> (accessed: October 2018).
- [25] D. Kahnfeld, R. Heidemann, J. Duras, P. Matthias, G. Bandelow, K. Lüsow, S. Kemnitz, K. Matyash, R. Schneider, *Plasma Sourc. Sci. Technol.* **2018**, 27(12), 124002.
- [26] D. M. Goebel, I. Katz, *Fundamentals of Electric Propulsion: Ion and Hall Thrusters, of JPL Space Science and Technology Series*, Wiley, Hoboken, New Jersey **2008**.

**How to cite this article:** Matthias P, Kahnfeld D, Schneider R, Yeo SH, Ogawa H. Particle-in-cell simulation of an optimized high-efficiency multistage plasma thruster. *Contributions to Plasma Physics*. 2019;e201900028. <https://doi.org/10.1002/ctpp.201900028>

## APPENDIX: A POWER BALANCE MODEL COEFFICIENTS AT DIFFERENT OPERATION STATES

**TABLE A1** Comparison of the input parameters between the MDO and self-consistently calculated coefficients based on the PIC simulation at different points of operation

Case	CE	CI	CT	$pc_1$	$pc_2$	$pc_3$	$pc_4$
MDO	0.25	0.07	0.68	0.06	0.119	0.160	0.254
200 mA	0.37	0.23	0.40	0.28	0.54	0.10	0.010
300 mA	0.33	0.22	0.45	0.31	0.64	0.10	0.010
400 mA	0.37	0.18	0.45	0.32	0.44	0.09	0.015
500 mA	0.33	0.20	0.47	0.31	0.50	0.09	0.013
600 mA	0.37	0.21	0.43	0.32	0.56	0.10	0.015
700 mA	0.39	0.18	0.43	0.21	0.50	0.09	0.012
800 mA	0.40	0.18	0.42	0.23	0.56	0.07	0.014



## 7 Erklärung

Hiermit erkläre ich, dass diese Arbeit bisher von mir weder an der Mathematisch - Naturwissenschaftlichen Fakultät der Universität Greifswald noch einer anderen wissenschaftlichen Einrichtung zum Zwecke der Promotion eingereicht wurde. Ferner erkläre ich, dass ich diese Arbeit selbständig verfasst und keine anderen als die darin angegebenen Hilfsmittel und Hilfen benutzt und keine Textabschnitte eines Dritten ohne Kennzeichnung übernommen habe.

---

(Daniel Lars Kahnfeld)

Greifswald, September 26, 2019



## 8 Acknowledgements

At this point I would like everyone who helped me during the compilation of this thesis. First and foremost I want to express deep gratitude to my supervisor Prof. Dr. Ralf Schneider. His constant support, guidance and the enlightening discussions substantially aided the completion of this thesis. He has created a great work environment within the CompuS group from which I want to thank all my current and former co-workers. Especially I want to thank Paul Matthias, Lars Lewerentz, Karl Luskow, Julia Duras, Gunnar Bandelow, Stefan Kemnitz, Marc Marschall and Peter Arlinghaus, who are not only colleagues but also friends. Our discussions on physical and numerical problems were fruitful and resulted in great collaborations. We traveled together, laughed together and had a lot of fun during our regular coffee breaks. My gratitude also goes out to Uwe Bittermann, who was always helping out with administrative matters and was never shy of a good anecdote. I also want to thank the German Space Agency DLR whose funding allowed me to work on this interesting topic and brought me to some great places at international conferences.

I am greatly indebted to my girlfriend Jenny Arndt for her ceaseless patience and support during my studies. She always cheered me up when I was down and motivated me on bad days. I am looking forward to more wonderful years with her. To my parents, Petra and Michael Kahnfeld, thank you for all the trust and support during all my studies. Last but not least, I thank all my friends who always helped me take my mind off of work during many great days and nights.